

**Pilkington Library**

Author/Filing Title ..... EAD E .....

.....

Vol. No. .... Class Mark ..... T .....

**Please note that fines are charged on ALL  
overdue items.**

**FOR REFERENCE ONLY**

0402587820



# **Investigation of Open Periodic Structures of Circular Cross Section and their Transition to Solid Circular Waveguide.**

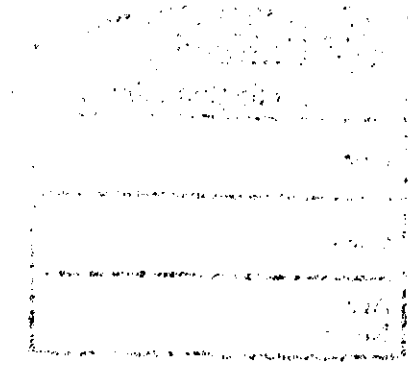
By

James C. Eade B.Eng(Hons) A.M.I.E.E


A Doctoral Thesis

Submitted in partial fulfillment for the requirements for the award of the  
degree of Doctor of Philosophy of Loughborough University

November 2000



© by J.C.Eade 2000

 <b>Loughborough University</b> Pilkington Library
Date <i>May 2</i>
Class
Acc No. <i>040258782</i>

## **Abstract**

Previous work has already modelled an open periodic cylindrical tube constructed from a Frequency Selective Surface (FSS), to form the Frequency Selective Guide (FSG). This model is used to expand the understanding of the FSG and known mode content that it can support. The results of the model have been authenticated directly by measurement techniques. The range of FSGs measurements undertaken was expanded to enable greater understanding of the structure utilising parameters that could not be included in the theoretical model. This extensive measurement set combines with the modelled data to provide a very comprehensive understanding of the FSG operation based on both physical and theoretical data. This extensive knowledge of the FSG performance will be utilised in the solution of the junction between a solid circular waveguide and the FSG. The theory is developed to model the junction using mode matching techniques. The assumptions made and the complications encountered due to the open nature of the structure are discussed. Reasons are given for the poor agreement between the computer simulation using the mode matching theory and the measured results. An alternative junction modelling technique, finite element method, is then used to obtain good agreement with the measured data. This method produced data detailing the field distribution of the modes within the FSG and the affect upon them of the transition. This gave an invaluable insight into the mechanism of operation of both the FSG and the junction.

### **Keywords**

Frequency Selective Surface (FSS)

Frequency Selective Guide (FSG)

Waveguide

Transition/Junction Modelling

Mode Matching

Finite Element

## **ACKNOWLEDGEMENTS**

I would like to thank my supervisor R.D.Seager for all his help and support during the course of this research. He has guided me through the bad times with lots of encouragement and has always been an understanding listener. Thank you Rob, and I wish you further success with the research and with the blossoming family.

I must also thank Loughborough University and particularly the Department of Electronic and Electrical Engineering for it's financial assistance in allowing me to undertake this research.

I am grateful to Gavin Cox for carrying out some of the scattering parameter and radiation pattern measurements used in this thesis. The measurement of some of the FSGs, numbers 3,4&5, used in the parameter study was an invaluable contribution.

I wish to express a great deal of gratitude to Dr. Jonathan Whitehurst and BAE Systems, Cowes, I.o.W. for the use the computing facilities, HFSS and for their continued support while writing up. The use of these facilities has added a great deal of extra scope and content to this thesis.

A big vote of thanks must also go Prof. J.C.Vardaxoglou and all the members of the Loughborough microwave research group. Dave, Nico, Mohan, Gavin and George you have all been good friends and we have helped each other through it all.

Finally, but not least, to Kirstie, my parents and family, thank you for all the unquestioning love and support over these hard and often trying years. I appreciate you more than I can express. Also thank you to everyone in Faraday, Dave, Stephen, Nic, Chris & Sarah you made this work a little more interesting!

# Table of Contents

<b>1. INTRODUCTION .....</b>	<b>3</b>
1.1 FSS BACKGROUND.....	5
1.2 THE BASIC FSG.....	6
1.3 TRANSITION PROBLEM DEFINITION .....	8
1.4 STRUCTURE OF THE THESIS .....	11
1.5 REFERENCES.....	12
<b>2. EXTENSION OF EXISTING FSG MODE THEORY. ....</b>	<b>15</b>
2.1 LITERATURE RELATING TO EXISTING LEAKY WAVE OPEN STRUCTURES.....	15
2.2 DETERMINATION OF MODE CONTENT OF FSG.....	21
2.3 NATURE OF MODES WITHIN THE FSG .....	29
2.4 IMPLICATIONS OF $k$ - $\beta$ DIAGRAMS ON ASCERTAINING THE PROPERTIES OF AN FSG MODE.....	43
2.5 REFERENCES.....	50
<b>3. INVESTIGATION OF FSG BY MEASUREMENT METHODS.....</b>	<b>53</b>
3.1 FSG DESIGN.....	53
3.2 DIMENSIONS OF THE FSG .....	56
3.3 FSG MANUFACTURE .....	56
3.4 MEASUREMENTS & CHARACTERISATION OF THE INITIAL FSG PRODUCED .....	60
3.4.1 <i>Set-up and measurement of Planer FSS sheet before being made into an FSG.....</i>	<i>60</i>
3.4.2 <i><math>S_{11}</math> &amp; <math>S_{21}</math> Test Equipment Set-up .....</i>	<i>62</i>
3.4.3 <i><math>S_{11}</math> &amp; <math>S_{21}</math> Measurement.....</i>	<i>63</i>
3.4.4 <i><math>S_{11}</math> &amp; <math>S_{21}</math> Interpretation .....</i>	<i>65</i>
3.4.5 <i>Radiation Pattern Equipment Set-up.....</i>	<i>68</i>
3.4.6 <i>FSG Radiation Patterns .....</i>	<i>69</i>
3.5 $S_{21}$ & $S_{11}$ PARAMETRIC STUDY BY MEASUREMENT METHODS .....	72
3.6 EXTRACTION OF FSG PROPAGATION CONSTANT .....	87
3.6.1 <i>Calculation of Propagation Constant from <math>S_{21}</math> measurements.....</i>	<i>88</i>
3.6.2 <i>Calculation of Propagation Constant from Radiation Pattern Measurement.....</i>	<i>100</i>
3.6.3 <i>Calculation of Propagation Constant from Short Circuit Radiation Patterns.....</i>	<i>102</i>
3.6.4 <i>Summary of Calculation of <math>\alpha</math> and <math>\beta</math> .....</i>	<i>106</i>
3.7 CONCLUSIONS AND COMMENTS ON FSG MEASUREMENTS .....	107
3.8 REFERENCES.....	108
<b>4. TRANSITION ANALYSIS BY MODE MATCHING METHOD. ....</b>	<b>109</b>
4.1 EXISTING WAVEGUIDE JUNCTION MODELLING TECHNIQUES .....	109
4.2 MODAL ANALYSIS OF WAVEGUIDE STEP JUNCTIONS .....	111
4.2.1 <i>FSG to Solid Waveguide Mode Matching with FSG as Feed.....</i>	<i>112</i>
4.2.2 <i>Solid Waveguide to FSG Mode Matching with Solid Waveguide as Feed.....</i>	<i>126</i>
4.3 DEVELOPMENT OF MODE MATCHING PROGRAM .....	129
4.3.1 <i>Solid Waveguide Step Discontinuity Program .....</i>	<i>130</i>
4.3.2 <i>FSG to Solid Waveguide Mode Matching Program.....</i>	<i>131</i>
4.3.3 <i>Solid Waveguide Integrals .....</i>	<i>133</i>
4.3.4 <i>FSG Integral Equations .....</i>	<i>135</i>
4.3.4.1 <i>Integration of the "FSG normalisation" Equation.....</i>	<i>138</i>
4.3.4.2 <i>Integration of the "Across Junction" Equation .....</i>	<i>141</i>
4.3.5 <i>Structure of Program .....</i>	<i>145</i>
4.4 PROGRAM TESTING & RESULTS. ....	146
4.5 REFERENCES.....	150
<b>5. TRANSITION ANALYSIS BY FINITE ELEMENT METHOD.....</b>	<b>153</b>
5.1 FUNDAMENTALS OF FINITE ELEMENT METHOD .....	154
5.1.1 <i>Presentation of Results Produced by HFSS. ....</i>	<i>156</i>
5.2 DEVELOPMENT OF TRANSITION MODEL .....	158

5.3	RESULTS OF HFSS SIMULATION OF AN FSG SIX WHOLE RINGS IN LENGTH WITH A SINGLE FEED PORT.....	168
5.3.1	<i>S<sub>11</sub> Results for the Six Element Whole Ring FSG Model – Measured and Simulated...</i>	170
5.3.2	<i>HFSS Field Plots of the Six Element Whole Ring FSG Model at 14.7GHz.....</i>	172
5.3.3	<i>HFSS Field Plots of the Six Element Whole Ring FSG Model Over an Extended Frequency Range.....</i>	184
5.4	RESULTS FOR THE TWELVE ELEMENT HALF RING FSG MODEL WITH TWO FEED SOLID WAVEGUIDE PORTS .....	193
5.4.1	<i>S<sub>11</sub> Results for the Half Ring FSG Model – Measured and Simulated. ....</i>	193
5.4.2	<i>S<sub>21</sub> Results for the Half Ring FSG Model – Measured and Simulated. ....</i>	196
5.4.3	<i>HFSS Field Plots of the Simulated 12 Element Half Ring FSG Model. ....</i>	199
5.4.4	<i>Radiation patterns for the Half Ring FSG Model – Measured and Simulated.....</i>	218
5.5	REFERENCES.....	220
6.	CONCLUSIONS AND RECOMMENDATIONS FOR FUTURE WORK.....	221

# 1. Introduction

The structures referred to in this work as Frequency Selective Guides or FSGs have been under development in the department of Electronic and Electrical Engineering at Loughborough University for some time [6-9] & [11-14]. They are fabricated from sheets of Frequency Selective Surface or FSSs, which are formed into long hollow tubes. These tubes can in theory have a cross-section of any shape, but so far the investigations have been mainly confined to tubes of cylindrical form [6] & [14] with some early rectangular examples having been made [11]. They look like conventional waveguides except that the walls are made from FSS and not metal.

The basic properties of the walls of these FSGs are similar to the properties seen in conventional planar FSS sheets. The FSS sheets are made from thin dielectric sheets with a periodic array of small copper elements on the surface of the sheet. An Electromagnetic (EM) wave, incident upon the FSS, will experience almost total reflection from the surface, at a particular frequency where the elements of the FSS resonate. Away from this resonant frequency the FSS will reflect almost none of the incident EM wave with the majority of the power transmitted through the sheet, for further information on FSS see section 1.1. When the wall of the FSG becomes reflective at the resonant frequency, the structure will behave like a waveguide. Power will be transmitted along the axis of the structure with virtually none lost through the FSS walls. At all other frequencies the FSG will allow the fields of an EM wave to radiate through the surface into free space like a periodic grating antenna.

With the extensive work already carried out into the theoretical modelling of the FSG by Loukos [9] and some limited measurement of the scattering parameters of real FSGs. The last major problem in the development of the FSG and covered in this work, was the investigation and modelling of a method of feeding the new structure. As it is not possible to practically place a source inside an FSG, some form of conventional transmission line must be used to feed the structure. The work to date has ignored the effect that the junction between the FSG and the transmission line



may have on the performance of the FSG. A greater understanding of the junction between the transmission line feed and the FSG will lead to improved information about the operation of any practical FSG. Information will be obtained about which propagation mechanisms, the modes of the EM fields, are actually excited in the FSG by the transition. Future workers will be able to use this information to build and feed FSG structures to perform to defined specifications.

The FSG can be used in any situation where conventional solid metal waveguides are currently used, but in particular where a light weight structure is required. As it is made from a dielectric with small amounts of metal contained in the elements on the surface it is inherently lighter in weight than a conventional waveguide. Another property of the FSG is that it could be used in an area of high magnetic flux without causing a large deformation to the surrounding magnetic fields. This was initially of particular interest to the research team at Loughborough University who hoped to use the FSG to build a microwave radiometer that could be placed inside a Magnetic Resonance Imaging (MRI) machine without a significant degradation of the MRI image [12]&[13]. The microwave radiometry and MRI scans could then be carried out, on a human body, simultaneously to enable 'hot spot' carcinomas to be located without the need for invasive surgery. The MRI scans are needed to provide information on the dielectric makeup of the body and so allow accurate image processing of the radiometer data. However, to date, funding has not been forthcoming for the project and it has not progressed beyond investigation of basic FSG structure of which this Ph.D. is a part.

The antenna properties of the FSG can also be used in applications that require a conical main beam that can be scanned away from the axis of the antenna electronically. This would utilise the FSG at frequencies away from the resonance point of the FSS wall where it behaves like a leaky wave antenna [16] & [17]. This class of scanning antenna is not new, but the fact that the FSG has walls that are open and periodic around the entire circumference, means that the main beams produced are conical and not pencil shaped. Scanning antennas have been used extensively for target tracking and as a high gain communications antenna where one end of the link is not stationary.

## 1.1 FSS Background

Frequency Selective Surfaces (FSS) have been under investigation for many years. One of the earliest references, Collin [1], described an ‘artificial dielectric’ made from a three dimensional array of conducting elements and gave expressions for the reflection and transmission coefficients. FSS has two main configurations; firstly a thin conducting sheet with a matrix of apertures cut through it, Aperture FSS and secondly a matrix of conducting elements usually supported on a thin dielectric sheet, Element FSS. This second form can be thought of, with regard to the metallised area, as a negative image of the first type. Some of the earliest work in the area of two dimensional arrays was carried out by Chen, [2]&[3], these papers detail the theory of analyses of the two forms of FSS and describe the properties that they exhibit. The dielectric sheet of the element FSS was originally omitted by Chen, but the analyses was extended to include it by Montgomery [4]. A great deal of further work has been carried out and a good résumé has been given by Mitra [5] and more recently by Vardaxoglou [15].

The scattering of EM waves propagating normal to and incident upon a sheet of element FSS, a dielectric sheet covered by a periodic array of identical conducting elements, is such that it exhibits very high transmission through the sheet, at frequencies away from the resonance of the elements. At the resonant frequency of the conducting elements, the sheet becomes highly reflective, with virtually no transmission through the surface. To an incident EM wave it appears to behave as if it were a continuous conducting sheet and not at all like the dielectric sheet with a small amount of conductor on its surface. The rate at which the FSS changes from being transmissive to reflective can be adjusted, along with the resonant frequency, by changing the dimensions and shape of conducting elements used in the FSS. Various authors have investigated many different types of FSS element and a diagram of three types of element used in planer FSS sheets is given in **Figure 1-1**. Each one has different scattering characteristics.

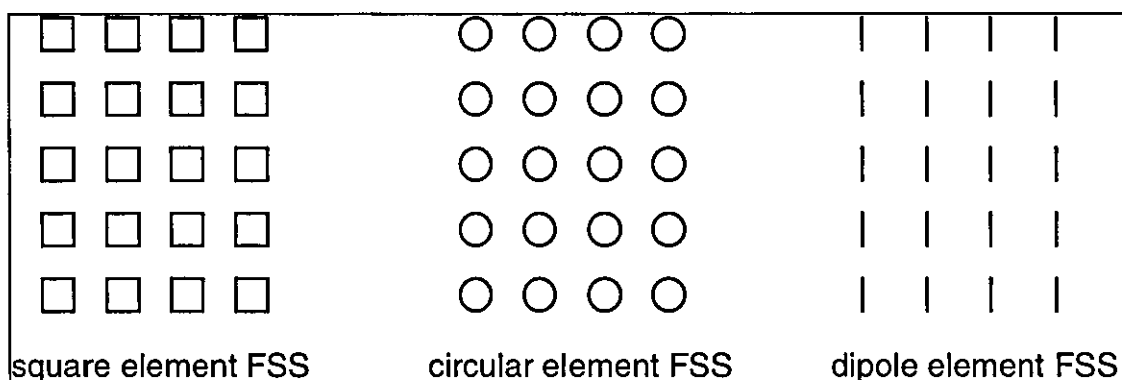


**Figure 1-1 Example of Three Types of Element used in Planer FSS Sheets**

As well as the Aperture FSS being the negative image physically of Element FSS, so too are its scattering properties. It appears to be near totally reflective at virtually all frequencies, except at the aperture resonant frequency, where it becomes almost totally transmissive. The properties of the FSS have thus made it ideal for use as a plane wave filter. It has been used extensively in many transmission systems at microwave and millimetre wave frequencies, either as a selective band pass filter or band stop filter or to make reflector antenna systems dual band [10].

## 1.2 The Basic FSG

A short section of FSG is shown in Figure 1-2. It is an FSG made from square loop element FSS on a thin dielectric substrate. The cross section of the FSG is clearly circular as this is the easiest cross section to model and manufacture. All the elements on the surface are identical and are square loops made from very thin copper sheet. Etching away the unwanted copper from a large sheet, the copper sheet having already been attached to the thin dielectric sheet, using PCB production techniques left only the square loops of the required dimensions on the dielectric surface. Once the elements are formed the dielectric sheet is rolled into a tube and the edges are secured together with adhesive along the seam.

The elements do not have to be square loops; they can be any shape as long as they are all identical and tessellate exactly into an array of uniform periodicity. Previously, Loukos [9] modelled dipole elements, but found that they had limited guiding properties. He found that square loop elements offered good guidance at resonance as

well as being easy to model. Consequently the use of square loop for the elements on the FSG surface will be continued in this work. He showed that the operation of an infinite length of FSG was governed by its element length,  $L$ , its array periodicity,  $D$ , and its radius  $r_0$ . The Loukos theory did not model the dielectric sheet present in real FSG's and this is also a design parameter that must be taken into account when building an actual FSG.

The Loukos model revealed that the infinite length square loop FSG could support three distinct Hybrid modes. The modes are hybrid because they contain all three E field components and all three H field components. This mode can be thought of as being made from the addition of a TE and a TM mode of the same order. This is caused by the open nature of the FSG structure and is unlike the modes found in solid waveguides. The distinct Hybrid modes were a surface wave that propagated at the lower frequencies along the surface of the FSG, and two leaky modes that propagated at the higher frequencies. One leaky mode was the  $EH_{11}$  mode as it contained a large amount of the  $TE_{11}$  mode and the other mode was the  $HE_{11}$  mode as this contained a high proportion of  $TM_{11}$  mode. This second mode propagated at a higher frequency than the first. Both of these modes were not confined within or bound to the structure surface and radiation leaked away into free space. However, at a particular resonant frequency for each mode the amount of power radiated was reduced to a very small level. At these frequencies the structure operated like a frequency selective waveguide with low loss.

In addition to the work to turn planar element FSS sheets into FSG work has also been carried out make horn antennas from FSS, using a technique similar to that of the FSG. Here Jayawardene [7],[8], instead of making tubes of constant cross-section, has rolled the FSS sheet into a cone. The tip of the cone was removed and the feed waveguide was attached to the hole that this left in the top of the cone. These structures have been dubbed Frequency Selective Horns (FSH). It is anticipated that the transition/feed work carried out here could also be applicable to the FSH feeds as well as the FSG junctions as they are made of the same material and exhibit similar properties.

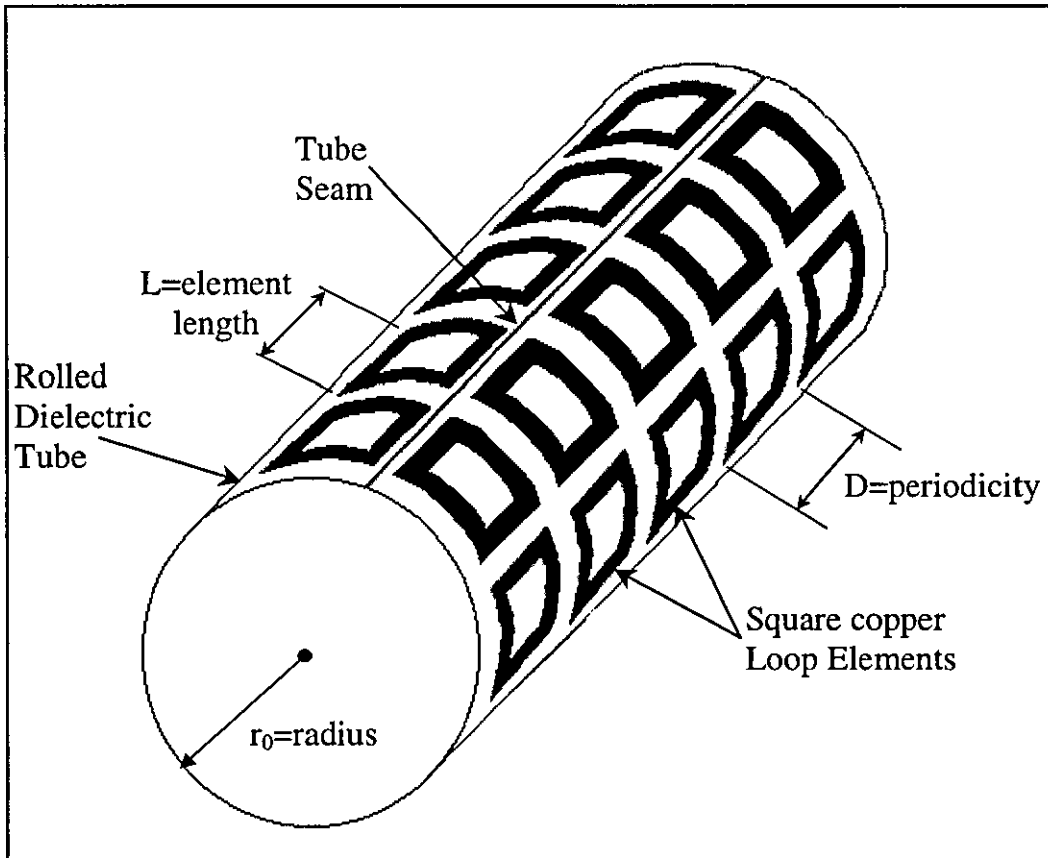


Figure 1-2 An example section of Square Loop FSG with 6 Elements around the circumference

### 1.3 Transition Problem Definition

The aim of this Ph.D. is to fully understand the operation of a transition from solid circular waveguide to FSG. The transition and FSG will be measured and modelled so that the 'real life' structure can be compared with the predicted infinite length FSG model [9]. The modelling of the junction will allow the effect of the transition on the modal field distributions to be assessed as the EM fields move from the feed structure to the FSG. The reflection and transmission coefficients of the measured and predicted results can be compared to ascertain the accuracy of the model.

The simplest junction that could be modelled is that between a standard circular waveguide and an FSG defined in section 1.2. Both the structures have the same basic shape and can both be defined in terms of the cylindrical co-ordinate system  $r, \phi, z$ .

The mode definitions are also similar for the two structures, the solid waveguide containing TE and TM modes and the FSG containing hybrid modes that have TE and TM components. The similar co-ordinate systems and mode definitions mean that no complicated axes redefinitions are needed in defining the junction between these structures. Also, solid circular waveguide was readily accessible, so that the measurements could be made without having to buy costly new equipment.

The solid waveguide and the FSG were positioned so that the axes of the two structures were aligned along the z axis. The junction between the structures was then defined as the transverse plane that was normal to the z axis. This ensured that the cross sections of both the structures were concentric circles in the junction plane. The direction of propagation in both structures was along the z axis, so the junction plane contained only the transverse modal fields. This junction set-up is shown in Figure 1-3, a standard section of circular guide is connected to a roughly similarly dimensioned section of FSG, an arbitrary step change can be added to the model if the diameter of the FSG should be different from that of the solid waveguide.

Also shown is the flange on the end of the solid waveguide. This flange is used when mating two solid waveguides together, however in this case the FSG has no flange and so it is not used for connection purposes. The presence of the mating flange on solid waveguide increases the complexity of the problem that must be solved. The diffraction of the field around the edges of the flange would have to be calculated as an integral part of the junction model.

The flange could be removed in which case the fields external to the solid waveguide must also be calculated as well as the fields external to the FSG. The external FSG fields must always be calculated, as they are inherently part of the modal fields of the FSG. However the fields on the exterior of the solid waveguide are not related directly to the fields inside the solid waveguide and just add extra complexity and calculations to the model. Alternatively the flange can be extended into an infinite conducting plane with a hole in the plane centred on the z axis and with the same radius as the solid waveguide. This then separates the space outside the radius of the FSG elements from the space outside the solid waveguide. This removes the need to

calculate the fields in this second region, as it is completely isolated from the fields of interest.

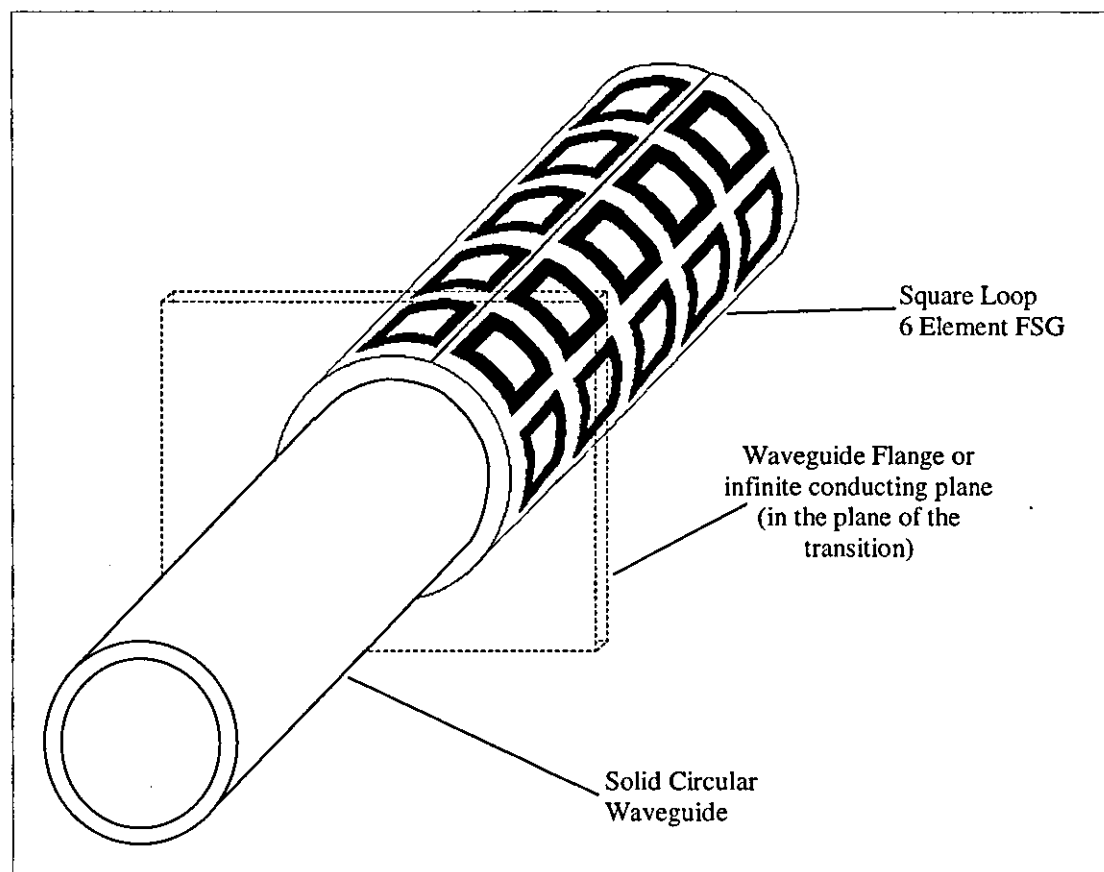


Figure 1-3 Simplified diagram of a Solid Waveguide to FSG Transition

However some reflection will occur from this plane as the exterior fields of the FSG bounce off its surface and a reflection coefficient will need to be taken into account for the fields at the plane. This will fundamentally affect the operation of the junction and so the modelled results must only be compared with junctions that also have large conducting plates in the plane of the transition. The EM fields outside the radius of the junction aperture along the plane will be simplified. No E field components parallel to the plane or H field components perpendicular to the plane will be present, reducing the number of mode field coefficients by half.

The length of the individual sections of solid waveguide and FSG has not been specified. Ideally it would, in both cases, be infinite in extent so that no other changes

in either of the structures affect the behaviour of the junction of interest. For physical measurements the short sections of each structure should be terminated with matched terminations to ensure that no reflected fields could interact with the junction and alter the measurements.

The analysis of the junction would ideally give not only the magnitude of the scattering parameters for the total field in each structure, but also the scattering parameter of each individual mode in each of the structures. This would also give full details of any mode conversion that may take place at the junction as well as the reflection and transmission of the fundamental mode.

#### 1.4 Structure of the Thesis

This thesis is organised as follows:-

Chapter 2 contains details concerning the mode spectrum of the FSG and further details on the theory of the infinite FSG modes. This chapter builds directly upon the work of Loukos [9] and makes use of his prediction program to find a large amount of the FSG mode spectrum. Details are given of the alterations that were made to the original method in order to find the mode spectrum. The mode spectrum that was found for a particular FSG is given along with a new method of displaying the complex eigenvalue information. Finally some detail is added to that which is given in [9] on the theoretical nature of the FSG modes produced by this theory for infinite length FSGs.

Chapter 3 presents a parametric investigation into the nature of FSG operation by measurement methods. The details of FSG construction are given along with the dimensions of the FSGs produced for the measurement study. The  $S_{11}$  and  $S_{21}$  scattering parameters were measured for each FSG over a range of frequencies. The radiation patterns of these FSGs were also measured. This measurement data was analysed qualitatively to identify some of the key features of FSGs and their modes of operation. The differences between the different FSGs manufactured were used to derive qualitative design trends of the effects of altering the FSG parameters. Finally several methods were compared that extracted the propagation constants of the FSG



from different measured data. The extracted data was then compared against the eigen value data found in the previous chapter and the agreement of this data was assessed.

Chapter 4 details the various options available for the theoretical modelling of the FSG to solid waveguide junction modelling. The selected mode matching theory is developed and adapted for the open structure of the FSG and the assumptions and simplifications are justified. The field integral equations required by the theory are given along with details about the development of the program to calculate the modal amplitudes. The testing procedure for the program is examined and the results produced by this program are presented along with thoughts about the reasons for it's failure to calculate any sensible values of reflection or transmission.

Chapter 5 looks at the junction modelling by the alternative method of finite element modelling. A brief outline is given into the operation of this version of the finite element method. The development of the computer models at increasing levels of complexity is explained along with descriptions of them. The main body contains the scattering, radiation patterns and field plots for the vast amount of data obtained by this simulation method. The simulated data is, where possible, compared to the measured data collected in chapter 3. Good agreement is seen between the finite element simulations and the measured information. The field plots are then used to confirm the qualitative information extracted from the measurements in chapter 3 as to how the modes propagate in the FSG. Due to the high level of detail contained in the field data from the finite element simulations the understanding of the operation of the FSGs is increased beyond that which was inferred from the measurements in chapter 3.

Conclusions and recommendations for possible further work to extend that which is presented here, is given in chapter 6.

### 1.5 References

[1] Field Theory of Guided Waves - R.E.Collin - McGraw-Hill, New York: 1960, ch.12, p.192.

- [2] Transmission Through a Conducting Screen Perforated Periodically with Apertures - C.C.Chen - IEEE Trans on Microwave Theory and Techniques - Vol.MTT-18, No.9, p.627-p.632, September 1970.
- [3] Scattering by a Two - Dimensional Periodic Array of Conducting Plates - C.C.Chen - IEEE Trans on Antennas and Propagation - Vol.AP-18, No.5, p.660-p.665, September 1970.
- [4] Scattering by an Infinite Periodic Array of Thin Conductors on a Dielectric Sheet - J.P.Montgomery - IEEE Trans on Antennas and Propagation - Vol.AP-23, No.1, p.70-p.75, January 1975.
- [5] Techniques for Analyzing Frequency Selective Surfaces - a Review - R.Mitra, C.H.Chan & T.Cwik - Proc of the IEEE - Vol.76, No.12, p.1593-p.1614, December 1988.
- [6] Propagation Characteristics of Frequency Selective Waveguides with Circular Cross-Section - G.Loukos & J.C.Vardaxoglou – Proc. Joint URSI UK 12<sup>th</sup> National Radio Science Colloquium and QMW Antenna Symposium, Queen Mary and Westfield College, London, 11<sup>th</sup>-13<sup>th</sup> July 1995.
- [7] In Band Radiation Performance of Conical Horn with Printed Elements - M.Jayawardene, G.Loukos & J.C.Vardaxoglou -
- [8] Evaluation of Frequency Selective Horn Antenna for use Within a Magnetic Resonance Imaging System - J.C.Vardaxoglou, M.Jayawardene, R.D.Seager, G.R.Cherryman & M.Horsfield –
- [9] Propagation Characteristics of Cylindrical Frequency Selective Guides – G.I.Loukos – Ph.D. Thesis, Loughborough University, 1998.
- [10] AK/C/S Bands Satellite Antenna with Frequency Selective Surface – M.Ando, K.Uendo, H.Kumazawa & K.Lagoshima – Electronics and Communications in Japan, Vol 66-B, 1983, p1665-1680.
- [11] Waveguide Guidance and Radiation from a Hollow Tube formed from Frequency Selective Surfaces – A.J.Robinson, J.C.Vardaxoglou & R.D.Seager – Electronics Letters, 29, 1993, p1531-1533.
- [12] Frequency Selective Horns - J.C.Vardaxoglou & G.I.Loukos – poster presentation in EPSRC's ITEC Conference 1996, Leeds University, April 1996.
- [13] Recent Advances in Frequency Selective Waveguides and Horn Antennas - J.C.Vardaxoglou, R.D.Seager, G.I.Loukos & M.Jayawardene – invited presentation, PIER's Conference 1996, Innsbruck, Austria.
- [14] Propagation Inside Strip Grating FSS Waveguides with Cylindrical Cross Section - G.I.Loukos & J.C.Vardaxoglou – Electronics Letters, 31, 1995 p778-779.

[15] Frequency Selective Surfaces – Analysis and Design - J.C.Vardaxoglou – Research Studies Press, Taunton, UK, 1997.

[16] FDTD Analysis of a Metal-Strip-Loaded Dielectric Leaky-Wave Antenna – M.Chen, B.Houshmand, T.Itoh – IEEE A&P, Vol 45, No8, August 1997, p1294.

[17] Design considerations for Leaky-wave Antennas – I.J.Bahl & K.C.Gupta - Proc. IEE, Vol123, No 12, December 1976, p1302.

## 2. Extension of Existing FSG Mode Theory.

In order to understand fully how the FSG works at different frequencies it is important to ascertain the complete mode content of the FSG, i.e. the number of modes that make up the field in the FSG at any one frequency. This will show which mode is dominant at which frequency. With this knowledge the FSG can be designed to behave as either a monomode guiding structure or a leaky wave antenna. The design can be altered to ensure that the most efficient mode is used at the frequency of operation. The full mode content is also a fundamental requirement if the transition is to be modelled using mode matching theory. A detailed account this theory and the reasons for using this method of transition modelling are given in chapter 4. This chapter will assume that the majority of modes of the FSG and propagation characteristics of each must be found.

The investigations carried out to date into the FSGs by Loukos [1] & [25] have concentrated on only three modes. These are the fundamental surface mode, the fundamental leaky ( $EH_{11}$ ) mode, both of which have been verified experimental (see chapter 3) and the next higher order leaky mode, the  $HE_{11}$  mode. This chapter details the work undertaken and the results found in the search to find a significant number of modes to approximate the complete set of modal solutions.

### 2.1 Literature Relating to Existing Leaky Wave Open Structures

As the FSG is an open structure it can never be truly guiding like a waveguide or a coax cable. In these transmission line structures the conductor is continuous and surrounds the field so that it is confined within it's cross section. Electromagnetic energy can never be radiated from the structure, unless some gap is formed in the outer conductor, like the well known slot waveguide antenna, p305 of [3]. However, there are many other types of transmission line which are open structures and do not have a confining outer structure. These include microstrip line, dielectric guides, slot

line, coplanar waveguide and coupled strip line. These structures as, with all open transmission lines, can exhibit radiation under certain circumstances. The radiation modes that exist in a dielectric guide are detailed in p316 of [2]. Also p303 of [3] gives a more general, but detailed account of the complete spectrum of field solutions that exist for any open structure.

It is well known that the fields that exist in any structure can be found by solving Maxwell's equations for the particular boundaries for that geometry. They also obey the radiation condition that all fields must decay to zero at infinity. For a structure that has a separable field solution an inhomogeneous equation can be formed, the solution to which gives the eigen modes of the structure, which correspond to the propagation constants of the modal fields. These modes fall into distinct categories. There are a number of discrete bound surface wave modes, which propagate along the structure. These modes have distinct real single valued solutions to the eigen mode equation. They have fields that exist outside the guide diameter that decay away to zero at infinity, but that only propagate in the direction parallel to the axis of the guide. They do not propagate away from the surface and so can be considered not to radiate energy from the structure.

The only other real solutions to the eigen value equation, for open structures, exist along a line where any value on that line is a valid solution. This line is known as the spectrum of radiation modes where the propagation constants obviously have an infinite number of values along it. These values correspond to either, modal fields that propagate away from the surface of the structure and account for the energy that radiates away from the structure, or to modes that are 'evanescent' which have purely imaginary propagation constants. The fields of these modes decay in all directions away from the field source and do not propagate.

Other solutions of the eigen mode equation can be found. These solutions have complex propagation constants and do not obey the radiation condition and so do not exist and can never be physically realised. They are unreal. One of these unreal solutions, however, has been found to be useful in studying the radiation field close into the open structure. Several authors have shown that the radiation field can, under

certain conditions, be approximated by the field of one of these unreal eigen modes. This unreal eigen solution has come to be called the leaky mode.

By looking at the work done on other open waveguide structures, and in particular the leaky mode, a better understanding can be found for the likely working of the FSG. The leaky wave mode of an open structure first came to prominence in the 1950's with several authors publishing early investigations into them; Zucker[4], Marcuvitz[5] & Glodstone & Oliner[6]. The first detailed work on the leaky mode was by Tamir & Oliner[7]. This work showed how the field integral equation could be solved to give all the proper and improper modes of an arbitrary structure. These eigen modes may have real, imaginary or complex propagation constants. The modes have been classified based on the field distribution and a full description of each is given. It states that if a pole of the eigen equation does not satisfy the radiation condition then it is an improper mode and although not part of the spectral (proper & physically realisable) solution it does contribute to the field in a limited region. It also states that the leaky mode cannot be orthogonal to any other mode and that normalisation is not possible. This is because the mode does not exist outside its limited region and so the integral, Equation 2-1, can not be evaluated.

$$\int_{S=0}^{\infty} ExH^* dS$$

Equation 2-1

Standard integration methods will give the total field as a continuous radiation spectrum and evanescent modes plus a set of discrete bound proper modes. A method is introduced, the steepest descent path integration, that allows the field to be made up of some of the leaky modes plus the set of discrete bound proper modes with reduced contribution from the complete spectrum. This method involves a transformation of the eigen mode poles from the twin Riemann sheet  $\gamma$  plane to the single sheet complex  $\phi$  plane, see Equation 2-2.

$$\gamma = k \sin \phi, k_r = k \cos \phi$$

Equation 2-2

In this plane the standard integration path can be deformed to allow a small portion of the radiation field(space wave) to be represented by the pole residues that correspond to the leaky modes. This allows the region over which the leaky mode exists to be identified and the magnitude of its contribution in that region to be defined.

It also states that if a complex proper wave is present then the pole will appear as a pair of degenerate modes (not orthogonal). One mode will be forward propagating and the other backward propagating, so that no net power propagation will occur. These mode pairs are associated with stored energy in a manner similar to evanescent modes in solid waveguide. Modes with complex eigen modes can either carry power into the radiation pattern or account for losses in a lossy structure.

A major class of open structures that support leaky modes, for which it possible to analytically determine the values of the propagation constants, are dielectric guides of uniform cross section. A subsection of these are optical fibers. The general behaviour seen in fibers is applicable when they are studied in terms of electromagnetic fields, found from the solution of Maxwells equation. Marcuse has confirmed, p24 [8], that the leaky mode of an optical fiber exists and can be thought of as representing a discrete part of the radiation field close to the fiber. The rest of the field consists of the remainder of the radiation mode continuum. This reference also confirms the procedure for the normalisation and orthogonalisation of the continuum of radiation modes. It also reiterates that it is not possible to apply this to the leaky modes.

The inability to normalise and apply orthogonality to the leaky mode hampers it's usefulness, but just 2 years later Sammut & Snyder [9] published useful approximations for these functions. It details two methods for approximating the orthogonality of leaky modes. The first is to truncate the leaky mode at some small distance from the guide where the mode will be finite and nearly power orthogonal. However some small part of the mode will not be orthogonal and so some coupling between modes will occur. The second approximation is found by deforming the path of integration of the orthogonality condition into the imaginary radius space. That is to say that as the real distance from the fiber core increases an imaginary term, that increases faster than the real term, must be added to the radius value. The imaginary radius will then act to cancel out the increasing field strength of the leaky mode when

the integral is evaluated. This form of orthogonality does lose the definition of power orthogonality. It is however an exact orthogonality condition that can be used on both proper and improper modes. This reference also re-states that for weakly leaky modes a long way from the source and close to the guide the radiation field is approximately the sum of the leaky modes.

In [10] Snyder & Love give an account of the process by which leaky modes form in optical fibers. This is given both in the form of a mathematical approach and a heuristic one, which may aid understanding of leaky modes a little more. It also reiterates the orthogonality and normalisation procedures for the leaky mode given in [9]. Confirmation of the presence of leaky modes in dielectric guides has been achieved by Shigesawa et al in [11], where they were able to predict and measure the presence of a leaky mode on a dielectric strip guide. To practically find the presence of the leaky mode the far field pattern was measured and the main beam of the radiated pattern was found. This main beam can be represented by the leaky mode and was compared to the beam that the theoretical leaky mode would produce.

Another open guiding structure where the presence of leaky modes has been studied in recent years is that of the widely used Microstrip Transmission Line. Oliner and his co-workers have carried out most of this work. In [12] they determined that higher order microstrip modes have a cutoff frequency where the propagation constant ceases to be real and becomes complex. These complex propagation constants correspond to leaky modes, which radiate either as space waves or surface waves away from the line. They also reiterate that not all leaky modes are physically realisable, even though they may be solutions of the eigenvalue equation. They make use of the Steepest Decent Path integration, described in [7], to show which modes are physically relevant. They found that the most of the radiation from an over moded microstrip line came from a single leaky mode. In [13] a leaky mode that has a similar field structure, in the proximity of the conductor, to that of the dominant mode is shown to exist. Measuring the  $S_{21}$  of a length of microstrip line and observing the frequency at which the slope of  $S_{21}$ /Frequency changes was used to authenticate the theoretical data. The reason for this being that below this frequency the line is subject only to resistive losses and above this frequency energy is also lost through radiation into the leaky mode. In [14] the frequency range over which the leaky mode is



analysed is lowered. As the frequency tends to 0 the real and imaginary parts of the propagation constant tend to infinity. This means that as the beam corresponding to the leaky mode approaches broadside it will broaden considerably and become very weak eventually becoming indistinguishable from the background radiation spectrum. It also states that if  $\beta$  increases so much that  $\beta/k > 1$ , the leaky mode can no longer contribute to the space wave at any angle from the normal.

Several of the preceding papers show that the leaky mode can be used to approximate the radiation field in a section of space close to the guide structure. This section is bounded on one side by the structure and on the other by a line at an acute angle to the structure that intersects the structure at the field source. A good diagram of this region of space is given in [7]. It shows wave fronts propagating at some angle away from the surface and power increasing away from the surface, as seen in [11]. The characteristic main beam of a leaky mode structure can be used as an antenna. There has been much published of the subject. One of the attractions of this type of antenna is that as the frequency changes the angle of the main beam changes as the value of  $\beta$  of the leaky mode changes, producing a frequency scanable antenna. Bahl & Gupta [15] give some useful general design equations to determine the beam characteristics for a leaky mode antenna. They also detail the Kirchoff-Huygens and steepest descent path methods for accurately predicting the radiation pattern of an antenna. Mitra & Kastner [16] have developed a spectral domain method for finding the radiation pattern of a leaky mode antenna. This reference also details how to obtain  $\beta$  from the angle of the main beam of the radiation pattern and  $\alpha$  from the width of the main beam.

One common method used to get a structure to exhibit leaky mode behaviour is to make the surface of the structure periodic in some way. This has been achieved with corrugations in the surface of the material itself or by adding periodic perturbations of another material, for instance metal strips (or slots) have been used extensively. These periodic leaky mode structures are obviously directly relevant to the FSG as it is also a periodic open structure. One of the first papers published on the subject was by Sigelmann & Ishimaru [17] in 1964. They studied a grounded dielectric slab with periodic metal strips on the upper surface. There is a good discussion on how the  $k/\beta$

diagram changes for periodic structures and how this relates to the complex  $\gamma$  diagram. An important point to remember is that the complex  $\gamma$  diagram changes with frequency. Each complex  $\gamma$  diagram is a cut plane through the  $k/\beta$  diagram at a particular value of  $k$ . Where the  $k/\beta$  diagram only shows the  $\beta$  values for  $\alpha=0$ , i.e. the x axis of the complex  $\gamma$  diagram. In the following year Li & Oliner [18] studied the leaky waves that existed on a simple parallel plate waveguide with periodic slots cut in one plate. They found that a leaky mode could exist on this fast wave structure regardless of the periodicity of the slots. They also investigated the relationship of wood scattering anomalies to plane wave incidence and the relation to leaky modes. In the late seventies work was undertaken to improve the leaky antenna properties of dielectric waveguides. This was done either by adding metal strips [21] or by changing the profile of the upper dielectric interface so that it resembles the toothed battlements of a castle [19], [20]. Itoh in [19] develops a structure where the  $k/\beta$  diagram shows the first negative harmonic of the fundamental is a leaky mode whilst all the other harmonics and the fundamental are surface wave modes. There is also a development detailing how mode coupling can cause a stop band to form for surface modes when  $\alpha$  &  $\beta$  values are equal. [20] gives detailed account of the development dielectric slab leaky wave antenna with measured results of the prototype antenna. Kobayashi et al [21] details the strip loaded leaky mode antenna. It determines the design relationships required in order to ensure only one leaky mode is significant in the radiation field and hence there is only one main beam. Finally, the paper by Shigesawa et al [22] is significant in that it investigates the conditions for coupling to take place between leaky modes. It found that for large leakage, there is coupling between two leaky modes if  $\beta$  &  $\alpha$  are equal for the two modes. If this condition is not met, then there can be no coupling effects between them.

## 2.2 Determination of Mode Content of FSG

The discovery of the major proportion of the mode spectrum of an FSG is important as it enables improved understanding of the propagation mechanisms at work in the FSG. This would then allow the determination of the excitation frequencies that give

rise to a mode that propagates with the least loss or a mode that would operate as the most efficient leaky wave antenna. The full mode content is also important, as it is a fundamental requirement if the transition is to be modelled using mode matching theory, which is covered in greater detail in chapter 4. In summary, this theory simultaneously approximates the total excitation field at the FSG feed to that of an infinite sum of incident and scattered FSG modes and scattered waveguide modes, the amplitudes of which are to be determined. The summations are then truncated so that only the most significant modes are included, and the amplitudes of these modes are ascertained by multiplying the equations by a set of orthogonal basis functions and integrating over the cross-section to form a complete system of independent equations. The equations are placed in matrix format and inverted to give the amplitudes of the truncated set of FSG modes. From these mode amplitudes the modes that are most readily excited by a particular feed can be determined. The feed characteristics may then be altered to give the desired mode content in the FSG, such that it will operate in a manner consistent with a particular design specification.

The investigations carried out to date into the FSGs by Loukos[1] and [25] have concentrated on only three modes. These are the fundamental surface mode, the fundamental leaky ( $EH_{11}$ ) mode and the next higher order leaky mode that being the  $HE_{11}$  mode. This section details the work undertaken and the results found in the search to find a significant number of modes from the complete mode spectrum.

The eigen value spectrum, other than the three discrete eigen values already found, was not previously known. As the FSG is an open structure it is unlikely that this spectrum will be similar to that of a solid waveguide, i.e., an infinite series of discrete eigen modes. It is likely that it will have a spectrum similar to other open structures, a finite number of discrete eigen modes (bound modes) and an infinite number of eigen modes that form a continuous spectrum of values (radiating and evanescent modes). An example of this type of eigen mode spectrum is given for dielectric slab guides in Collin [24] p474. The reason for the difference between the spectrum for this type of guide and that of solid guides is because the modal field solutions must satisfy the radiation condition ( $|\underline{E}|$  &  $|\underline{H}| \rightarrow 0$  as  $\underline{r} \rightarrow \infty$ ). This difference with a continuous spectrum can be visualised by considering what happens in a solid guide as the

waveguide walls are moved towards infinity. The spacing between the solutions of the infinite discrete spectrum reduces, until at infinity the spacing disappears and the spectrum becomes continuous. The radiation modes propagate in both  $r$  and  $z$  and are not bound to the guide, so energy is lost from the guide via these modes. It should be noted that these are not leaky waves as the fields are proper and tend to zero at infinity. A leaky mode, by definition, does not obey the radiation condition and has a field strength that tends to infinite at infinity. Indeed it can be proved that a surface guide can have leaky modes p31 [8]. These modes have propagation constants ( $k_z$ ) with real values and the phase constant ( $\beta_z$ ) equal to those of radiation modes that lie in the continuous spectrum. However, unlike the radiation modes they are complex valued and have an imaginary part, the attenuation constant ( $\alpha_z$ ). The  $\beta_z$  values of the leaky modes can only have discrete values and according to [7] are not part of the spectral field solution that exists for an open structure. As they do not obey the radiation condition they can never physically exist. They can however be used to represent the field contribution from the continuous radiation modes in a limited region close to the outside of the guide, as shown in [7]. If sufficient leaky modes of the FSG could be found then they can replace the continuous radiation spectrum and hence mode matching at the FSG to solid waveguide junction becomes a viable prospect. The mode matching method can not be used if a continuous radiation spectrum is present, as detailed in chapter 4. The field representation used for the FSG then ceases to be that of the spectral field and becomes an approximation of it, the spatial field.

The modes of an infinite length of FSG were found using a program developed by Loukos, the theory of which can be found in [1]. In essence the theory uses Floquet modes to allow an FSG of infinite extent in the  $z$  and  $\phi$  co-ordinates to be represented by a finite unit cell. The field equations are then simplified by imposing the transverse boundary conditions and the radiation condition. A trial value of the propagation constant ( $k_{z0}$ ) for the fundamental Floquet mode is then substituted into the equation before the element currents are approximated by a set of roof top basis functions. The method of moments is applied to the resulting system of equations to simplify them into a convenient matrix form. The determinant of the characteristic matrix is taken

and if the trial propagation constant is a root (eigen value) of the characteristic equation then the determinant will be zero.

In order to find the eigen values of the FSG, which give the propagation constant, many trial values must be used and many iterations of the calculation performed to find the determinant's zeros by trial and error. These trial propagation constants must be complex ( $k_{z0} = \beta_{z0} - j\alpha_z$ ) as the structure is open. It is confirmed in [7] that modes with complex propagation constants may exist in an open structure. This greatly increases the number of trial computations that have to be performed, as both the real and imaginary values must be varied independently. In [1] the values of the free space propagation constant and the FSG phase and attenuation constants have been normalised to the FSG periodicity to make graph plotting easier. The same normalisation process will be adopted here and trial values over the normalised ranges  $\beta_{z0}D_z/2\pi = 0$  to 1.0,  $\alpha_zD_z/2\pi = 0$  to 1.5 and  $kD_z/2\pi = 0.1$  to 0.65 will be used. This search range was considerably more extensive than that previously used.

The computer program that implemented the FSG propagation constant prediction model was not user friendly and required constant attention and manipulation in order to find an eigen value at a single frequency. In its basic form the program calculated the determinant of the characteristic matrix for each trial value. At each frequency the user defined the range of the trial values of normalised beta & normalised alpha to use by declaring the start, stop and step value of each. Initially the normalised alpha value was held constant while the normalised beta value was incremented by the step size from its start point to its stop point. The value of normalised alpha was then incremented and the sweep over all the normalised beta trial values was repeated. This process was repeated until the determinant for every trial value in the specified search range had calculated.

The determinant can never become zero because of the truncation of numerical values that inevitably occurs in a numerical system and that only the first twenty to thirty Floquet modes can be used. Instead a sharp minimum in the determinant value is observed at the trial value which is the closest approximation to the actual value of the eigen root. The degree to which the determinant tends to zero can be taken as a measure as to how good an approximation to the eigen root the trial value is.

To assist in the location of the roots, Loukos, used a minimum value determination routine in the program. This routine could only find the minimum value of the determinant for a fixed value of normalised alpha, i.e. with normalised beta as the variable. The on screen output consisted of a minimum value and it's location for each normalised alpha value. This then required the user to interpret these numerical outputs and to determine the position of the minima in normalised alpha as well as normalised beta.

As the program was run interactively, and hence was more costly than batch processes, at the Manchester Computer Centre the roots needed to be found as quickly as possible. This reduction in run time was achieved by reducing the size of the search space in alpha and beta. With a smaller search space there was no guarantee that the minimum would lie within it. To overcome this, the user was required to have some skill and practice in interpreting the data by spotting trends. Once a trend was spotted the user would abort the process and change the search space to a more appropriate set of values before re-starting the program to find the root more quickly. This process required large amounts of user input and costly processor time and the number of roots found was solely down to the skill of the operator.

To find the complete eigen spectrum a more rigorous, lower cost method was required. The program was altered so that it was straight forward to use and to enable it to run as a batch process. As a batch process it was found that the program would run on the Loughborough University Sun and HP workstations, although taking more than twice the time to run than on the Manchester super computer for the same search space. The use of a different computing platform meant a large reduction in computing costs. With the batch program very large search spaces could be used and although these could take many hours the fact that the program now needed no user input meant that it could be run overnight if necessary. In fact the entire search space was used in one go for each frequency in the search range of  $k_0$ .

This generated a very large amount of data and although the minimum finding code was useful it did not always give correct answers and could only find the first minimum in any row of beta data for a fixed alpha value. If multiple minima existed

on the same row the later ones were ignored. With the increased search space and more minima likely to be found a robust and fast method was required to pin point all the minima. A more complex minimum finding algorithm could have been developed, but it was felt that this would again leave the user removed from the actual output data and vital information and trends may be lost. It was decided that the best way to process all the relevant data quickly and easily was with a graphical method and example is shown in Figure 2-1. With visual processing the user can identify the minimum values from the graphical data far more easily than from tabular data. The graphical method that was chosen to display the data was a three dimensional surface plot, one for at each frequency simulated.

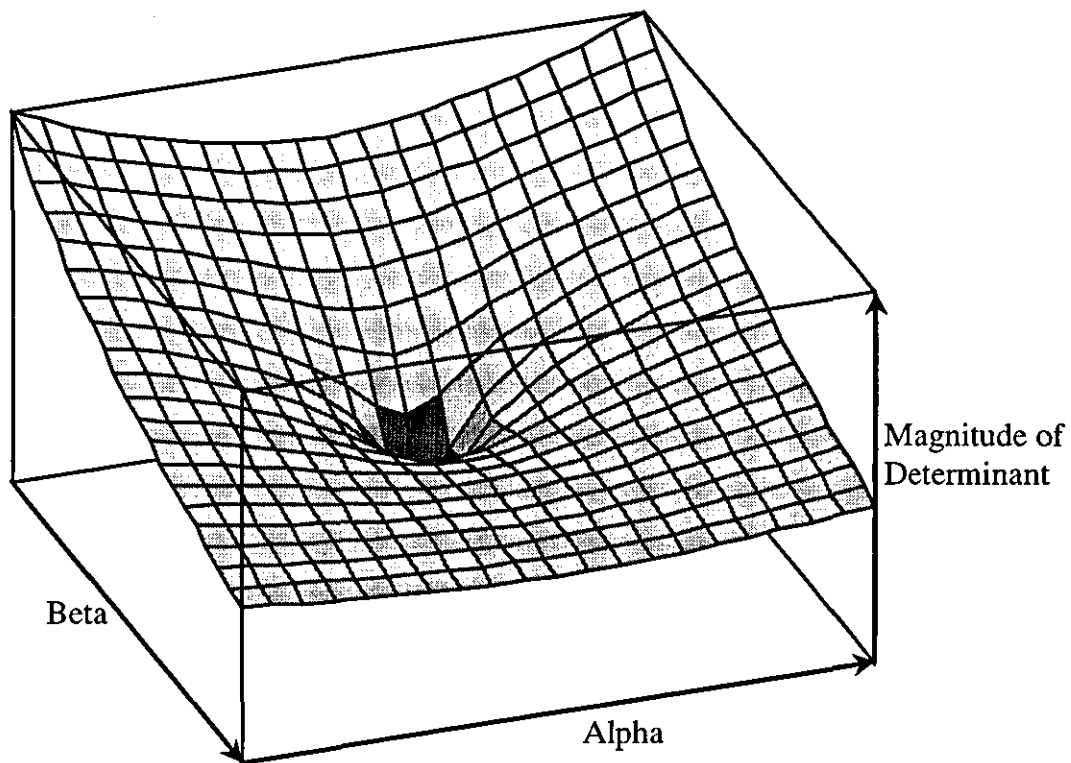


Figure 2-1 Surface plot showing a minimum in a small alpha and beta search space.

The axis of the surface plot were the beta values along the x axis, the alpha values along the y axis with the magnitude of the determinant shown as a height up the z axis above the  $z=0$  plane. The magnitudes of the determinants were very small numbers with a very large range. This initially made the surface difficult to plot so a log magnitude scale is chosen on all surface plots for the Z axis. All the log magnitude data points were then combined to form a shaded three dimensional surface

representation of the determinant values. The minima corresponding to the roots appear in this surface as deep spiked holes and the closest approximation of the root is the data point at the tip of the spiked hole. The user can quickly identify where these spikes are and determine if further investigation of the root is required with a finer separation between the trial values in the small area around the root. As can be seen in Figure 2-1, the position of the minimum is not very clear when the surface is viewed from above. However if the surface is rotated through  $180^\circ$ , as shown in Figure 2-2, the minimum appears as a maximum and is very easy to pinpoint. All subsequent surface plots were plotted similarly, with the underside uppermost, so that all the minima can be found easily.

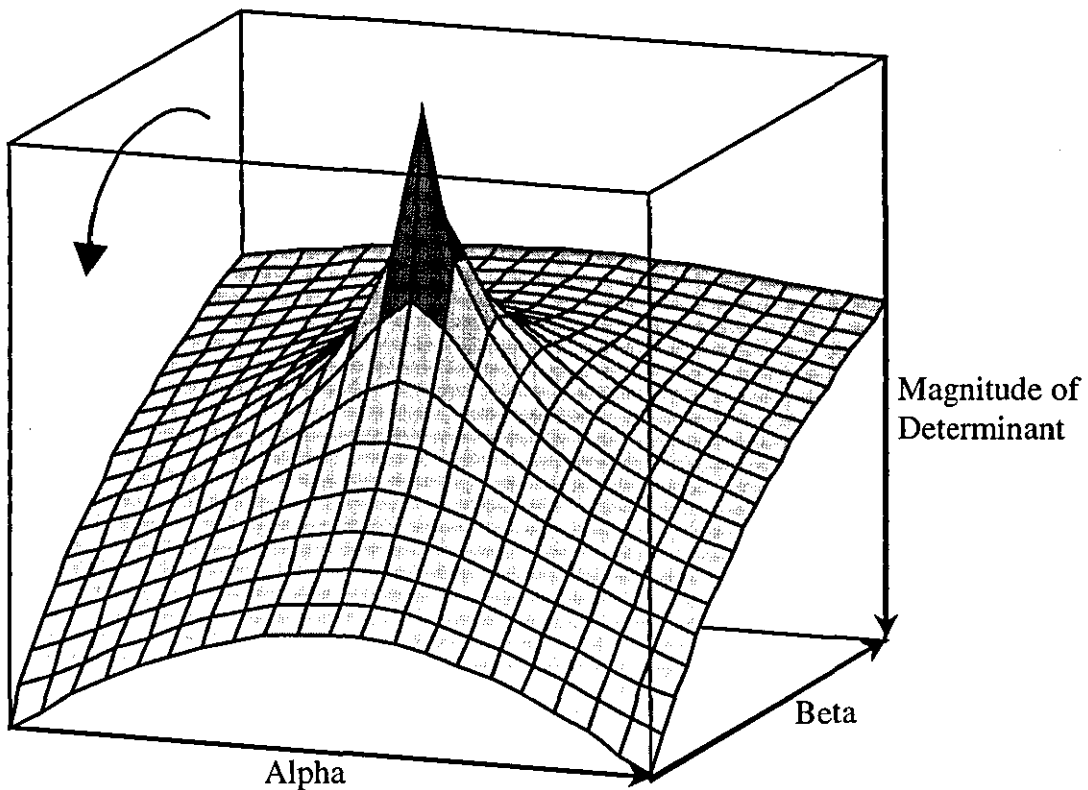


Figure 2-2 Surface plot showing the same minimum as Figure 2-1 rotated  $180^\circ$  about the alpha axis.

It was also felt that the only way to be sure that all the eigen roots of the spectrum could be found was to search the entire search space given previously. The required range for the fundamental beta value was found to be a normalised value between zero and one. As these beta roots are those of Floquet modes, then the fundamental



Floquet mode normally resides between these normalised values. If it should move outside this range then the beta value of a higher order Floquet mode must move into this range as the fundamental value leaves. This is a fundamental property of Floquet modes, a detailed description is given on p195 of [23], and means that the beta value of one Floquet mode of the eigen mode will always be in the zero to one normalised beta range. A normalised separation of 1 is the same as actual separation in beta of  $2\pi D_z$  (rads/m) which is equal to the separation between Floquet modes by definition, see Equation 2-3. This states that the phase constant of each Floquet mode is related to the fundamental phase constant by integer multiples of  $2\pi D_z$ .

$$k_{zq} = \frac{2\pi}{D_z} q + k_{z0}$$

Equation 2-3

The normalised alpha and free space propagation number can of course have any positive value. However a limit was placed on the normalised alpha of between 0 and 1.6. This corresponded to an attenuation along the FSG from zero nepers/m in the lossless case to nearly 1150 nepers/m, which is so lossy as to render any mode with that amount of loss to not be a significant contributor to any measurement. These modes will still be present in the aperture however and will need to be taken into account in order to match the fields correctly. The normalised free space propagation constant was varied from 0.1 to 0.65 corresponding to a frequency range from 3.6GHz to nearly 24GHz and a frequency range well beyond that which has been measured in chapter 3 (to which any data here will be compared). For the first sweep over the search space the step size between the trial values was set to be relatively large. This was 0.1 for both normalised beta and alpha, thus for each frequency 15,000 trial values of the determinant were calculated. Once the surface was plotted and the positions of the minima were determined from it. Many small search spaces that bracketed an area around each of the minima could then be run separately. These small search spaces can be run with very small steps 0.0005 in beta and alpha, so that the root can be found very accurately.

### 2.3 Nature of Modes Within the FSG

The FSG design to have the full mode content investigated was the same as that designated as FSG 1 in chapter 3. This consisted of square loop elements 6.6mm by 6.6mm with the conductor 0.942mm wide. In the model the conductor had no thickness and was constructed from a perfect conductor. The elements were all 7.85mm from the axis of the FSG and curved as if they were on the surface of a cylinder, so that all parts of the elements were the same distance from the axis. Unlike the samples that were made, the computer model required no dielectric to keep the elements in position and they were surrounded by free space. The periodicity between the elements in the axial and circumferential directions was 8.22mm, which gave 6 complete unit cells around the circumference of the FSG. The search space detailed previously was used and one of the resulting surface plots, for normalised  $k_0=0.35$  (12.7GHz), is shown in Figure 2-3 rotated through  $180^\circ$  so that the underside of the surface is uppermost.

From the surface plot the “peaks” which are the minima, giving the positions of the eigen solutions, can be easily seen. They are distributed around three edges of the plot where the beta values are close to zero and one and where the alpha values are close to zero. Curiously there is also a large discontinuity in the surface. This vertical escarpment in the surface exists at the point where normalised  $\beta=0.35$ , the same value as the normalised  $k_0$  value at which the simulation was run. This value of beta corresponds to that used in the simulation code to make the distinction between the fast and slow wave regions. Values of beta that are less than the current value of  $k_0$  are designated fast waves and values of beta greater than  $k_0$  are designated slow waves. This distinction between fast and slow waves is covered in more depth in Section 2.4. In general slow waves tend to be surface type modes and fast waves, can be radiative, evanescent or leaky modes. This clear separation on the surface makes it very easy to tell by inspection whether a mode is fast or slow.

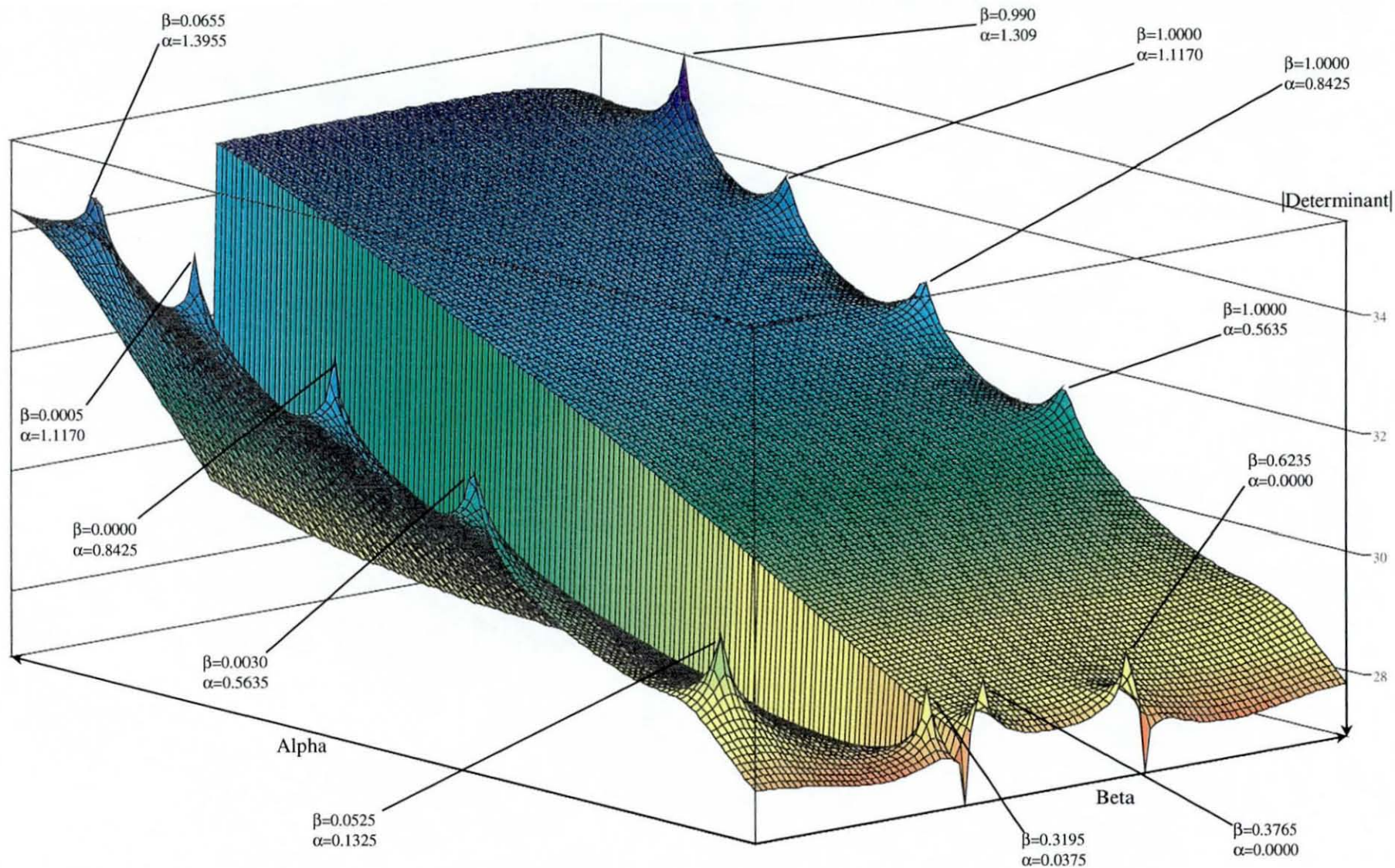


Figure 2-3 Surface plot of complete search space for FSG 1 at  $K_{z0}D_z/2\pi=0.35$

The minima in the fast wave region can be designated by the values of their propagation constants, confirmed in [7]. The modes that have beta values of zero, or virtually zero, are evanescent modes. These three peaks have very high values of attenuation and no beta value. They do not propagate in the z direction, although there may be some transverse power flow. The other three fast wave minima almost certainly represent leaky modes. The two modes with values of beta around 0.05 will radiate energy at approximately 10° from the normal to the FSG. The beam width will be considerably larger for the mode with the highest attenuation as it will radiate energy from a shorter length of FSG than the mode with lower attenuation. The attenuation for both these modes (1066nepers/m and 101nepers/m) is far too large for them to be considered for a practical leaky wave antenna suggested by [15]. The radiation angle of a leaky mode can be approximated using the equation below given in [14].

$$\sin^{-1}(\beta/k_0)=\theta_m$$

Equation 2-4

The final peak in the fast wave region corresponds to another leaky wave mode, which has a main beam that is closer to endfire at 66°. This mode also has a significantly lower attenuation constant of just 28nepers/m. This mode could be of use in a leaky wave antenna although the attenuation is still far higher than that required for a resonant structure waveguide.

The minima in the slow wave can be divided into two groups. Those with zero attenuation and those with beta values of one. The modes with zero attenuation are surface wave modes. It should be noted that these modes have beta values that place them an equal distance from the  $\beta=0.5$  centreline of the surface. The significance of this will be discussed later in this section. The mode at  $\beta=0.99$  and very high attenuation is a lossy surface wave from [7]. This mode is a fundamental Floquet mode and is consistent with a mode that is bound to the surface, but does not propagate for any significant distance as it is very highly attenuated. These highly attenuated Floquet modes may be higher order Floquet modes that are backward propagating, as will be discussed later. The other three peaks in the slow wave region and clustered around the  $\beta=1$  value are the next higher order Floquet modes ( $q=1$ ) of

the three evanescent modes on the opposite edge of the search space in the fast wave region. This is obvious as the alpha values are identical for each pair of minima and are separated by  $\beta=1$  or  $D_z/2\pi$ , the separation between adjacent Floquet modes.

The values quoted in Figure 2-3 are those taken from subsequent fine step investigations around each of the minima seen on surface plot. Each minima was “gated” with a range in alpha and beta of +/- .01 centred on the value taken from the surface plots. This is a range twice that of the previous search step and represents the maximum area within which the minimum could lie. The simulation was then re-run with this range at the same  $k_0$  value and the fine search step of 0.0005 in alpha and beta. The resulting surface plots for two of the minima from Figure 2-3 are shown in **Figure 2-4** and **Figure 2-5**.

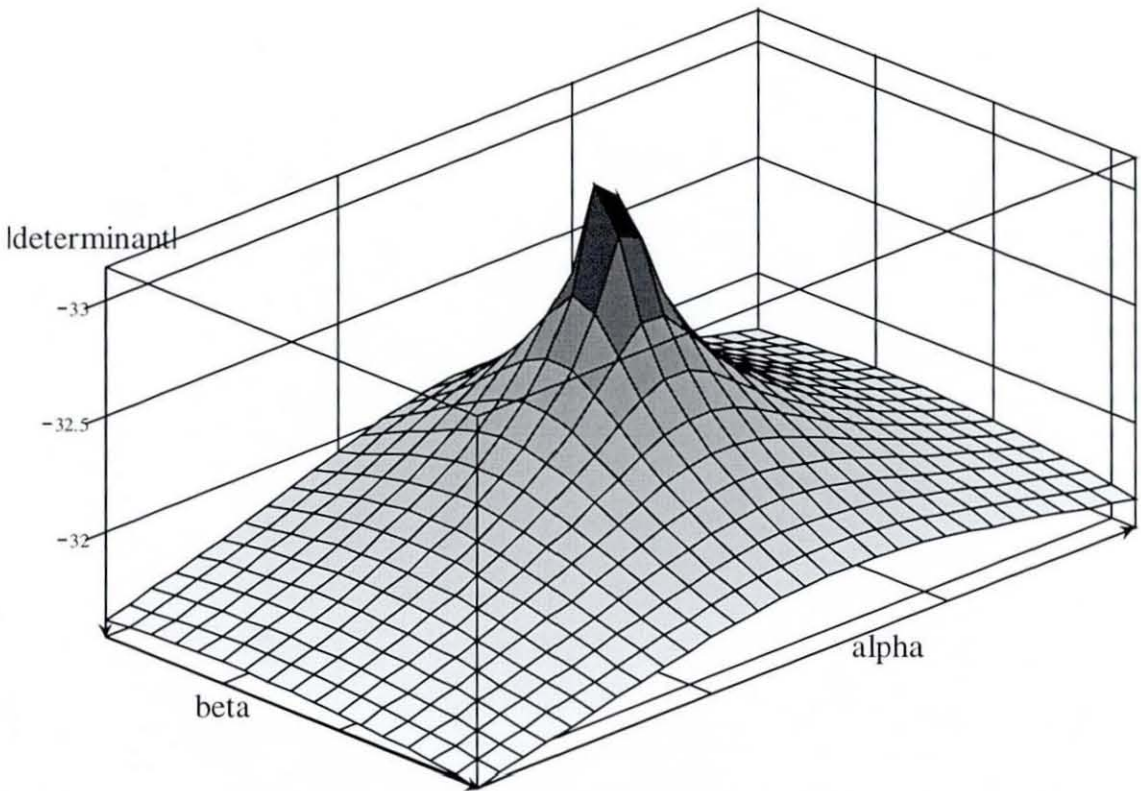


**Figure 2-4** Close-up of first evanescent mode,  $\beta=0.0030$  &  $\alpha=0.5635$  @  $k_0=0.35$ . Showing how 0.0005 steps reveal the change in position of the minimum.

The minima in both **Figure 2-4** and **Figure 2-5** can be seen to have sharp peaks that indicate that they tend to a zero determinant value and are good approximations of the eigen roots. The value of the alpha and beta value can be calculated from the graph by

counting the squares from the point where the “peak” occurs to a known point. The two graphs illustrate the differences between a minimum that occurs on the edge of the search space and is a minimum in one dimension only and one that has a minimum in both alpha and beta dimensions.

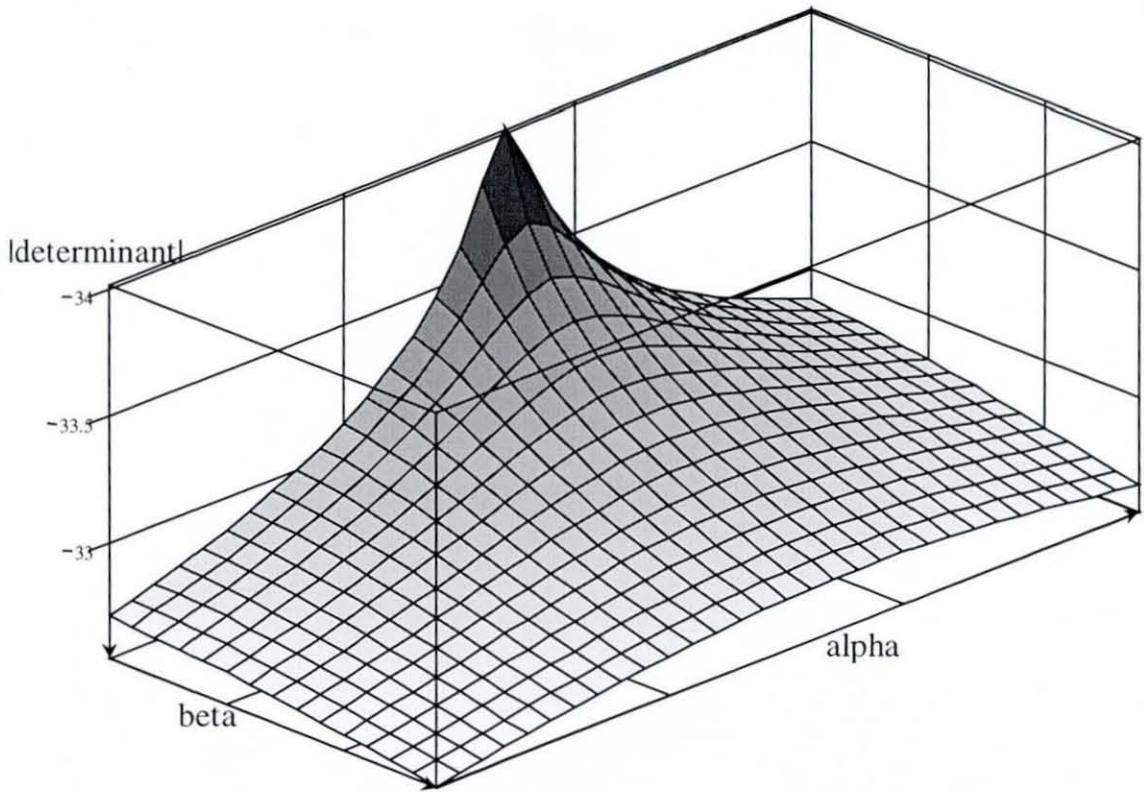


**Figure 2-5 Close-up of second evanescent mode,  $\beta=0$  &  $\alpha=0.8425$  @  $k_0=0.35$ . Showing how 0.0005 steps reveal the change in position and shape of the minimum.**

With the mode spectrum examined for one frequency the value of  $k_0$  was changed so that the operation of the FSG with frequency could be ascertained. The value of normalised  $k_0$  was incremented from 0.1 to 0.6 in 0.025 steps. Around  $k_0=0.4$  this was increased to steps of 0.01 in order to provide some finer detail at this crucial point. For comparison with the previous surface plot at  $k_0=0.35$  in Figure 2-3, the surface plot of  $k_0=0.4$ , equivalent to 14.7GHz, is included in

Figure 2-6.

This surface is similar to that in Figure 2-3 except that all the minima have moved. Some like the fast evanescent modes and very leaky mode have moved very little with

the large change in  $k_0$ . Others have moved considerably, the fast leaky mode closest to the discontinuity has moved even closer to, but separate from it and the attenuation has continued to fall. So the main beam of this mode will appear closer to endfire and with reduced beamwidth. The largest change has taken place in the lowest leaky mode that previously radiated near normal to the FSG. The beta value has changed significantly to 0.2205, which gives rise to a main beam  $33^\circ$  from the FSG normal. The attenuation has also fallen significantly to 4.2nepers/m. This value is of the correct order of magnitude to be used as a leaky mode antenna and if it were to fall lower then low loss propagation may be possible with the mode in an open resonant waveguide. This mode is approaching its resonant frequency, where its attenuation will become a minimum.

The other major change to the distribution of minima is the movement of the surface wave modes. The surface plots at the intervening frequencies show that the eigen values move together and meet at  $\beta=0.5$  and  $\alpha=0.0$ . They then combine into one eigen value with constant beta value of  $\beta=0.5$  and with increasing values of  $\alpha$  as  $k_0$  increases. This could be mistaken for a lossy surface wave if the information about the combination of the two lossless surface modes were not known. This process of the meeting of two surface waves is described on p216 in [23]. The two surface waves form a degenerate pair, which act as a modal stopband. This stopband is characterised by the constant beta value and the increasing alpha value.

The remaining “peaks” at  $\beta=0$ ,  $\alpha=0.826$  &  $\beta=0.7795$  &  $\alpha=0$  in the surface plots were investigated, along with all the others to improve accuracy, with fine step gated plots. It was found that these “peaks” were in fact local minima that did not tend to zero, as can be seen in Figure 2-8 for  $\beta=0$ ,  $\alpha=0.826$ . If this plot of the minimum is compared with same minimum in the plot at  $k_0=0.35$ , in Figure 2-5, then the root that had appeared to tend to zero, now certainly does not.

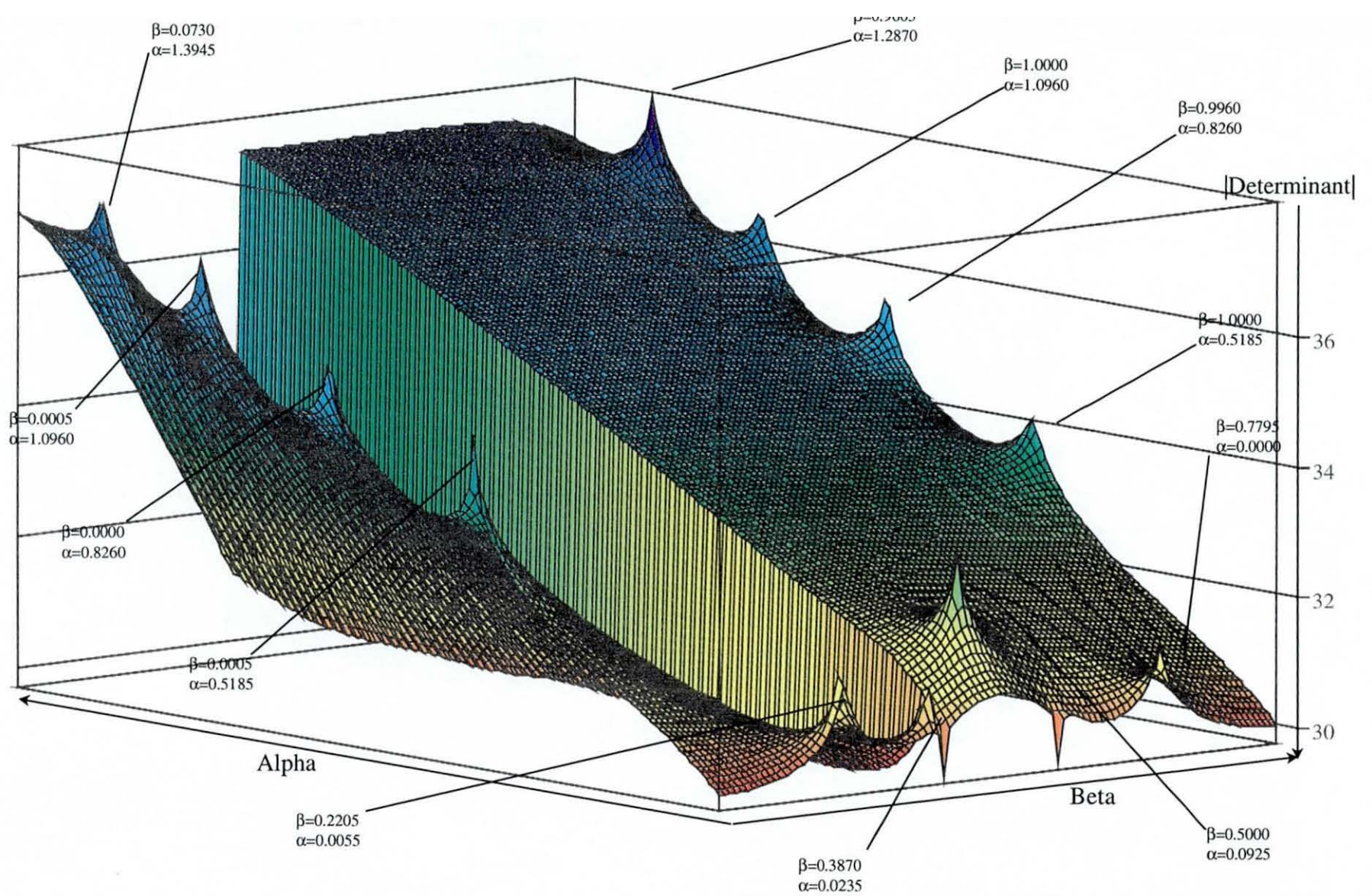
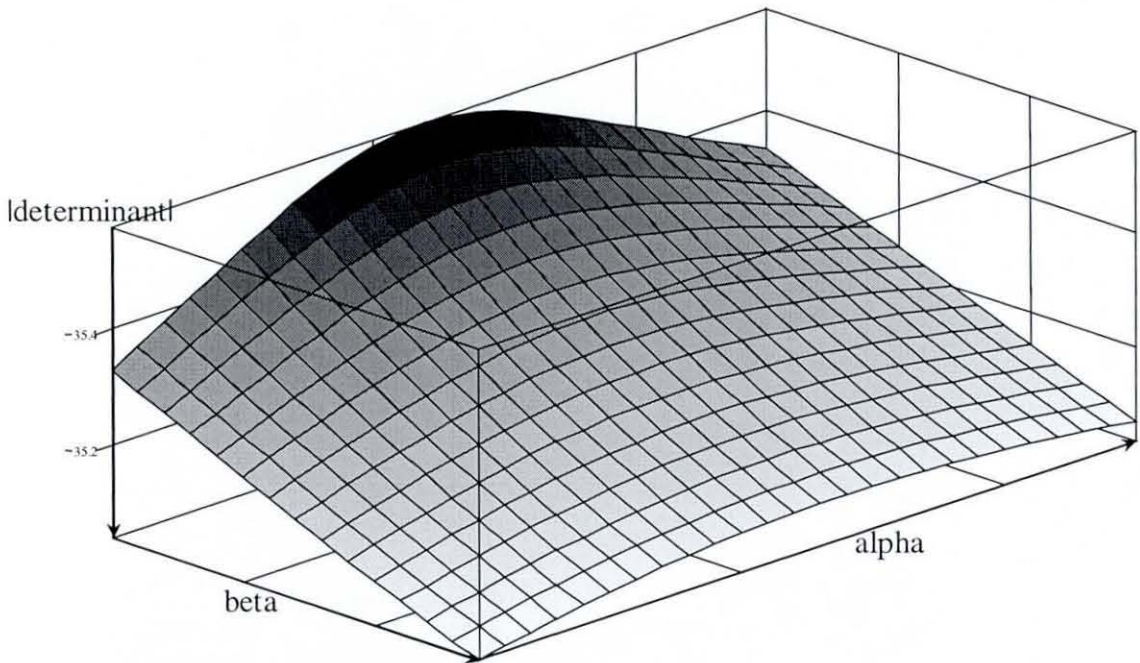


Figure 2-6 Surface plot of complete search space for FSG 1 at  $K_{z0} D_z / 2\pi = 0.4$



The fact that at lower frequencies the root was present and had a  $\beta=0$  value gives a clue to the fate of the root. Instead of the root moving to increasing beta values with increasing  $k_0$  values it has moved to negative beta values. These values are outside the search space and hence the bottom of the minimum where it tends to zero can not be seen. The local minimum that is left is a section through one edge of the actual 2 dimensional minimum. This decreasing beta movement of the root is confirmed by the movement of the  $n=-1$  backward travelling Floquet mode from  $\beta=1, \alpha=0.8425$  at  $k_0=0.35$  to  $\beta=0.996, \alpha=0.826$  at  $k_0=0.4$ . From a basic knowledge of conic sections this can be extended to say that any local minimum at the edge of the search space is a section from a root that falls outside the search space. The relevance of these roots will be covered in the following section on the decision making process in the model.



**Figure 2-8 Close-up of second evanescent mode,  $\beta=0.0$  &  $\alpha=0.8260$  @  $k_0=0.40$ . Showing how 0.0005 steps reveal the minimum tending to zero.**

**Figure 2-9** shows a fine step detail plot for the lowest evanescent mode in the  $k_0=0.4$  spectrum for comparison against the same mode at  $k_0=0.35$  in **Figure 2-4**. This also shows some small movement of the root in the  $-\beta$  direction.

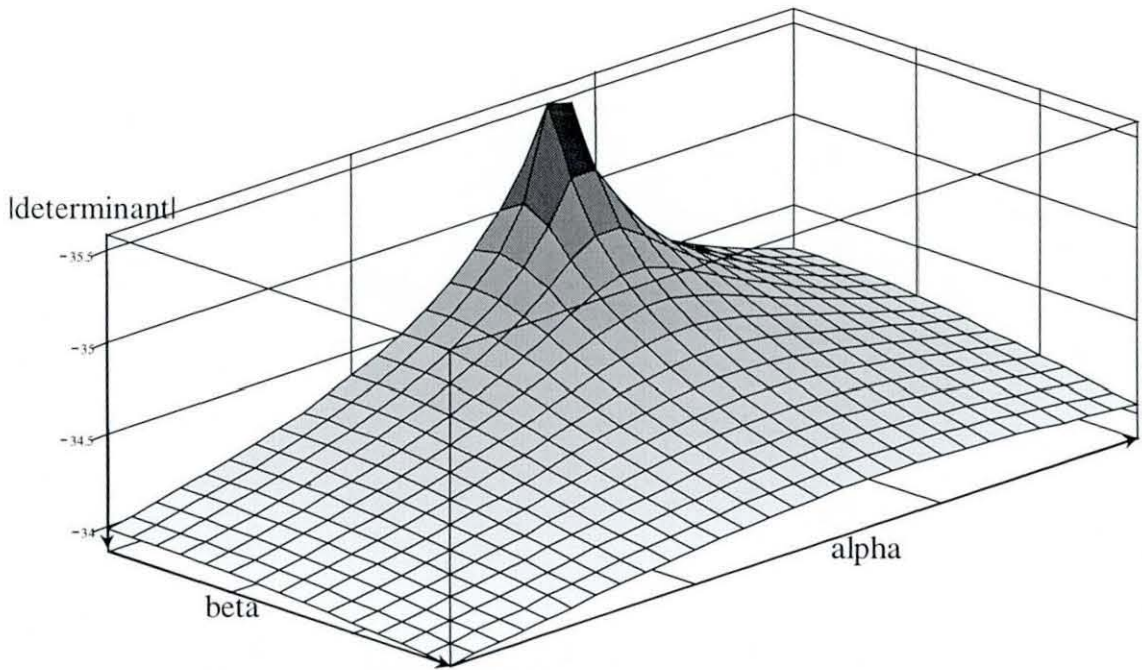


**Figure 2-9 Close-up of first evanescent mode,  $\beta=0.0005$  &  $\alpha=0.5185$  @  $k_0=0.40$ . Showing how 0.0005 steps reveal the minimum tending to zero.**

The extraction of the eigen mode roots from the surface plots gives a large amount of data that needs to be drawn together. One of the most desirable analyses required was to combine the roots from all the different frequencies. So that the frequency response of each mode in the FSG can be formed. This information will enable the FSG operation to be better understood and compared to the measured values. It will, most importantly, enable the resonant frequency of the FSG to be found. This is the point where the leaky wave attenuation becomes a minimum value. This process was found to be easy at values of  $k_0 < 0.4$  as there were relatively reasonably stationary few roots. Above this value the number of roots increases very fast and the values of alpha and/or beta begin to change rapidly for some modes. In fact above  $k_0=0.5$  it became impossible to be certain if roots on adjacent frequency plots were of the same mode. This could be alleviated to some degree by taking frequency steps much closer together. However as these frequencies are above the frequency range of primary interest for mode matching, it was decided not to do very fine steps and to leave a break in any response where the locus of a eigen value is not one hundred percent certain.

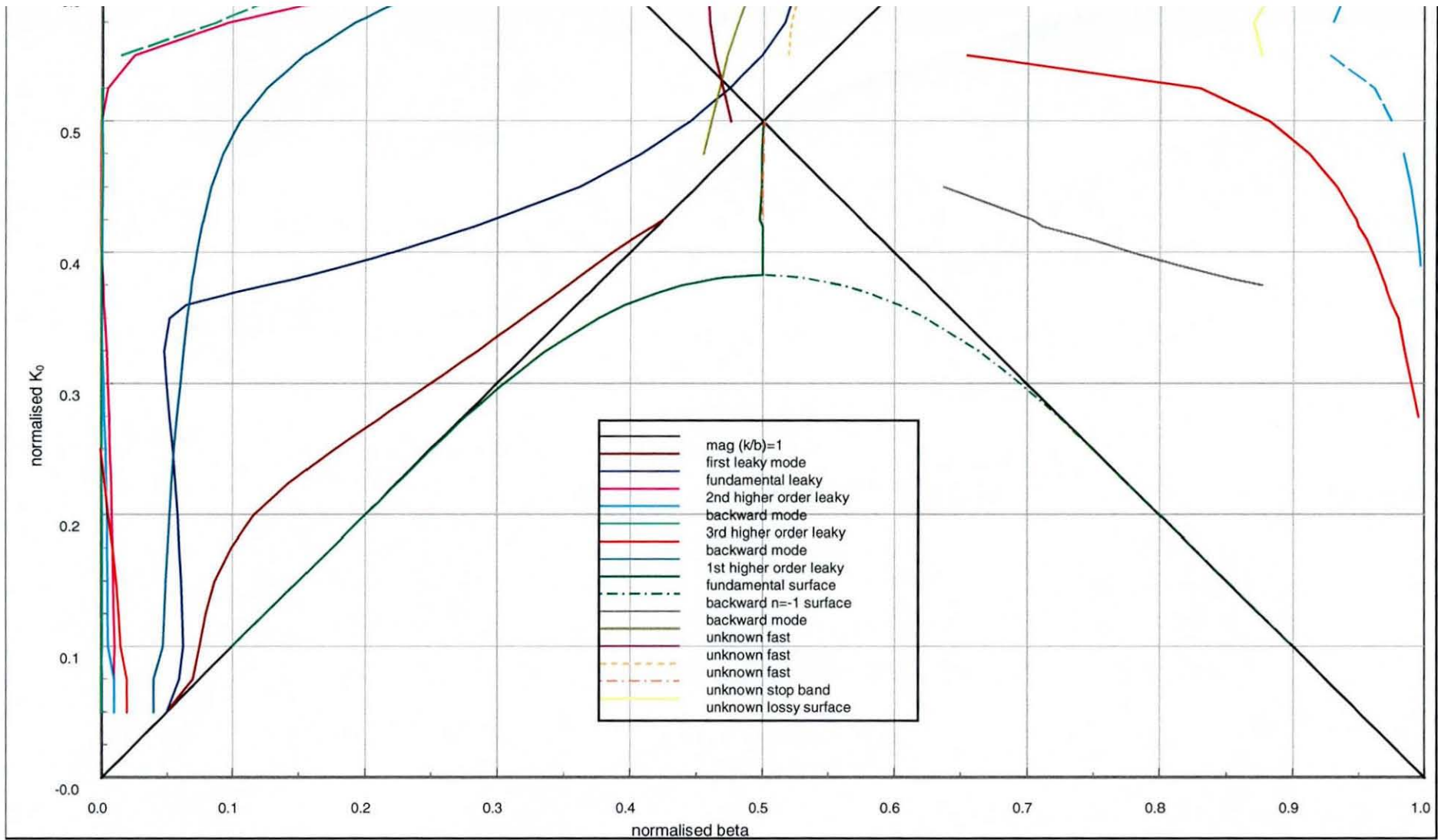


Figure 2-9  $k_0/\beta$  Diagram showing the fundamental mode spectrum of the FSG.

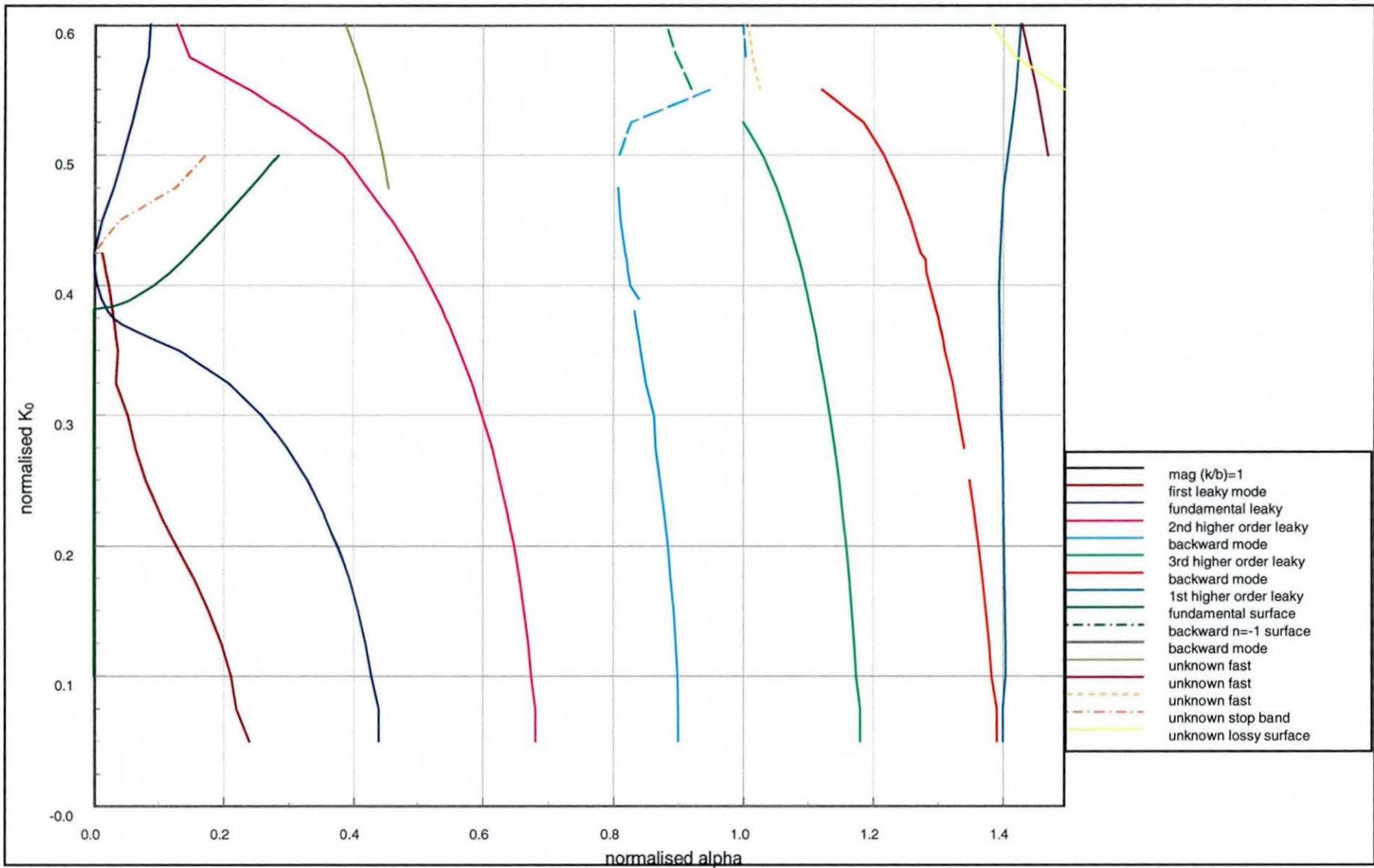


Figure 2-10  $k_0/\alpha$  Diagram showing the fundamental mode spectrum of the FSG.

Figure 2-10 shows the changes of the beta values of the fundamental Floquet eigen mode spectrum with frequency and Figure 2-11 shows the change of the alpha value with frequency. It must be remembered that these are complex roots and so both graphs must be viewed together and neither can be taken in isolation.

The fundamental lossless surface mode and the  $n=-1$  Floquet mode of the backward travelling surface mode are shown in Figure 2-10. They depart from the TEM mode (shown as the line where  $\beta=+/-k_0$ ) and arch towards each other and meet at  $\beta=0.5$  and  $k_0=0.38$ . As already stated this point is the beginning of a stop band for this surface mode. The modes become degenerate and the beta value remains constant, the increase in  $\alpha$  value can be seen in Figure 2-11 from this point finally finishing at  $\alpha=0.2840$  an attenuation of 217nepers/m. It is stated in [7], when degenerate this pair of modes is not orthogonal, have no net power flow and are associated with stored energy.

The mode of most interest is the fundamental leaky mode as found by Loukos in [1]. The beta and alpha of Figure 2-10 & Figure 2-11 show that it is a leaky mode with initially a slight backward propagation with decreasing attenuation. As the rate at which the attenuation decrease increases the mode propagates in the forward direction. The beta curve in this region looks more like associated with a fast propagating mode. In this region at  $k_0=0.411$  the attenuation becomes a minimum value of 0.5nepers/m. At this point the FSG is operating as a resonant structure and the loss is reduced to a minimum value and the mode phase constant crosses the  $TE_{11}$  curve of a solid waveguide of the same radius.

There does appear to be a type of leaky wave cutoff, a point where the mode changes from a very lossy mode that radiates close to the normal, to a mode that exhibits all the standard leaky mode characteristics. One that has a rapidly changing beta value and a narrow main beam of radiation. The second and third higher order leaky modes plotted in Figure 2-10 & Figure 2-11 both appear to adhere to this same cutoff phenomenon. However the first leaky mode and first higher order leaky mode do not adhere to this. The first leaky mode appears to be a quasi TEM mode always having a steadily decreasing attenuation and a beta value that does not stray far from the TEM

line. At  $k_0=0.42$  the mode crosses the TEM line and is lost. At this time it is unclear what this leaky mode truly is. The final leaky mode designated as the first higher order leaky mode also does not have a similar cutoff. It does undergo a rapid change in the beta value, and this is not accompanied by a rapid decrease in the attenuation. The alpha value does in fact rise very slightly. This mode is so lossy that it will exist over very short lengths of FSG and have very wide beams if it is excited.

The modes designated as backward modes in Figure 2-10 & Figure 2-11 are the backward travelling equivalents of the leaky modes previously described. However as these start to propagate with increased  $-\beta$  values they move out of the search space and the plot is lost. However the fact that they are backward travelling is confirmed by the appearance of the  $n=-1$  mode moving in a  $-\beta$  direction from the  $\beta=1.0$  edge of the search space. A value in this region of the search space must have an  $n=0$  Floquet mode  $-D_z/2\pi$  away in the beta value. This confirms what was suspected about the minimum seen in **Figure 2-8** at  $k_0=0.4$ .

Finally the group of modes are included in Figure 2-10 & Figure 2-11 and are labelled unknown fast, stop band and lossy surface. These 5 modes are fast, stop band and lossy surface modes as labelled. They suddenly appear in the spectrum and with no history of their movement it is difficult to be certain in their identification. There is however some concern over the decision making used in the model and the validity of these modes for inclusion in the physical space field is unclear. This is discussed in more depth in the next section 2.4 and so no further classification of these modes will be carried out.

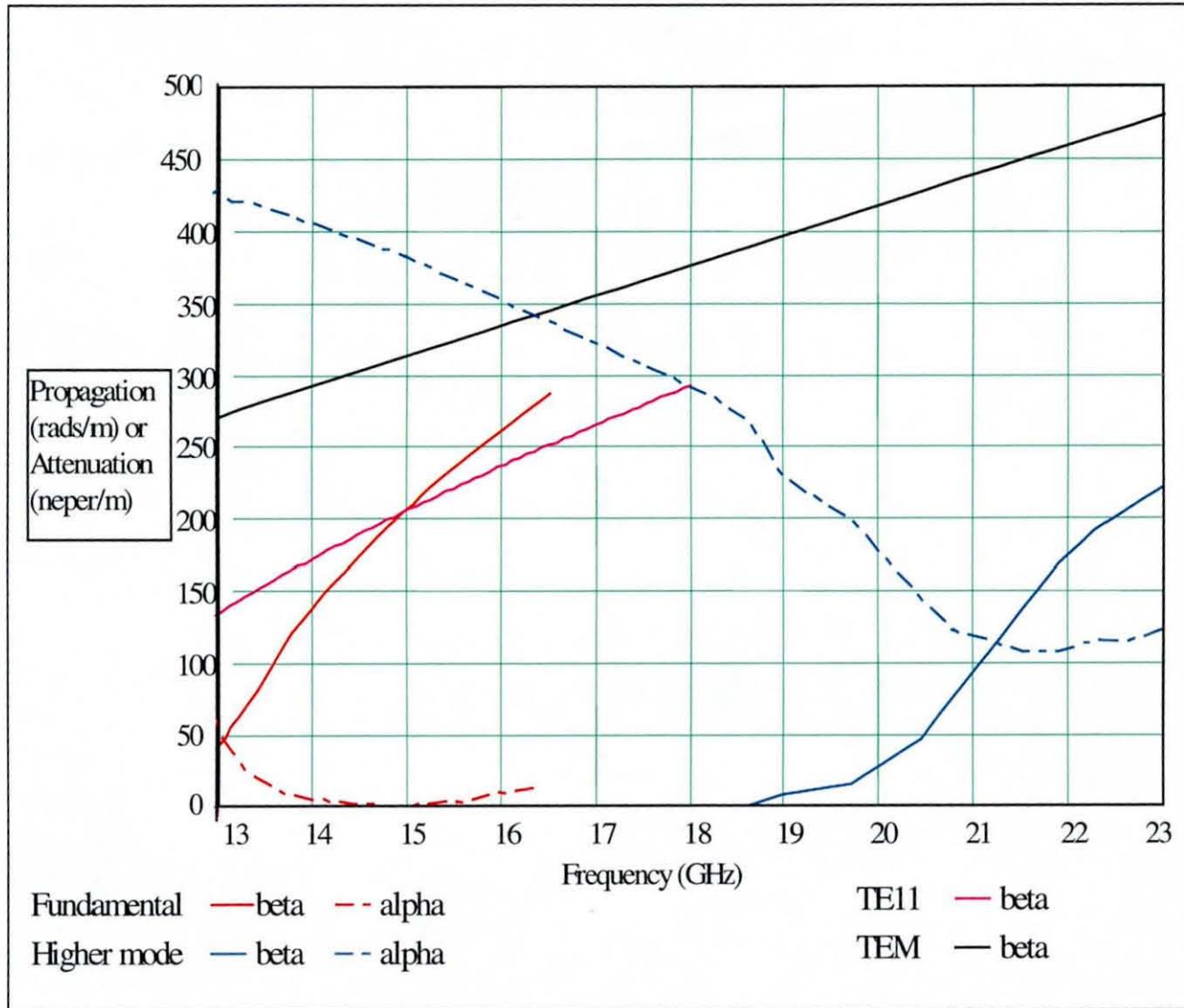


Figure 2-11 Phase and attenuation constants against frequency for the 1<sup>st</sup> two leaky modes.

The mode designated second higher order mode was investigated further to find out exactly if it resonated as the fundamental mode did. From Figure 2-10 & Figure 2-11 it was clear that it remained in its very lossy, virtually evanescent state until its 'cutoff' frequency was reached. It then clearly starts to propagate in the z direction. It was desirable to know if it did have a resonance like the fundamental. Did it behave in a similar fashion to a second higher order mode in a solid guide? Of course, being a leaky mode it would still have attenuation. The program was run many times with a small localised search space, the frequency being increased each time and the position of the peak found. It was necessary to move the search space each time in order to keep the peak within range. The predicted values for the second higher mode are shown in Figure 2-12 along with the TEM, TE<sub>11</sub> solid guide and the fundamental leaky mode.

From Figure 2-12 it is clearly evident that indeed the second higher mode has some similarities to the second higher mode in solid guides. It does have a pseudo cutoff, around 19 GHz, after which it begins to propagate with greatly reduced attenuation. Notice how the attenuation falls generally as the frequency increases, but falls even more sharply at the cutoff frequency. Unfortunately the attenuation is very high, even at the resonant point, taken to be around 21.5 GHz. This would make it unsuitable for any practical use, as the mode would die away before propagating any distance.

#### 2.4 Implications of k-β diagrams on ascertaining the properties of an FSG mode

In the previous section several mentions were made of the decision making code in the Loukos model [1]. This process was required to ensure that all the trial roots of the eigenvalue equation were physically realisable roots of the characteristic equation and represented real spectral modes, or that they were unreal non-spectral roots that had physical meaning within a limited area, i.e. leaky modes that represented the radiation field in a sector close to the FSG. This process is required, as the trial roots of the axial propagation constant  $k_z$  are complex and so when the transverse radial propagation constant  $k_r$  is calculated from Equation 2-5 there are two possible complex values that it can take. Some of these values are realisable and some are physically impossible. Only the physically relevant values of  $k_r$  can be used in the



calculation to find the determinant and these determine the classification of the mode, when a root is found.

$$k_r = \sqrt{(k_o^2 - k_z^2)}$$

Equation 2-5

In [1] Loukos gives the decision making used in his model for each Floquet mode as either:-

Leaky Wave (i.e.  $\alpha_r > 0$  &  $\beta_r > 0$ ) WHEN  $q=0$  &  $\beta_z < k_0$  OR  $q < 0$  &  $k_0 > \beta_z > 0$

OR

Surface Wave (i.e.  $\alpha_r < 0$  &  $\beta_r < 0$ ) WHEN  $q=0$  &  $\beta_z > k_0$  OR  $q > 0$  OR  $q < 0$  &  $\beta_z < -k_0$

OR

Proper Radiative (i.e.  $\alpha_r < 0$  &  $\beta_r > 0$ ) WHEN  $q < 0$  &  $0 > \beta_z > -k_0$

N.B. In all these cases  $\alpha_z \leq 0$  in order that these waves are physical in the  $z$  direction as we have a passive, non amplifying, system and  $q$  is the Floquet mode number in the  $z$  direction

The field propagation in  $z$  is defined by  $e^{-jk_{zq}z}$  and  $k_{zq} = \frac{2\pi}{D_z}q + k_{z0}$  with  $k_{z0} = \beta_z - j\alpha_z$  ..

In the radial direction inside the FSG the fields are governed by the Bessel function of the first kind  $J_n(k_{rq}r)$  and outside the FSG by the Hankel function of the second kind

$H_n^{(2)}(k_{rq}r)$  where  $k_{rq} = \sqrt{k_0^2 - k_{zq}^2}$  so that  $k_{rq} = \beta_r - j\alpha_r$

This information is traditionally displayed on a twin surfaced Riemann sheet which relates the  $k_z$  values to the  $k_r$  values see Figure 2-13. The branch cuts corresponding to the continuous spectrum of radiation modes are shown as dotted lines. The possible values of  $\beta_r$  &  $\alpha_r$  are shown in the respective quadrants for particular values of  $\beta_z$  &  $\alpha_z$ . N.B. As the external fields are defined by Hankel functions of the *second kind*, proper and improper Riemann sheets have been interchanged with respect to those that are usually quoted in texts, where the external fields are denoted by Hankel functions of the *first kind*.

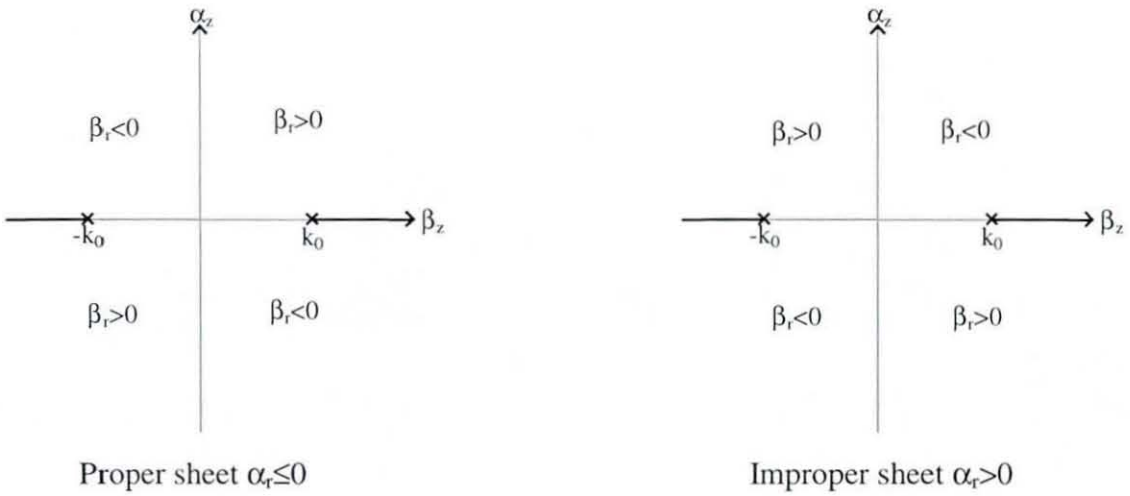
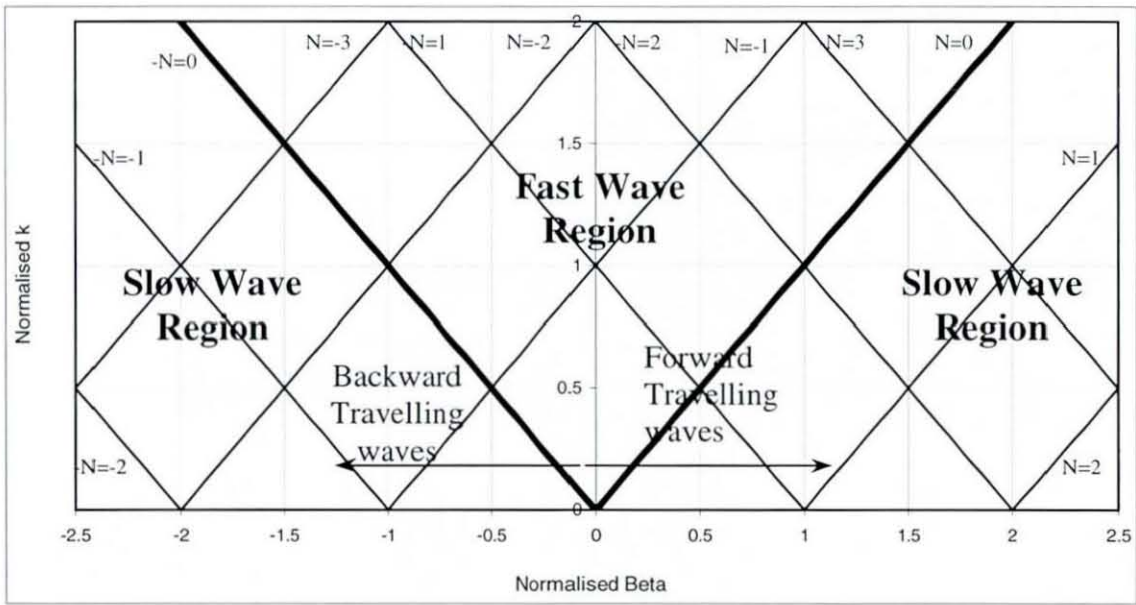


Figure 2-13 Two surfaced Riemann sheets for the equation  $k_{rq} = \sqrt{k_0^2 - k_{zq}^2}$

Two sheets are required to represent the mapping of one complex value to another. The branch cut that links the two sheets is represented by the dashed axis. If the locus of a point crosses the branch cut on one of the sheets, then it switches to the identical point on the branch cut of the other sheet and the locus continues on the other sheet. More detailed information on Riemann sheets can be found in [23]. From [3] the modes of the continuous radiation and evanescent spectrum lie along the branch cuts of the proper sheet. The lines that represent the Loukos decision making are vertical lines through the  $|\beta_z|=k_0$  on the proper and improper sheets. A  $\beta_z$  value between zero and  $k_0$  is forced onto the improper sheet and so is a leaky mode, all other values fall on the proper sheet and so are real modes. This is the reason for the discontinuity in the value of the determinant surface. The modes are forced from one sheet to another without having passed through the branch cut, except at  $\alpha_z=0$ .

For any value of  $\alpha_z$  the useful information about Floquet modes can be displayed on a  $k/\beta$  diagram, as described on 191 in [23]. This format of diagram has already been presented in Figure 2-10 and was used extensively by Loukos in [1]. It stems from the plotting of the boundary between fast and slow wave regions for unattenuating structures, the line where  $k_0 = \pm \beta_z$ . If the modal field in question is represented by a infinite sum of Floquet modes, this mode is known from [23] as a Bloch wave and these lines are repeated an infinite number of times at  $k_0 = \pm (\beta_z 2\pi/D_z)$  as shown in **Figure 2-14**.



**Figure 2-14**  $k/\beta$  Diagram for Floquet Modes and  $\alpha_z=0$ .

The Floquet modes of a Bloch wave are characterised as each having different phase velocities, but identical group velocities from the well known Equation 2-6.

$$v_{gn} = \frac{\partial \omega}{\partial \beta_n}$$

Equation 2-6

This implies that all energy in each Floquet mode is transmitted along the structure at the same speed and reaches a distant point at the same instant. A single forward propagating Bloch wave is formed from both forward and backward travelling Floquet modes. A mode that is forward propagating, yet backward travelling has a phase velocity in the  $-\beta$  direction, but a group velocity in the  $+\beta$  direction.

The  $k/\beta$  diagram in **Figure 2-14** shows that there is only one region in which fast waves can exist. Any Floquet mode in this region must be a fast wave. All other Floquet modes outside this region must remain slow waves at all times. The replication of the  $|n|=0$  fast and slow wave boundary along the axis to the other origin values of  $|n|>0$ , allows easy identification of the point when a higher order Floquet mode enters or leaves the fast region. This occurs when the locus of the fundamental mode crosses one of the higher order boundary lines. This means that the corresponding higher order Floquet mode has entered or left the fast wave region, so

the loci of the higher order Floquet modes do not have to be tracked. From [23] in open structures, the modes of the fast region tend to be radiative in nature. The decision making used in [1] is taken from this  $k/\beta$  diagram. If  $\beta_z$  falls into the slow wave region then it is a surface wave. If it is a forward propagating fast wave then it is a leaky mode and a backward propagating fast mode is backward radiative. The  $k/\beta$  diagram shown in **Figure 2-14** can be thought of as lying along the  $\alpha=0$  axis of a Riemann sheet. The Riemann sheet is drawn for a fixed value of  $k_0$  and as this is changed the sheet can be moved accordingly up or down the  $k_0$  axis of the  $k/\beta$  diagram. The point where the branch cut starts is the line that separates the fast and slow regions on the  $k/\beta$  diagram.

However [23] suggests that the  $k/\beta$  diagram should be altered if the propagation constants are complex and the attenuation is non zero, as in the case of the FSG.

$$(\beta_r - j\alpha_r)^2 = k_o^2 - \beta_z^2 + \alpha_z^2 + 2j\alpha_z\beta_z$$

Equation 2-7

Equation 2-7 shows that in order for  $\beta_r^2 - \alpha_r^2$  to be zero then  $k_o^2 = \beta_z^2 - \alpha_z^2$ . The significance of  $\beta_r^2 - \alpha_r^2 = 0$  is that this marks the boundary between fast and slow wave in the  $k/\beta$  diagram and is any point where  $\beta_r^2 = \alpha_r^2$ . This means that for any mode with attenuation the boundary between the fast and slow wave moves to form a hyperbola as shown in **Figure 2-15**. The position of the branch cuts on the Riemann sheet is unaltered with attenuated mode and is given by the conditions that  $2j\alpha_r\beta_r = 0$  &  $\beta_r^2 - \alpha_r^2 \geq 0$ . This translates to the position already given in Figure 2-13 for the branch cut that either  $\alpha_z = 0$  or  $\beta_z = 0$  &  $k_o^2 \geq \beta_z^2 - \alpha_z^2$ .

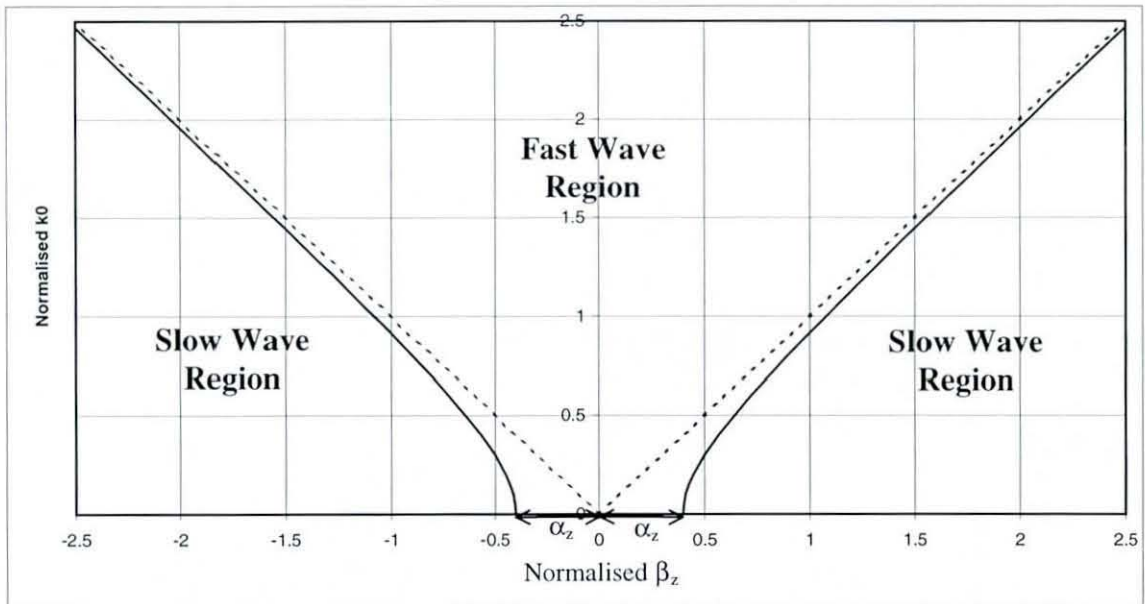


**Figure 2-15  $k/\beta$  Diagram showing the fundamental  $n=0$  separation lines deformed by attenuation  $\alpha_z$ .**

This means that as the attenuation increases then the slow wave region shrinks and the fast wave region gets bigger. This means that the boundary between fast and slow waves is not invariant with  $\alpha$ . It should be noted though that not only does the displacement of the boundary increase with increasing attenuation, but it also becomes more blurred. When there is zero attenuation the wave is either a radiative mode or a surface mode, with increased attenuation this becomes a little more of a grey area in the vicinity of the boundary. It becomes a case of the mode behaving more with the characteristics of one mode type, but still with some aspects of the other. The degree to which this is true depends on the proximity of the root to the boundary.

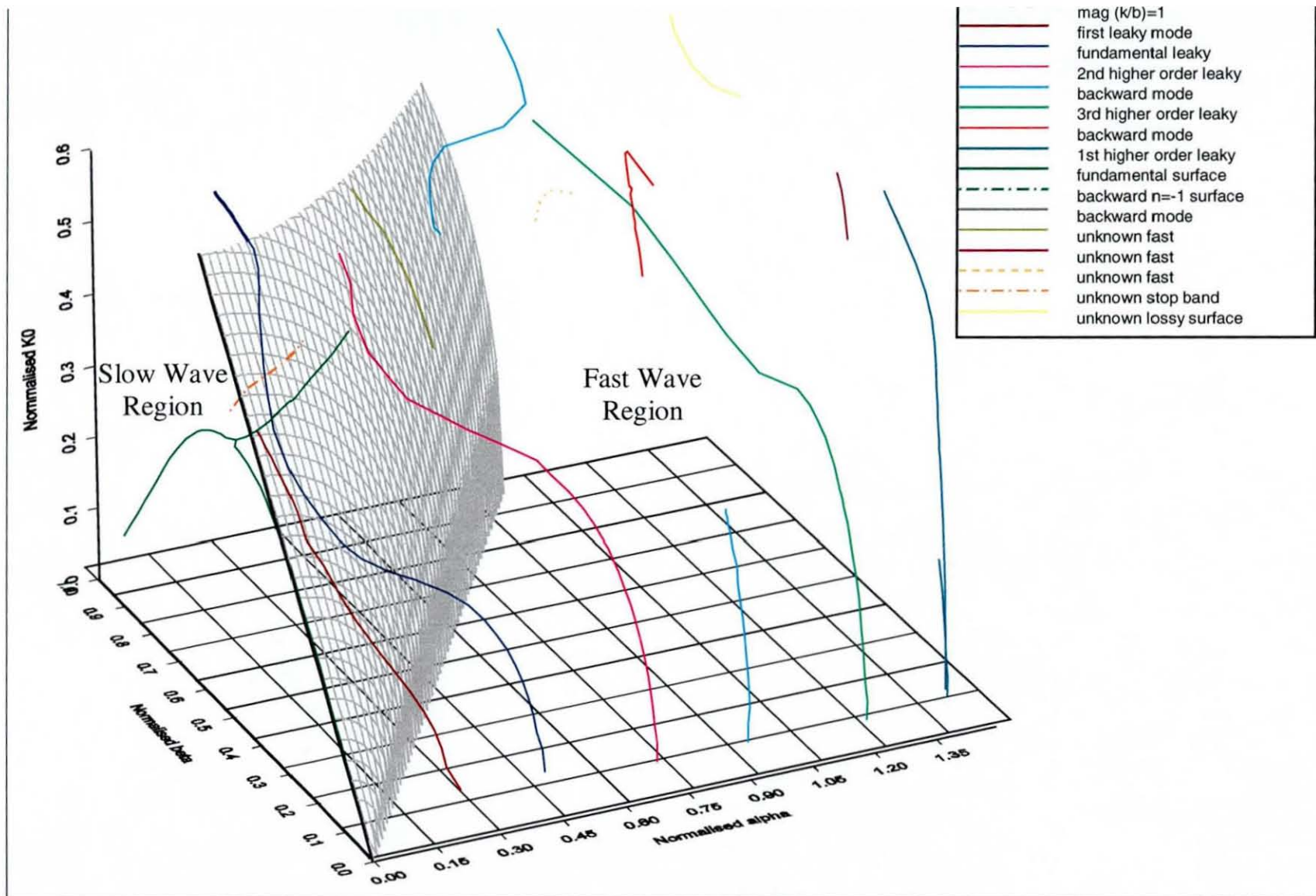


Figure 2-15 3D plot of  $k/\beta/\alpha$  Diagram. Showing the separation surface between the slow and fast wave region & the Eigen mode roots for FSG1.

With the new knowledge of the  $k/\beta$  diagram when attenuation is present, a series of altered  $k/\beta$  diagrams can be placed on a Riemann parallel to the position of the  $\alpha=0$   $k/\beta$  diagram talked about earlier. A three dimensional representation cannot be made which combines the Riemann sheet and the  $k/\beta$  diagram, see Figure 2-16. With modern computer plotting packages this diagram can be rotated on screen to view each part from the best angle. It unfortunately does not translate to static two dimensional representations very well. The full benefit to the researcher would be to have this three dimensional graph represented in virtual reality. This is beyond the remit of this work, but the author believes that this three dimensional graph is a useful first step the development of more informative three dimensional graphical methods. The advantage of this is that the separation boundary of the fast and slow regions can be seen for all values of  $k_0$ ,  $\beta_z$  and  $\alpha_z$ .

The three dimensional  $k/\beta/\alpha$  graph of Figure 2-16 allowed the easy investigation of the proximity of the loci of the eigen roots to the surface that made up the boundary between the slow and fast wave regions. In most cases there was seen to be sufficient separation between them to make any concerns about any alterations required to the decision making, of the model from [1], unnecessary. However in the region of  $k_0 > 0.45$  the appearance of the unknown modes of Figure 2-10 & Figure 2-11 does cause some concern. However the decision in chapter 4 to carry out mode matching around the resonant frequency reduced the criticality for this investigation to be carried out in this piece of work. It is recommended that this area of the mode spectrum, at higher  $k_0$  values, be looked into more closely with close attention paid to changing the decision making employed in [1] to take account of the attenuation constant.

## 2.5 References

- [1] Propagation Characteristics of Cylindrical Frequency Selective Guides – G.I.Loukos, Ph.D. thesis Loughborough University 1997.
- [2] Light Transmission Optics – D.Marcuse, Van Nostrand Reinhold Co, New York, 1972.
- [3] Open Electromagnetic Waveguides – T.Rozzi & M.Mongiardo, The Institution of Electrical Engineers, London, 1997.

- [4] The Guiding and Radiation of Surface Waves – F.J.Zucker – Symposium on modern advances in microwave techniques, polytechnic Institute of Brooklyn, New York, 1954, p403.
- [5] On Field Representations in Terms of Leaky Modes or Eigenmodes – N.Marcuvitz – Trans IRE, AP-4, 1956, p192.
- [6] Leaky Wave Antennas: Part 1 – Rectangular Waveguides – L.O.Goldstone & A.A.Oliner – IBID, AP-7, 1959, p307.
- [7] Guided Complex Waves Part 1. Fields at an interface & Part 2. Relation to radiation patterns – T.Tamir & A.A.Oliner – proc I.E.E., vol 110, No2, February 1963, p310 & p325.
- [8] Theory of Dielectric Optical Waveguides – D.Marcuse, Academic Press, 1974.
- [9] Leaky Modes on a Dielectric Waveguide: Orthogonality and Excitation – R.Sammut & A.W.Snyder – J.Applied Optics, Vol 15, No 4, April 1976, p1040.
- [10] Optical Waveguide Theory - A.W.Snyder & J.D.Love – Chapman & Hall Ltd, 1983, Chapter 24, p487.
- [11] Direct Experimental confirmation of New leakage Effects on Open Dielectric Strip Waveguides – H. Shigesawa, M.Tsuji, J.S.Myung, S.T.Peng & A.A.Oliner, IEEE MTT-S Digest, 1983, p293.
- [12] The Nature of the Leakage from Higher modes on Microstrip Line – A.A.Oliner & K.S.Lee, IEEE MTT-S Digest, 1986, p57.
- [13] Existence of a Leaky Dominant Mode on Microstrip Line with an Isotropic Substrate: Theory and Measurements – D.Nghiem, J.T.Williams, D.R.Jackson & A.A.Oliner – IEEE MTT, Vol 44, No 10, October 1996, p1710.
- [14] Leakage from Higher Modes on Microstrip Line with Applications to Antennas – A.A.Oliner – J. Radio Science, Vol 22, No 6, November 1987, p907.
- [15] Design considerations for Leaky-wave Antennas – I.J.Bahl & K.C.Gupta - Proc. IEE, Vol123, No 12, December 1976, p1302.
- [16] A Spectral Domain Approach for Computing the Radiation Characteristics of a Leaky-Wave Antenna for Millimeter Waves – R.Mitra & R.Kastner – IEEE A&P, Vol29, no4, July 1981, p652.
- [17] Radiation from Periodic Structures Excited by an Aperiodic Source – R.A.Sigelmann & A.Ishimaru – IEEE A&P, october1964?, p354.
- [18] Scattering Resonances on a Fast-Wave Structure – R.C.M.Li, A.A.Oliner – IEEE A&P, Vol13, No6, November 1965, p948.



- [19] Application of Gratings in a Dielectric Waveguide for Leaky-Wave Antennas and Band-Reject Filters – T.Itoh - IEEE MTT, vol25, No 12, December 1977, p1134.
- [20] Dielectric Grating Antennas – S.T.Peng & F.Schwering - Research & Development technical Report, CORADCOM, July 1978.
- [21] Dielectric Rod Leaky-Wave Antennas for Millimeter-Wave Applications – S.Kobayashi, R.Lampe, R.Mitra & S.Ray – IEEE A&P, Vol 29, No 5, september 1981, p822.
- [22] Coupling Between Different Leaky-Mode Types in Stub-Loaded Leaky Waveguides – H.Shigesawa, M.Tsuji, P.Lampariello, F.Frezza & A.A.Oliner - IEEE MTT, Vol 42, No8, August 1994, p1548.
- [23] Antenna Theory part2 – R.E.Collin, F.J.Zucker – McGraw-Hill Book Company, New York, 1969.
- [24] Field Theory of Guided Waves – R.E.Collin - McGraw-Hill Book Company, New York, 1960.
- [25] Propagation Characteristics of Frequency Selective Waveguides with Circular Cross-Section - G.Loukos & J.C.Vardaxoglou – Proc. Joint URSI UK 12<sup>th</sup> National Radio Science Colloquium and QMW Antenna Symposium, Queen Mary and Westfield College, London, 11<sup>th</sup>-13<sup>th</sup> July 1995.

## 3. Investigation of FSG by Measurement Methods

The open structure of metallic elements that is periodic in two directions and formed into a cylinder of circular cross section referred to as a “Frequency Selective Guide” (FSG), has been modelled and described extensively by Loukos in [6]. However, little measurement work, of a structured nature, had been undertaken to investigate experimentally the physical characteristics of the structure and to ascertain the accuracy of the results produced by the model. Only when the measured propagation constants match the predicted values can the accuracy of the model be assured.

The measurements of the FSG can also be used themselves to deduce many of the properties of the structure independently from the data obtained from the model. As the FSG is an open structure that has been found to exhibit a mixture of both open and closed properties, measurement techniques can be employed that are traditionally used either for only open radiating structures or else for closed non radiative structures. Use was made of broadside radiation plots taken at many individual frequencies to give a rough frequency response of the radiation field. As well as these radiation pattern measurements, reflection and transmission scattering parameters were also taken over a large frequency range, by treating the FSG as a two port device.

### 3.1 FSG Design

Before any measurement work could be undertaken, FSG's of a high quality and manufactured to strict production standards were designed and built. The FSG modelled by the computer program consists of identical freestanding metal elements at a constant radial distance from the FSG axis and separated from each other by a constant periodic distance in the axial and circumferential directions. In reality the elements require some structural support to make it possible to manufacture the FSG.

The support material used must be of a suitable dielectric type, which is not going to alter the properties of the FSG significantly. It must also allow easy construction of the metallic elements upon its surface. Design procedures are listed here: -

- The first requirement when designing an FSG is the frequency of operation. In most cases this will be the frequency at which the FSG resonates and where the least amount of leakage occurs. However it could also be a frequency away from resonance where a specified amount of power is radiated at a specific angle, in the leaky region of FSG operation. In this investigation it was required that the resonant frequency be within the frequency band at which the feeding waveguide operates. Ideally if the resonant frequency is in the centre of the band this allows investigation of the characteristics not only at resonance, but also the characteristics during the transition into and from the resonant region, the leaky region.
- To determine the size of the elements ( $L$ ) and the spacing between them. It should be noted that the element size added to the spacing between adjacent elements is called the periodicity ( $D$ ) and is the distance between adjacent element centres. The element size and periodicity define the resonant frequency and behaviour of the array. As a starting point computer model, developed previously at Loughborough University, that calculates the resonant frequency of a planar sheet of FSS. This program has a run time considerably faster than the FSG modelling program and so is ideal to gain an indication of the element size and periodicity required. The program was run with the excitation plane wave incident upon the FSS at an angle of around  $60^\circ$ . This was done because it was felt that we would get a more accurate value of the element size and periodicity than if we used the normal incident case. Drawing a parallel with solid waveguide theory, then propagating modes within the guide must also be incident upon the guide surface at some acute angle. The angle used though was decided upon arbitrarily as this step is only used to get an initial starting point for the next stage of the design. This can be seen to be a valid technique in section 3.4.1, where the measured results of the FSS sheet are presented.
- A further difficulty in defining the element periodicity dimensions of the FSG is that the circumference must be an integer multiple of periodicity. This is necessary so that a uniform array is seen around the circumferential direction and

the cylinder has an overall rotational periodicity of  $2\pi$ . The elements used are square loops and have side lengths and periodicities identical in both directions. This simplification makes the calculation of the array dimensions easier and ensures that the arms of the loop resonate at the same frequency in each direction.

- Once the rough size and periodicity of the FSG elements has been established, these dimensions, along with the radius of the FSG, are used as inputs into the FSG simulation program written by Loukos [6]. This program only produces the values of solutions to the boundary value problem, see chapter 2 for details, at a particular frequency. The output consists of either the complex propagation constants of the various modes in the FSG, or the model field patterns, allowing confirmation that the modes are either EH or HE. The program must be run many times at different frequencies to find the resonant frequency of the structure. This has been identified as being the point at which the value of the real part of the propagation constant in the axial direction ( $\beta_z$ ) of the fundamental FSG mode plot intersects the  $TE_{11}$  mode plot of a solid guide of identical radius. As at resonance the FSS is reflective and approximates to the PEC boundary of the solid waveguide and so should have similar phase constants. Alternatively it is the point where the imaginary part of the propagation constant in the axial direction ( $\alpha_z$ ) of the fundamental FSG mode is a minimum.
- Once the resonant frequency has been found it can be compared with that given in the specification. If there is not a close match then the element size, periodicity or FSG radius can be altered and the FSG simulation program run again, this process is repeated until the desired resonant frequency is obtained. Guidelines of how this may be done are detailed in chapter 2.
- The width of all the conductor arms in the square loop was set to  $1/7^{\text{th}}$  of the length of the arm in this study. This was done to reduce the computation time required by the FSG modelling program, see [6] for details. Also the separation between elements should be designed to be as large as possible in relation to manufacturing tolerances that may cause a variation in the element size. It was found that for arrays where the resonators were designed to be spaced very close together, the manufacturing tolerances of the FSS caused the variation in actual spacing to be large. When elements are very close together very high levels of mutual coupling are seen between the element edges. When placed very close

together small changes in the spacing can cause very large changes in the magnitude of the inter element coupling and this gives rise to a large and noticeable shift in the resonant frequency of the elements.

### 3.2 Dimensions of the FSG

Loukos had modelled several circular cylindrical FSGs, with square loop resonating elements of particular dimensions. Although not all of ideal size, i.e. the radius was not the same as that of a standard waveguide (e.g. C140 = 7.35mm), one did have a radius of 7.85mm, only slightly oversized. It was felt that the feed guide and the FSG should have a similar radius so that the effect of the change from solid waveguide wall to the FSG wall made of resonant elements was isolated from any effects caused by the change in wall radius. The predicted resonant frequency of this FSG was 15.3GHz. This frequency was within our test equipment's operating range, unlike the others modelled. Although this frequency coincides with the cut-off frequency of the next higher order mode in the solid feed waveguide (C140), it was felt that this would not be a problem. The feed waveguide would remain in single mode operation at the input because it can only be fed by a  $TE_{10}$  mode from the rectangular waveguide and the transition between the rectangular and circular waveguide will only convert this mode into the  $TE_{11}$  mode.

The FSG dimensions were: -

Radius = 7.85mm

Periodicity of square unit cells along the circumference  $\phi$  and along the axis z

( $D_\phi, D_z$ ) = 8.22mm (which gives 6 unit cells around the circumference in  $\phi$ )

Length of each side of square conductor ( $L_\phi, L_z$ ) = 6.85mm

Width of conductor line (W) = .9786mm

Length of FSG section = 28.1mm

### 3.3 FSG Manufacture

It was decided to use an established composite material consisting of a copper sheet 18 $\mu$ m thick with an attached Mylar dielectric backing, that came in two thicknesses either 0.03mm or 0.04mm,  $\epsilon_r = 3.0$  and  $\tan \delta \cong 0.03$ . The metal elements on the

surface of the FSG can be manufactured from the copper sheet by using the same etching technique used in PCB manufacture. The etching removes most of the copper sheet apart from the places where a patch of copper is required to form the array of elements of the correct shape. This technique is widely available and inexpensive, so many iterations of the design can be manufactured cheaply while prototyping. The end result is a planar sheet of metal elements on a thin dielectric substrate, the Frequency Selective Surface (FSS). This was then rolled into a tube to form the FSG and the edges stuck together.

Although FSG's had been made previously for measurement, by this same method, they were very crudely made, suffering from poor longitudinal uniformity and a distinctly non-circular cross section. Development of a methodical production procedure would allow FSG's to be manufactured repeatedly to the high standard needed to obtain good measurement results.

The production procedure developed is: -

- Once the FSG element size, periodicity and radius has been finalised then the FSG can be made. To etch the copper elements from the sheet using the standard PCB production process, a photonegative mask must first be produced with the element design upon it. The design was drawn using a CAD package, to accurately place the square loop elements of the correct size, shape and line width into the matrix of elements, which forms the FSS. The design was transferred onto an acetate sheet with a photo plotter. This sheet was then used to create a photonegative mask of the design on another acetate sheet.
- When exposed with ultra violet light through the photonegative mask the design was transferred onto a photo-resist layer that was stuck onto the surface of the copper. The unwanted copper and unexposed photo-resist was eaten away in an acid bath to leave the array of square loop elements. Although some undercutting of the elements by the acid is possible the etching process is very accurate and produces elements to within  $\pm 6\mu\text{m}$  of the mask dimensions. It was found however that the mask production technique using the photo plotter with 0.1mm pens was only accurate to  $\pm 0.1\text{mm}$ . The error in pen placement and ink spreading from the pen when it dwelled for any length of time, meant that it was highly likely that the elements would not all be exactly identical. As no other

facility was available, it was hoped that these accuracy limitations would not have a significant effect upon measured FSG results especially as the Loughborough Microwave group had obtained good agreement between measured and predicted scattering parameters for planar elemental FSS sheets using this production process.

- Before the planar FSS sheets were turned into FSGs, the frequency response of the sheet was measured. This ensured that the resonant frequency of the planer array was as expected and the FSS had been produced correctly. It also meant that later comparison between resonant frequencies of the planar FSS and the FSG was possible, see section 3.4.1.
- The excess dielectric around the edge of the strip of elements was trimmed so that the sheet was exactly the correct length; an integer number of elements, and width, again an integer number of elements equal to the circumference of the FSG cylinder plus one to two millimetres to act as an overlap at the join or seam. The overlap is positioned so that when the sheet is rolled into a cylinder the periodicity between the adjacent elements across the seam is the same as that between any other two elements on the sheet. Also the overlap dielectric should not project under any of the elements on the other side of the sheet so that the cylinder is as symmetrical as possible. The overlapping dielectric edges were stuck together with spray mount adhesive, which gave a very even layer of glue and stayed tacky for several minutes, allowing fine adjustments to be made to the positioning of the overlap seam.
- The sheet was rolled with the elements on the inside of the tube so that the feeding fields act directly on the element and not on the element having first passed through the dielectric. To achieve a good shaped cylinder the tube should be rolled on a former machined to a diameter such that the dielectric can be formed into a cylinder of the correct circumference and therefor an integer number of elements with the correct periodicity, see Figure 3-1. The former was made from a length of aluminium as it is cheap, relatively light and ridged enough not to deform while being machined. The rolling process was only possible because the material was thin and had low rigidity. It was assumed that the thickness of the dielectric sheet would have a minimal impact on the FSG operation, although it was known that dielectric materials cause some increase in the electrical length of the loops.

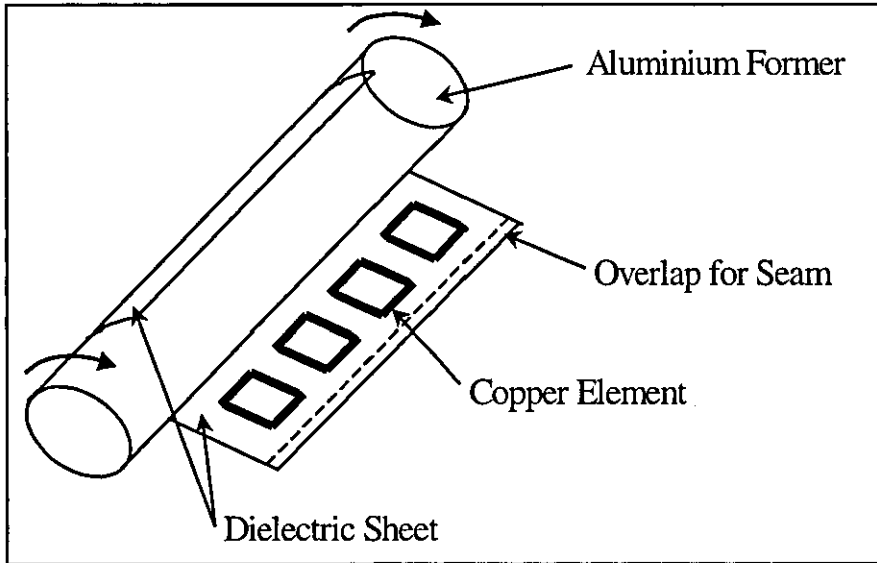


Figure 3-1 FSS sheet being rolled on its former to make an FSG.

- In order for the FSG to have a good circular cross section the sectors of the circumference with metal elements must have the same radius of curvature as the dielectric only segments between the conductors. It was found that a former of the correct diameter could not induce sufficient bending stress on each element to ensure that it held the correct curvature when the former was removed. In fact the elastic rigidity in the elements meant that they sprang back into their original flat form without the former present. The FSG produced therefore had an undesirable multi-sided polygonal cross section (hexagonal in this case), where the corners were formed by the dielectric between the elements that could bend. The standard way to treat the metal so that it has the correct curvature would be to heat it while it is curved and then to cool it quickly. However this method is not practical as the Mylar dielectric melts at a far lower temperature. A method was required where more bending stress and curvature could be put into the elements so that when the stress was released they would sprang back to the desired curvature. The method adopted to form a circular FSG cross section was to wrap the sheet around a much smaller diameter former. When this was done tightly, so that the strip was wound many times round the thinner rod, the copper was forced to take on some shape. When the strip was unwound it was found to have slightly too much curvature, but this disappeared once the FSG was place on the correct size former and drawn



tight and the seam sealed firmly. The cross section of the FSG was now almost perfect in cross section shape and of the correct radius. It was found that the thicker the dielectric sheet the easier it was to form the circular cross section and the better the FSG held the finished shape. Wherever possible the finished FSGs were stored on the formers to ensure that they were not damaged or lost the all-important circular cross section.

### 3.4 Measurements & Characterisation of the Initial FSG Produced

The first FSG produced to the design dimensions given in section 3.2 was tested thoroughly with  $S_{11}$ ,  $S_{21}$  scattering parameters and radiation patterns being taken over a large frequency range. This data was analysed and hypotheses about the modes of operation of the FSG were made. Before the FSG was constructed the FSS sheet was measured and these results are given first.

#### 3.4.1 Set-up and measurement of Planer FSS sheet before being made into an FSG

The FSS sheet was held taut on a supporting, picture like, frame which in turn was placed upon a rotating stand in the centre of the anechoic chamber. A plane wave source was placed about 1.5m in front of the FSS sheet with the centre of its main beam aimed at the centre of the sheet. A similar receive horn was placed a similar distance behind the sheet, again with the main beam aimed at the centre of the sheet. Both the horns were connected to an HP8410 scalar network analyser in order to take the measured transmission response of the FSS as shown in Figure 3-2. The transmission response was measured over the frequency range 12-18 GHz at several different angles of incidence. Measurement of the FSS limited to a maximum angle of incidence of  $60^\circ$ , at angles beyond this the edge of the frame partially obscure the FSS and so affected the measurements. The orientation of the transmit horn was such that the E field vector is always parallel to the FSS surface while it was rotated, this is a TE incident field measurement.

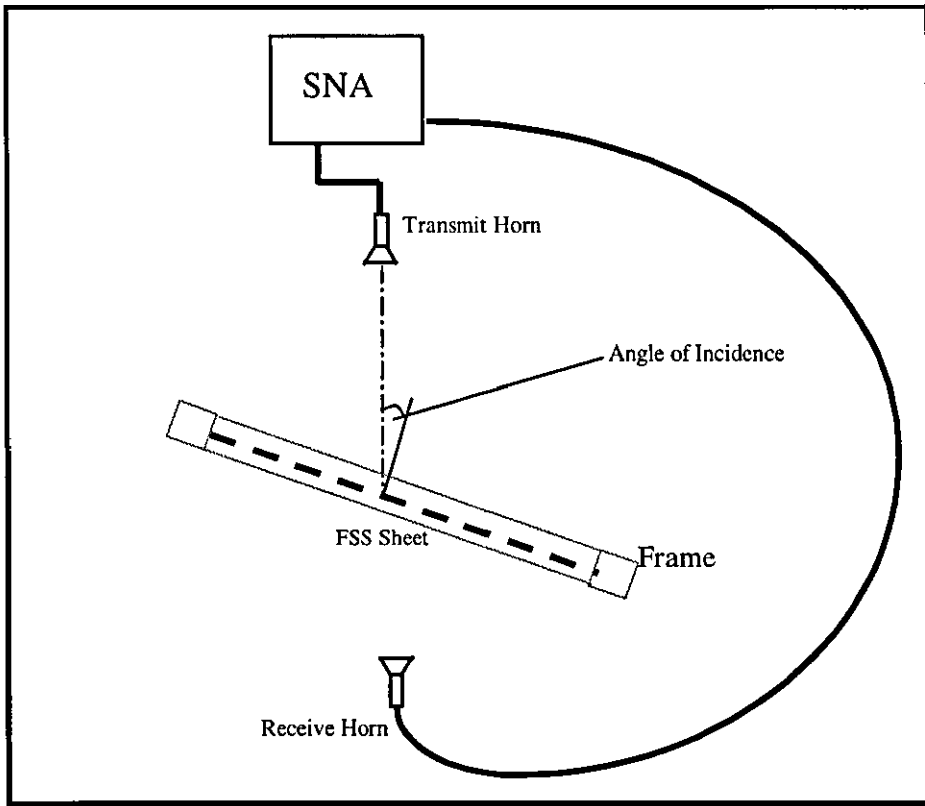


Figure 3-2 Equipment Set-up for the Measurement of the Planer FSS

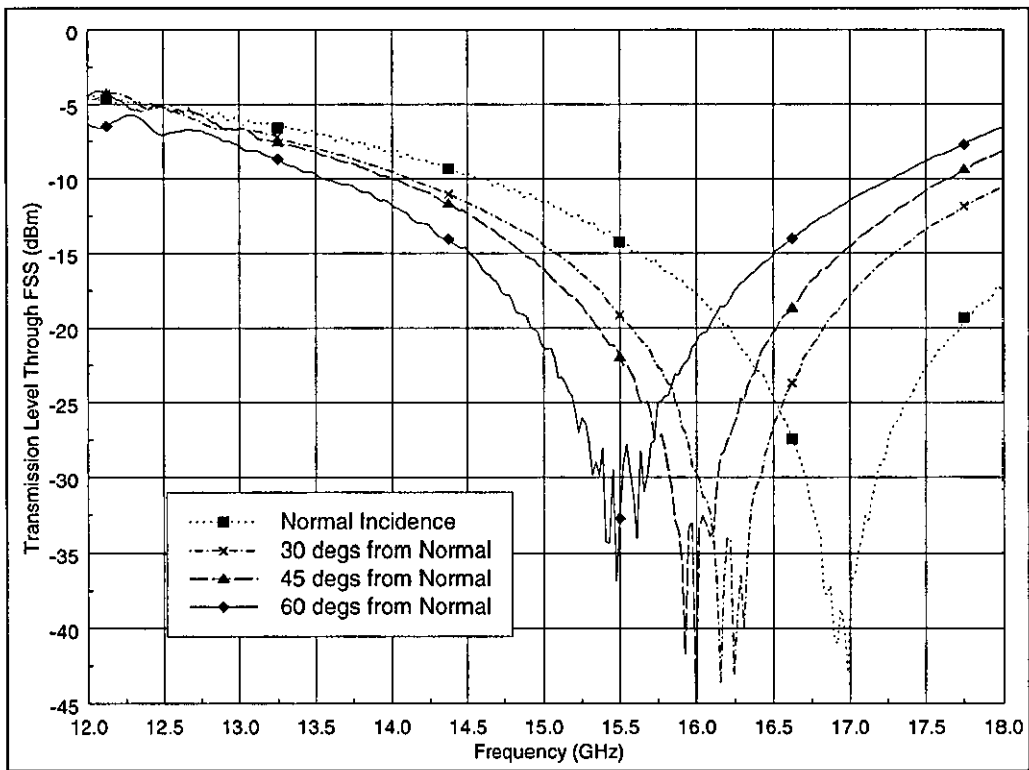


Figure 3-3 Frequency Response of the Planer FSS sheet used to make FSG 1

The transmission plots obtained were as expected and identical to the standard theoretical form of FSS response [7]. These showed a large sharp dip in the transmission plot at resonance where the sheet becomes highly reflective to the incident field and the transmitted power is at a minimum, Figure 3-3. The resonance point shifts to lower frequencies as the angle of incidence is increased. Here if the incident wave is  $60^\circ$  then the resonance is 15.5GHz and is close to the measured value of 15.2GHz, the resonance of the FSG. This shows that the design technique that uses the planer modelling program, with  $60^\circ$  incident fields as a starting point for the FSG design, is a valid and time saving method.

#### 3.4.2 $S_{11}$ & $S_{21}$ Test Equipment Set-up

The  $S_{21}$  &  $S_{11}$  scattering parameters of the FSG were measured using an HP 8410B Vector Network Analyser with the test set-up shown Figure 3-4. The coaxial cable from the analyser was connected to WG18 rectangular waveguide via standard commercially available post transitions that excite the fundamental  $TE_{10}$  mode. A tapered rectangular to circular transition was used to convert the  $TE_{10}$  mode of the rectangular guide to the fundamental  $TE_{11}$  mode of the C140 circular guide. The FSG was then placed on the end of the C140 guide, these both having similar diameters. The C140 guide was used to ensure that any evanescent modes created at the rectangular to circular transition had died away before the signal was fed into the FSG. Following the FSG another identical circular to rectangular transition converted the circular FSG modes back into rectangular waveguide modes. For  $S_{21}$  measurements any evanescent modes generated by the transitions were allowed to die away in another section of rectangular waveguide before reaching another probe transition and the coaxial cable connected to the second port of the analyser. A matched termination replaced this transition for the  $S_{11}$  measurements and again was a standard commercially available rectangular waveguide item. Ideally a matched termination would have been placed directly on the end of the FSG replacing the circular waveguide or circular to rectangular transition, but not enough is known about the operation of the FSG to build one at this point.

To attach the FSG to the solid waveguide a small length (3cm) of expanded polystyrene was turned on a lathe, so that half of it was the same radius as the FSG and the other end was the same radius as the solid waveguide. This was then inserted into the waveguide ends, such that they snugly butted up against each other. This method ensured that both the FSG and waveguide were co-axial and secure, while being easy to move and change if required during development. Clearly a more permanent method would need to be developed if this were to be used in a practical environment. The dielectric constant of the polystyrene is very close to air and so should have relatively little effect on the transition performance.

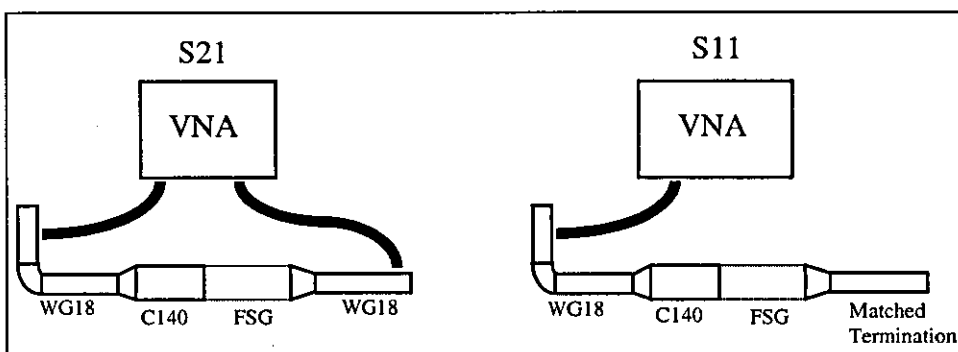


Figure 3-4 Test Equipment Set-up

A standard calibration procedure of through, short circuit, offset short circuit and matched termination measurements were used to set the analyser reference plane to the end of the C140 waveguide. The FSG was removed and the far circular transition was attached to the C140 circular guide. The analyser calibration routine was then followed for the appropriate  $S_{21}$  or  $S_{11}$  procedure. Taking either an  $S_{21}$  measurement of the connection through solid waveguide or an  $S_{11}$  measurement with the matched termination in place then tested the calibration. The calibration test values were as expected, 0dB in both cases, so the calibration was accurate.

### 3.4.3 $S_{11}$ & $S_{21}$ Measurement

The  $S_{21}$  frequency response obtained for the 0.04mm thick dielectric FSG had several distinct regions, see Figure 3-5. In region “A” from 12 -13 GHz it can be seen that there is a 4dB periodic fluctuation superimposed onto a -7dB horizontal line that

gentle rolls off to  $-15\text{dB}$ . In region “B” there is a very sharp drop in  $S_{21}$  to a minimum value of  $-35\text{dB}$  followed by a slower rise back towards the “A” region value. Region “C” contains a shallow maximum that forms the top of a bell curve, which peaks at a maximum value of  $-4.3\text{dB}$  at  $15.1\text{GHz}$ . In the final region the fall-off of the bell curve continues to such a low level, that it is hard to distinguish any signal amongst the noise floor of the analyser.

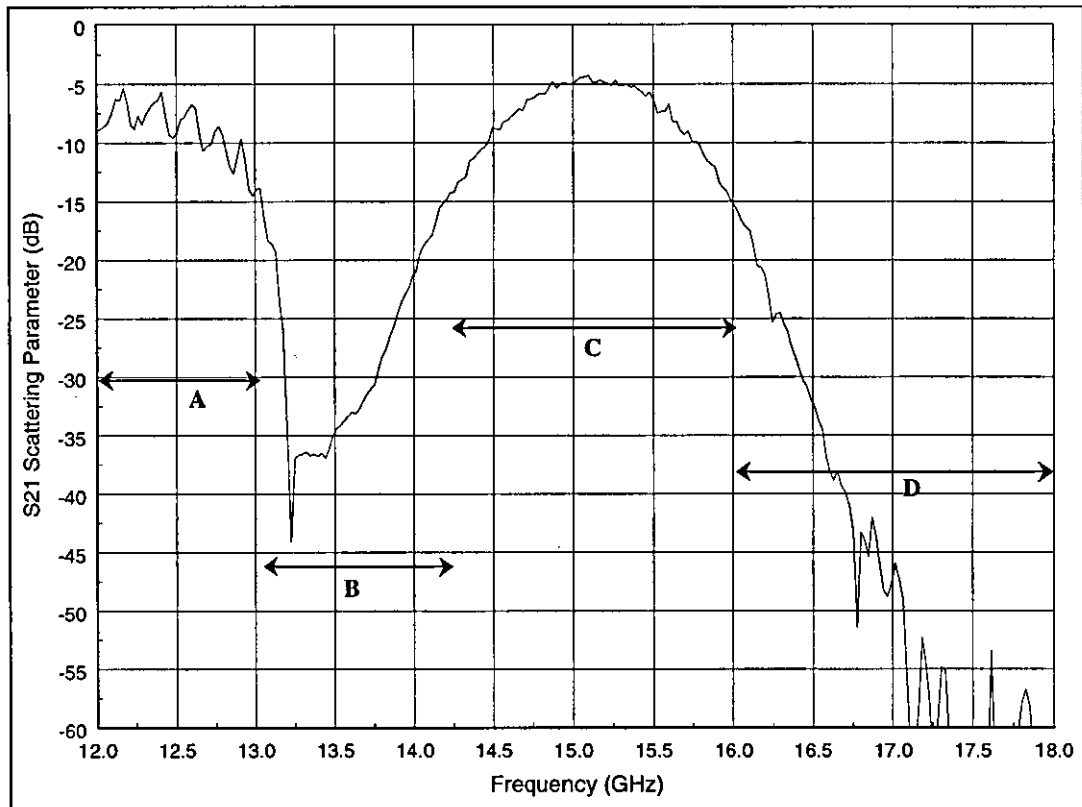


**Figure 3-5 Initial  $S_{21}$  Measurement of the FSG with a Solid Waveguide at Each End, with FSG Dimensions  $D=8.22\text{mm}$ ,  $L=6.6\text{mm}$ ,  $r=7.85\text{mm}$ ,  $t=0.04\text{mm}$  & length= $28.1\text{cm}$ .**

The  $S_{11}$  response of the FSG was then taken see Figure 3-6. There were some very large ripples in the response, up to a maximum of  $13\text{dB}$  peak to peak with an average magnitude of  $6$  to  $7\text{dB}$ , seen in regions “A” & “C”. The average level of  $S_{11}$  in region “A” was about  $-13\text{dB}$  and in region “C” that had dropped to  $-20\text{dB}$ . Region “B” has a relatively ripple free response sloping from  $-13\text{dB}$  to  $-20\text{dB}$ . Finally Region “D” has a slope in the opposite direction going from  $-20\text{dB}$  to  $-9\text{dB}$  where it flattens out at that level.

### 3.4.4 S11 & S21 Interpretation

These scattering parameter responses will now be analysed to try to extract a rationale for the behaviour of the FSG that would give rise to these results. They can also be tied into the known theory about the FSG that comes from analysing the results of the Loukos simulations and given in [6]. The main points of the theory suggest that there is a surface wave with a real propagation constant that propagates along surface of the elements of the FSG at low frequencies. As the frequency increases further then this mode is replaced by a leaky mode that has an improper complex propagation constant. This leaky mode is not entirely bound to the FSG and a proportion of the modal energy radiates away from the FSG. However the theory also predicts that at a particular resonant frequency of the structure the amount of radiation that leaks away from the FSG is reduced to a minimum value.

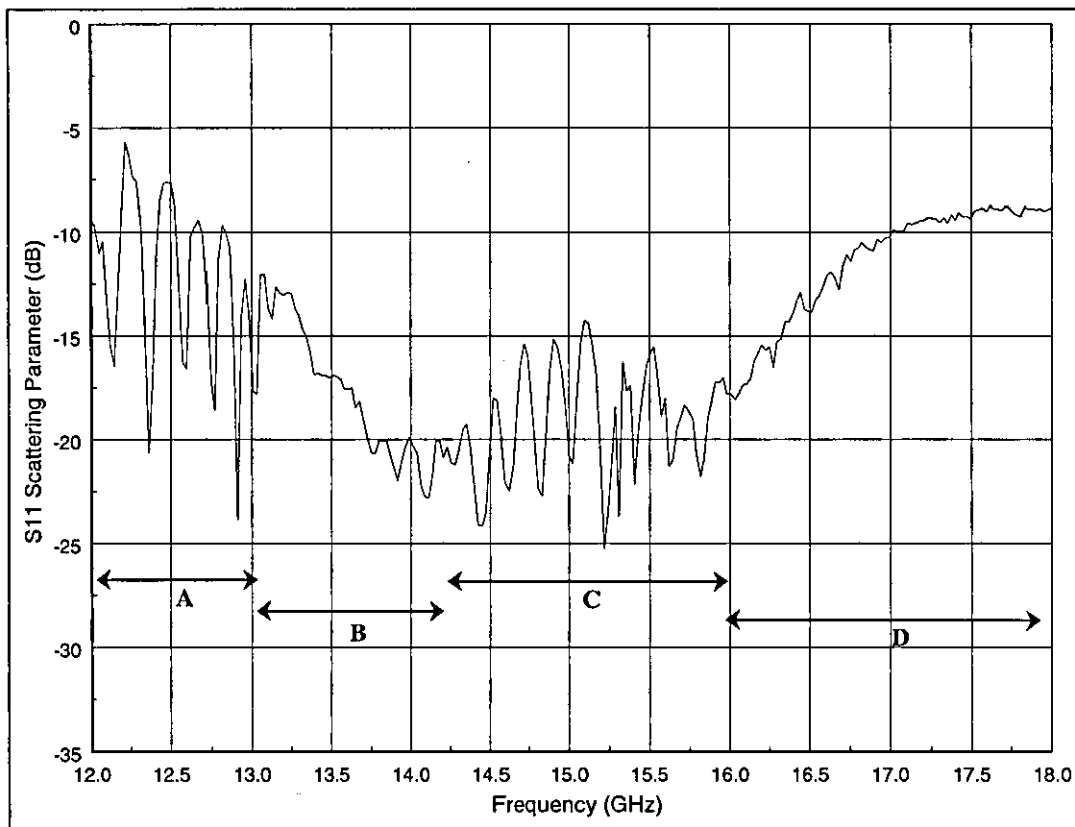


**Figure 3-6 Initial S<sub>11</sub> Measurement of the FSG with a Solid Waveguide at Each End, with FSG Dimensions D=8.22mm, L=6.6mm, r=7.85mm, t=0.04mm & length=28.1cm.**

Looking at the low frequency region “A” the  $S_{21}$  results show that a reasonable amount of power is being transmitted to the second port, certainly more than would be expected if the FSG were removed and the waveguides were left open ended. Also the ripple in the  $S_{11}$  measurements is indicative of a standing wave being created between two imperfectly matched junctions with a length of guiding structure between them. It is thought that a small standing wave is being set up within the FSG, between the two waveguide to FSG transitions. The average  $S_{11}$  match is also slightly better than would be expected for an open-ended waveguide radiating into free space. This evidence suggests that the FSG is guiding the fields to some extent in region “A”, but it does not prove the presence of a surface wave as theory suggests there should be. The evidence that it is indeed a surface wave is anecdotal, but compelling. The structure of any surface wave mode is such that some of the field is contained inside the structure, while a large amount exists on the outside of the structure [8] & [2].

Here it propagates along the exterior of the surface, but does not radiate away from it as it is bound to the surface. With a large amount of the modal field energy propagating along the outside of the FSG an annulus of RAM, internal radius  $\cong 8\text{mm}$  & external radius  $\cong 80\text{mm}$ , placed around the FSG, but not touching the surface, would have a large effect on a surface wave mode. It would have virtually no effect on a mode that existed largely within the FSG. With the RAM not in close proximity to the surface the currents that exist on the surface of the FSG should not be disturbed. It should only suppress and disrupt the external fields of a surface wave mode causing the amount of transmitted surface wave mode power to be attenuated. Indeed the only affect seen on the  $S_{21}$  plot was significant reduction of the values seen within region “A”. The other regions remained virtually unchanged by the presence of the RAM. Therefore, the measurements (that there is some guidance which is attenuated by the presence of the RAM) indicate that a surface wave mode does propagate along the FSG at low frequencies as the theory suggested.

The next region “B” shows a very sudden drop in the magnitude of the  $S_{21}$  value, indicating that very little power is reaching the far end of the FSG. At the same time the ripples in the  $S_{11}$  plot disappear, while the value of  $|S_{11}|$  also becomes less and

the amount of reflected power is reduced. As the transmitted and reflected powers are both reduced, then by the law of conservation of energy there can only be one place for the power to go, it must be radiated. The structure can no longer support the surface wave mode and power is radiated away from the feed and FSG surface. Indeed the very nature of a leaky wave mode is that it must radiate power away from the structure surface at some angle that is frequency dependent. It is likely that the surface wave is replaced by a leaky wave mode that has a very high imaginary part to its propagation constant. This means that virtually all its power is radiated before the mode reaches the far end of the FSG.

As region "B" moves into region "C" the  $S_{21}$  value steadily increases until it reaches its maximum value. The  $S_{11}$  value continues to decrease towards its lowest level where it enters the "C" region where more ripples occur. Here the standing wave pattern has returned showing that the fields are again being guided and that a standing wave is being set up along the FSG. Again because the  $S_{11}$  value is low there must be a good match and little reflection off the first transition back down the solid guide at port 1. The increase in the  $S_{21}$  value must mean that less power is being radiated and more must be contained inside the FSG, again evidence of FSG becoming more guiding. Indeed the maximum amount of power received at port 2 (maximum  $|S_{21}|$ ) coincides with the maximum magnitude of ripple in  $S_{11}$  and hence the largest standing wave inside the FSG. This ties in very nicely with the theory that the leaky wave becomes progressively less radiative until at some resonant frequency there is a minimum amount of loss and maximum amount of containment of power within the FSG.

Finally as the frequency increases further and the plots move from region "C" into "D" the  $|S_{21}|$  value reduces from its maximum value until there is virtually no power transmitted to port 2. At the same time the standing wave ripple disappears and the reflection off the first solid waveguide to FSG transition increases to its maximum value. However as the  $S_{11}$  levels off at  $-9\text{dB}$  then not all the incident power is reflected, little power reaches port 2 and the remainder must again be radiated. This again ties in well with the FSG theory as it states that after the resonant frequency the amount of radiation from leaky wave modes will again increase significantly. So



much so that what power does enter the FSG is lost through the walls before any can reach port 2.

Further confirmation that regions “B”, “C” & “D” are leaky wave regions was obtained by the absorber experiments described previously when discussing the nature of the surface mode in region “A”. A guided leaky wave will not suffer a significant change in  $S_{21}$  when the absorber is held in position, because the majority of its field is contained within the guide. The proportion of the power that leaks out through the walls has been radiated. It does not affect the fields within the FSG whether the radiation is absorbed by the RAM or whether it reaches the far field. It has already left the FSG structure and hence the value of  $S_{21}$  is changed little by the presence of the absorber.

#### 3.4.5 Radiation Pattern Equipment Set-up

In order to obtain a final confirmation of the above measurement characterisation theory it was decided to measure the radiation patterns of the FSG at various frequencies. As the structure is open and leaky modes must radiate, by definition, it should be possible to measure the radiated power patterns in an anechoic chamber. The radiated energy from a leaky mode has one main beam that emerges at some acute angle to the axis of propagation of the mode. The angle and beam size is directly related to the frequency and the amount of leakage the mode has. Indeed the amount of power radiated is a measure of how well the structure is containing the field; no radiation would be detected for a solid wave guide for example. The FSG was placed in the microwave anechoic chamber with the measurement system as shown in Figure 3-7. The matched load was attached to the circular to rectangular transition at the far end of the FSG, similar to the  $S_{11}$  case, to absorb any power that reached the far end of the guide. The measured power pattern was via a solid waveguide horn connected to the second port of a HP8410 scalar network analyser. The instrument was set to its maximum power output with the first port of the analyser connected to the solid waveguide of the input feed to the FSG. The receive horn was then rotated around the centre point of the FSG from  $-70^\circ$  to  $70^\circ$  on a stabilised arm 1.5 meters long. This should be in the far field of the radiation pattern

for measurements above 12GHz. As this measurement is of the radiation pattern at an angle to the axis of the solid waveguide no calibration or normalisation of the system could be carried out as it might be for a waveguide horn for example. The radiation measured at these off axis angles can only be measured once the FSG is in place and so the only meaningful normalisation is to the peak value of any beam recorded in the radiation pattern.

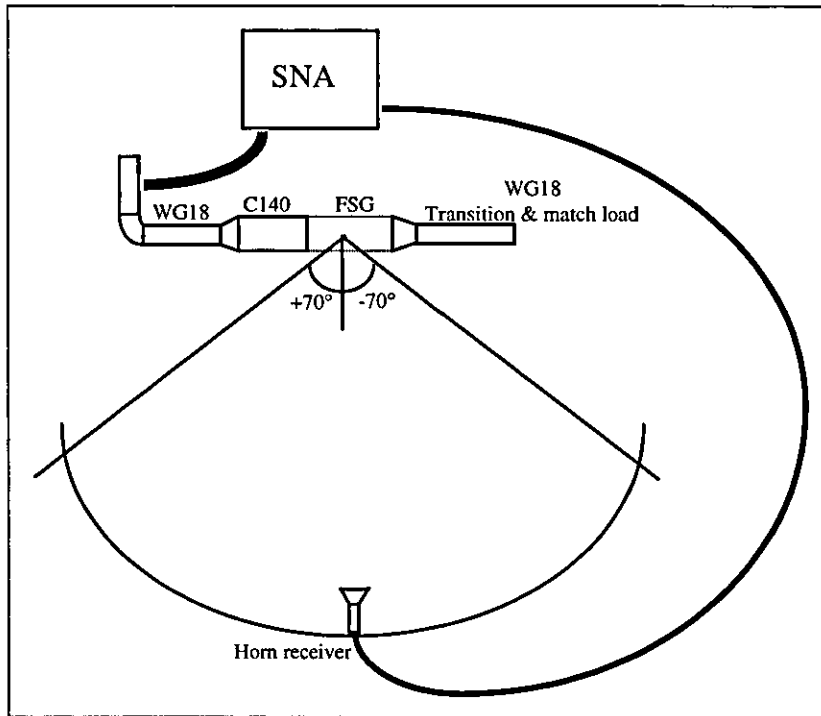


Figure 3-7 Test Equipment Set-up for Radiation Pattern Measurement

### 3.4.6 FSG Radiation Patterns

The radiation pattern measurements were repeated for several frequencies over the band displayed in the  $S_{21}$  &  $S_{11}$  measurements above and are all displayed in Figure 3-7. The frequencies at which the pattern was measured were 12, 13.5, 14, 14.5, 15, 15.5, 16, 16.5 GHz with the FSG in place. Also included in the graph is a comparison measurement at 12GHz without the FSG present, i.e. the radiation pattern for an open-ended waveguide. It is worth noting that other radiation patterns were taken at higher frequencies for the open ended waveguide without the FSG present, but the patterns were almost identical to the 12GHz pattern displayed here. This invariance in open-ended waveguide patterns is in stark contrast to the patterns for the FSG. These

clearly show marked differences in the patterns at each frequency. The 12GHz FSG pattern is not that different from that of the open ended waveguide. This along with the low magnitude of the measured pattern is a clear indication that very little power is radiated at this frequency and that indeed a surface wave mode must exist at this frequency (region "A" of Figure 3-6).

All the other patterns between the frequency range of 13.5 to 16.5 GHz are very different. There is clearly a main beam of radiated power associated with each one. The main beams all occur between  $-15^\circ$  &  $-55^\circ$ , which is always an acute angle with the axis of propagation along the FSG. The higher the frequency the closer the main beam to the axis the lower the frequency the closer the main beam to the normal to the axis. This shows yet another property of a leaky wave mode, where by the main beam is scanned from the normal towards the end-fire axis by changing the frequency. Antenna designers often exploit this property as it allows them to produce scanning antennas simply by changing the frequency of operation. The relative magnitude and beam width of each main beam also changes with increasing frequency. At 13.5 GHz the beam is wide with a low magnitude, as the frequency increases the beam gets narrower and more intense.

These frequencies are in section "B" of graph Figure 3-5 and show that the leaky mode only starts to form at 13.5 GHz as not all of the radiated energy is being channelled into a well defined beam rather it radiates over a broad range of angles. At 14GHz the leaky mode is fully formed and produces the narrow well-defined main beam as expected. It should be noted that the asymmetrical shape of the beam is very indicative of the presence of the leaky mode. The side of the beam closest to the FSG is very steep and the side closest to the normal is very shallow, as explained in [4].

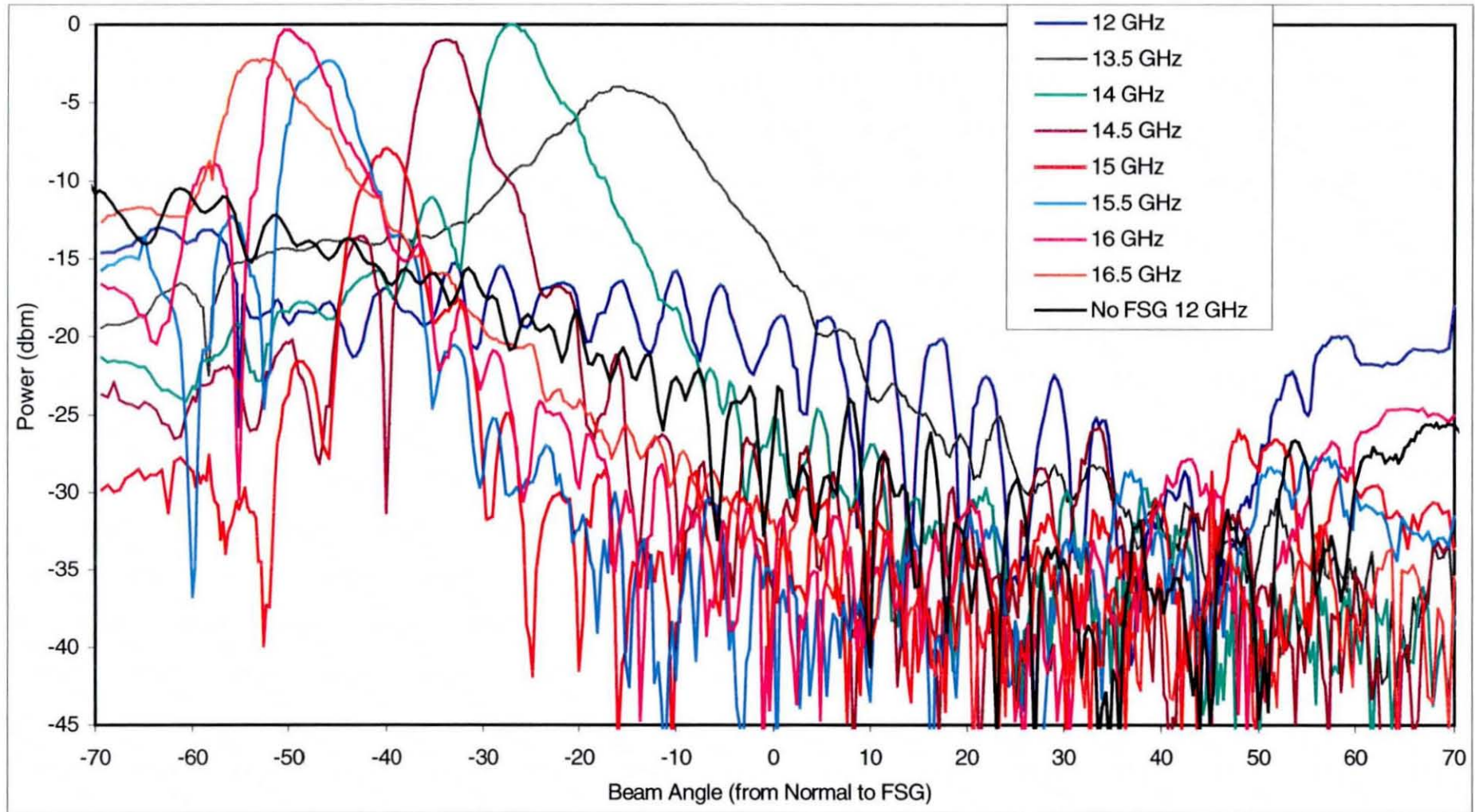


**Figure 3-8 Radiation patterns for FSG1 at different frequencies.**

As the frequencies change through the “C” region of Figure 3-5 the magnitude of the main beam reduces. With the minimum value recorded at 15GHz, which is the closest measurement point to the postulated resonant frequency of the FSG. This confirms the theory that the radiated power from the FSG should become low at the resonant frequency. After 15GHz the main beam magnitude becomes large again reaching a maximum value at 16GHz. It should be noted that in this region of well-defined leaky modes the patterns are almost symmetrical about resonant frequency. This same well-defined symmetry about the resonance is also seen in Figure 3-5 in region “C”. The leaky mode becomes more or less radiative regardless of how the resonant frequency is approached. Finally the radiation pattern at 16.5GHz shows the magnitude of the main beam falling off and some beam width broadening. This is certainly due, in part, to the increased mismatch at the input feed to the FSG. The beam broadening is not as bad as at 13GHz so it does not suggest a return to poorly defined leaky modes, but possibly it points to increased total radiation over a wider beam width.

### 3.5 $S_{21}$ & $S_{11}$ Parametric Study by Measurement Methods

With the basic operation of the FSG understood a parametric study of the FSG concept was undertaken. This involved making several different FSGs each having one or two parameters altered to see the affect that this had upon the operational characteristics when measured. This information can then be pulled together to give a fuller insight into how the FSG operates and an idea of some of the design considerations when making an FSG.

However when the characterisation measurements of the previous chapter were being taken a strange variation in the results was observed from one measurement to next. If an FSG was measured, removed from the set-up and then replaced and re-measured, the S parameter values changed. Although the general shape of the response didn't change the amount of ripple at various points along the response altered each time the measurement was repeated. By trying various set-up procedures it was discovered that the variation was being caused by the orientation of the seam, where the supporting dielectric overlaps at the join of the two edges, relative to the polarisation of the incident  $TE_{11}$  field from the feed C140 waveguide. The variation of

the  $S_{21}$  as the seam angle changes relative to the  $TE_{11}$  polarisation vector is shown in Figure 3-9. As the angle moves away from  $0^\circ$  towards  $90^\circ$  the response at resonance gets steadily worse until at  $90^\circ$  the response with a minimum  $|S_{21}|$  value at resonance and the largest ripple is seen throughout the frequency range. The frequency where surface wave cut off occurs also increases along with an increase in the resonant frequency and the frequency at which the leaky wave region starts. However there is not a corresponding increase in the frequency at which the leaky wave region ends and so the range over which the leaky wave exists decreases. After  $90^\circ$  the response improves until at  $180^\circ$  it reaches the same values as seen at  $0^\circ$ . The same cyclic variation is observed as the seam angle is rotated from  $180^\circ$  to  $360^\circ$ .

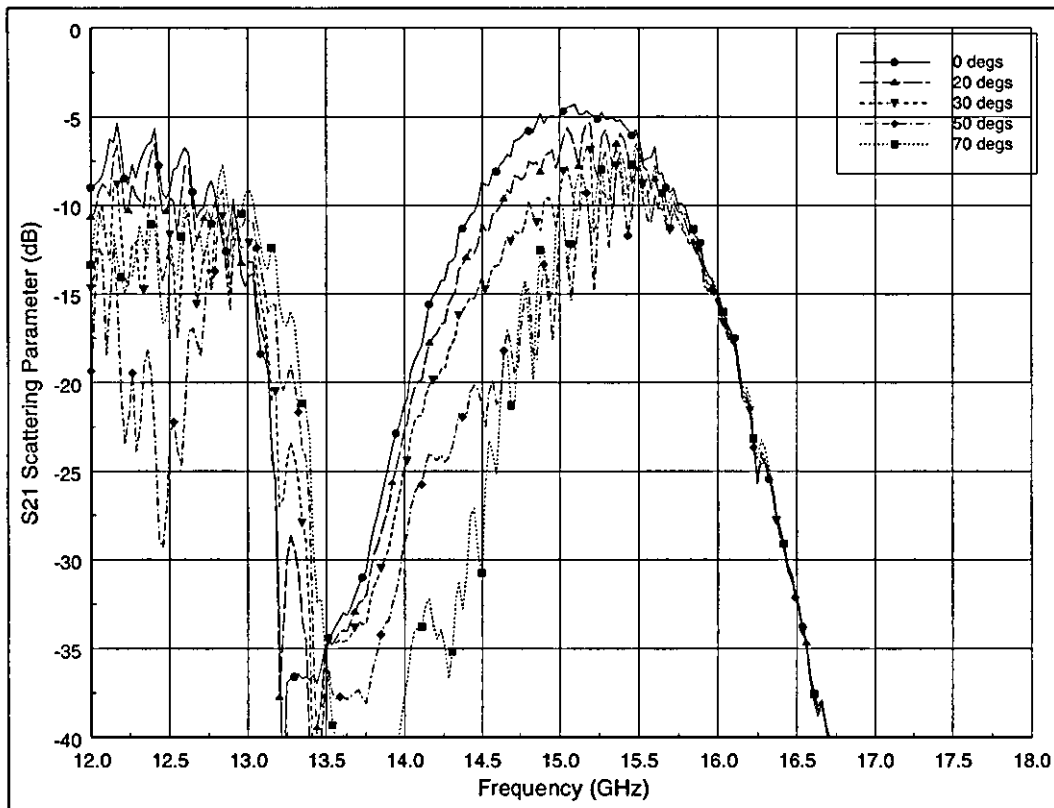


**Figure 3-9 Graph of measured  $|S_{21}|$  Vs frequency as the seam of the FSG is rotated away from the feed  $TE_{11}$  polarisation vector, for C140 at each end, for  $D=8.22\text{mm}$ ,  $L=6.6\text{mm}$ ,  $r=7.85\text{mm}$ ,  $t=.04\text{mm}$ , length= $28.1\text{cm}$ .**

The only possible cause for this variation can be that of the angle between the seam and the polarisation vector of the feed waveguide. The only other difference that occurs as the FSG is rotated is that the polarisation vector of the feed will cut the

square loop at the top of the guide at a different place. However it can not be due to this as there are six loops around the circumference of the FSG, which would imply a different rate of variation in the  $S_{21}$  measurement. This means that when rotated by  $60^\circ$  the FSG would have exactly the same pattern of metalisation at the same angle to the feed polarisation vector is seen at  $0^\circ$ . This would then be manifested in the  $S_{21}$  patterns having a  $60^\circ$  cyclic variation in response rather than the  $180^\circ$  variation that we observe. This proves that the variation seen in the  $S_{21}$  is due to the effect of the increased dielectric thickness and glue of the seam, where it unbalances the  $TE_{11}$  field of the feed.

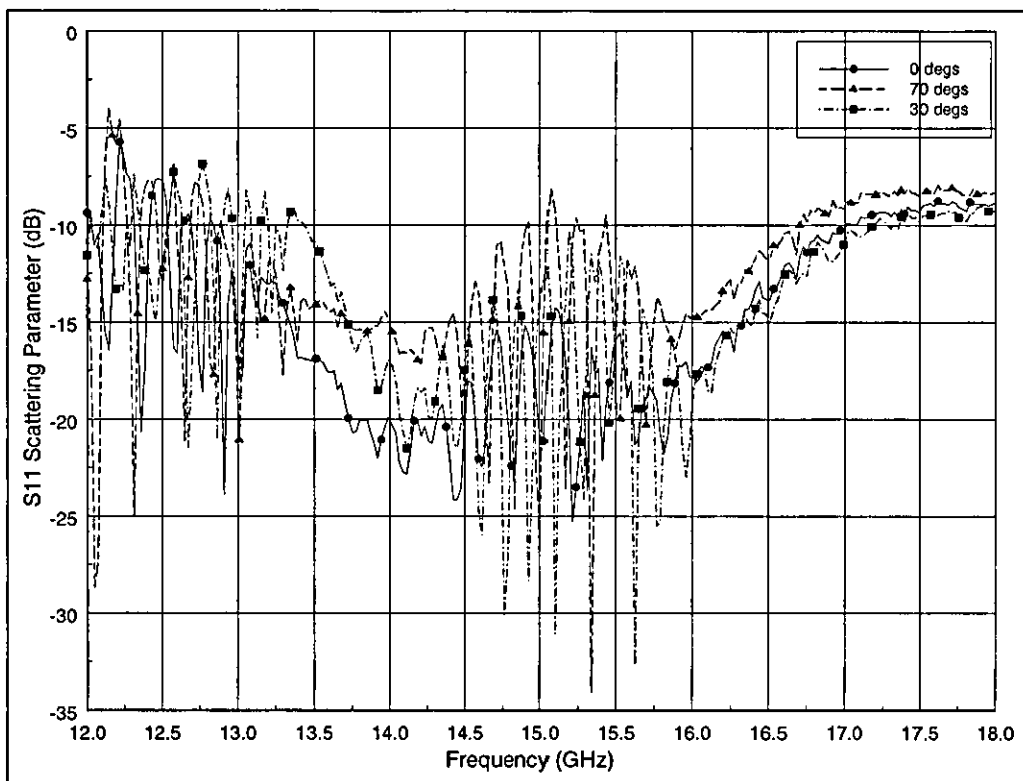


Figure 3-10 Graph of measured  $|S_{11}|$  Vs frequency as the seam of the FSG is rotated away from the feed  $TE_{11}$  polarisation vector, C140 at each end, for  $D=8.22\text{mm}$ ,  $L=6.6\text{mm}$ ,  $r=7.85\text{mm}$ ,  $t=.04\text{mm}$ , length= $28.1\text{cm}$ .

Figure 3-10 shows that the effect is seen in the  $S_{11}$  response as well as in the  $S_{21}$ . It again shows that the magnitude of the ripples increases as the seam approaches  $90^\circ$  and that the amount of reflection back down the feed guide also increases. This corresponds to the  $S_{21}$  graph where a decrease in the transmission down the guide on

the far side of the FSG is observed. N.B. it should be noted that all the data shown in the preceding graphs (Figure 3-5, Figure 3-6, Figure 3-8) were all taken with the seam orientation at  $0^\circ$  to the feed polarisation vector.

The first FSG manufactured was on a 0.04mm thick layer of Mylar dielectric. There was another thickness of Mylar dielectric material available which was thinner than was first used, 0.03mm. The use of two different thicknesses of dielectric will allow the affect of the dielectric on the FSG operation to be ascertained. The other parameters that can be altered are the size and spacing of the elements and the radius and number of elements around the circumference. The effect on performance of the structure of the FSG elements themselves can then also be ascertained.

With the first FSG that was made referred to as number 1, the other FSGs that were manufactured were referenced as: -

2. Radius = 7.85mm

Periodicity ( $D_\phi, D_z$ ) = 8.22mm (giving 6 unit cells around the circumference in  $\phi$ )

Length square conductor ( $L_\phi, L_z$ ) = 6.85mm

Width of conductor line (W) = 0.9786mm

Dielectric thickness = 0.03mm

Length of FSG section = 280mm

3. Radius = 7.54mm

Periodicity ( $D_\phi, D_z$ ) = 9.48mm (giving 5 unit cells around the circumference in  $\phi$ )

Length square conductor ( $L_\phi, L_z$ ) = 7.80mm

Width of conductor line (W) = 1.11mm

Dielectric thickness = 0.04mm

Length of FSG section = 284mm

4. Radius = 7.54mm

Periodicity ( $D_\phi, D_z$ ) = 9.48mm (giving 5 unit cells around the circumference in  $\phi$ )

Length square conductor ( $L_\phi, L_z$ ) = 7.80mm

Width of conductor line (W) = 1.11mm

Dielectric thickness = 0.03mm

Length of FSG section = 284mm

5. Radius = 12.07mm

Periodicity ( $D_\phi, D_z$ ) = 9.48mm (giving 8 unit cells around the circumference in  $\phi$ )



Length square conductor ( $L_\phi, L_z$ ) = 7.80mm

Width of conductor line (W) = 1.11mm

Dielectric thickness = 0.04mm

Length of FSG section = 284mm

$S_{21}$  measurements were taken for the 0.03mm thick dielectric FSG number 2. The results obtained were very similar to those of the 0.04mm thick dielectric Figure 3-5 with the maximum value at resonance slightly higher at -4 dB. There was also a small shift in the resonant frequency from 15.1GHz to 15.3GHz when the thickness of the dielectric was reduced. A comparison of the  $S_{21}$  responses for the two different dielectric thicknesses of FSG 1 & 2 is given in Figure 3-11. The change in resonant frequency can be clearly seen along with a shift upwards in frequency of the whole  $S_{21}$  response. The obvious cause for the increase in frequency is the reduced amount of dielectric supporting the FSG elements, which reduces the dielectric loading effect on the elements. Although the change in thickness is small at just 0.01mm, the high coupling fields that are thought exist between elements amplify the affect of dielectric loading for the small change in thickness. The thicker or higher the dielectric constant the lower the frequency of operation and the greater dissipation losses. This accounts well for the decrease in magnitude and resonant frequency with increased dielectric thickness. A reduction in the magnitude of the surface wave response is also observed. The reason for this is unclear, a possibility is that a reduction in the amount of dielectric changes the way the surface wave propagates.

The effect of the thickness of the dielectric on the  $S_{11}$  measurements is shown in Figure 3-12. Again these measurements tie up exactly with the  $S_{21}$  measurements. The surface wave of the 0.03mm thick dielectric FSG has a higher cut-off frequency, shown by the ripples at the lower frequencies finishing at 13.5GHz. The slope of the  $S_{11}$  graph as it moves into the leaky region is similar and starts to ripple again at 14.1GHz and eventually reaches a very similar average  $S_{11}$  value in the leaky resonant region. It then becomes less matched following a similar path, as it becomes less leaky. This shows the same characteristic as seen in the  $S_{21}$  graph; the bandwidth of the leaky region is reduced as the dielectric becomes thinner.

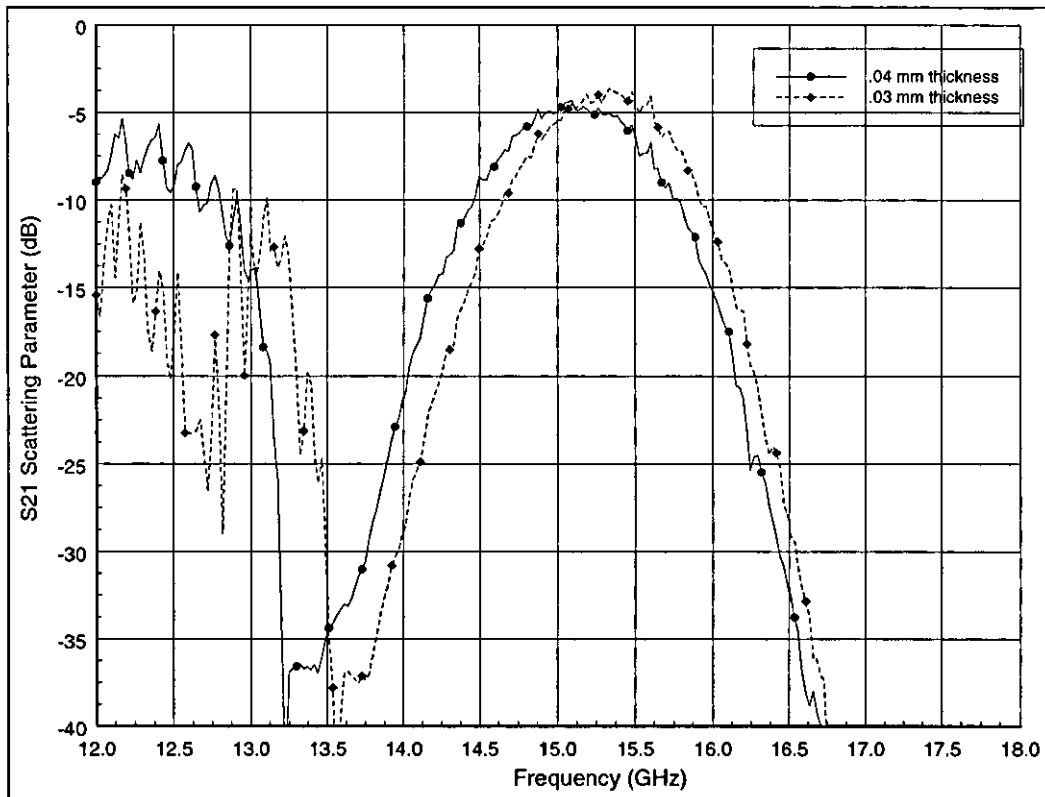


**Figure 3-11 Graph of measured  $|S_{21}|$  Vs frequency as the thickness of the dielectric sheet is altered for FSG 1 & 2 with a  $0^\circ$  seam angle, C140 at each end, for  $D=8.22\text{mm}$ ,  $L=6.6\text{mm}$ ,  $r=7.85\text{mm}$ , seam angle= $0$ , length= $28.1\text{cm}$ .**

To confirm that the above affect is indeed correct the 3<sup>rd</sup> and 4<sup>th</sup> FSG's were built. As the periodicity and elements are of a completely different design, if a similar effect is observed then it is certain that the thickness of the Mylar dielectric is having a loading affect on the elements.

At this time, it was also decided to ascertain what the affect of the dielectric alone was on the scattering parameters if the elements of the FSG were removed. To this end the copper cladding was etched away to leave just the Mylar sheets and these were then used to make dielectric tubes of the same length and radius as FSG's number 3 & 4. Also a baseline measurement of the  $S_{21}$  was made with an air gap of 284mm left between the two ends of the solid guides. This data has been collated together into a single graph and is shown in Figure 3-13.

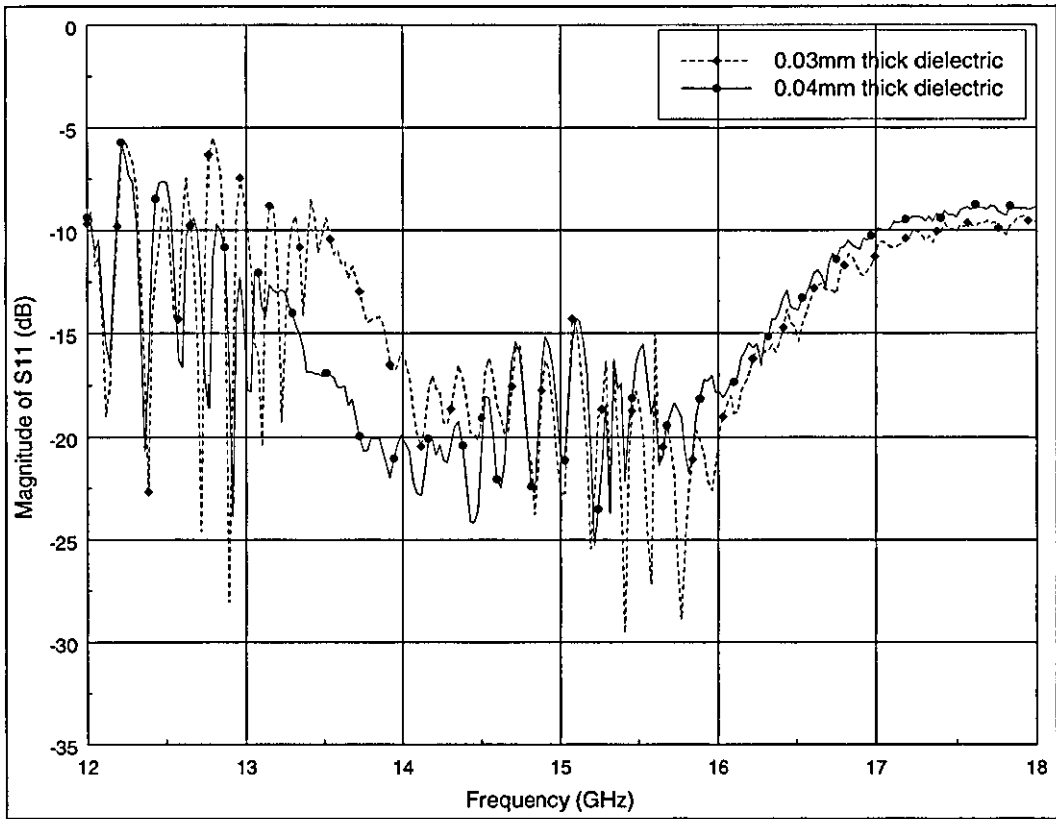
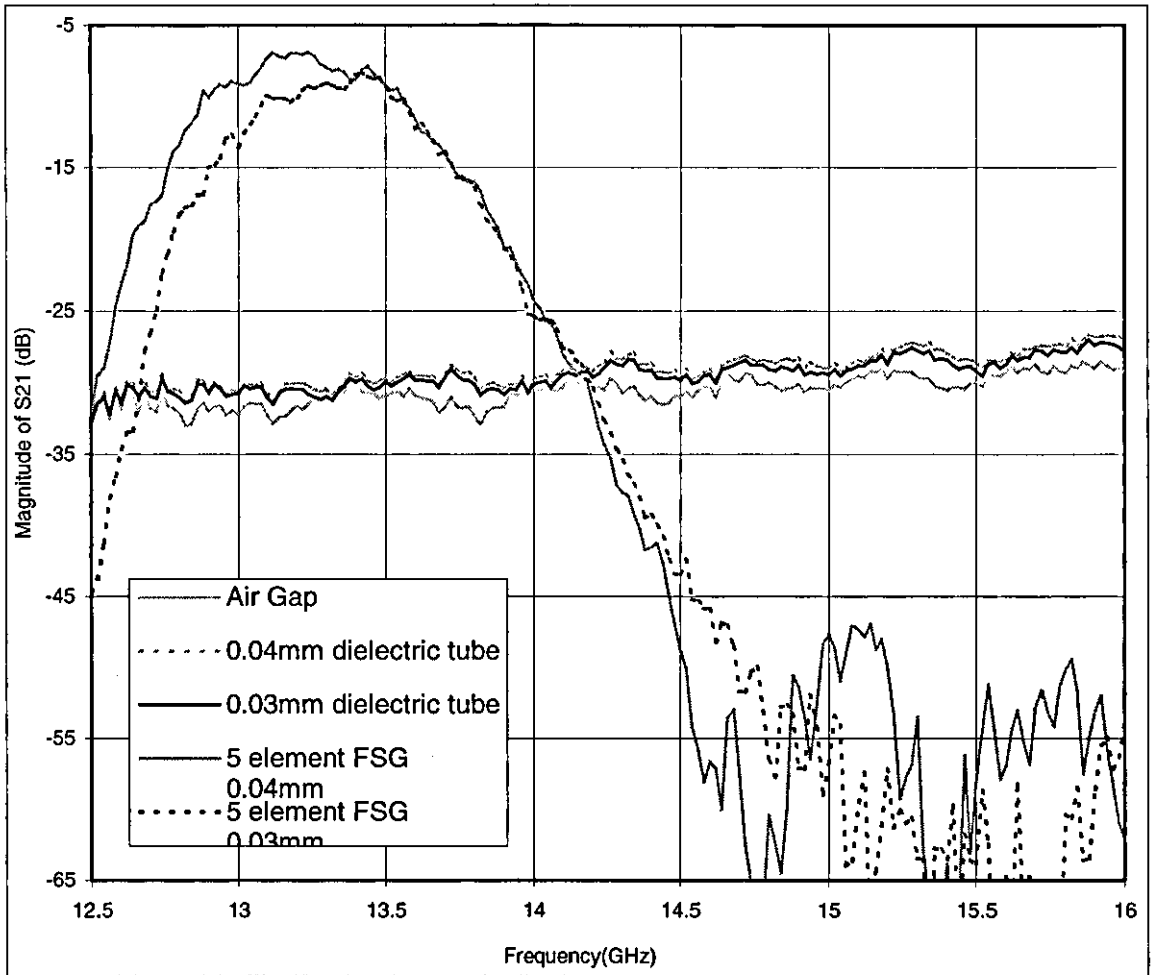


Figure 3-12 Graph of measured  $|S_{11}|$  Vs frequency as the thickness of the dielectric sheet is altered for FSG 1 & 2 with a  $0^\circ$  seam angle, C140 at each end, for  $D=8.22\text{mm}$ ,  $L=6.6\text{mm}$ ,  $r=7.85\text{mm}$ , seam angle= $0$ , length= $28.1\text{cm}$ .

First let us consider the  $S_{21}$  and  $S_{11}$  of the air gap between the feed waveguides and the dielectric tubes. The  $S_{21}$  in Figure 3-13 of the air gap is a relatively flat response around  $-30\text{dB}$ , with a slight slope upwards from the low frequency to the higher frequency. The  $S_{11}$  response has far more ripple than the  $S_{21}$  response, so trends become important, rather than actual values. A trend line would show a fairly straight line starting at  $-10\text{dB}$  at  $12.5\text{GHz}$  and finishing at  $-28\text{dB}$  at  $16\text{GHz}$ . The open end of the feed waveguide radiates power into free space around it, the match to free space getting steadily better as the width of the waveguide becomes wider in terms of wavelengths and as the match improves more power is radiated. The other open ended waveguide has a fixed area and so only receives a proportion of the radiated power. Again the amount of received power increases very slightly due to the increase in the effective area as the wavelength decreases.



**Figure 3-13  $|S_{21}|$  Comparisons of FSGs 3 & 4 and Dielectric Tubes and the Air Gap with a  $0^\circ$  seam angle.**

The  $S_{11}$  of the dielectric tubes in Figure 3-14 are also very similar to that of the air gap. The sometimes quite considerable ripples occur in the same places for response and they are only a few dBs lower in value. The  $S_{21}$  of the dielectric tubes in Figure 3-13 is also almost identical to the air gap measurements. This time they were only slightly higher (2 to 3dB) than the air gap values and differed from each other, due to the changes in dielectric thickness, by only 1 dB. The dielectric tubes have a very small effect in increasing the field transmitted from the feed waveguide to the receive waveguide. The effect is, however, very small when compared to the measurements taken for the FSG's, as can be seen in Figure 3-13 & Figure 3-14. It is truly the FSG elements that give rise to the leaky mode and the surface wave and not the dielectric.

It is quite clear from Figure 3-13 & Figure 3-14 that FSG's 3 & 4 resonate at different frequencies from that seen in FSG's 1 & 2; 13.2GHz & 13.4GHz as opposed to 15.1GHz & 15.3GHz. It should also be noted that the shapes of the S21 graphs are similar for the two designs. The difference with FSG 3 & 4 is that they are designed to resonate at a lower frequency than the design used for FSG 1 & 2, further comment will be on this shortly. From the figures it can be seen that a similar effect is seen for the changes in thickness of the dielectric layer. The thicker dielectric reduces the resonant frequency of the FSG by 0.2GHz, the same amount as seen with FSG's 1 & 2. As we are considering two completely different FSG's and measurements taken on different occasions the cause can be taken to be dielectric loading.

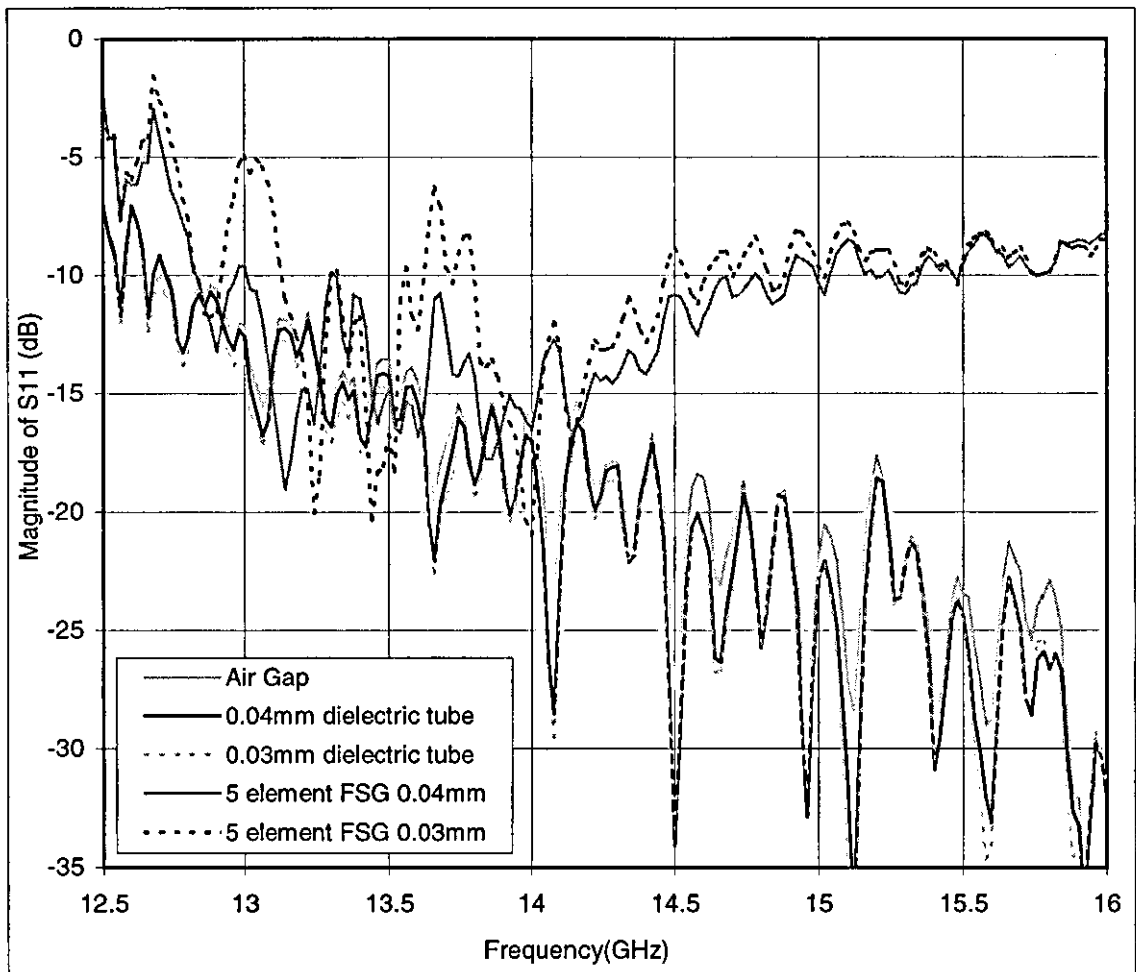


**Figure 3-14**  $|S_{11}|$  comparison of FSGs 3 & 4 and dielectric tubes and the air gap with a  $0^\circ$  seam angle.

As the design for FSG's 3 & 4 resonated at a lower frequency, Figure 3-15 & Figure 3-16 are given to allow an easy comparison of FSG's 1, 3 & 5, each of which has a different design. It is very obvious in Figure 3-15 that the response for FSG 3 & 5 is a

similar response to FSG 1 but shifted down in frequency. They have been shifted so much so that the surface wave region “A” in Figure 3-5 is below the cut-off of the feeding waveguide. For this reason the surface wave region cannot be measured for FSG 3 & 5. For these FSG’s we are left with the leaky wave region with the resonant frequency at the upper centre of the bell curve followed by the roll off of the upper leaky radiative region. The main difference between FSG 1 and FSG 3 & 5 is the change in size of the periodicity and length of elements. From planar FSS theory [7] it is known that changing these dimensions will change the resonant frequency of the structure.

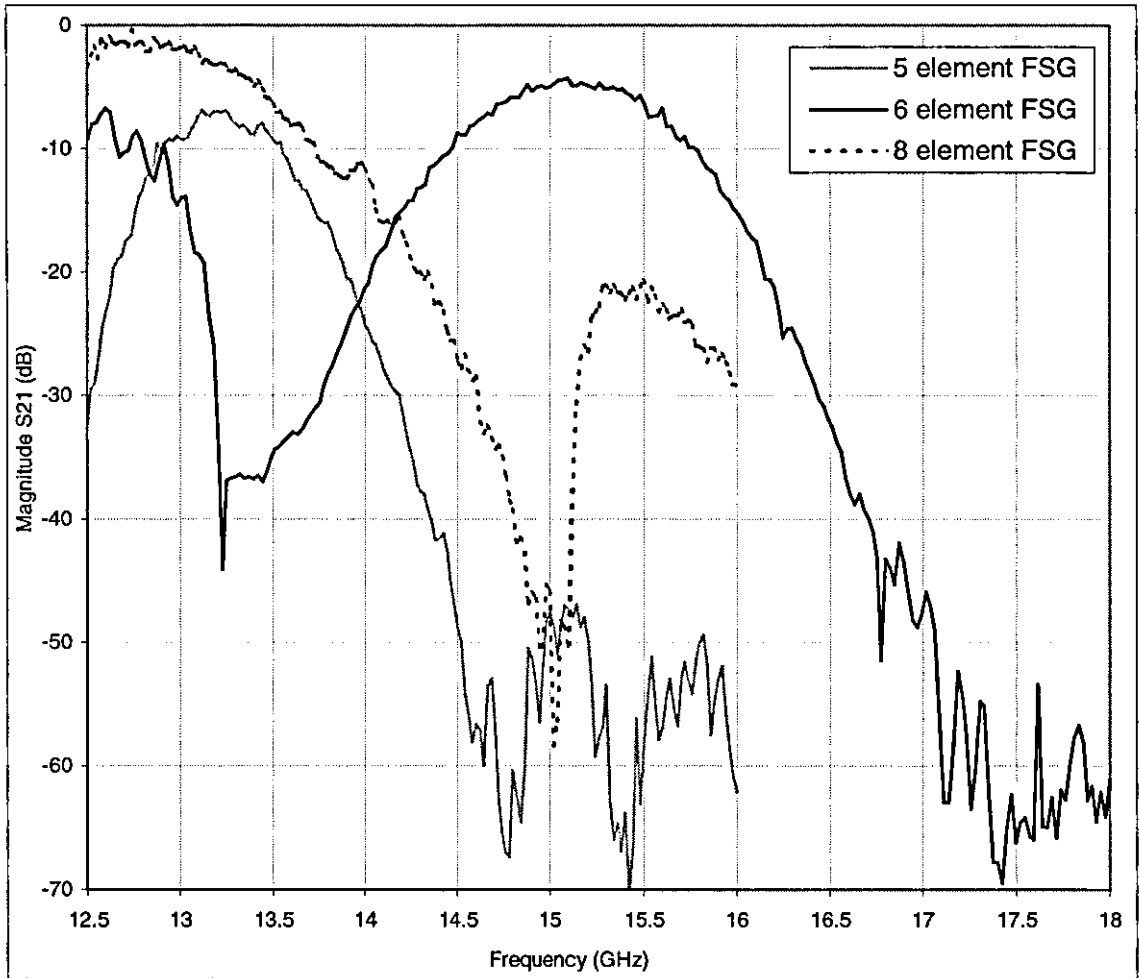


**Figure 3-15  $S_{21}$  Comparisons of FSGs 1,3 & 5 with a  $0^\circ$  seam angle.**

However it must be acknowledged that these were not the only dimensions to change between FSG1 and FSG 3 & 5. The radius and the number of elements were also altered. As stated earlier, because the FSG is a cylinder the parameters of element size and periodicity, radius and number of elements are all interlinked and changing one of

these parameters invariably changes the others. To ascertain which one of these changes had the greatest affect on the resonant frequency FSG 5 was made with the same periodicity and element size as FSG 3, but with a different number of elements and radius. As can be seen from Figure 3-15 the change in resonance between FSG 1 and FSG 3 was from 15.1GHz to 13.2GHz (1.9GHz), but the change between FSG 3 and FSG 5 was from 13.2GHz, to 12.7GHz (0.5GHz). The FSG resonant frequency must therefore, like the planar FSS theory, be controlled more by the element size and spacing than by the radius and the number of elements. However they all play some part and so any FSG design must take all of these factors into account making it a very complicated process.

The important things to notice about the FSG 3 response in Figure 3-15 and Figure 3-16, apart from the resonance shift, is that the peak magnitude of the  $S_{21}$  is lower than that of FSG 1. With a considerably narrower bell curve followed by a familiar region where no  $S_{21}$  could be measured.

The  $S_{11}$  graph shows similar standing wave ripples in the resonance region, but with a high or average value. The region is also narrower as noted for the  $S_{21}$  graph and the trace settles to a similar level as that for FSG 1. As well as moving the resonance, the mismatch between the feed waveguide and the FSG is worse and more leaky radiation occurs through the FSG walls, shown by the narrowness of the leaky region and lower  $S_{21}$  peak value. FSG 5 on the other hand has the widest and highest  $S_{21}$  response yet seen, suggesting that leaky radiation is considerably less for this design and at resonance has the maximum containment of field seen in the measurement study. The match between the feed and the FSG is also the lowest seen as well. All the evidence points to the fact that the number of elements and radius is inversely related to the amount of leakage there is in the leaky mode. As the number of elements/radius increases then the amount of leakage decreases.

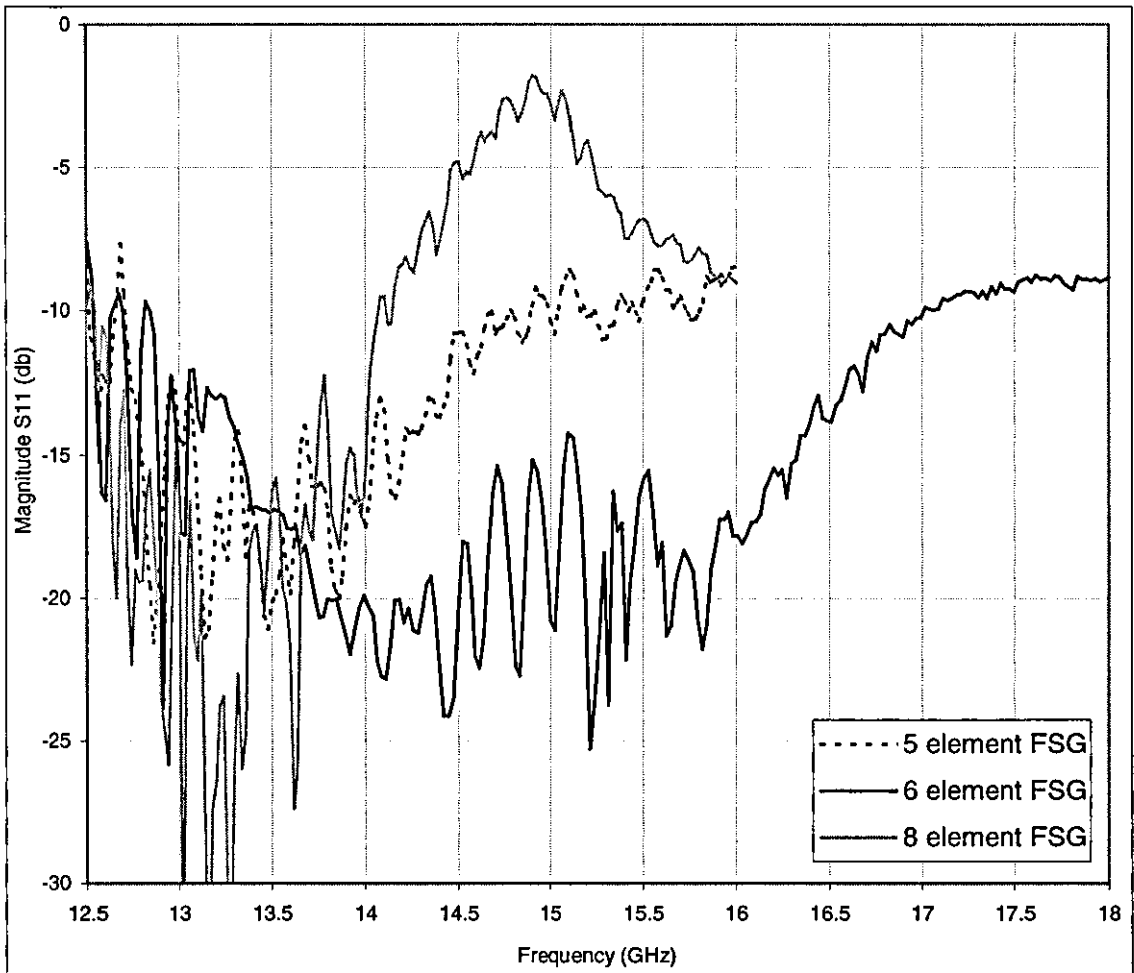


**Figure 3-16  $|S_{11}|$  Comparisons of FSGs 1,3 & 5 with a  $0^\circ$  seam angle.**

However FSG 5 has a feature not seen in either of the other two designs. At 15 GHz the point where  $|S_{21}|$  reaches its lowest value  $|S_{11}|$  also reaches its highest value, a level not seen in any other FSG response. Most of the power is not entering the FSG and is being reflected back down the feed. The level of  $|S_{11}|$  however then fell away towards the  $-10\text{dB}$  level where all the other  $|S_{11}|$  plots levelled off. At the same time the value of  $|S_{21}|$  increased suddenly to  $-22\text{dB}$  and then started to decay away slowly. In solid waveguides this kind of sudden change in S parameters occurs when the waveguide is capable of supporting more than one propagating mode, the waveguide becomes over-moded. It is unclear at this stage what exactly is causing the observed characteristics. It does occur at the correct frequency for the C140 feed waveguide to over-mode, but it is unlikely to be this alone as it was not seen in measurements of FSG 1 to 4. Also, in solid waveguides there is a small finite transition band before the higher order mode will start to propagate with a significant



magnitude, this is not in excess of 0.5GHz as in this case. It could well be either the over-moding of the FSG itself or some complex interaction between the feed guide over-moding and reacting with the FSG, as this FSG has the lowest loss of any of the FSGs tested. Further work would need to be carried out to discover what this phenomenon is, but it has been deemed beyond the scope of this Thesis at present.

To complete the investigation into FSGs 3 & 5 the radiation patterns were also measured using the same equipment set-up as shown in Figure 3-7 and methodology used for FSG 1. Again the graphs show patterns normalised to the maximum beam measured over the frequency range, the pattern with the FSG absent is also included for reference. The results, see Figure 3-17 & Figure 3-18, were as expected, a main beam emerging from the side of the FSG at some frequency dependent angle. The angle from the normal to the FSG increased as the frequency increased.

The magnitude of the beam and beam-width also varied, as before, a minimum value was seen in both cases at a frequency corresponding to resonance, proving that at resonance the field is contained within the FSG and the leakage is minimised, although not eliminated. For a beam to have maximum possible magnitude then the frequency must be such that it is in the mid point between the resonant frequency and the frequency that corresponds to a minimum value on the  $S_{21}$  curve. There are two such maximum magnitude beams possible from the FSG one either side of the resonant frequency. However Figure 3-17 has only one maximum beam as the lower point is below the cut-off of the feed waveguide.

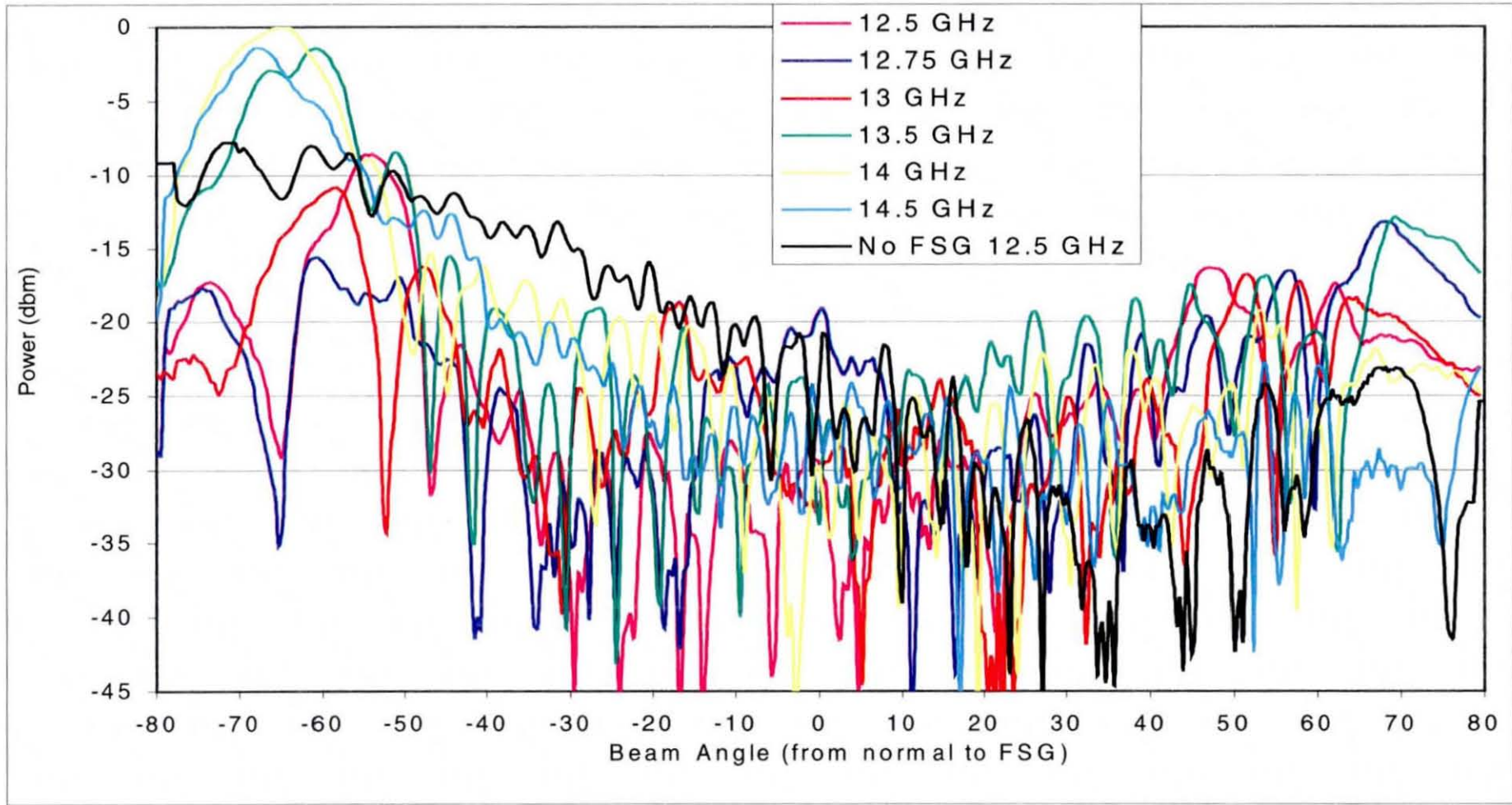


Figure 3-17 Radiation patterns for FSG 5 at different frequencies.

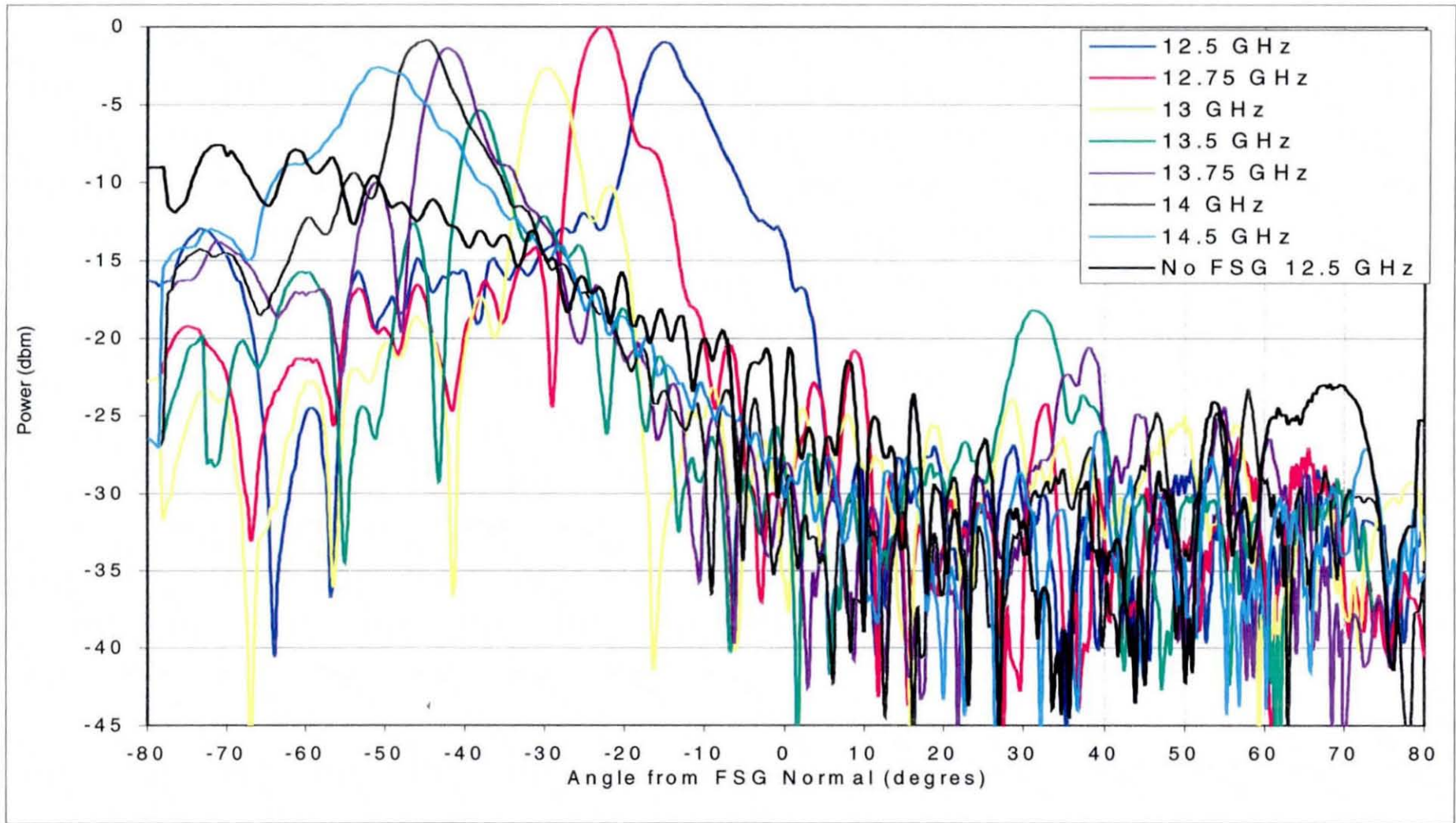


Figure 3-18 Radiation patterns for FSG 3 at different frequencies.

It should be noted in all the radiation patterns that the difference between the maximum and minimum main beam value changes with the number of elements. When the FSG has a low number of elements the reduction in the main beam value is small at resonance, confirming that the leakage is high. As the number of elements goes up the main beam value gets increasingly lower at resonance, confirming that the leakage is low.

By measuring different FSG's it has been ascertained that the FSG has a propagating surface wave region that gives way to a leaky radiative region. This leaky region has an area within it where the elements resonate and reduce the amount of leakage. The thickness of the dielectric was found to have a loading effect on the response, increasing the thickness shifted all the frequency points down in frequency. The orientation of the seam with respect to the feed  $TE_{11}$  polarisation vector was found to have a big influence on the performance. The best being achieved when the angle between them was  $0^\circ$ . All the FSG parameters of radius, periodicity and size of elements and number of elements affect the resonant frequency. However the ones with the greatest influence are the periodicity and element length. The number of elements and radius appears to have the greatest influence on the amount of leakage through the FSG wall at resonance. As the number/radius increases the leakage decreases.

### 3.6 Extraction of FSG Propagation Constant

The results in the preceding section give a good idea of how the FSG functions, but these measurements can not be directly compared to the results from an infinite FSG analysis program. The output from the program is the complex propagation constant of the FSG. The practical measurements must be manipulated to extract the propagation constant information from them. Several measurements and methods were identified as suitable candidates with which to extract this information. These were: -

- Use the  $S_{21}$  (or  $S_{11}$ ) measurement to calculate the propagation constant directly. This can either be done directly ignoring the junction transitions between the FSG

and the solid guide, or else using multiple measurements of different lengths of FSG to eliminate the junctions.

- Use the radiation pattern beam angle and magnitude to find the beta ( $\beta$ ) and alpha ( $\alpha$ ) parts of the propagation constant respectively. This makes use of the fact that the leaky wave main beam is radiated at an angle dependent upon the phase constant ( $\beta$ ) and it's magnitude is related to the loss ( $\alpha$ ).
- The final method is related to the previous method, but requires the radiation pattern to be made with a short circuit over the far end of the FSG. This reflects some of the leaky mode back down the FSG and another beam is produced radiating in the opposite direction to the first. The elements of the propagation constant are then found from the difference between the two beam magnitudes and the angle between them.

### 3.6.1 Calculation of Propagation Constant from $S_{21}$ measurements

A lot of information about the FSG can be obtained from the  $S_{21}$  (and  $S_{11}$ ) response. The measured scattering parameters are those of the entire system under test, consisting of the two FSG to solid waveguide junctions and the length of FSG itself. In order to obtain FSG propagation constants or junction scattering parameters the two sets of information will have to be de-embedded. A study was done to see if by taking repeated measurements, the propagation constants could be extracted from the effects of the junctions. In order to do this the whole system must first be modelled. The FSG system was converted into an idealised block diagram. The junctions between the solid feed guides and the FSG are represented as two blocks each with it's own set of scattering (S) characteristics and the FSG as an attenuated transmission line connecting the blocks together. From transmission line theory this is represented by  $e^{-jk l}$  where  $e$  is the natural number,  $j$  is the imaginary operator,  $k$  is the complex propagation constant (which has a real phase constant  $\beta$  and an imaginary attenuation constant  $-j\alpha$  and  $l$  is the length of (or distance down) the transmission line. The block diagram of the FSG as it was tested is shown in Figure 3-19, with the FSG represented by the parallel lines in the centre and modelled as a perfect leaky transmission line with propagation factor  $e^{-j(\beta+j\alpha)l}$ .

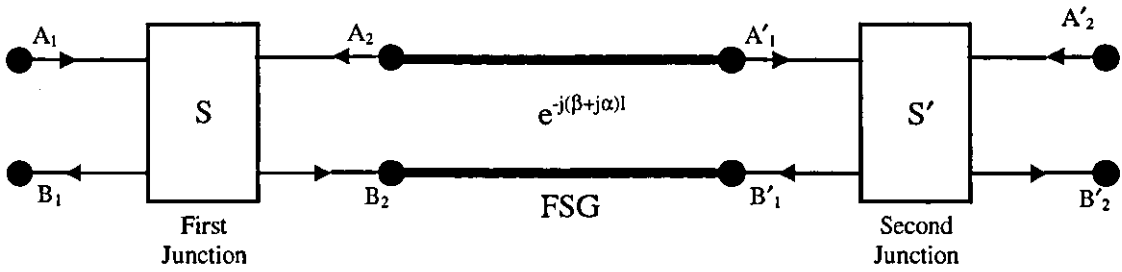


**Figure 3-19 Block Diagram of the FSG under Test.**

The junction blocks above have the scattering S matrix form of: -

$$\begin{bmatrix} b_1 \\ b_2 \end{bmatrix} = \begin{bmatrix} S_{11} & S_{12} \\ S_{21} & S_{22} \end{bmatrix} \begin{bmatrix} a_1 \\ a_2 \end{bmatrix} \quad \& \quad \begin{bmatrix} b'_1 \\ b'_2 \end{bmatrix} = \begin{bmatrix} S'_{11} & S'_{12} \\ S'_{21} & S'_{22} \end{bmatrix} \begin{bmatrix} a'_1 \\ a'_2 \end{bmatrix}$$

Equation 3-1

Where a and b are the field magnitudes in and out of the junction boxes at each of its ports.

The S11 measurements in the previous section were measured at port 1 of the first junction and the S21 was measured from port 1 of the first junction to port 2 of the second junction. Using Mason's rules to cascade the S parameters of the S blocks and the intervening transmission line the system S11 and S21 equations can be written in terms of the above as: -

$$S_{11} = S_{11} + \frac{S_{21}S'_{11}S_{12}e^{-2j(\beta+j\alpha)L}}{1 - e^{-2j(\beta+j\alpha)L}S_{22}S'_{11}}$$

Equation 3-2

$$S_{21} = \frac{S_{21}S'_{21}e^{-j(\beta+j\alpha)L}}{1 - e^{-2j(\beta+j\alpha)L}S_{22}S'_{11}}$$

Equation 3-3

Where in the above L is the length of the FSG.

In order to reduce the number of unknowns some products were combined into a single unknown, i.e.  $S_{21}S'_{21} = xS_{21}$  in Equation 3-4. This reduced the number of unknowns allowing the propagation constant to be found more easily, we now have 3

and not 5. However it would not allow the junction S parameters to be calculated, but it would give an idea of their values.

$$S_{21} = \frac{xS_{21}e^{-j(\beta+j\alpha)L}}{1 - e^{-2j(\beta+j\alpha)L}xS_{22}}$$

Equation 3-4

Of course if the junctions are reciprocal then  $S_{21}$  &  $S_{22}$  of the first junction will be the same as the  $S'_{21}$  &  $S'_{11}$  of the second junction, but this will not be assumed yet. If the problem can be solved it would also yield values of the propagation constant, it being the remaining unknown. It must be remembered that all the unknowns and scattering parameters are complex values, which makes the calculations very much harder. A similar procedure could be carried out for Equation 3-2, but it obviously has four and not three unknowns, as is the case for Equation 3-4.

It was decided that if we measured the  $S_{21}$  of three different lengths of FSG, then two of the unknowns could be eliminated and the third unknown found. In order to achieve this two more FSGs were made, from the 0.03mm thick dielectric sheet, which were shorter than the first 0.03mm thick dielectric FSG number 2. These other FSGs were 23.9cm and 20.7cm long, made in the same manner as before, and with the same periodicity, radius and element size.

The  $S_{21}$  responses for these new lengths were taken with the same test set-up and procedures as before. Again there was a variation of the  $S_{21}$  values dependent on the orientation of the FSG in the  $\phi$  direction. The graphs of the responses obtained were very much like those obtained for the longer 0.03mm thick dielectric FSG. There were two definite regions, a slow wave region which died away, followed by a leaky wave 'band pass' type region with a break between them. Following the leaky region there was almost no  $S_{21}$  value recorded above the noise floor of the analyser. The changes in orientation also had a similar effect, with seam aligned to the polarisation vector of the feed guide, the position where the resonance value became a maximum and the magnitude of the ripples minimised. As the orientation was moved away from

this angle the resonance value became lower and the ripples became increasingly large.

Figure 3-20 shows the responses of the three 0.03mm thick dielectric FSGs of design 2 with different lengths. Each plot was taken at the seam angle corresponding to  $0^\circ$  from the  $TE_{11}$  polarisation vector. It should be noted that although each FSG has the same element size and spacing, which it was thought would give the same resonant frequency, this was clearly is not the case and more will be said about this shortly. Also notice that the upper skirts, or  $S_{21}$  roll off, of the responses are more or less coincidental with each other for each length and is thought to be linked to the movement in resonant frequency. The reduction in the maximum value of  $S_{21}$  at the resonance as the length increases is to be expected, as more energy will radiate as the leaky mode has further to travel and hence the  $S_{21}$  value will drop. With this data from the three FSGs of different lengths the propagation constants can be found using a numerical equation solving routine in the PC mathematics package, MathCad.

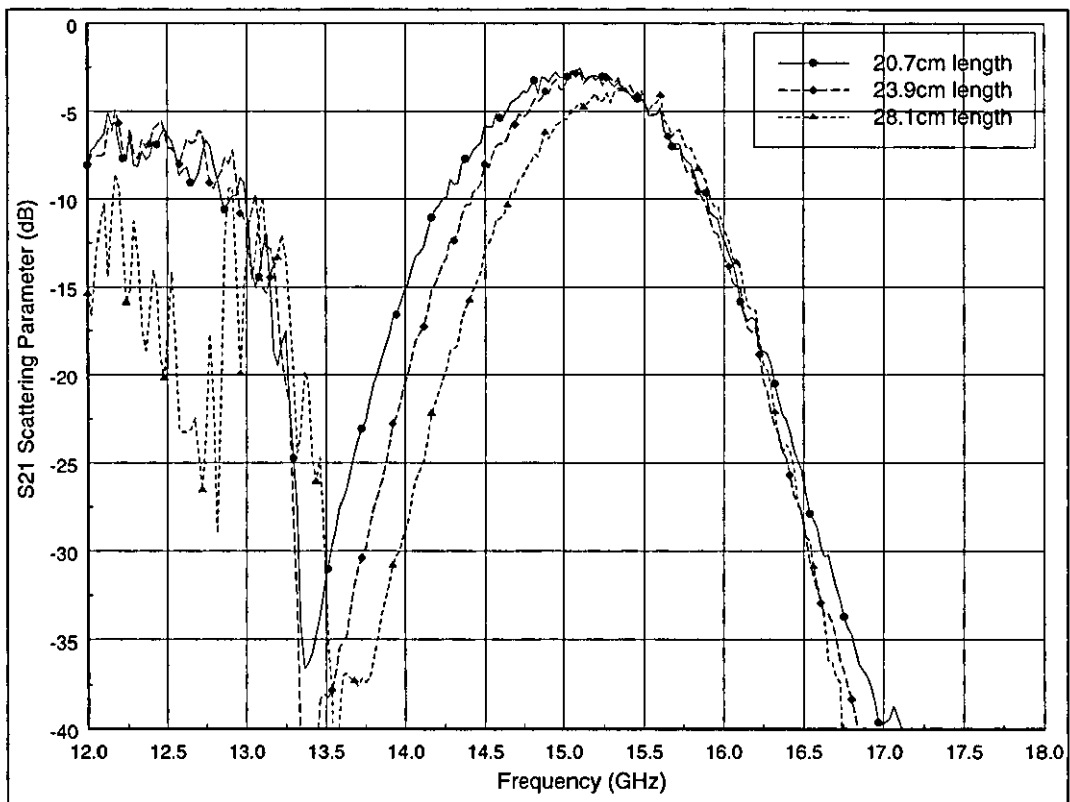


Figure 3-20  $S_{21}$  for different lengths of FSG 2, for  $D=8.22\text{mm}$ ,  $L=6.6\text{mm}$ ,  $r=7.85\text{mm}$ ,  $t=.03\text{mm}$ , seam angle= $0^\circ$ .



Initially the package was tested to see how accurate it was at solving three  $S_{21}$  simultaneous equations of Equation 3-4 for a known set of values. The  $S_{21}S'_{21}$ ,  $S_{22}S'_{11}$ ,  $\beta+j\alpha$  quantities were set to arbitrary values, with the same ones being used for each length. The  $S_{21}$  was then calculated for each length using Equation 3-4. Using these calculated values of  $S_{21}$  the numerical solution routine was used to find the arbitrary values which generated them. To this end, the equations to be solved for each length were declared in the routine, along with any other restrictions, such as the  $\beta$  solution being positive and the  $\alpha$  solution being negative (i.e. a leaky wave), and the initial guess values. The numerical routine uses these initial guess values as a starting point from which to iteratively converge on a solution. Not all initial values will converge to the same solution or indeed converge at all. In evaluating this method one of the most important things is to estimate how close to the real solution the initial guess values need to be. To this end the initial guess values were placed close to the actual solutions, but then moved further away in order to give an idea of this method.

Example of MathCad program: -

First define the arbitrary values of  $xS_{21}$  and  $xS_{22}$  and the  $S_{21}$  equation as a function of the propagation constant  $k$  and the FSG length  $l$ .

$$xS21 := 0.55 e^{\frac{\pi}{3}i} \quad xS22 := .014 e^{i \frac{\pi}{6}}$$

$$S21(k, l) := \frac{xS21 e^{-i \cdot k \cdot l}}{1 - xS22 e^{-2i \cdot k \cdot l}}$$

Calculate the three  $S_{21}$  values with the arbitrary values.

$$S21(-.5733i + 206.382, .281) = 0.42727 - 0.18293i$$

$$S21(-.5733i + 206.382, .239) = -0.19562 + 0.43374i$$

$$S21(-.5733i + 206.382, .207) = -0.3253 + 0.35722i$$

Define function to solve equation

$$L1 := .281 \quad L2 := .239 \quad L3 := .207$$

$$XS21 := .65 \cdot e^{i \frac{5\pi}{12}} \quad XS22 := .01 \cdot e^{i \frac{3\pi}{12}} \quad K := -1 \cdot i + 210 \quad \leftarrow 3 \text{ initial guess values}$$

Given

$$\frac{XS21 \cdot e^{-i \cdot K \cdot L1}}{1 - XS22 \cdot e^{-2i \cdot K \cdot L1}} = t0 \quad \text{Re}(K) > 0 \quad \leftarrow \text{declaration of system to solve.}$$

$$\frac{XS21 \cdot e^{-i \cdot K \cdot L2}}{1 - XS22 \cdot e^{-2i \cdot K \cdot L2}} = t1 \quad \text{Im}(K) < 0$$

$$\frac{XS21 \cdot e^{-i \cdot K \cdot L3}}{1 - XS22 \cdot e^{-2i \cdot K \cdot L3}} = t2$$

Values of transmission to 5 sig figs.

$$\text{trans}(t0, t1, t2) := \text{Find}(K, XS21, XS22)$$

$$\text{trans}(0.42727 - 0.18293j - 0.19562 + 0.43374j - 0.3253 + 0.35722j) = \begin{bmatrix} 206.38187 - 0.57341i \\ 0.27502 + 0.47632i \\ 0.01213 + 0.007i \end{bmatrix}$$

$$k := 206.382 - i \cdot .5733 \quad xS21 = 0.275 + 0.47631i \quad xS22 = 0.01212 + 0.007i$$

$$\text{trans}(0.42727 - 0.18293j - 0.19562 + 0.43374j - 0.3253 + 0.35722j) = \begin{bmatrix} k \\ xS21 \\ xS22 \end{bmatrix} = \begin{bmatrix} -0.00013 - 0.00011i \\ 2.2051810^{-5} + 2.6479310^{-6}i \\ 5.8528910^{-6} - 8.814210^{-7}i \end{bmatrix}$$

It was found that for the solution to converge to the correct value the initial guess value for xS12 and xS22 could be as far as 50% from their actual values. The attenuation constant could vary by as much as 200%, but the phase constant has to be quite accurate, the guess value being within 5% of the actual value. \*

With this information it was decided that this method could find the required values of the junction S products and the propagation constant. The  $S_{21}$  values, from 14GHz to 16.2GHz, for the three lengths of FSG were read into the application. From a set of initial guess values, a solution to the system of simultaneous equations was attempted for each frequency. However it was found that no solution could be found from any of the guess values that were tried. As only one  $\beta$  guess value could be supplied to the numerical equation solving routine, then for any  $\beta$  values outside the 5% tolerance range, no solution will be found. As there is a large range of frequencies being solved

for then there must be a corresponding large range of  $\beta$  values and hence no solution was found.

The range of data was therefore divided into several parts so that a different  $\beta$  guess value could be assigned to each range, where all the solutions would have their  $\beta$  values within the 5% tolerance. A rough idea of what the guess value should be was gained from the Loukos prediction program, although the actual values from the program were never used. To simplify matters initially, it was also decided to remove the dependence on supplying guess values for the S products by eliminating them from the equation, they can be calculated separately once the propagation constant has been found. The single simplified Equation 3-5, replaced the three simultaneous equations in the definition block of the numerical solution routine and was solved by the method already described.

$$\frac{t1 \cdot t2 \cdot [e^{-i \cdot K(L1+2 \cdot L2+L3)} - e^{-i \cdot K(3 \cdot L1+L3)}]}{t2 \cdot [e^{-i \cdot K(2 \cdot L1+2 \cdot L2)} - e^{-i \cdot K(2 \cdot L1+2 \cdot L3)}] + t1 \cdot [e^{-i \cdot K(L1+L2+2 \cdot L3)} - e^{-i \cdot K(3 \cdot L1+L2)}]} = t3$$

Equation 3-5

Where  $t1, t2, t3$  are the  $S_{21}$  values for the three lengths ( $L1, L2, L3$ ) of FSG and  $K$  is the propagation constant. Note that now only one initial guess value need be provided. The frequency range again had to be split into small sections, because of the small tolerance range over which beta could be found for one guess value.

When all the small frequency sections of the solved propagation values are stitched together the overall solution for the propagation constant for real and imaginary magnitude across the entire frequency range is shown in Figure 3-21.

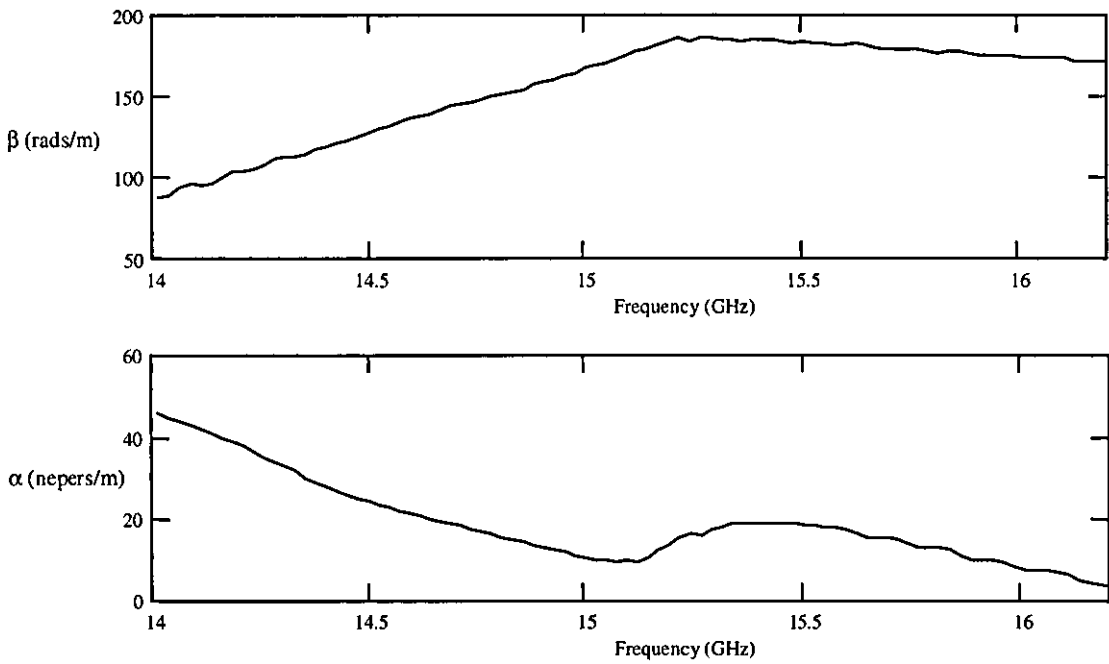


Figure 3-21 Real & imaginary propagation constants as calculated from three  $S_{21}$  measurements from different lengths of FSG 2.

As can be seen the results look plausible until 15.2 GHz, with decreasing attenuation approaching the resonance point, the point where the least amount of power leaks through the FSG wall and  $\beta$  smoothly increasing over the initial frequency range. However after the resonance point the solutions found appear to be incorrect with the  $\beta$  value decreasing with increasing frequency and the attenuation initially rising as expected but then reversing and falling away towards low values. The  $\beta$  value should have continued to increase with increasing frequency and the attenuation should have continued to increase as more power is radiated through the FSG wall.

The solution obtained clearly does not fit the model of FSG operation based on the evidence collected to date. However the numerical solution method is not at fault because closer consideration of the three  $S_{21}$  curves in Figure 3-20 does indeed give the result obtained as a plausible solution to Equation 3-5. As mentioned previously the resonance points of the three FSGs are at different frequencies and after this point the roll off skirts of the 3 plots are almost coincidental. This means that the evaluated propagation constant for this region must be such that it gives almost identical  $S_{21}$  values even though the length has changed. A change in length should yield a

different set of  $S_{21}$  plots if the propagation constant is the same for each FSG measured, they should never have plots that are near identical. Therefore the propagation value found is correct, but only for the flawed data that was used in this extraction technique.

The problem with the  $S_{21}$  values of the three FSGs of different lengths is that although the etched elements on the surface are identical, they are unfortunately not completely identical in cross section. The supporting dielectric tubes are the problem; they are all slightly elliptical and the major and minor axes of the ellipses are never the same from one FSG to another. This arises because the rolling process during manufacture can never be truly identical when carried out by hand. Also closer inspection reveals small undulations and depressions that appear randomly around the circumference and along the length. These arise when handling the FSGs, even though great care was taken when moving and storing them and such dimples are inevitable purely because the structure is so delicate.

Given that the FSGs are not identical then it is not surprising that the resonant frequencies and  $S_{21}$  plots are different for each one, even though the elements used are identical. This implies that the uniformity and degree to which the cross-section is circular have a pronounced effect on the performance of the FSG. By making the FSGs from thin Mylar sheet they are very susceptible to small local deformations in the cylinder surface. In order to try to reduce the effect of the manufacturing differences the  $S_{21}$  measurements for three different lengths were repeated for FSG 5 by cutting small amounts off one end after each measurement was taken. This means that most of the FSG is identical for each measurement, although it means that the measurements can never be repeated as the longer lengths are by definition destroyed in order to make the shorter lengths.

The results are shown in Figure 3-22, with the raw data on the left hand side and the data when smoothed on the right hand side. The smoothing was carried out to remove the small ripple in the raw data plots. When the numerical solution method is applied to the raw data, meaningful propagation constant values cannot be found as the relationship between the  $S_{21}$  values changes from one frequency to the next due to the ripple. The ripple is no worse than that seen before, but for FSG 5 because the loss at

resonance is small the three plots are closer together and so they do stay in a consistent order or separation. The raw measurements were smoothed to try to overcome this problem, but as can be seen in Figure 3-22 the plot for the shortest length has some very low ripple values near resonance which meant that instead of the 22.1cm values being consistently above those of the other two plots it is below them around the resonance point. This makes it impossible to extract meaningful propagation constants from this data as well. The fluctuations in the magnitudes are caused by deformations and dimples in the dielectric support caused while handling the FSG during cutting. From this work it is obvious that another production method is required for accurate measurements to be undertaken. A more robust structure would also be required should any commercial exploitation be undertaken. The opportunity to explore these alternative construction methods was unfortunately not at my disposal during the course of this Ph.D.

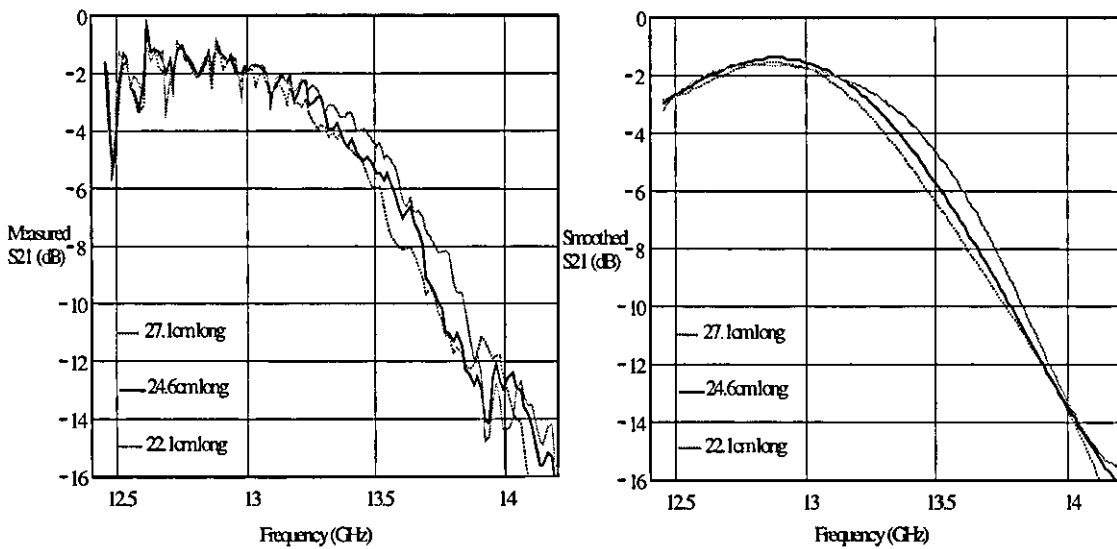


**Figure 3-22 Measured data for 3 different lengths of FSG 5 & the same data when it has been smoothed.**

All efforts to extract the propagation constant from the S<sub>21</sub> measurement had so far failed due to the inaccuracies in measuring multiple lengths of similar FSGs. It was therefore decided to obtain an estimate of the propagation constant from a single length of FSG by ignoring the effect of the solid waveguide to FSG transitions. If the unknown S parameters of the transitions are set to unity then the equation of the S<sub>21</sub> that needs to be solved is that of Equation 3-6.

$$S_{21} = \frac{e^{-j(\beta+j\alpha)L}}{1 - e^{-2j(\beta+j\alpha)L}}$$

Equation 3-6

This can be done by again employing the MathCad numerical solution method, only this time much simplified with only Equation 3-6 in the equation definition area and only one guess value, that of the propagation constant. Again due to the large frequency range and low tolerance of  $\beta$  in solving the equation the range had to be split into several smaller sections. Solutions could be found for all the values and a relatively smooth curve was produced for  $\beta$  and  $\alpha$ . The curves for the whole frequency range for  $\beta$  and  $\alpha$  are shown in Figure 3-23 & Figure 3-24, along with the curves obtained by other methods and from the theoretical program simulations. This estimate of  $\beta$  using the  $S_{21}$  data produces results that are below the predicted value and there is a slight kink in the line from 15.7GHz to 16GHz. This is a subsection of the solution where there is a dip in the  $S_{21}$  data values, which causes the downward shift in the propagation constants,  $\alpha$  &  $\beta$ . Apart from this the line runs parallel to the theoretical line. However the frequency at which the  $TE_{11}$  line crosses the  $S_{21}$   $\beta$  line from Equation 3-6, if the kink is removed and the line smoothed, is 15.7GHz. This is much too high because the effect of the dielectric should move this point to below the predicted 15.4GHz.

The prediction was run for the design of FSG1, but with no allowance for the dielectric substrate. It is the same data as shown in chapter 2. Also included, for reference, is the  $\beta$  value of the  $TE_{11}$  mode that exists in a solid waveguide of the same radius as FSG1. The intersection of the  $TE_{11}$   $\beta$  with that of the FSG mode  $\beta$  defines the resonant frequency of the FSG. Using this the program predicts the resonant frequency to be 15.4GHz, which is in good agreement with the predicted resonance frequency given by the minimum in the  $\alpha$  plot of 1neper/m at 15.4GHz.

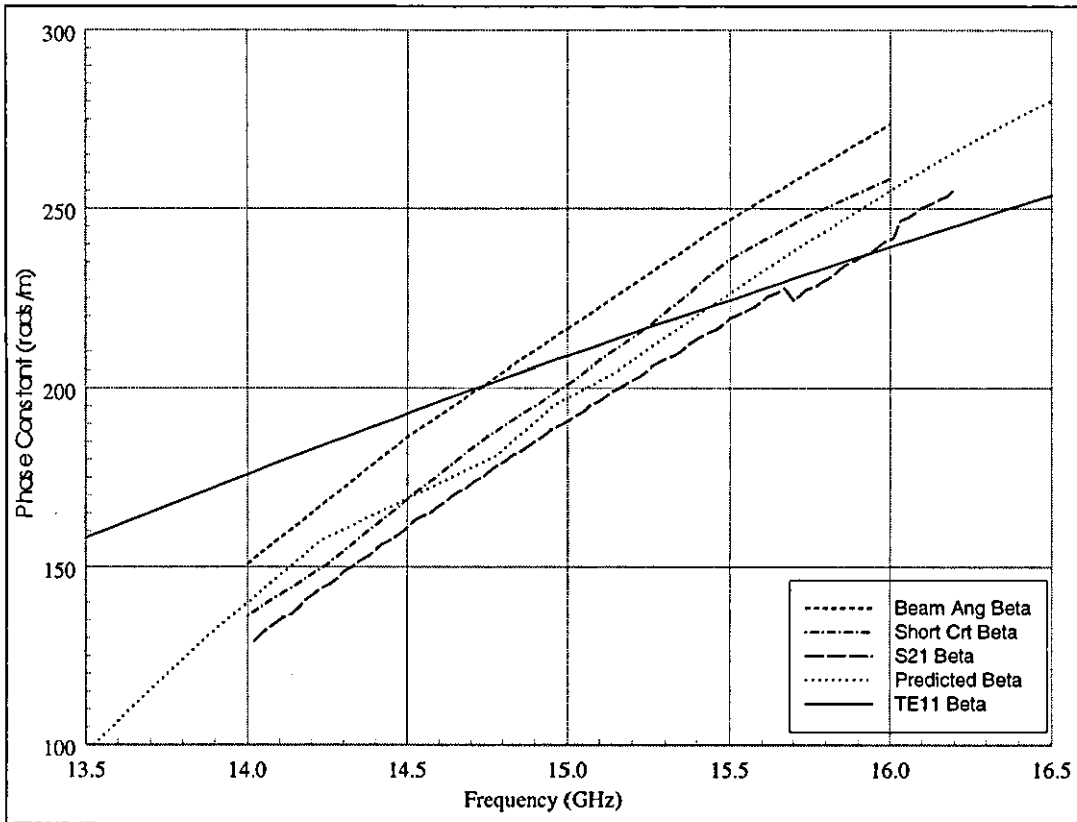


Figure 3-23 Comparison of  $\beta$  calculated theoretically by different methods from measured data

The alpha values for the S21 estimate follow a similar curve to the predicted, but the values of attenuation are much higher, 4nepers/m compared with a prediction of 1nepers/m. This is partly due to the presence of the dielectric, which increases the structures dissipative losses and also causes the shift downwards in frequency of the point at which minimum attenuation occurs, the resonant frequency 15.1GHz. However part of this higher value of attenuation is caused by the reflections from the junctions between the FSG and the solid feed guide. As they could not be de-embedded from the  $S_{21}$  values they will result in errors in the calculated propagation constant. This could well be the cause for the frequency at the  $TE_{11}$  crossing point on the  $\beta$  line not matching the minimum resonance point on the  $\alpha$  plot.



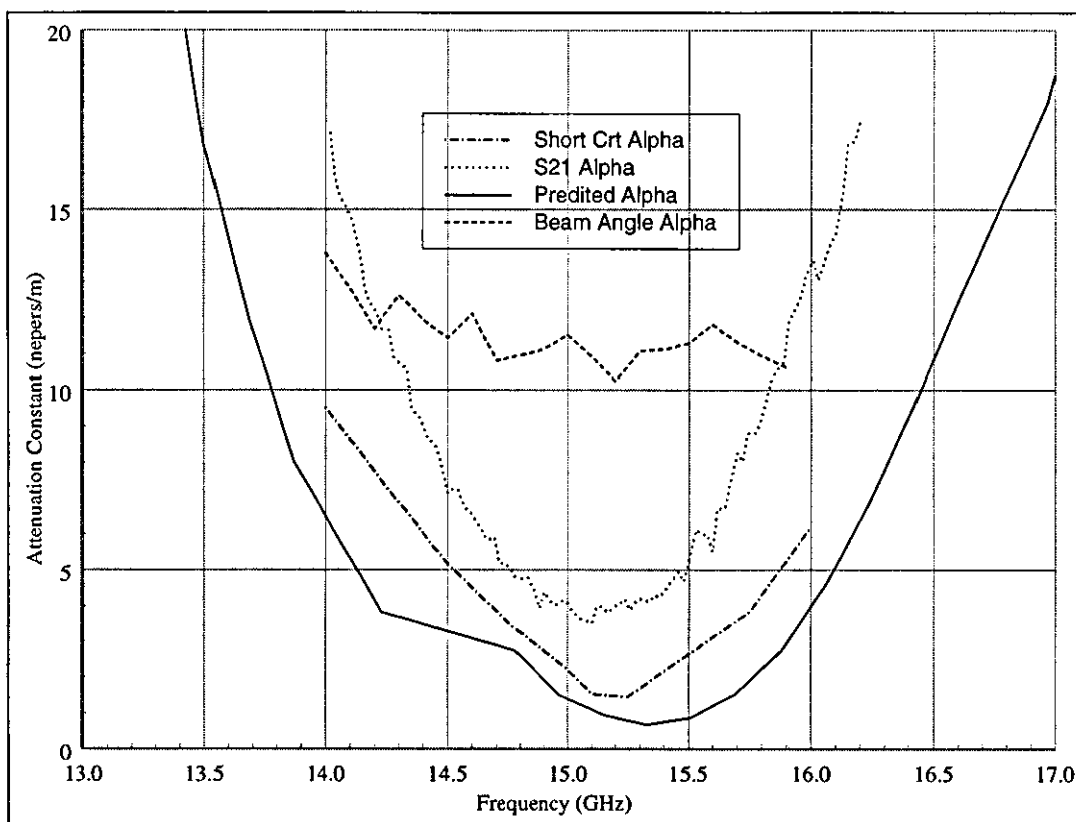


Figure 3-24 Comparison of  $\alpha$  calculated theoretically by different methods from measured data.

### 3.6.2 Calculation of Propagation Constant from Radiation Pattern Measurement

This method takes advantage of the fact that the structure can support leaky wave modes. As shown in Figure 3-8 the radiated energy from the leaky structure has a single main beam, which emerges at an oblique angle to axis of the FSG. The angle and size of the beam are directly related to the propagation constant of the mode [1] & [3 - 5]. In order to find the propagation constant of the FSG it is merely necessary to measure the FSG radiation pattern at different frequencies and find the angle of the main beam and its magnitude. The FSG was set-up in the microwave anechoic chamber as shown in Figure 3-7 and detailed in 3.4.5. The system was set up as shown above with the matched load attached to the circular to rectangular transition. No calibration of the system was possible and a raw value of the power received at the test horn was recorded.

The FSG used to test this method was FSG 1 with the 0.04mm thick dielectric support to match the extracted constants gained via the S21 method. The change in the beam angle as the frequency increases is clearly seen in Figure 3-8.

$$\beta = k_0 \sin \theta_{mb}$$

Equation 3-7

From [3]  $\theta_{mb}$  in Equation 3-7 is the angle from the normal to the FSG surface and from this the value of  $\beta$  can be found. Equation 3-8 gives the relationship between the width of the beam and the attenuation constant. The measure of the beam magnitude used to calculate the  $\alpha$  value is the angle between the -3dB points either side of the main beam in radians,  $\theta_{-3dB}^{rads}$ . As the leaky mode gets wider more energy is being radiated and hence the attenuation constant must be higher.

$$\alpha = \frac{k_0 \theta_{-3dB}^{rads} \sqrt{1 - \left(\frac{\beta}{k_0}\right)^2}}{2}$$

Equation 3-8

As can be seen in Figure 3-23 & Figure 3-24, it was found that this beam angle method gave poor results for both  $\beta$  &  $\alpha$ . This is due to two difficulties associated with the chamber in which the measurements were taken. The positioning of the FSG perpendicular to the line joining the 0° position of the measurement horn and the centre of the FSG was very hard to achieve with the equipment. There is no permanent jig to support the device under test in the chamber and so on each measurement occasion a makeshift jig must be erected and aligned to support the FSG and feed waveguides. This is relatively easy for horns and other antennas with symmetrical geometries as the patterns themselves can be used in the alignment process. As the leaky FSG has asymmetrical beams that do not radiate normal to the FSG this was not possible. The FSG was aligned by eye using protractors and straight edges. It is conceivable that the miss-alignment may have been as much as 10°. The equipment that measures the angle of receive horn in the chamber is also inaccurate. It is thought that this could be as much as 5° out for each measurement. In all the

maximum possible error in these measurements could be  $15^\circ$  and would account for the poor correlation of the  $\beta$  values to the predictions. The  $TE_{11}$  crossing point is 14.7GHz instead of the predicted 15.4GHz. There is no way that dielectric loading could have caused 700MHz of downshift in the value which must be primarily caused by measurement errors.

Also it was difficult to find the -3dB points on the beam patterns collected. The angle at which the -3dB point occurred had to be interpolated from the adjacent points that it fell between. With a non-linear pattern with quite often a large spread in values between points it is very hard to find the beam widths to any certainty, especially when compounded by the difficulties in measuring the angles with any great accuracy. This resulted in the  $\alpha$  values being very different from those predicted and followed no discernible path or were even close to the expected shape of the attenuation constant. Given the measuring difficulties, this method should not be used and a better way of finding the propagation constant was required.

### 3.6.3 Calculation of Propagation Constant from Short Circuit Radiation Patterns

In order to find the propagation constant of the FSG from the radiation beam pattern, but without the need for exact alignment of the equipment, a forward and reverse beam measurement system was employed. This involved replacing the matched termination and the circular transition at the far end of the FSG with a short circuit. This was a metal plate three times the diameter of the FSG and was held over the far end of the FSG with a small lug on it to hold the FSG in place. The effect of the short circuit was to reflect all the energy reaching the far end of the FSG back down the guide. These reflected fields are also in the form of FSG modes and travel down the guide in the same way as the forward travelling waves. So these modes also radiate power in the form of a leaky wave main beam. The beam now makes a positive angle to the normal from the FSG surface, as the first beam angle was measured as negative. As both leaky waves must have the same propagation constant they must also leave the guide at an angle from the FSG normal with the same magnitude. Now it is the angle between these two main beams, which can be related to the  $\beta$  value by the Equation 3-9.

$$\beta = k_0 \cos\left(\frac{\pi - \theta_D}{2}\right)$$

Equation 3-9

Where  $\theta_D$  is the angle between the main beams in radians and is far easier to measure. As the  $0^\circ$  point of the receive horn positioner does not need to be aligned with the FSG normal the measurement inaccuracies will be reduced by 1/3 and all alignment errors are removed. Also further enhanced accuracy is achieved because the error contributed by the angle measuring equipment is halved, as the measured angle is twice as large as before.

The attenuation constant can also be found using this short circuit measurement, not by using the -3dB points and beam width as before, but by looking at the difference in magnitude between the peak values of the forward and backward main beams (N). The magnitude of the beam is due to the leakage of energy from the FSG as a mode travels along its length (L). This loss of energy is expressed as the attenuation per unit length. Hence the difference between the two beams is related to how much energy was lost from the guide, in the form of radiation, whilst it travels up and then back down the FSG. This assumes that the short circuit is a perfect reflector and that no energy is lost there. The equation governing the calculation of  $\alpha$  by this method is given in Equation 3-10.

$$\alpha = -\frac{\ln(10^{\frac{N}{10}})}{2L}$$

Equation 3-10

The equipment was set up as given in Figure 3-7, but with the matched termination replaced by the short circuit. All other set-up procedures were followed as before for the radiation pattern measurements. FSG 1 was measured and the resulting radiation patterns are shown in Figure 3-25; the FSG seam was again aligned to the polarisation vector of the TE<sub>11</sub> feed mode.

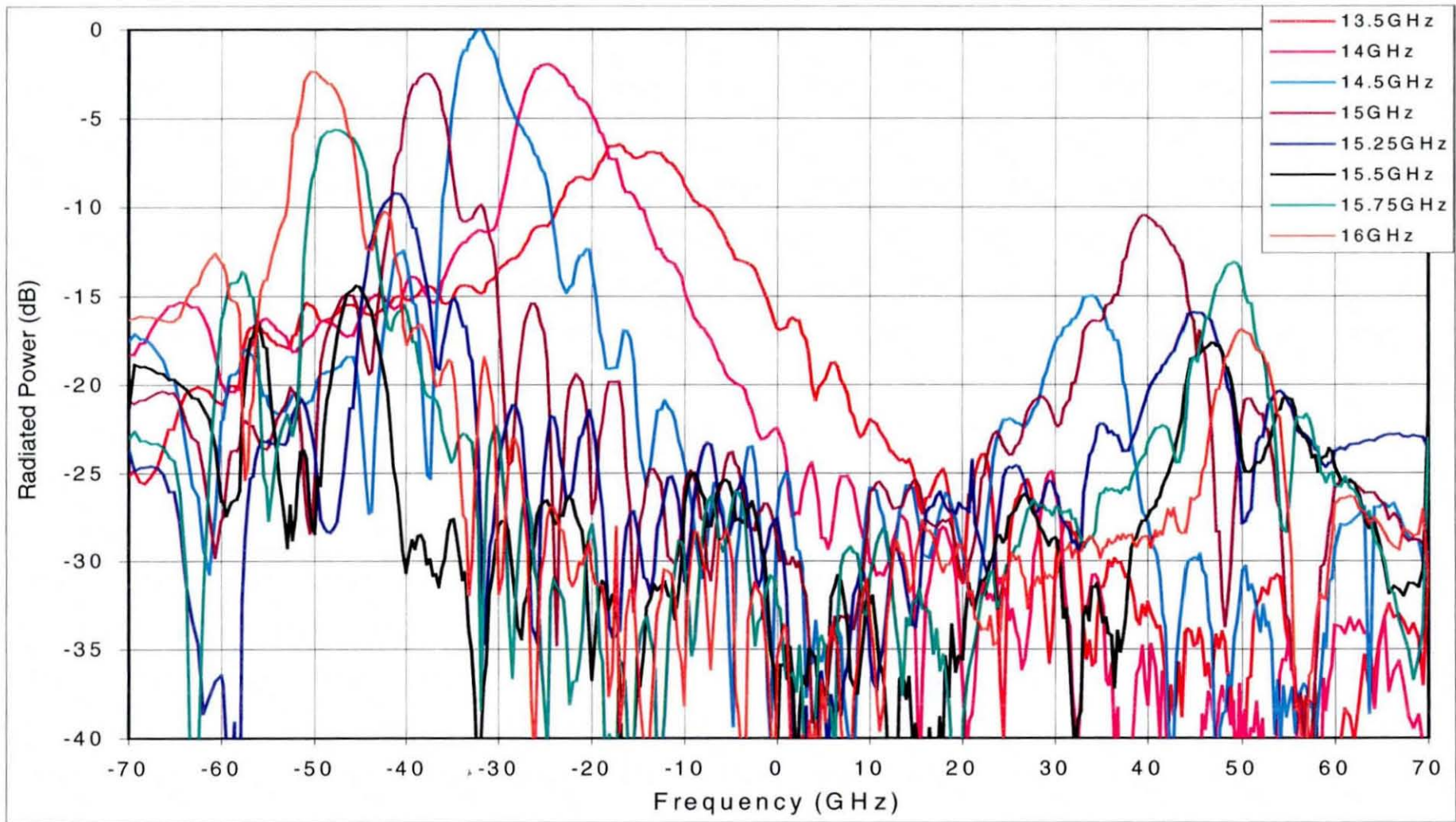


Figure 3-25 Short circuited radiation patterns for FSG 1 at different frequencies.

It is noticeable how the patterns have changed from Figure 3-8 with the addition of the short circuit. From 14GHz onward sufficient energy reaches the short circuit to be reflected back and form a leaky mode travelling in the opposite direction. The beams caused by the reflection are smaller mirror images of the forward main beams. The beam peaks do not occur at the same angle from  $0^\circ$  suggesting that the normal of the FSG is not correctly aligned, in this instance it is  $4^\circ$  out of alignment, but alignment is not required in this method. The reflected beams also follow the same behaviour as the main beams. They move away from the normal with increasing frequency and they increase in magnitude from the lowest frequency to a maximum and then reduce to a minimum at resonance before increasing again towards the maximum value and then reducing before they disappear.

Once this data was collected it was analysed with the aid of the MathCad package. The data was sorted to find the maximum beam angles and magnitudes in the forward and reverse direction for each frequency. From this the angle  $\theta_D$  between them and the difference in magnitude  $N$  was calculated. The  $\beta$  and  $\alpha$  values were calculated using Equation 3-9 & Equation 3-10 for each frequency. Once all the frequencies had been computed the  $\beta$  and  $\alpha$  plots were added to Figure 3-23 & Figure 3-24 to help ascertain which method of propagation constant calculation was best.

The frequency at which the  $TE_{11}$  line crosses the  $\beta$  plot calculated by the short circuit method is 15.2GHz. This is only 200MHz lower than that of the predicted resonance point. This is about the amount expected, from the earlier parameter study, for the dielectric loading on the manufactured FSG. The line is also reasonably parallel to the predicted plot although the relatively low number of points in each of these lines hampers an accurate measurement. The resonant frequency predicted by the crossing point on the  $\beta$  graph matches the resonant frequency implied by the minimum attenuation value on the  $\alpha$  graph, of 15.2GHz. This is the only method by which this occurs and thus matches the comparison in the predicted  $\beta$  and  $\alpha$  traces of Figure 3-23 & Figure 3-24. The difference in magnitude of  $1\text{neper/m}$  in the attenuation constant minimum value between the short method and the predicted is also far more acceptable. The increased level of the extracted value at  $2\text{neper/m}$  is far more likely to be purely due to the increased losses in the dielectric and the conductors. The fact that

all of these factors match only for the calculated propagation constants from the short circuited radiation pattern method suggests that it is the best method with which to do the extraction. The other methods are not reliable enough to be used to calculate the propagation constant with the equipment available.

#### 3.6.4 Summary of Calculation of $\alpha$ and $\beta$ .

The  $\alpha$  calculations based on the measured results show a minimum (resonance point) at 15.1GHz ( $S_{21}$  method) and 15.2GHz (short circuit method) while the simulation predicts a resonance at 15.4GHz. The beam angle method is so poor that a position of the resonance cannot be found. The variation from predicted to calculated value from the short circuit method can primarily be put down to the dielectric loading effect of the substrate. Apart from this the agreement is good, although the measured values are higher, 4nepers/m ( $S_{21}$  method) and 2nepers/m (short circuit method) than the prediction of 1nepers/m. It would be expected with dielectric and lossy metal being present that the calculated values would be higher. However the  $S_{21}$  estimate must be incorrect due to the junctions have not being taken into account. The values of  $\alpha$  obtained by the short circuit method are generally closer to the predicted values.

The three calculated values track the slope of the predicted  $\beta$  well and in terms of percentage values they are close to the predicted, with the short circuit method values being the closest. Calculated resonant frequencies from the point at which the TE<sub>11</sub> line is crossed vary from 14.7GHz (beam angle) through 15.2GHz (short circuit) to 15.9GHz ( $S_{21}$  method). This crossing point frequency for the short circuit method is the only one that matches the resonant frequency given by the  $\alpha$  value being a minimum. The variation in the value given by the beam angle method can be attributed to the set-up errors discussed earlier while the  $S_{21}$  method variance can be partly attributed to the effects of the transitions (FSG to solid guide), as discussed above for the  $\alpha$  results. More information on the extraction process can be found in [9] & [10].

### 3.7 Conclusions and Comments on FSG Measurements

This study has shown that, at some frequencies, reasonable guidance can be obtained from cylindrical FSGs with square resonators. However, the transmission losses are quite high. To use this technology for a commercial system the losses would need to be significantly reduced and the structure ruggedised. The poor transmission measured is partly due to mismatches at the transitions as well as leakage from the guiding system. The results here suggest that a route to reducing the leakage at resonance is to increase the number of resonators around the circumference of the FSG.

The effect of the dielectric substrate is obvious in terms of reduction of resonant frequency and increased loss. An increase in the number of resonators in the circumference gives improved guidance/less leakage. To make use of the FSG as a guiding structure either oversized FSGs or dielectrically loaded FSGs, which would reduce the radius to that of the feed while allowing more circumferential resonators, would be required.

The short circuit method gives improved accuracy for measurements of  $\alpha$  and  $\beta$ , but getting accurate readings around the resonant frequency is extremely difficult, particularly when a higher number of circumferential elements are used because of the very low power levels leaking from the guide. A more rugged, solid construction would allow the extraction of  $\alpha$  and  $\beta$  from the  $S_{21}$  parameters accurately even at frequencies where the leaky main beams do not exist.

Although the values of  $\alpha$  and  $\beta$  calculated from the short circuit method do not match the predicted ones exactly, they are close enough to provide strong support that the prediction program developed by Loukos [6] does provide accurate propagation constants for an infinite length of FSG. This confirmation of the accuracy of the prediction program means that the evaluation of the junction effect between the FSG and the solid feed guide can begin in earnest.



### 3.8 References

- [1] FDTD Analysis of a Metal-Strip-Loaded Dielectric Leaky-Wave Antenna – M.Chen, B.Houshmand, T.Itoh – IEEE A&P, Vol 45, No8, August 1997, p1294.
- [2] Radiation Characteristics of  $HE_{11}$  – Type Wave from Dielectric Rod Antenna with Periodic Surface – H.Kubo, K.Yamaguchi & I.Awai – IEEE A&P, Vol44, No8, August 1996, p1063.
- [3] A Spectral Domain Approach for Computing the Radiation Characteristics of a Leaky-Wave Antenna for Millimeter Waves – R.Mitra & R.Kastner – IEEE A&P, Vol29, No4, July 1981, p652. –
- [4] Direct Experimental confirmation of New leakage Effects on Open Dielectric Strip Waveguides – H. Shigesawa, M.Tsuji, J.S.Myung, S.T.Peng & A.A.Oliner, IEEE MTT-S Digest, 1983, p293.
- [5] Design considerations for Leaky-wave Antennas – I.J.Bahl & K.C.Gupta - Proc. IEE, Vol123, No 12, December 1976, p1302.
- [6] Propagation Characteristics of Cylindrical Frequency Selective Guides – G.I.Loukos – Ph.D. Thesis, Loughborough University, 1998.
- [7] Frequency Selective Surfaces – Analysis and Design - J.C.Vardaxoglou – Research Studies Press, Taunton, UK, 1997.
- [8] Field Theory of Guided Waves - R.E.Collin - McGraw-Hill, New York: 1960.
- [9] Study of Cylindrical resonant Structures Constructed from Frequency Selective Surfaces – J.C.Eade, R.D. Seager, G.J.Cox & J.C.Vardaxaglou – International Journal of Electronics, accepted Oct 2000.
- [10] A Study of Frequency Selective Waveguides (FSG) of Circular Cross Section - J.C.Eade, R.D. Seager, G.J.Cox & J.C.Vardaxaglou - 22<sup>nd</sup> Antenna Symposium, Queen Mary & Westfield College.

## 4. Transition Analysis by Mode Matching Method.

As with FSS there has been a great deal of work undertaken by many authors into the analyses of discontinuities that occur in the many forms of transmission line that exist. It was hoped that an existing waveguide junction model could provide a suitable method to act as a base from which the FSG discontinuity could be modelled, especially as one half of the junction is a solid waveguide. The intention is then to extend the theory so that the open structure on the other side of the junction is included. However, other methods used in open guiding structures other than waveguides should not be ruled out initially as it may be possible to start from an open structure discontinuity model and force one side of it to be a waveguide.

### 4.1 Existing Waveguide Junction Modelling Techniques

One of the earliest waveguide junction modelling methods used was approximation by the variational principle. Marcuvitz used this on the waveguide T-junction problem [1]. However this can only provide information about the dominant mode interactions at the junction. As the FSG is an open periodic structure, the interactions between many more modes must be found, which would not be possible with this technique. Therefore any solution that could be found by this method could only ever give a partial and incorrect approximation of the solid waveguide to FSG junction. It was felt that this method was not directly applicable to the junction problem under investigation.

An analytic Fourier Transform method [2] matches the transverse E and H fields at a waveguide 'T' junction in the frequency domain by using the Fourier transform of the junction continuity equation. For a more flexible solution it was decided that a numerical method would prove more versatile than an analytic one as less work would be required to develop it for new junction configurations.

Finite element and finite difference methods have been used where the geometry of the discontinuity becomes complex and/or inhomogeneous or anisotropic objects are

involved. In this method the region surrounding the discontinuity boundary is split into many polygonal sub-regions. These sub-regions are then used as points or areas at which the field calculations, dependent on the method, are performed. The appropriate boundary conditions are applied along with a suitable algorithm, used to find the solution as quickly as possible. It is used widely in the solution of rectangular waveguide junctions and [3],[4] are just two of the papers written on the subject, where only a two dimensional mesh of points needs to be generated. In the FSG discontinuity problem a three dimensional mesh of points would be required in the model to provide sufficient information to solve the required problem to a high degree of accuracy. This then demands a very large amount of computer memory to store the vast number of data values taken at each point.

The Least-Squares Boundary Residual Method (LSBRM), first proposed in [11], has been used to good effect in the solution of a five port rectangular waveguide junction [5]. This method forms a continuity equation of the transverse E and H fields expressed as a truncated series of waveguide modes. An error function is then formed by summing the product of each field, with its complex conjugate and integrating over the boundary. The coefficients are then found by finding the minimum unique value for this error function. Although this method does not suffer from any relative convergence problems, it does have a very slow convergence rate and so requires large matrices in order to achieve good accuracy, which again implies large computer memory requirements.

The method of moments has been applied to junctions by replacing the aperture fields with the equivalent imaginary magnetic current walls at the boundary [6],[7]. The method of moments and Galerkins approach are then used to solve for the fields on either side of the discontinuity. This method also requires large matrices to expand the currents as a series of bases functions, hence large memory, and also suffers from the relative convergence phenomenon.

The model that was chosen was the Modal Analysis Method. It was first proposed by Wexler [8] and Clarricoats and Slinn [9] and at the same time and has been used extensively to model these types of two dimensional waveguide discontinuities. In this approach the transverse fields are matched in each waveguide on either side of the

common connecting aperture. Each E and H field is expanded as an infinite series of normal waveguide mode functions that exist in the two respective waveguides. The amplitudes of each mode in the continuity equation across the junction are then expressed as an infinite series of waveguide mode amplitudes from the opposite side of the junction. This produces two infinite sets of simultaneous linear equations, which can be truncated and solved for the mode coefficients and from these the generalised scattering matrix formed. This method does suffer from relative convergence problems when the infinite series on each side of the waveguide are truncated, but this can be avoided with the correct choice of series sizes that are used. This produces matrices of modest size, and hence reasonable memory requirements, whilst maintaining a very high degree of accuracy. Therefore this method was chosen to model the FSG discontinuity.

In addition to the low memory requirements, the other great advantage of this method over other forms of transition modelling is that the amplitude of each mode in the each structure is known. If the amplitudes are known then it will be instantly possible to calculate which mode in the solid waveguide excites which FSG mode. This information will allow the determination of the most efficient method and design required to transfer maximum power into the FSG. As the FSG mode is a Bloch mode made from many Floquet modes then it may be that several solid waveguide modes will produce the best matched structure.

#### 4.2 Modal Analysis of Waveguide Step Junctions

After the original papers written by Wexler and Clarricoats and Slinn, many other papers have been written which build on and improve the method either generally or make it more applicable to a particular discontinuity situation. One such improvement was developed by Masterman and Clarricoats [10] and by Masterman alone in [19]. The method was improved to cope with infinitely thin conducting iris's placed in the junction plane and containing an arbitrary number of arbitrarily shaped apertures. By manipulation, the number of simultaneous equations needing to be solved was also reduced. This form of modal analysis was preferred as the basis of the solid waveguide to FSG discontinuity due to its simplified nature over the

original, thus requiring less computer memory. Also this method gave more flexibility as it allowed an intermediate matching section of modal basis functions to be inserted for the aperture fields. If this eventuality should arise the model could be easily expanded to incorporate it without the need for a major rewrite of the program.

The modal analysis proposed by Masterman is, as previously stated, concerned with the general case of an infinitely thin conducting iris placed at the junction of two different waveguide sections. As the initial investigation does not require the presence of the conducting iris, the theory quoted here shall be that of this simplified case. That is a step discontinuity junction between two dissimilar guiding structures of different cross sectional concentrically mounted. There are two possible junction set-ups for the solid waveguide to FSG discontinuity. The feed can either be from the FSG with reflection from the junction in the FSG and transmission into the solid waveguide calculated. Or the feed can be from the solid waveguide with reflection from the junction in the solid waveguide and transmission into the FSG calculated. Although the junction is reciprocal, it was found that the FSG fields had to be treated differently depending if it was the feed or not. These two cases will be handled separately in the following two sections.

#### 4.2.1 FSG to Solid Waveguide Mode Matching with FSG as Feed

With a large amount of the FSG eigen value spectrum found in Chapter 2, the mode matching theory can now be developed for the solid waveguide to FSG transition. As mentioned above mode matching works by expressing the fields in the aperture between the two structures as an infinite summation of all the possible modes that exist in the FSG. Each mode must have a particular amplitude such that the summation of all the modes equals the aperture field exactly. The aperture field is then expressed by a similar infinite summation of all the possible modes of the solid waveguide. The summations from each side of the aperture are then equated to each other and the unknown modal amplitudes solved from the simplification of the resulting simultaneous equations. The aperture of the junction between an infinite length of FSG and an infinite length solid circular waveguide is defined as being at  $z=0$ . The aperture fields can then be thought of as the summation of those modes in

the FSG taken at an infinitesimally small step into the FSG, in the  $-z$  direction, at a point  $z=0^-$ . Correspondingly the solid waveguide mode summation can be thought to take place at  $z=0^+$ .

The fact that the FSG is an open structure means that the fields beyond the radius  $r=r_0$  of the FSG elements must be taken into account and consequently so must the fields that will exist beyond the radius of the solid waveguide. This makes the problem very complicated as the solid waveguide wall is an annulus in cross section and divides the  $z=0^+$  region into two unconnected regions. To simplify the problem let the width of the solid waveguide wall be extended to infinity. The removal of this region from the field equations can also be achieved by placing an infinite conducting plane at  $z=0$  and cutting a hole in it, centred on the waveguide axis and of the same radius  $r=r_0'$  as the solid waveguide, as seen in Figure 4-1. This then prevents the fields from outside the FSG entering the region above the solid waveguide. This, it must be said, is not a perfect simplification as it will reflect propagating waves off it and hence the solution is only valid for junctions incorporating large conducting planes. However at this early stage it is hoped that this will allow a reasonable insight into the way the junction and model behaves.

It is assumed here that both guide structures are semi-infinite in the respective direction away from the junction. This ensures that there are no other discontinuities to reflect power back into the junction for any mode. This also ensures that the only incident modes are those of the feed, whose magnitudes are set at the start of the analysis. An alternative method of ensuring that no unwanted incident modes reach the junction is to say that a perfectly matched load terminates the structure on either side of the junction. If more junctions need to be modelled then the perfectly matched load terminations can be removed and several junctions can be cascaded together. A detailed procedure to do this is given in [19] and allows all the transmitted and reflected mode amplitudes to be calculated. For the FSG to solid waveguide junctions the analysis will be limited to calculating the amplitudes for a single junction with perfectly matched load terminations in place.

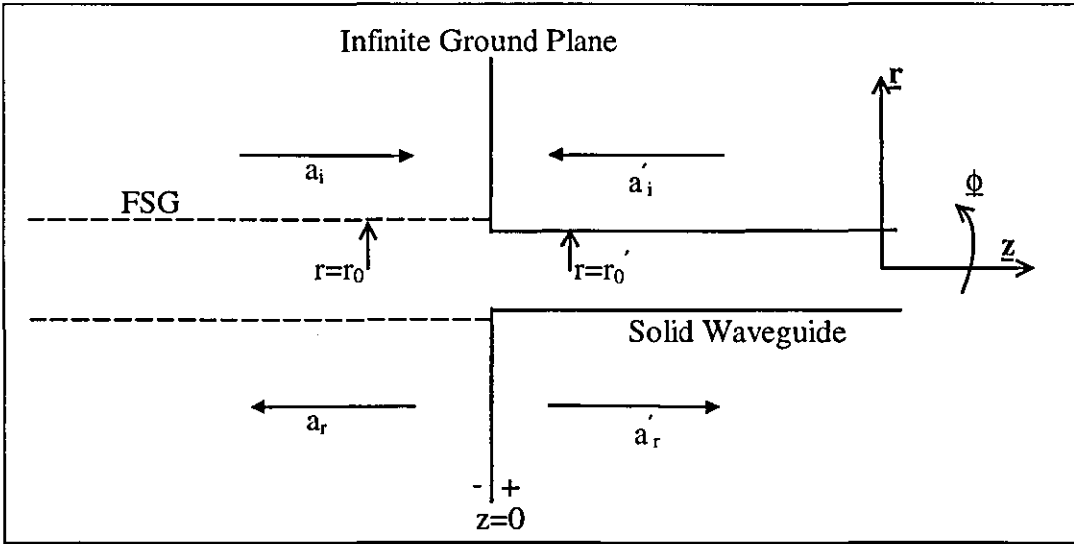


Figure 4-1 Set-up of FSG to solid waveguide transition – cross section through the  $\phi=0$  plane

To define the sum of FSG modes that gives the complete spectrum presents the greatest challenge for this method. The mode spectrum must consist of *all* the *real* modes of the structure. For an open structure, such as the FSG, this is the sum of Bloch waves that are formed entirely from real Floquet modes and the summation of the infinite radiation spectrum. See Equation 4-1 for the summation of the transverse E fields and Equation 4-2 for the summation of the transverse H fields.

$$E_t = \sum_{m=1}^{\infty} (a_{im} + a_{rm}) e_m^{HY} + \int_0^{\infty} (a_i^{rad}(k_r) + a_r^{rad}(k_r)) e^{rad}(k_r, r, \phi) \cdot dk_r$$

Equation 4-1

$$H_t = \sum_{m=1}^{\infty} (a_{im} - a_{rm}) h_m^{HY} + \int_0^{\infty} (a_i^{rad}(k_r) - a_r^{rad}(k_r)) h^{rad}(k_r, r, \phi) \cdot dk_r$$

Equation 4-2

where:-

$a_{im}$  &  $a_i^{rad}(k_r)$  are the modal coefficients in the FSG of Bloch modes and radiation modes respectively incident on (travelling towards) the junction.

$a_{rm}$  &  $a_r^{rad}(k_r)$  are the modal coefficients in the FSG of Bloch modes and radiation modes respectively reflected (travelling away) from the junction.

$e_m^{HY}, h_m^{HY}, e^{rad}, h^{rad}$  are the transverse electric and magnetic field components of the  $m^{\text{th}}$  hybrid Bloch mode and transverse components of the radiation field in the FSG respectively. The summation of the radiation modes becomes an integration over  $k_r$  because of the continuous nature of the infinite set and  $k_r$  is used rather than  $k_z$  as it is the transverse summation.

The integration of the radiation modes cannot be defined because the radiation spectrum of the FSG is not known and hence the total aperture field of the FSG can not be found. However as discussed in chapter 2 and proved in [24] & [26], a good approximation for the radiation fields close to the surface of an open structure is the field summation of the leaky modes of the structure. This approximation only holds to the boundary of the observation angle calculated by the steepest decent method in [24]. The steepest decent method also defines which leaky modes of the structure should be included in the summation, some leaky mode poles can be found in the complex  $k_r$  plane, but cannot be included in the physical approximation of the radiation field. The observation angle and the valid leaky mode contributors can not be calculated for the FSG because the modal solutions were found numerically and contain Floquet modes.

This problem was overcome with the aid of information in [25], Lee et al used mode matching to analyse the junction between two dielectric slab waveguides, both open structures. They approximated the radiation field integral in the aperture summations to a summation of leaky modes. They showed that the observation angle could be safely approximated by the angle of the main beam of each leaky mode in the summation. As already discussed in chapter 3 the angle of the main beam is proportional to the  $\beta_z$  value of the leaky mode propagation constant. Thus as the set of discrete propagation constants was found in chapter 2 the observation angles over which all the leaky modes are valid approximations is known.

It was also felt that initially if the frequency at which this matching program was run was restricted to values very close to the resonant frequency, then most of the field is contained within or very close to the FSG. If the vast majority of the field is in the vicinity of the FSG surface then intuitively the error in the approximation of the



radiation field must be reduced. There is less field that is not accounted for in the leaky modes within the angle of the main beam as most is within the FSG and [25] states that the field within the surface of the structure is very well defined by the leaky mode.

However the modes that should be used in the approximation are still not known and cannot be calculated. However [25] does state that in most cases the fundamental leaky mode will fully approximate the radiation field inside the observation angle. So the strategy adopted was that of a trial and error approach. The radiation field will initially be approximated by the fundamental leaky Bloch mode, which should be sufficient. If the resultant transmission and reflection coefficients did not match the measured results, then it will be assumed not to be sufficient and more leaky modes will be added. This approach is similar to that taken by Masterman [19] to get the correct number of modes in each aperture summation to overcome the relative convergence phenomenon. It is expected that as well as finding the correct number of leaky modes experimentally the total numbers of modes required in each guide to overcome the relative convergence phenomenon will also have to be deduced experimentally.

So when the radiation mode integral is replaced by a sum of leaky hybrid Bloch modes transverse aperture E and H fields can be approximated as a single summation of FSG hybrid Bloch [16] modes. Here no distinction is made between the leaky modes and real modes as they are all discrete solutions found in chapter [2] and so the two summations can be combined.

$$E_t \approx \sum_{m=1}^{\infty} (a_{im} + a_{rm}) e_m^{HY} \qquad H_t \approx \sum_{m=1}^{\infty} (a_{im} - a_{rm}) h_m^{HY}$$

Equation 4-3

The transverse aperture fields can also be expressed as a summed series of modes taken from the solid waveguide.

$$E_t' = \sum_{n=1}^{\infty} (a_{in}' + a_{rn}') e_n' \qquad H_t' = \sum_{n=1}^{\infty} (a_{in}' - a_{rn}') h_n'$$

Equation 4-4

where:-

$a_{im}$  &  $a'_{in}$  are the modal coefficients of modes incident on (travelling towards) the junction in the FSG and solid waveguide respectively.

$a_{rm}$  &  $a'_{rn}$  are the modal coefficients of modes reflected from (travelling away) the junction in the FSG and solid waveguide respectively.

$e_m^{HY}, h_m^{HY}, e'_n, h'_n$  are the transverse electric and magnetic field components of the  $m$ th hybrid Bloch mode (real or leaky) and  $n$ th mode in the FSG and solid waveguide respectively. The mode subscripts vary from  $m$  &  $n=1$  (the fundamental mode) to  $\infty$ . The FSG hybrid mode consists of a doubly infinite sum of Floquet modes over the integers  $p$  &  $q$  (each varies from  $-\infty$  to  $\infty$ ) which represent the Floquet mode number in the  $\phi$  and  $z$  directions respectively. Such that:-

$$e_m^{HY} = \sum_{p=-\infty}^{\infty} \sum_{q=-\infty}^{\infty} c_{mpq} e_{mpq} \quad h_m^{HY} = \sum_{p=-\infty}^{\infty} \sum_{q=-\infty}^{\infty} c_{mpq} h_{mpq}$$

Equation 4-5

N.B. in this work any quantity which is denoted with an apostrophe is one from the output guide, anything that has no apostrophe is from the input guide.

The transverse aperture field is equated to both of the infinite sums of transverse modes, one from the FSG and the other from the solid waveguide. As they can be taken to identically match the aperture field, a continuity equation of the transverse E and H fields across the junction can be formed.

$$E_t \approx E_{app} = E'_t = \sum_{m=1}^{\infty} (a_{im} + a_{rm}) e_m^{HY} \approx \sum_{n=1}^{\infty} (a'_{in} + a'_{rn}) e'_n$$

Equation 4-6

$$H_t \approx H_{app} = H'_t = \sum_{m=1}^{\infty} (a_{im} - a_{rm}) h_m^{HY} \approx \sum_{n=1}^{\infty} (a'_{in} - a'_{rn}) h'_n$$

Equation 4-7

Substituting the Floquet mode representation of the Hybrid E field in Equation 4-6 and then vector post-multiplying through by the basis function  $h'_N$ , being an  $N^{\text{th}}$  H mode transverse field function taken from the solid waveguide, gives:-

$$\sum_{m=1}^{\infty} (a_{im} + a_{rm}) \left( \sum_{p=-\infty}^{\infty} \sum_{q=-\infty}^{\infty} c_{mpq} e_{mpq} \right) \times h'_N \approx \sum_{n=1}^{\infty} (a'_{in} + a'_{rn}) e'_n \times h'_N$$

Equation 4-8

As vector cross products are distributive Equation 4-8 can be rearranged to give:-

$$\sum_{m=1}^{\infty} (a_{im} + a_{rm}) \sum_{p=-\infty}^{\infty} \sum_{q=-\infty}^{\infty} c_{mpq} (e_{mpq} \times h'_N) \approx \sum_{n=1}^{\infty} (a'_{in} + a'_{rn}) e'_n \times h'_N$$

Equation 4-9

Equation 4-9 can then be integrated over the area of the solid waveguide cross section,  $s'$ , to give:-

$$\sum_{m=1}^{\infty} (a_{im} + a_{rm}) \sum_{p=-\infty}^{\infty} \sum_{q=-\infty}^{\infty} c_{mpq} \int_{s'} e_{mpq} \times h'_N \cdot ds \approx \sum_{n=1}^{\infty} (a'_{in} + a'_{rn}) \int_{s'} e'_n \times h'_N \cdot ds$$

Equation 4-10

Where  $N$  can be used to represent the subscript of any waveguide mode from  $n = 1, 2, 3, \dots, \infty$  and therefore the basis function can be any solid waveguide mode.

When the orthogonality of the waveguide modes in the solid waveguide is applied to Equation 4-10, the right hand side of the equation can be simplified so that only non zero values are included in the summation. This occurs only when  $n=N$  i.e. for the mode in the summation that is identical to the basis function. All the other modes in the summation produce a zero value for the integration. N.B. Orthogonality does not apply to the integral on the left hand side of the equation as the mode functions are for a different guide and so are not solutions to Maxwell's equations under the same boundary conditions. Then the simplified equation becomes Equation 4-11.

$$a'_{iN} + a'_{rN} \approx \frac{\sum_{m=1}^{\infty} (a_{im} + a_{rm}) \sum_{p=-\infty}^{\infty} \sum_{q=-\infty}^{\infty} c_{mpq} \int_{s'} e_{mpq} \times h'_N \cdot ds}{\int_{s'} e'_N \times h'_N \cdot ds}$$

Where  $N = 1, 2, 3, \dots, \infty$

Equation 4-11

Waveguide orthogonality simply states that the vector product of the E field of any mode and the H field of any mode, that can exist in the **same** lossless waveguide (so that they are solutions of the same boundary conditions), when integrated over the cross sectional area of the waveguide will be zero, **unless** the E and H fields are from the same mode. The proof of this property of waveguide modes is explained on p225 in [14] and given in Equation 4-12.

$$\int_{s'} e_k \times h_l \cdot ds = \delta_{kl} \equiv \begin{cases} 0 & \text{for } k \neq l \\ 1 & \text{for } k = l \end{cases}$$

Equation 4-12

$$\int_0^{\infty} E_a \times H_b^* \cdot ds = \delta_{ab}$$

Equation 4-13

The orthogonality given in Equation 4-12 is more commonly seen as Equation 4-13 where the complex conjugate of the H field has been taken. This form of the orthogonality equation is likened to the calculation of the Poynting vector of a mode; it is the mode power orthogonality equation. Ideally, power orthogonality would be used because if two modes are power orthogonal then the fields do not interact and no power can flow between the modes. The field orthogonality given in Equation 4-12 does not imply that power cannot flow between two modes only that the fields do not interact. Marcuse on p30 of [18] details that complex propagation constants associated with the modal fields of open structures can only found to be orthogonal with the use of the field orthogonality equation, Equation 4-12. This equation will work equally well for solid enclosed waveguides, but again with the power orthogonality dropped.

It should be noted that if many different values of N are tried in Equation 4-11 one after another, N separate equations will be formed, each one having as its subject the incident and reflected amplitudes of that particular mode and not dependent on any other mode from the solid waveguide. If the dependence on the incident and reflected modal amplitudes of the FSG is removed then the equations could be solved for the amplitude of each solid waveguide mode in turn.

Returning to E field aperture equation a similar procedure must be applied to Equation 4-7, but this time pre-multiplying by the basis function of the  $M^{\text{th}}$  FSG mode  $e_M$ .

$$\sum_{m=1}^{\infty} (a_{im} - a_{rm}) e_M^{HY} \times h_m^{HY} \approx \sum_{n=1}^{\infty} (a'_m - a'_{in}) e_M^{HY} \times h'_n$$

Equation 4-14

Substituting the Floquet mode summation of Equation 4-5 for the FSG hybrid mode in Equation 4-14.

$$\sum_{m=1}^{\infty} (a_{im} - a_{rm}) \sum_{p=-\infty}^{\infty} \sum_{q=-\infty}^{\infty} c_{Mpq} e_{Mpq} \times \sum_{p=-\infty}^{\infty} \sum_{q=-\infty}^{\infty} c_{mpq} h_{mpq} \approx \sum_{n=1}^{\infty} (a'_m - a'_{in}) \left( \sum_{p=-\infty}^{\infty} \sum_{q=-\infty}^{\infty} c_{Mpq} e_{Mpq} \right) \times h'_n$$

Equation 4-15

To simplify Equation 4-15 the fact that vector cross products are distributive can be used. Instead of the two Floquet mode summations being vector multiplied together, each individual E Floquet mode is vector multiplied in turn with each of the H Floquet modes and all of the vector products are then summed together.

$$\sum_{m=1}^{\infty} (a_{im} - a_{rm}) \sum_{p=-\infty}^{\infty} \sum_{q=-\infty}^{\infty} c_{Mpq}^2 (e_{Mpq} \times h_{mpq}) \approx \sum_{n=1}^{\infty} (a'_m - a'_{in}) \sum_{p=-\infty}^{\infty} \sum_{q=-\infty}^{\infty} c_{Mpq} (e_{Mpq} \times h'_n)$$

Equation 4-16

As with Equation 4-10, Equation 4-16 can also be integrated over a cross section, Equation 4-18. However, this time it must be the cross section of the FSG which, as it

is an open structure, has an infinite cross sectional area. Some simplification can be made to the integration of the right hand side of Equation 4-16 as the transverse field of the solid waveguide does not exist beyond the radius of the waveguide wall. The integral over the cross sectional area outside must therefore vanish, Equation 4-17. Where  $S$  is the infinite cross sectional area over which the FSG integral is taken,  $S'$  is the cross sectional area of the waveguide and  $S_0 = S - S'$ , is the difference between them.

$$\int_{S_0} e_{Mpq} \times h'_n \cdot ds = 0$$

Equation 4-17

$$\sum_{m=1}^{\infty} (a_{im} - a_{rm}) \sum_{p=-\infty}^{\infty} \sum_{q=-\infty}^{\infty} c_{Mpq}^2 \int_S e_{Mpq} \times h_{mpq} \cdot ds \approx \sum_{n=1}^{\infty} (a'_{rn} - a'_{in}) \sum_{p=-\infty}^{\infty} \sum_{q=-\infty}^{\infty} c_{Mpq} \int_{S'} e_{Mpq} \times h'_n \cdot ds$$

Equation 4-18

In order to follow the mode matching form given by Masterman [19] Equation 4-18 must be simplified by applying the orthogonality conditions to the Floquet modes. However, the Floquet modes can either be real proper or improper leaky modes. Improper leaky modes cannot ordinarily be normalised or orthogonalised. The fields of a proper mode decay to zero as they approach infinity and so from the proof in [18] any proper mode of an open structure is orthogonal to any other proper mode. The fields of the improper leaky modes do not decay as they approach infinity, they increase, so they can never be orthogonal as the integral in Equation 4-12 cannot be defined.

However, Sammut & Snyder [26] offer two methods for approximating the orthogonality of leaky modes. The first is to truncate the leaky mode at some small distance from the guide where the mode will be finite and nearly power orthogonal. However, some small part of the mode will not be orthogonal and so some coupling between modes will occur. The second approximation is found by deforming the path of integration of the orthogonality condition into the imaginary radius space. That is

to say that as the real distance from the fiber core increases, an imaginary term that increases faster than the real term must be added to the radius value. The imaginary radius will then act to cancel out the increasing field strength of the leaky mode when the integral is evaluated. This form of orthogonality does lose the definition of power orthogonality. It is however an exact orthogonality condition that can be used on both proper and improper modes.

Lee [25] opts to use Sammut & Snyders first technique and sets the distance over which the orthogonality approximation is applied for the leaky modes to be the same as that of the observation angle. This has already been defined for the FSG as the main beam angle of the mode and the only area over which the leaky mode exists in this model. All the required techniques are assembled to simplify the mode matching equations and approximate the values of the mode coefficients. When applying the orthogonality condition to a leaky mode the radius of integration was reduced to the angle of the main beam, otherwise for a proper mode the upper limit of integration was left at infinity. The integrand was also in the form  $E \times H$  as the equations are still dealing with complex propagation values and  $E \times H^*$  will not work under these conditions.

For any Proper mode:-

$$\int_0^{2\pi\infty} \int_0 e_k \times h_l \cdot r dr d\phi = \delta_{kl} \equiv \begin{cases} 0 & \text{for } k \neq l \\ 1 & \text{for } k = l \end{cases}$$

Equation 4-19

For any leaky mode:-

$$\int_0^{2\pi r_{MB}} \int_0 e_k \times h_l \cdot r dr d\phi = \delta_{kl} \equiv \begin{cases} 0 & \text{for } k \neq l \\ 1 & \text{for } k = l \end{cases}$$

Equation 4-20

When the orthogonality conditions, Equation 4-19 & Equation 4-20, are applied to Equation 4-18 the equation is simplified to a form similar to Equation 4-11 and gives Equation 4-21.

$$a_{iM} - a_{rM} \approx \frac{\sum_{n=1}^{\infty} (a'_{rn} - a'_{in}) \sum_{p=-\infty}^{\infty} \sum_{q=-\infty}^{\infty} c_{Mpq} \int_{S'} e_{Mpq} \times h'_n \cdot ds}{\sum_{p=-\infty}^{\infty} \sum_{q=-\infty}^{\infty} c_{Mpq}^2 \int_{S'} e_{Mpq} \times h_{Mpq} \cdot ds}$$

Where  $M = 1, 2, 3, \dots, \infty$

Equation 4-21

There are now two infinite sets of linear simultaneous equations, given by Equation 4-11 & Equation 4-21. Obviously these two infinite sets must be truncated, so that they can be solved. Let the value of  $M$  range from 1 to  $M'$  and the value of  $N$  range from 1 to  $N'$ . The summations of FSG modes must also be truncated, so let  $m$  range from 1 to  $m'$  and  $n$  range from 1 to  $n'$ . So  $M'$  becomes the total number of FSG testing basis functions;  $N'$  becomes the total number of solid waveguide testing basis functions;  $m'$  becomes the total number of FSG modes and  $n'$  becomes the total number of solid waveguide modes. The infinite summation of Floquet modes must also be truncated, again the infinite summation can not be evaluated numerically. The first  $2P+1$  &  $2Q+1$  modes are taken, so the range becomes  $p=-P$  to  $P$  and  $q=-Q$  to  $Q$ . The large number of simultaneous equations they can be written in a concise matrix form, so Equation 4-11 becomes:-

$$\begin{bmatrix} a'_{i1} \\ \vdots \\ a'_{iN'} \end{bmatrix} + \begin{bmatrix} a'_{r1} \\ \vdots \\ a'_{rN'} \end{bmatrix} \approx \begin{bmatrix} R_{11} & \cdots & R_{1m'} \\ \vdots & & \vdots \\ R_{N'1} & \cdots & R_{N'm'} \end{bmatrix} \left( \begin{bmatrix} a'_{i1} \\ \vdots \\ a'_{im'} \end{bmatrix} + \begin{bmatrix} a'_{r1} \\ \vdots \\ a'_{rm'} \end{bmatrix} \right)$$

Equation 4-22

Where the elements of the matrix  $R$  are given by the equation:-

$$R_{ij} = \frac{\sum_{p=-P}^P \sum_{q=-Q}^Q c_{j pq} \int_{S'} (e_{j pq} \times h'_i) \cdot ds}{\int_{S'} e'_i \times h'_i \cdot ds}$$

Equation 4-23



Where  $i$  and  $j$  are the matrix row and column number of the particular  $R$  value being calculated. This matrix form can be written in compressed form for convenience as:-

$$\mathbf{a}'_i + \mathbf{a}'_r \approx \mathbf{R}(\mathbf{a}_i + \mathbf{a}_r)$$

Equation 4-24

Similarly the same treatment can be carried out on Equation 4-21:-

$$\begin{bmatrix} a_{i1}' \\ \vdots \\ a_{iM}' \end{bmatrix} - \begin{bmatrix} a_{r1}' \\ \vdots \\ a_{rM}' \end{bmatrix} \approx \begin{bmatrix} S_{11} & \cdots & S_{1n'} \\ \vdots & & \vdots \\ S_{M1} & \cdots & S_{Mn'} \end{bmatrix} \left( \begin{bmatrix} a_{r1}' \\ \vdots \\ a_{rm}' \end{bmatrix} - \begin{bmatrix} a_{i1}' \\ \vdots \\ a_{in}' \end{bmatrix} \right)$$

Equation 4-25

Where the elements of the matrix  $S$  are given by the equation:-

$$S_{ij} = \frac{\sum_{p=-P}^P \sum_{q=-Q}^Q c_{ipq} \int_s e_{ipq} \times h_j' \cdot ds}{\sum_{p=-P}^P \sum_{q=-Q}^Q c_{ipq}^2 \int_s e_{ipq} \times h_{ipq}' \cdot ds}$$

Equation 4-26

Which can be written in compressed form for convenience as:-

$$\mathbf{a}_i - \mathbf{a}_r \approx \mathbf{S}(\mathbf{a}'_r - \mathbf{a}'_i)$$

Equation 4-27

This system of simultaneous equations can be simplified by matrix pre-multiplying Equation 4-24 by  $\mathbf{S}$ . It can then be rearranged and substituted into Equation 4-27 for  $\mathbf{S}\mathbf{a}'_r$ , eliminating it from the equations. The resulting set of simultaneous linear equations can then be solved for  $\mathbf{a}_r$ , given that the incident mode coefficients  $\mathbf{a}_i$  &  $\mathbf{a}'_i$  are already known:-

$$\mathbf{a}_i - \mathbf{a}_r \approx \mathbf{S}\mathbf{R}\mathbf{a}_i + \mathbf{S}\mathbf{R}\mathbf{a}_r - 2\mathbf{S}\mathbf{a}'_i$$

Equation 4-28

Which is rearranged to give:-

$$(\mathbf{I} + \mathbf{SR})\mathbf{a}_r \approx (\mathbf{I} - \mathbf{SR})\mathbf{a}_i + 2\mathbf{S}\mathbf{a}_i'$$

Equation 4-29

To make  $\mathbf{a}_r$  the subject of the equation, it is necessary to matrix pre-multiply the equation by the inverse of  $\mathbf{I} + \mathbf{SR}$ .

$$\mathbf{a}_r \approx (\mathbf{I} + \mathbf{SR})^{-1}(\mathbf{I} - \mathbf{SR})\mathbf{a}_i + 2(\mathbf{I} + \mathbf{SR})^{-1}\mathbf{S}\mathbf{a}_i'$$

Equation 4-30

If the inverse of  $\mathbf{I} + \mathbf{SR}$  is to be found then  $\mathbf{SR}$  must be a square, non singular matrix. If the matrix product  $\mathbf{SR}$  is to be square then the number of basis functions in the FSG must be the same as the number of FSG modes chosen to represent the aperture field,  $M' = m'$ . Similarly the number of basis functions in the solid waveguide must be the same as the number of solid waveguide modes chosen to represent the aperture field,  $N' = n'$ .

The values of  $M'$  and  $N'$  relative to each other will be investigated. For solid waveguides [10] shows that this method can suffer from the relative convergence phenomenon. The degree and speed at which the mode matching method converges is dependent not only on the number of modes used in each guide, but also on their ratio. In [10] Masterman details a procedure allowing the correct numbers of waveguide modes to be used in each guide to ensure that the numerical solution converges with the least number of modes. To determine the optimum ratio, the normalised susceptance of the discontinuity was plotted against  $M$  for different ratios of  $M'/N'$ . This gave the ratio of the number of basis functions in each waveguide, for the most rapid convergence of the solution, equal to the ratio of the waveguide radius', see Equation 4-31. If a different ratio is used then more modes will be required in each guide to get convergence.

$$\frac{M'}{N'} = \frac{r_0}{r_0'}$$

Equation 4-31

Once the values of  $a_r$  have been found then the values of  $a'_r$  can be found by substituting  $a_r$  into Equation 4-24 to give:-

$$a'_r \approx \mathbf{R}(a_i + a_r) - a_i$$

Equation 4-32

The above theory shows how the values of the coefficients of the modes scattered from the FSG to solid waveguide junction can be approximated. These coefficients can be used to calculate the scattering parameters of the junction and to determine how the modes make the transition from one structure to the next.

#### 4.2.2 Solid Waveguide to FSG Mode Matching with Solid Waveguide as Feed

For the solid waveguide to FSG transition, a similar procedure to that detailed in section 4.2.1 is employed. The diagram in Figure 4-2 shows the junction to be modelled. In this instance the FSG is not the feed structure and all items related to it are denoted with an apostrophe. The solid waveguide is the feed structure and all items related to it have no dash. Again both structures are assumed to have perfectly matched load terminations and the incident coefficients are known for all the waveguide modes.

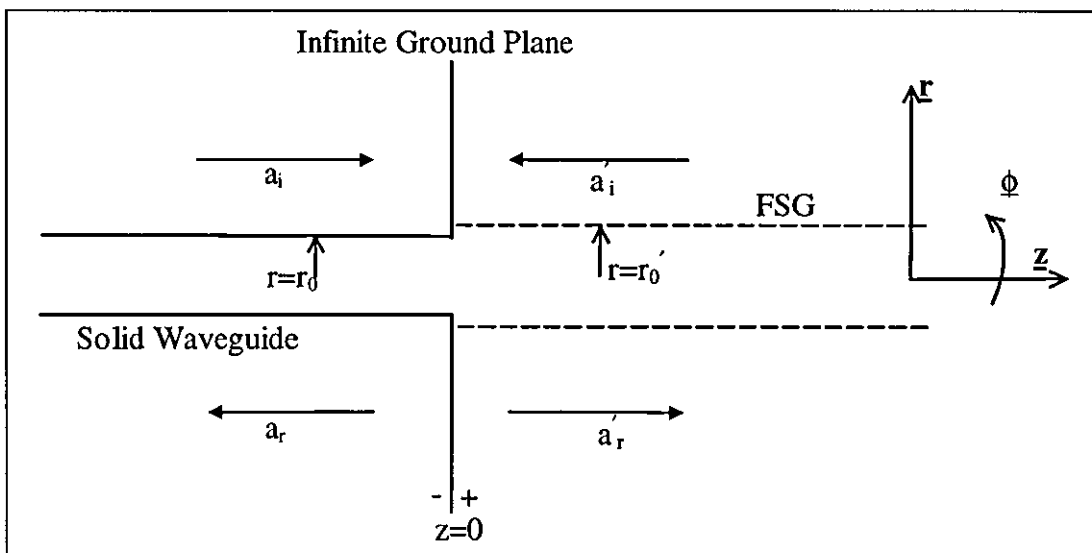


Figure 4-2 Solid waveguide to FSG transition – cross section through the  $\phi=0$  plane

In the above diagram  $a_i$  and  $a_r$  represent the modal field amplitudes of the modes incident on and reflected from the junction in the solid waveguide. Similarly  $a'_i$  and  $a'_r$  represent the modal field amplitudes of the modes incident on and reflected from the junction in the FSG. As in Equation 4-5 the transverse aperture fields can be expressed as a summation of modes from each structure that forms the junction. These two summations can be equated to each other and here the hybrid FSG mode is given as the summation of it's Floquet modes:-

$$E_{app}^T = E^{T-} = E^{T+} = \sum_{m=1}^{\infty} (a_{im} + a_{rm}) e_m = \sum_{n=1}^{\infty} (a'_{in} + a'_{rn}) \sum_{p=-\infty}^{\infty} \sum_{q=-\infty}^{\infty} c_{npq} e'_{npq}$$

Equation 4-33

$$H_{app}^T = H^{T-} = H^{T+} = \sum_{m=1}^{\infty} (a_{im} - a_{rm}) h_m = \sum_{n=1}^{\infty} (a'_{rn} - a'_{in}) \sum_{p=-\infty}^{\infty} \sum_{q=-\infty}^{\infty} c_{npq} h'_{npq}$$

Equation 4-34

where  $m$  is the mode number in the solid waveguide,  $e_m$  is the transverse electric modal field distribution of the  $m^{\text{th}}$  mode and  $h_m$  is the transverse magnetic modal field distribution of the  $m^{\text{th}}$  mode in the solid waveguide.  $n$  is the mode number of distinct Bloch modes (not Floquet) in the FSG and  $p$  and  $q$  number the Floquet modes that exist in the  $\phi$  and  $z$  directions for a particular Bloch mode.  $e'_{npq}$  is the transverse electric modal field distribution of the  $n^{\text{th}}$  eigen mode solution and  $p^{\text{th}}$  and  $q^{\text{th}}$  Floquet modes and  $h'_{npq}$  is the transverse magnetic modal field distribution of the  $n^{\text{th}}$  eigen mode and the  $p^{\text{th}}$  and  $q^{\text{th}}$  Floquet modes in the FSG.

To simplify the magnetic field equation of Equation 4-34 vector pre-multiply through by an e mode basis function from the solid waveguide and integrate over the infinite plane at  $z=0$ . This process is identical to that employed in Equation 4-21 except that the guide on the feed side of the junction is solid waveguide and so a solid waveguide basis function is used.

$$a_{im} - a_{rm} = \frac{\sum_{n=1}^N (a'_{rn} - a'_{in}) \sum_{p=-P}^P \sum_{q=-Q}^Q c_{npq} \int_S e_M \times h'_{npq} \cdot ds}{\int_S e_M \times h_M \cdot ds}$$

Equation 4-35

The cross-sectional area of the solid waveguide is  $S$ , the integral outside this region is zero. The summation of Floquet modes has been truncated to only include the most significant  $2P+1$  and  $2Q+1$ . As in Equation 4-21 the number of hybrid Bloch modes in the FSG has been truncated to  $N$  and  $M$  basis functions were used to test the solid waveguide modes. This then generates  $M$  simultaneous equations which can again be expressed in matrix form as:-

$$\begin{bmatrix} a_{i1} \\ \vdots \\ a_{iM} \end{bmatrix} - \begin{bmatrix} a_{r1} \\ \vdots \\ a_{rM} \end{bmatrix} = \begin{bmatrix} S_{11} & \cdots & S_{1n} \\ \vdots & & \vdots \\ S_{M1} & \cdots & S_{Mn} \end{bmatrix} \left( \begin{bmatrix} a'_{r1} \\ \vdots \\ a'_m \end{bmatrix} - \begin{bmatrix} a'_{i1} \\ \vdots \\ a'_{in} \end{bmatrix} \right)$$

Equation 4-36

where the elements  $[S]$  are given by:-

$$S_{ij} = \frac{\sum_{p=-P}^P \sum_{q=-Q}^Q c_{j pq} \int_s e_i \times h'_{j pq} \cdot ds}{\int_s e_i \times h_i \cdot ds}$$

Equation 4-37

To simplify the electric field equation it is necessary to follow a procedure similar to that given in Equation 4-14. Vector post multiply Equation 4-33 by the testing function  $h_N^{HY}$  of the magnetic field of  $N^{\text{th}}$  Bloch mode in the FSG. The Floquet mode summation has again been substituted for the Bloch mode in Equation 4-38.

$$\sum_{m=1}^{\infty} (a_{im} + a_{rm}) e_m \times \sum_{p=-\infty}^{\infty} \sum_{q=-\infty}^{\infty} c_{Npq} h'_{Npq} = \sum_{n=1}^{\infty} (a'_{in} + a'_{rn}) \left( \sum_{p=-\infty}^{\infty} \sum_{q=-\infty}^{\infty} c_{npq} e'_{npq} \right) \times \left( \sum_{p=-\infty}^{\infty} \sum_{q=-\infty}^{\infty} c_{Npq} h'_{Npq} \right)$$

Equation 4-38

If the cumulative vector product simplification similar to that in Equation 4-16 is carried out and the equation is integrated over the infinite cross sectional area  $s'$  on the plane at  $z=0$  the result is Equation 4-39.

$$\sum_{m=1}^{\infty} (a_{im} + a_{rm}) \sum_{p=-\infty}^{\infty} \sum_{q=-\infty}^{\infty} c_{Npq} \int_S e_m \times h'_{Npq} \cdot ds = \sum_{n=1}^{\infty} (a'_{in} + a'_{rn}) \sum_{p=-\infty}^{\infty} \sum_{q=-\infty}^{\infty} c_{npq}^2 \int_S e'_{npq} \times h'_{npq} \cdot ds$$

Equation 4-39

Following the procedure used in Section 4.2.1, Equation 4-39 would now be simplified by the orthogonality conditions to produce a system of N simultaneous equations. However the partial radius orthogonality condition is only valid out to the radius of the main beam. In this case the radius of the main beam is zero as the junction plane is the source of the FSG modes. If the junction is the source of the FSG modes then the approximations used in [24],[25] & [26], that the radiation field is approximated by the leaky mode summation, break down. If the approximation breaks down then the fact that the leaky modes are not orthogonal is no longer important as the entire analysis for the solid waveguide to FSG junction is invalid. This junction model will not be taken any further, but the FSG to solid waveguide model will be implemented.

### 4.3 Development of Mode Matching Program

Throughout the development of the program to implement the mode matching theory detailed in Section 4.2.1, a structured software engineering design methodology was used. This allowed the program development to be broken up into several distinct sections: definition of program functions and requirements; conversion of functions and requirements into a conceptual data flow diagram; conversion of data flow diagram into a structure chart that depicts the program elements; coding the program and testing the program to ensure it meets the design. Although more time is spent designing the program before any code is written, this makes the task a simpler one as it separates the creative design of the program to meet the functions required, from coding the algorithms. Once coding starts it is simply a matter of concentrating on the syntax of converting the design of the program in the structure chart into the computer language. The code produced is also of a high quality as the structure chart drives the program to be written in a well formatted and structured way so that at any point it is easy to derive the functionality from the code, unreadable “spaghetti code” is avoided.

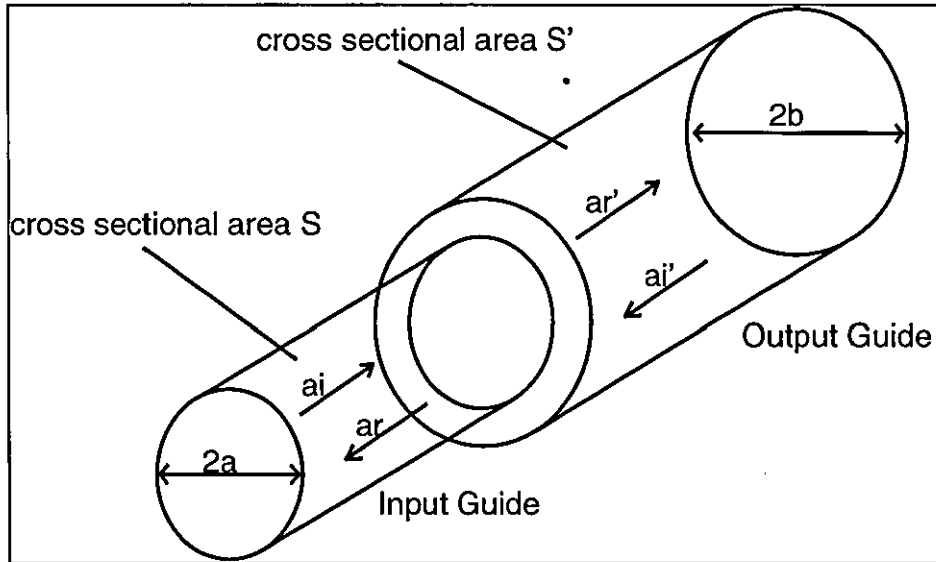
It also improves the testing of the program as the design documents generated in the initial stages give a clear definition of how the program is to function. Simple test data can be build up from the design documents and the expected answers calculated. This can then be fed into the program and the results compared to ensure that the program functions as expected.

This software engineering approach also proved invaluable during the lifetime of the project as it significantly speeded up any required alteration of the program to change the functionality. The change can be made to the data flow diagram and then fed into the structure chart and so the relevant areas of the program that need changing are easily identified. It is then a simple matter to change the program code to reflect the change in the structure chart. Over the duration of the project the use of the software design approach undoubtedly saved time and improved understanding of the program operation.

#### 4.3.1 Solid Waveguide Step Discontinuity Program

To develop a good understanding of the mode matching method it was felt that an initial computer model should be written to replicate the simple case of a step discontinuity between two solid circular waveguides. The solid waveguides had different radii, which formed the step in the plane of the junction as seen in Figure 4-3. The extra insight gained into the design and development of the code to achieve the simple case would give a stable, workable platform on which to base the FSG junction work. This work gave valuable experience and insight into the details of the mode matching analysis technique.

The mode matching method implemented for the solid circular waveguide step junction was that of Masterman as detailed in [19]. The equations and theory formulated in [19] were transformed via the structured software engineering approach into a data flow diagram and a structure chart of the design. The program was then coded to the design, which was implemented in a highly modular way, to make future development easier, and tested.



Once the program was tested an example was tried for which published results were available. The results of the percentage of transmitted and reflected power given in [12] were replicated to a very high degree of agreement and are shown in Figure 4-4. To further test the validity of the results given by the program, good agreement with other published work was found. The results given in [19] and [10] were emulated with some simple post processing of the mode amplitudes to get the values in the correct format of the mode conversion coefficient. This gave an indication as to how much of the fundamental input mode was converted into a higher order mode in the output waveguide. Again the results from the program, written with the structured software design procedure, was a good match to that given in [10].

#### 4.3.2 FSG to Solid Waveguide Mode Matching Program

The solid waveguide mode matching modelling program can be changed so that it calculates the mode amplitudes at the FSG to solid waveguide junction. This was achieved by changing the software design and then the program. The mode matching theory relies on taking the integrals of the vector cross products in order to simplify the equations. The integration process can be achieved in two ways, either by a numerical integration routine or else with a predetermined integrated analytic



equation. The numerical integration process takes the integral and using many numerical samples over the integration range calculates by successive approximation the value of the integral. The accuracy and time taken to carry it out is dependent on the number of steps in the approximation process, however there is some degree of flexibility with this process as the integrand expression can be changed to reflect changes in the transition structure.

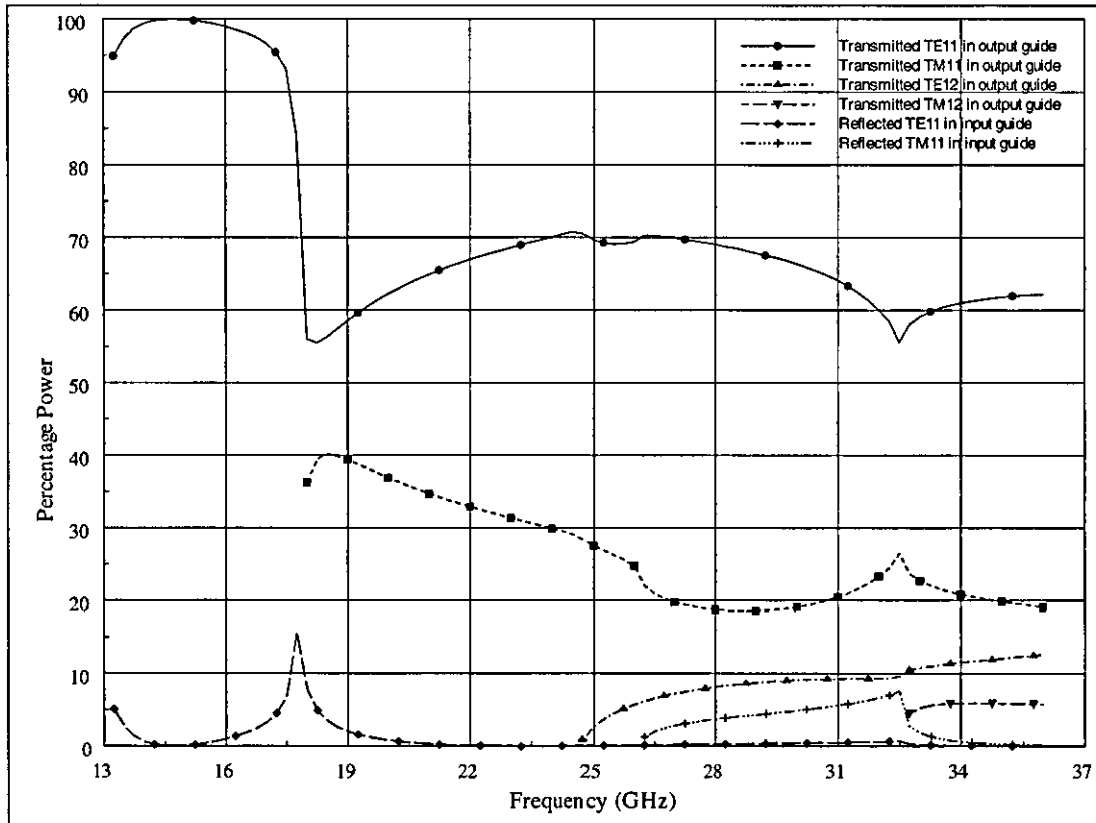


Figure 4-4 Percentage power transmitted through and reflected from the step discontinuity, for circular waveguides with a radius ratio of  $b/a=1.47$  &  $a=7\text{mm}$

The alternative requires the vector cross product of the fields to be pre-calculated. The integral is then derived analytically and an equation that gives the value of the integral from the input program variables is “hard coded” into the program. It is absolutely accurate and is very quick to execute, however there is no flexibility to change the structure under investigation, as the program is limited to solving only one problem. To change the setup of the problem to be simulated requires a change to the program code. It is also not always possible to integrate an expression analytically; if this should be the case for a particular problem then a numerical method must be used. As there already exists expressions for the definite integrals where the integrand is

formed from both fields in the solid waveguide, it was decided to solve analytically the integrals involving FSG fields. Despite the lack of flexibility, the accuracy and speed of execution in the analytical approach make it the most desirable as there are many modes, with a large number of these being made up of many Floquet modes.

### 4.3.3 Solid Waveguide Integrals

The solid waveguide integrals are given in [19], but were calculated by the author for the previous solid waveguide step junction. There are two forms of the solid waveguide integral equation used in the denominator of the  $R$  matrix, depending on whether the mode in the integrand is TE or TM. The transverse field equations used to represent the E and H fields in the solid waveguide for the TE and TM mode are Equation 4-40 & Equation 4-41. As all the fields are time dependent as  $e^{j\omega t}$  this factor is assumed in all field equations and has been dropped from the written forms given here.

For TE modes:-

$$e_r = \frac{n}{k_c r} J_n(k_c r) \sin(n\phi) \quad h_r = -\frac{\beta}{\omega\mu} J'_n(k_c r) \cos(n\phi)$$

$$e_\phi = J'_n(k_c r) \cos(n\phi) \quad h_\phi = \frac{n}{k_c r} \frac{\beta}{\omega\mu} J_n(k_c r) \sin(n\phi)$$

Equation 4-40

$$\text{Where } k_c = \frac{j_{nm}}{a} \quad \& \quad j_{nm} \text{ is the } m^{\text{th}} \text{ zero of } J_n$$

For TM modes-

$$e_r = -J'_n(k_c r) \cos(n\phi) \quad h_r = -\frac{n}{k_c r} \frac{\omega\epsilon}{\beta} J_n(k_c r) \sin(n\phi)$$

$$e_\phi = \frac{n}{k_c r} J_n(k_c r) \sin(n\phi) \quad h_\phi = -\frac{\omega\epsilon}{\beta} J'_n(k_c r) \cos(n\phi)$$

Equation 4-41

Where  $k_c = \frac{j'_{nm}}{a}$  &  $j'_{nm}$  is the  $m^{\text{th}}$  zero of  $J'_n$

For a TE mode in the Waveguide:-

$$\int_s \mathbf{e}_t \times \mathbf{h}_t \cdot ds = \frac{\omega\mu}{\beta} \int_s \left( \frac{n^2}{k_c^2 r^2} J_n^2(k_c r) \sin^2(n\phi) + J_n'^2(k_c r) \cos^2(n\phi) \right) \cdot ds$$

Equation 4-42

When the order of the mode is zero,  $n=0$  then by Lommel's equation, given in Reilton [23] p.52 and applying the simplification that  $J'_0(k_c a) = 0$  for TE modes, Equation 4-42 becomes:-

$$\int_s \mathbf{e}_t \times \mathbf{h}_t \cdot ds = \frac{a^2 \omega\mu\pi}{\beta} J_1'^2(k_c a)$$

Equation 4-43

When the order of the mode is non zero,  $n>0$  then applying an integration method similar to that given in Waldron [22] p.58 and the simplification that  $J'_n(k_c a) = 0$  for TE modes, Equation 4-42 becomes:-

$$\int_s \mathbf{e}_t \times \mathbf{h}_t \cdot ds = \frac{a^2 \omega\mu\pi}{2\beta} \left( 1 - \frac{n^2}{k_c^2 a^2} \right) J_n^2(k_c a)$$

Equation 4-44

N.B. It was found by carrying out the above integration that the integral formula given in Waldron p.58 has a misprint, the correct form is quoted here.

For a TM mode in the waveguide:-

$$\int_s \mathbf{e}_t \times \mathbf{h}_t \cdot ds = \frac{\omega\epsilon}{\beta} \int_s \left( \frac{n^2}{k_c^2 r^2} J_n^2(k_c r) \sin^2(n\phi) + J_n'^2(k_c r) \cos^2(n\phi) \right) \cdot ds$$

Equation 4-45

When the order of the mode is zero, n=0 then by Lommel's equation given in Relton [23] p.52 and applying the simplification that  $J_0(k_c a) = 0$  for TM modes, Equation 4-45 becomes:-

$$\int_s \mathbf{e}_t \times \mathbf{h}_t \cdot ds = \frac{a^2 \omega \epsilon \pi}{\beta} \left( J_1'^2(k_c a) + \left( 1 - \frac{1}{k_c^2 a^2} \right) J_1^2(k_c a) \right)$$

Equation 4-46

When the order of the mode is non zero, n>0 then applying an integration method similar to that given in Waldron [22] p.58 and the simplification that  $J_n(k_c a) = 0$  for TM modes, Equation 4-45 becomes:-

$$\int_s \mathbf{e}_t \times \mathbf{h}_t \cdot ds = \frac{a^2 \omega \epsilon \pi}{2\beta} J_n'^2(k_c a)$$

Equation 4-47

#### 4.3.4 FSG Integral Equations

Apart from these solid waveguide integral expressions, there are two other integrals, which must be evaluated. The integral of the vector cross product, where both the E and H transverse fields are from the FSG, exist in the denominator of the elements of the S matrix in Equation 4-26. This integral appears similar to that used to normalise proper modes, however, as improper modes are contained in the integrand it is not a normalisation integral. However, this integral will be referred to as the “FSG normalisation” integral for want of a better description, even though it is understood that it is not. The other integral forms the numerator of both the S and R matrices and has transverse E fields from the FSG and transverse H fields from the solid waveguide. This integral will be referred to as the “across junction” integral and has two forms, the type of H field mode in the integrand, TE or TM, determines which one should be used and both forms will be derived.

The analytic process for evaluating a definite integral involving the  $p^{\text{th}}$  &  $q^{\text{th}}$  Floquet mode of the  $n^{\text{th}}$  Bloch wave of the FSG is given here. The transverse hybrid field equations of the of the  $p^{\text{th}}$  &  $q^{\text{th}}$  Floquet mode of the  $n^{\text{th}}$  Bloch wave of the FSG are given in [20]. The field equations quoted in [20] are for general circularly polarised modes where the field value is proportional  $e^{jn_p\phi}$ . However, the equipment used to make the measurements in chapter 3, to which this analysis will be compared, can only excite linearly polarised modes. Therefore the transverse field equations used inside the FSG from [20] have been converted into linearly polarised form and given in Equation 4-48.

$$\begin{aligned}
 e_{rnpq} &= -\frac{n_p \tilde{b}}{r} J_{n_p}(k_{rq}r) \cos(n_p \phi) e^{-jk_{zq}z} - \frac{k_{rq} k_{zq} \tilde{a}}{\omega \epsilon} J'_{n_p}(k_{rq}r) \cos(n_p \phi) e^{-jk_{zq}z} \\
 e_{\phi npq} &= k_{rq} \tilde{b} J'_{n_p}(k_{rq}r) \sin(n_p \phi) e^{-jk_{zq}z} + \frac{nk_{zq} \tilde{a}}{\omega \epsilon r} J_{n_p}(k_{rq}r) \sin(n_p \phi) e^{-jk_{zq}z} \\
 h_{rnpq} &= -\frac{n_p \tilde{a}}{r} J_{n_p}(k_{rq}r) \sin(n_p \phi) e^{-jk_{zq}z} - \frac{k_{rq} k_{zq} \tilde{b}}{\omega \mu} J'_{n_p}(k_{rq}r) \sin(n_p \phi) e^{-jk_{zq}z} \\
 h_{\phi npq} &= -k_{rq} \tilde{a} J'_{n_p}(k_{rq}r) \cos(n_p \phi) e^{-jk_{zq}z} - \frac{n_p k_{zq} \tilde{b}}{\omega \mu r} J_{n_p}(k_{rq}r) \cos(n_p \phi) e^{-jk_{zq}z}
 \end{aligned}$$

Equation 4-48

To make the calculation of the integral simpler it was found to be necessary to alter the value of the coefficients  $\tilde{a}$  &  $\tilde{b}$  which determine the amount of TE of TM component in the hybrid mode. These coefficients were replace with the coefficients A & B and are related to each other by the equation:-

$$A = \frac{\omega \cdot \epsilon \cdot \tilde{a}}{k_{rq}} \quad \& \quad B = \frac{\omega \cdot \mu \cdot \tilde{b}}{\eta_0 k_{rq}}$$

Equation 4-49

Such that the transverse field equations inside the FSG  $r \leq r_0$  become:-

$$\begin{aligned}
 e_{rnpq} &= \left[ -\frac{k_{zq}A}{\omega\epsilon} J'_{n_p}(k_{rq}r) \cos(n_p\phi) - \frac{n_p B}{k_{rq}r} J_{n_p}(k_{rq}r) \cos(n_p\phi) \right] e^{-jk_{zq}z} \\
 e_{\phi npq} &= \left[ \frac{n_p k_{zq}A}{\omega\epsilon k_{rq}r} J_{n_p}(k_{rq}r) \sin(n_p\phi) + B J'_{n_p}(k_{rq}r) \sin(n_p\phi) \right] e^{-jk_{zq}z} \\
 h_{rnpq} &= \left[ -\frac{n_p A}{k_{rq}r} J_{n_p}(k_{rq}r) \sin(n_p\phi) - \frac{k_{zq}B}{\omega\mu} J'_{n_p}(k_{rq}r) \sin(n_p\phi) \right] e^{-jk_{zq}z} \\
 h_{\phi npq} &= \left[ -A J'_{n_p}(k_{rq}r) \cos(n_p\phi) - \frac{n_p k_{zq}B}{\omega\mu k_{rq}r} J_{n_p}(k_{rq}r) \cos(n_p\phi) \right] e^{-jk_{zq}z}
 \end{aligned}$$

Equation 4-50

The transverse field equations outside the FSG  $r > r_0$  become:-

$$\begin{aligned}
 e_{rnpq} &= \left[ -\frac{k_{zq}A}{\omega\epsilon} \frac{J_{n_p}(k_{rq}a)}{H_{n_p}^{(2)}(k_{rq}a)} H_{n_p}'^{(2)}(k_{rq}r) \cos(n_p\phi) - \frac{n_p B}{k_{rq}r} \frac{J'_{n_p}(k_{rq}a)}{H_{n_p}'^{(2)}(k_{rq}a)} H_{n_p}^{(2)}(k_{rq}r) \cos(n_p\phi) \right] e^{-jk_{zq}z} \\
 e_{\phi npq} &= \left[ \frac{n_p k_{zq}A}{\omega\epsilon k_{rq}r} \frac{J_{n_p}(k_{rq}a)}{H_{n_p}^{(2)}(k_{rq}a)} H_{n_p}^{(2)}(k_{rq}r) \sin(n_p\phi) + B \frac{J'_{n_p}(k_{rq}a)}{H_{n_p}'^{(2)}(k_{rq}a)} H_{n_p}'^{(2)}(k_{rq}r) \sin(n_p\phi) \right] e^{-jk_{zq}z} \\
 h_{rnpq} &= \left[ -\frac{n_p A}{k_{rq}r} \frac{J_{n_p}(k_{rq}a)}{H_{n_p}^{(2)}(k_{rq}a)} H_{n_p}^{(2)}(k_{rq}r) \sin(n_p\phi) - \frac{k_{zq}B}{\omega\mu} \frac{J'_{n_p}(k_{rq}a)}{H_{n_p}'^{(2)}(k_{rq}a)} H_{n_p}'^{(2)}(k_{rq}r) \sin(n_p\phi) \right] e^{-jk_{zq}z} \\
 h_{\phi npq} &= \left[ -A \frac{J_{n_p}(k_{rq}a)}{H_{n_p}^{(2)}(k_{rq}a)} H_{n_p}'^{(2)}(k_{rq}r) \cos(n_p\phi) - \frac{n_p k_{zq}B}{\omega\mu k_{rq}r} \frac{J'_{n_p}(k_{rq}a)}{H_{n_p}'^{(2)}(k_{rq}a)} H_{n_p}^{(2)}(k_{rq}r) \cos(n_p\phi) \right] e^{-jk_{zq}z}
 \end{aligned}$$

Equation 4-51

In Equation 4-51 the Bessel function,  $J_n$ , which describes the field with respect to  $r$  is replaced by a Hankel function of the second kind. They are both cylindrical functions with the Bessel function representing fields that are standing waves and the Hankel function represents fields that exist to infinity. The sign of the complex  $k_{rq}$  value will determine whether the field is proper, improper, propagating or evanescent.

#### 4.3.4.1 Integration of the “FSG normalisation” Equation

As there are two separate sets of equations that describe the FSG fields in each region the integral for each region can be handled separately. So concentrating on the fields inside the FSG, where  $r \leq r_0$  the “FSG normalisation” integral  $\int_s e_{npq} \times h_{npq} \cdot ds$  can be evaluated to give an analytic expression for the integration. As the fields are solely transverse, the integral can be written as Equation 4-52.

$$\int_s e_{npq} \times h_{npq} \cdot ds = \int_{\phi=0}^{2\pi} \int_{r=0}^{r_0} (e_{rnpq} \cdot h_{\phi npq} - e_{\phi npq} \cdot h_{rnpq}) \cdot r dr d\phi$$

Equation 4-52

The field dependence on  $e^{-jk_{zq}z}$  is dropped from all subsequent equations as it is a factor in all the equations and so is assumed. Substituting the transverse field equations into Equation 4-52, the equation becomes:-

$$\begin{aligned} \int_s e_{npq} \times h_{npq} \cdot ds = & \int_{\phi=0}^{2\pi} \int_{r=0}^{r_0} \left( \left( -\frac{k_{zq}A}{\omega\epsilon} J'_{n_p}(k_{rq}r) \cos(n_p\phi) - \frac{n_p B}{k_{rq}r} J_{n_p}(k_{rq}r) \cos(n_p\phi) \right) \right. \\ & \cdot \left( -AJ'_{n_p}(k_{rq}r) \cos(n_p\phi) - \frac{n_p k_{zq} B}{\omega\mu k_{rq}r} J_{n_p}(k_{rq}r) \cos(n_p\phi) \right) \\ & - \left( \frac{n_p k_{zq} A}{\omega\epsilon k_{rq}r} J_{n_p}(k_{rq}r) \sin(n_p\phi) + BJ'_{n_p}(k_{rq}r) \sin(n_p\phi) \right) \\ & \left. \cdot \left( -\frac{n_p A}{k_{rq}r} J_{n_p}(k_{rq}r) \sin(n_p\phi) - \frac{k_{zq} B}{\omega\mu} J'_{n_p}(k_{rq}r) \sin(n_p\phi) \right) \right) \cdot r dr d\phi \end{aligned}$$

Equation 4-53

Multiplying out the brackets of Equation 4-53 and simplifying the terms gives:-

$$\int_s \mathbf{e}_{npq} \times \mathbf{h}_{npq} \cdot d\mathbf{s} = \int_{\phi=0}^{2\pi} \int_{r=0}^{r_0} \left( \frac{A^2 k_{zq}}{\omega \epsilon} \left( J'_{n_p}(k_{rq} r) \cos^2(n_p \phi) + \frac{n_p^2}{k_{rq}^2 r^2} J_{n_p}^2(k_{rq} r) \sin^2(n_p \phi) \right) \right. \\ \left. + \frac{B^2 k_{zq}}{\omega \mu} \left( J'_{n_p}(k_{rq} r) \sin^2(n_p \phi) + \frac{n_p^2}{k_{rq}^2 r^2} J_{n_p}^2(k_{rq} r) \cos^2(n_p \phi) \right) \right. \\ \left. + \frac{AB n_p}{k_{rq} r} J_{n_p}(k_{rq} r) J'_{n_p}(k_{rq} r) \right. \\ \left. \left( \sin^2(n_p \phi) + \cos^2(n_p \phi) + \frac{k_{zq}^2}{\omega \epsilon \mu} (\sin^2(n_p \phi) + \cos^2(n_p \phi)) \right) \right) \cdot r dr d\phi$$

Equation 4-54

It is easy to carry out the integration in Equation 4-54 with respect to  $\phi$ . As the hybrid mode can never have a zero order, the integral over 0 to  $2\pi$  of  $\sin^2(n_p \phi)$  or  $\cos^2(n_p \phi)$  is always  $\pi$ . This leads to further simplification of Equation 4-54 to give:-

$$\int_s \mathbf{e}_{npq} \times \mathbf{h}_{npq} \cdot d\mathbf{s} = \pi \int_{r=0}^{r_0} \left( \left( \frac{A^2 k_{zq}}{\omega \epsilon} + \frac{B^2 k_{zq}}{\omega \mu} \right) \left( J'_{n_p}(k_{rq} r) + \frac{n_p^2}{k_{rq}^2 r^2} J_{n_p}^2(k_{rq} r) \right) \right. \\ \left. + \frac{2AB n_p}{k_{rq} r} J_{n_p}(k_{rq} r) J'_{n_p}(k_{rq} r) \left( 1 + \frac{k_{zq}^2}{\omega \epsilon \mu} \right) \right) \cdot r dr$$

Equation 4-55

Making use of the same identity used to integrate the solid waveguide field equations and the fact that the last term in Equation 4-55 is the integration of the product of a function and its differential, gives:-



$$\int_s e_{npq} \times h_{npq} \cdot ds = \pi \left[ \left( \frac{A^2 k_{zq}}{\omega \epsilon} + \frac{B^2 k_{zq}}{\omega \mu} \right) \left( J_{n_p}'^2(k_{rq} r) + \frac{2}{k_{rq} r} J_{n_p}(k_{rq} r) J_{n_p}'(k_{rq} r) \right) + \left( 1 - \frac{n_p^2}{k_{rq}^2 r^2} \right) J_{n_p}^2(k_{rq} r) \frac{r^2}{2} + \frac{AB n_p}{k_{rq}^2} J_{n_p}^2(k_{rq} r) \left( 1 + \frac{k_{zq}^2}{\omega \epsilon \mu} \right) \right]$$

Equation 4-56

Therefore the analytical integral equation for the fields inside the FSG is:-

$$\int_s e_{npq} \times h_{npq} \cdot ds = \pi \left[ \left( \frac{A^2 k_{zq}}{\omega \epsilon} + \frac{B^2 k_{zq}}{\omega \mu} \right) \left( J_{n_p}'^2(k_{rq} r_0) + \frac{2}{k_{rq} r_0} J_{n_p}(k_{rq} r_0) J_{n_p}'(k_{rq} r_0) \right) + \left( 1 - \frac{n_p^2}{k_{rq}^2 r_0^2} \right) J_{n_p}^2(k_{rq} r_0) \frac{r_0^2}{2} + \frac{AB n_p}{k_{rq}^2} J_{n_p}^2(k_{rq} r_0) \left( 1 + \frac{k_{zq}^2}{\omega \epsilon \mu} \right) \right]$$

Equation 4-57

By a similar procedure the integral involving the fields external to the FSG can be calculated. However, the integrated equation differs depending on whether the Floquet mode being integrated is a proper or improper mode. This is purely because the integration limits have to be altered if it is an improper mode. The integration limits of a proper mode are from  $r=r_0$  to  $r=\infty$ , however, an improper mode cannot, by definition, be integrated to infinity as the integral is divergent. An artificial upper integration limit can be set at the boundary of the region where the leaky mode approximates the radiation field as discussed in section 4.2.1, so the integrated equation for proper modes is:-

$$\int_s \mathbf{e}_{npq} \times \mathbf{h}_{npq} \cdot d\mathbf{s} = \pi \left( \left( \frac{A^2 J_{n_p}^2(k_{rq} r_0) k_{zq}}{\omega \epsilon H_{n_p}^{(2)2}(k_{rq} r_0)} + \frac{B^2 J_{n_p}'^2(k_{rq} r_0) k_{zq}}{\omega \mu H_{n_p}'^{(2)2}(k_{rq} r_0)} \right) \right. \\ \left. \left( H_{n_p}'^{(2)2}(k_{rq} r_0) + \frac{2}{k_{rq} r_0} H_{n_p}^{(2)}(k_{rq} r_0) H_{n_p}'^{(2)}(k_{rq} r_0) + \left( 1 - \frac{n_p^2}{k_{rq}^2 r_0^2} \right) H_{n_p}^{(2)2}(k_{rq} r_0) \right) \frac{r_0^2}{2} \right. \\ \left. + \frac{AB n_p J_{n_p}(k_{rq} r_0) J_{n_p}'(k_{rq} r_0)}{k_{rq}^2 H_{n_p}^{(2)}(k_{rq} r_0) H_{n_p}'^{(2)}(k_{rq} r_0)} H_{n_p}^{(2)2}(k_{rq} r_0) \left( 1 + \frac{k_{zq}^2}{\omega \epsilon \mu} \right) \right)$$

Equation 4-58

The integrated equation for improper modes with the artificial integration limit set to

$r=r_e$  :-

$$\int_s \mathbf{e}_{npq} \times \mathbf{h}_{npq} \cdot d\mathbf{s} = \pi \left( \left( \frac{A^2 J_{n_p}^2(k_{rq} r_0) k_{zq}}{\omega \epsilon H_{n_p}^{(2)2}(k_{rq} r_0)} + \frac{B^2 J_{n_p}'^2(k_{rq} r_0) k_{zq}}{\omega \mu H_{n_p}'^{(2)2}(k_{rq} r_0)} \right) \right. \\ \left( H_{n_p}'^{(2)2}(k_{rq} r_e) + \frac{2}{k_{rq} r_e} H_{n_p}^{(2)}(k_{rq} r_e) H_{n_p}'^{(2)}(k_{rq} r_e) + \left( 1 - \frac{n_p^2}{k_{rq}^2 r_e^2} \right) H_{n_p}^{(2)2}(k_{rq} r_e) \right) \frac{r_e^2}{2} \\ - \left( \left( H_{n_p}'^{(2)2}(k_{rq} r_0) + \frac{2}{k_{rq} r_0} H_{n_p}^{(2)}(k_{rq} r_0) H_{n_p}'^{(2)}(k_{rq} r_0) + \left( 1 - \frac{n_p^2}{k_{rq}^2 r_0^2} \right) H_{n_p}^{(2)2}(k_{rq} r_0) \right) \frac{r_0^2}{2} \right) \\ \left. + \frac{AB n_p J_{n_p}(k_{rq} r_0) J_{n_p}'(k_{rq} r_0)}{k_{rq}^2 H_{n_p}^{(2)}(k_{rq} r_0) H_{n_p}'^{(2)}(k_{rq} r_0)} \left( 1 + \frac{k_{zq}^2}{\omega \epsilon \mu} \right) \left( H_{n_p}^{(2)2}(k_{rq} r_e) - H_{n_p}^{(2)2}(k_{rq} r_0) \right) \right)$$

Equation 4-59

#### 4.3.4.2 Integration of the “Across Junction” Equation

The “across junction” integral that appears in the numerator of both the  $S$  matrix, in Equation 4-26, and the  $R$  matrix, in Equation 4-23, is the vector cross product of the  $\mathbf{E}$  field from the FSG and the  $\mathbf{H}$  field from the solid waveguide. As solid waveguide modes are involved as seen in Section 4.3.2, the expression must be calculated for both the TE and TM waveguide modes. The first integral equation given will be that for the interaction of the hybrid FSG mode with the TE mode in the solid waveguide,

followed by the integral for the TM mode. The integral that must be evaluated can be written, using the notation of the  $R$  &  $S$  matrices, as Equation 4-60.

$$\int_{S'} (e_{mpq} \times h'_n) \cdot ds = \int_{\phi=0}^{2\pi} \int_{r=0}^{r_0'} (e_{rmpq} h'_{\phi n} - e_{\phi mpq} h'_{rn}) \cdot r dr d\phi$$

Equation 4-60

Where  $e_{mpq}$  is the hybrid E field  $p^{\text{th}}$  and  $q^{\text{th}}$  Floquet modes of the  $m^{\text{th}}$  Bloch mode in the FSG with  $e_{rmpq}$  and  $e_{\phi mpq}$  the radial and circumferential field components of the mode. Also,  $h'_n$  is the H field of the  $n^{\text{th}}$  mode of the solid waveguide with  $h'_{rn}$  and  $h'_{\phi n}$  the radial and circumferential field components of the mode. Substituting the component field values given in Equation 4-50 for the FSG & in Equation 4-40 the TE mode of the solid waveguide into Equation 4-60 gives:-

$$\int_{S'} (e_{mpq} \times h'_n) \cdot ds = \int_{\phi=0}^{2\pi} \int_{r=0}^{r_0'} \left( \left( -\frac{k_{zq} A}{\omega \epsilon} J'_{m_p}(k_{rq} r) \cos(m_p \phi) - \frac{m_p B}{k_{rq} r} J_{m_p}(k_{rq} r) \cos(m_p \phi) \right) \right. \\ \left. \left( \frac{nk'_z}{\omega \mu k_c r} J_n(k_c r) \sin(n\phi) \right) - \left( \frac{m_p k_{zq} A}{\omega \epsilon k_{rq} r} J_{m_p}(k_{rq} r) \sin(m_p \phi) + B J'_{m_p}(k_{rq} r) \sin(m_p \phi) \right) \right) \\ \left( -\frac{k'_z}{\omega \mu} J'_n(k_c r) \cos(n\phi) \right) \cdot r dr d\phi$$

Equation 4-61

When Equation 4-61 is expanded the terms will contain functions of either  $\cos(m_p \phi) \sin(n\phi)$  or  $\sin(m_p \phi) \cos(n\phi)$ . It can easily be shown that regardless of the values of  $m_p$  and  $n$ , when either of these functions is integrated over the interval  $[0, 2\pi]$  the result is zero. In order to get a non-zero result the integrand should be of the form  $\sin^2(x)$  or  $\cos^2(x)$ . This can be achieved by rotating the linear polarisation vector of the solid waveguide mode through  $90^\circ$ . This will add a  $\pi/2$  factor to the solid waveguide sin and cos functions to give  $\sin(n\phi + \pi/2)$  and  $\cos(n\phi + \pi/2)$ . Using trigonometrical identities these can be simplified to  $\sin(n\phi + \pi/2) = \cos(n\phi)$  and  $\cos(n\phi + \pi/2) = \sin(n\phi)$ . Further if the value of  $m_p = n$  then the trigonometrical functions in the integrand will be of the form  $\sin^2(n\phi)$  or  $\cos^2(n\phi)$  and the integral will

equal  $\pi$ , as the order of the hybrid mode can never be zero. Applying the rotation of the TE polarisation vector and the condition that, for a non-zero result the order of the FSG Floquet mode must equal the order of the solid waveguide TE mode,  $m_p = n$ , giving:-

$$\int_{S'} (e_{mpq} \times h_n') \cdot ds = \int_{\phi=0}^{2\pi} \int_{r=0}^{r_0'} \left( -\frac{Ank_{zq}k_z'}{\omega^2 \epsilon \mu k_c k_{rq} r} (k_{rq} J_n'(k_{rq} r) J_n(k_c r) \cos^2(n\phi) + k_c J_n(k_{rq} r) J_n'(k_c r) \sin^2(n\phi)) - \frac{Bk_z'}{\omega \mu} \left( J_n'(k_{rq} r) J_n'(k_c r) \sin^2(n\phi) + \frac{n^2}{k_c k_{rq} r^2} J_n(k_{rq} r) J_n(k_c r) \cos^2(n\phi) \right) \right) \cdot r dr d\phi$$

Equation 4-62

Carrying out the integration with respect to  $\phi$  Equation 4-62 becomes:-

$$\int_{S'} (e_{mpq} \times h_n') \cdot ds = \pi \int_{r=0}^{r_0'} \left( -\frac{Ank_{zq}k_z'}{\omega^2 \epsilon \mu k_c k_{rq} r} \left( \frac{k_{rq} J_n'(k_{rq} r) J_n(k_c r)}{r} + \frac{k_c J_n(k_{rq} r) J_n'(k_c r)}{r} \right) - \frac{Bk_z'}{\omega \mu} \left( J_n'(k_{rq} r) J_n'(k_c r) + \frac{n^2}{k_c k_{rq} r^2} J_n(k_{rq} r) J_n(k_c r) \right) \right) \cdot r dr$$

Equation 4-63

To integrate Equation 4-63 with respect to  $r$  an identity used in the “across junction” integration of the solid waveguide step discontinuity program of section 4.3.1 is used; it is also given on p237 of [22]. This identity gives the integrated equation for the second term in Equation 4-63. The first term was integrated by noticing that  $J_n'(ax)J_n(bx) + J_n(ax)J_n'(bx)$  is the differential of  $J_n(ax)J_n(bx)$  when differentiated with respect to  $x$  by the UV method. Thus the integral equation of Equation 4-63 becomes:-

$$\int_{S'} (e_{mpq} \times h_n') \cdot ds = \pi \int_0^{r_0'} \left[ -\frac{Ank_{zq}k_z'}{\omega^2 \epsilon \mu k_c k_{rq}} J_n(k_{rq} r) J_n(k_c r) - \frac{Bk_z'}{\omega \mu} \left( \frac{k_c r J_n'(k_{rq} r) J_n(k_c r) - k_{rq} r J_n(k_{rq} r) J_n'(k_c r)}{k_c^2 - k_{rq}^2} \right) \right]$$

Equation 4-64

Which when evaluated over the interval  $[0, r_0]$ , the “across junction” integral between the FSG and solid waveguide TE mode becomes:-

$$\int_S (e_{mpq} \times h_n) \cdot ds = \pi \left( -\frac{Ank_{zq}k'_z}{\omega^2 \epsilon \mu k_c k_{rq}} J_n(k_{rq}r_0) J_n(k_c r_0) - \frac{Bk'_z}{\omega \mu} \left( \frac{k_c r_0 J'_n(k_{rq}r_0) J_n(k_c r_0) - k_{rq} r_0 J_n(k_{rq}r_0) J'_n(k_c r_0)}{k_c^2 - k_{rq}^2} \right) \right)$$

Equation 4-65

For a TM mode in the solid waveguide Equation 4-61 is re-written as Equation 4-66. It should be noted in Equation 4-66 that as long as  $|m_p|=n$  then the  $\phi$  integration will be non-zero. No manipulation of the TM polarisation vector is required to achieve this non-zero result.

$$\int_S (e_{mpq} \times h_n) \cdot ds = \int_{\phi=0}^{2\pi} \int_{r=0}^{r_0} \left( \left( -\frac{k_{zq}A}{\omega \epsilon} J'_{m_p}(k_{rq}r) \cos(m_p \phi) - \frac{m_p B}{k_{rq}r} J_{m_p}(k_{rq}r) \cos(m_p \phi) \right) \left( -\frac{\omega \epsilon}{k'_z} J'_n(k_c r) \cos(n\phi) \right) - \left( \frac{m_p k_{zq}A}{\omega \epsilon k_{rq}r} J_{m_p}(k_{rq}r) \sin(m_p \phi) + B J'_{m_p}(k_{rq}r) \sin(m_p \phi) \right) \left( -\frac{n \omega \epsilon}{k_c r k'_z} J_n(k_c r) \sin(n\phi) \right) \right) \cdot r dr d\phi$$

Equation 4-66

Following the same integration steps as given for the TE mode, the integration of the TM mode over the cross sectional area of the solid waveguide is given by Equation 4-67.

$$\int_S (e_{mpq} \times h_n) \cdot ds = \pi \left( \frac{Bn\omega \epsilon}{k'_z k_c k_{rq}} J_n(k_{rq}r_0) J_n(k_c r_0) + \frac{Ak_{zq}}{k'_z} \left( \frac{k_c r_0 J'_n(k_{rq}r_0) J_n(k_c r_0) - k_{rq} r_0 J_n(k_{rq}r_0) J'_n(k_c r_0)}{k_c^2 - k_{rq}^2} \right) \right)$$

Equation 4-67

#### 4.3.5 Structure of Program

With the integral equations evaluated and available in an analytical format the program design was possible. The design was developed on a computer based CASE tool, in this instance EASYCASE Pro 4.21. This allowed different levels of the design to be built up graphically. Descending to a lower level allowed more graphical diagrammatic detail to be given about an item in the design. At the lowest level a text description of the operation is given. This top down approach, split into levels, allows the outline of the whole program and sub-sections of it to be given more detail at each level. The CASE tool ensures that changes made at the more detailed levels of one sub-section are fed back up to the top levels and cascaded down into other sub-sections that may be affected by the change. In Appendix A all the design diagrams are listed in descending level order, in the CASE tool they would pop up when the higher level object is clicked upon. The text details have been collated and listed after the diagrams in a similar order.

The data flow diagram, see Appendix A, of the program converts the theory of section 4.2.1 into a segmented logical structure. The segments are arranged such that the data flowing between them will produce the desired result, in this case the mode coefficients. This also allows the data requirements of the program to be analysed. The data that is required for each operation in the segmented theory can be easily identified. This allows all the variable declarations of the program to be made and to ensure that all the input data is available. The data inputs to the program are also given in the text description section of the data flow diagram.

The basic structure of the program is to initially assemble all the required information with which to operate. This is via data files containing constants and the zeros of the Bessel functions for the calculation of the solid waveguide propagation constants. A file formatted from the output of the altered Loukos program containing all the information on the FSG propagation constants and the values A & B of the relative strength of the TE and TM mode components. Also, a control file containing all other required parameters and the information needed to ensure the program will execute as desired.

The next stage is to calculate the values of the integrals for each mode combination using the expressions calculated previously. Summing the integrated values of the relevant “across junction” modes and dividing by the lower “normalisation” integral value then forms the elements of the R and S matrix. These matrices are multiplied together, the unit matrix is added and the resulting matrix is inverted. The values of the coefficients can then be found after some further simple matrix manipulation.

The structure chart of the program was then developed from the data flow diagram, with a few elements evolving from the stepped discontinuity in the solid waveguide design. The structure chart breaks the data flow diagram down further and is a graphical representation of the program structure. It shows where decision points and loops are required and a word description of the exact operation of each small section of code. The structure chart is included in Appendix A after the data flow diagram. Again the structure chart, like the data flow diagram, is hierarchical. The top most level breaks the program into its basic functions. Then each successive level adds more detail to each item until the program is almost written in a type of pseudo computer language. However this is far easier to write with no attention paid to the syntax, because it is not the actual computer language, the focus can be placed on getting the functionality correct. As with the data flow diagram the CASE tool allows each level of chart to be accessed by clicking on the object. All the charts have been placed in Appendix A in descending order and all the text information has been collated after the diagrams.

#### 4.4 Program Testing & Results.

The testing strategy was designed to ensure that the program worked at all stages and to build confidence in the results that it produced. Once the program was written the theory was rechecked for accuracy in the equations used and their manipulation. The conversion of the theory into the data flow diagram and then into the structure chart was desk checked and “walked through” to ensure that it produced the desired information correctly. The program was then cross-checked with the structure chart to ensure that the code matched the design.

The structure chart was studied to identify the crucial areas of the program. These consisted not only of the expressions and the values that they produced, but also key decision points, i.e. points that governed the number of time the program went around a summation loop, or whether it had identified the correct solid waveguide mode. A set of limited test data was then drawn up that would test these crucial areas. If the test data ran through all the decision points and gave the correct answers then the probability that the program was working correctly was very high. The test data was not limited in the variety of values and mode types used, but just in the number of modes and Floquet modes executed. The reason for this being that, for each mode in the test data, all the results had to be calculated manually, with the aid of a mathematical calculation program called MathCad. The manual calculations being taken directly from the theory and not from the program. If the program and manual results matched, this ensured that the program was working correctly. The manual calculations also provided all the interim answers at each stage of the calculation process, which could be compared against the program step by step to pin point where any incorrect value might have been generated.

The number of Floquet modes was limited to just the fundamental for each of the FSG modes, purely because of the length of time taken to carry out the manual calculations. To ensure that the Floquet mode processing was tested, a separate set of data was developed. This consisted of one mode in the FSG, but with +/- five Floquet modes in both the p and q Floquet indices. Five modes were present in the solid waveguide, each one with a different mode order value, in order to test the “across junction” integral equations where  $|m_p|=n$ .

Once the program results for the test cases have been thoroughly checked against the manual calculations then the next stage of testing is to identify the number of leaky modes required to get a good approximation to the radiation field. This can only be done experimentally by comparing the results that have only one leaky mode with the measured data presented in chapter 3. If the measured and simulated data are wildly different then more leaky modes must be added until good agreement is achieved. However at the same time notice must be taken of whether the relative convergence phenomenon is at work for the FSG to solid waveguide mode matching model. For



each trial of leaky modes it is prudent to change the number of Floquet and Bloch modes in the FSG and the number of modes in the solid waveguide. This is potentially a huge amount of testing that would take some time. The extent of the relative convergence phenomenon testing that is required cannot be ascertained until testing starts. For solid waveguides Masterman used a maximum of thirty six modes, although he found that rapid convergence could be achieved with six modes if the correct ratios were chosen.

The first set of test data chosen for each structure consisted of the first four FSG and solid waveguide modes. The value of  $k_0$  was set to 320.661, 15.3GHz, which was the resonant frequency of the FSG. The FSG was the same 6 element one used in chapter 2 and designated FSG 1 in chapter 3. The FSG dimensions were:  $r_0=7.85\text{mm}$ , periodicity  $D_\phi, D_z = 8.22\text{mm}$ , conductor length  $L_\phi, L_z = 6.85\text{mm}$ , conductor width  $W = 0.9786\text{mm}$  and FSG length = 28.1cm. The solid waveguide had dimensions comparable to a section of C140 solid circular waveguide and had  $r_0' = 7.66\text{mm}$ . In fact the structure under test is identical to that tested in chapter 3. The first four solid waveguide modes had phase constants of  $k_z' = 244.19$  (TE<sub>11</sub>); 508.18 (TM<sub>11</sub>); 707.09 (TE<sub>12</sub>); 930.45 (TM<sub>12</sub>) radians/m. The four FSG modes had propagation constants of  $k_{z0} = 216, 0.7645$  (resonant fundamental leaky); 319.2, 11.85 (first leaky mode); 382.2, 106.3 (surface mode in stop band); 0, 379.9 (evanescent mode). The number of Floquet modes was forced to just the fundamental value for this test  $p=q=0$ . The input mode was the resonant fundamental leaky mode and had a unit amplitude of 1.

The values of the coefficient amplitudes for the reflected FSG modes were:- (0.9968, -1.357·e<sup>-5</sup>), (-3.65·e<sup>-4</sup>, -5.976·e<sup>-5</sup>), (-3.445 e<sup>-3</sup>, 4.505·e<sup>-3</sup>) & (-1.4628, 0.1106) in order of the listing in a previous paragraph.

The values of the coefficient amplitudes for the transmitted solid waveguide modes were:- (-2.522, -22.592), (-1.96·e<sup>-3</sup>, -2.4·e<sup>-3</sup>), (1.867, -0.362) & (2.711·e<sup>-4</sup>, 2.352·e<sup>-5</sup>) in order of listing in previous paragraph.

These coefficients were placed into the normalisation equations for each mode to give the mode power for the proper modes and an approximate value for the improper

modes. This is expressed as a percentage of the approximate power in the incident mode.

Reflected percentage power for the FSG modes were:- 99.36%,  $5.011 \cdot e^{-5}\%$ ,  $1.682 \cdot e^{-4}\%$  &  $1.662 \cdot e^{-4}\%$  in order of listing coefficient amplitudes.

Transmitted percentage power for the solid waveguide modes were :-  $1.096 \cdot e^{-3}\%$ ,  $1.74 \cdot e^{-11}\%$ ,  $1.127 \cdot e^{-5}\%$ ,  $3.36 \cdot e^{-14}\%$  in order of listing coefficient amplitudes.

The manually calculated values matched those produced by the simulation program. However the values calculated are clearly incorrect. They predict that virtually all the power is reflected back from the junction. The measurements in chapter 3 show that at resonance the power transmitted through the FSG was a maximum. As only one junction is being simulated and because no dielectric is present it would be expected more than 50% of the incident power would be transmitted through the junction into the solid waveguide.

All the matrix manipulation operations were checked for agreement between the simulation program and the manual values. When these were found to match exactly, all the field equations and the values placed in the R and S matrices were examined all agreed with the same accuracy. There appeared to be no error in the calculation of the values in the computer program compared to the values calculated manually. With programming error eliminated as the cause of the incorrect amplitude values another error must be found. The integral equation derivations were checked and re-checked and no error was found. The accuracy of the data obtained from the infinite FSG program used in chapter 2 was re-checked and this too was found to be accurate.

The manually calculated values were then inspected closely and the mechanism by which the amplitude error was generated in the amplitude coefficients was found. It lies in the normalisation of the FSG mode by the factor given in Equation 4-57, Equation 4-58 & Equation 4-59. The normalisation, by Equation 4-58 or Equation 4-59 of the fields external to the FSG radius, give answers similar to those of the solid waveguide normalisation. However Equation 4-57, which calculates the normalisation

value for the fields of the FSG modes inside the element radius gives believable answers for the surface mode and evanescent mode, but for the leaky modes the calculated value is  $10^5$  times larger than for the solid waveguide. The relative size of these modes is critical, as is seen in this case when the elements of the R and S matrices are populated. The R matrix ends up being populated with many values almost equal to 1, as was seen in the earlier solid waveguide step simulations. The S matrix though was populated by very small values some as small as  $10^{-10}$ . The SR matrix is consequently full of small values and this is swamped by the unit matrix and leads to the poor amplitude coefficients.

The fact that normalisation seems to work for the surface mode and evanescent mode suggests that it is in itself not at fault. The only inputs that have not been independently checked are the values that govern the relative amplitudes of the TE and TM modes in the hybrid FSG modes. This data is generated by another program written by Loukos [27] that calculates field plots. The program and data produced by it has not been authenticated. It is not certain that this data is the cause of the problem. It could be an error in the normalisation of the leaky mode fields. The error got worse when more Floquet modes were added so it cannot be due to a lack of mode information. After many months this mode matching investigation was brought to a close in favour of obtaining the data using another method as detailed in chapter 5.

#### 4.5 References

- [1] Waveguide Handbook - N.Marcuvitz - (radiation Laboratory series, vol.10) New York, Mcgraw-Hill, 1951.
- [2] An Analytic Series Solution for H-Plane Waveguide T-Junction - K.H.Park & H.J.Eom - IEEE Microwave and Guided Wave Letters. Vol.3, No.4, p.104-p.106, April 1993.
- [3] Numerical Analysis of Waveguide Discontinuity Problems Using the Network Model Decomposition Method - G.Wen - IEEE Trans on Microwave Theory and Techniques - Vol.MTT-39, No.10, p.1766-p.1770, October 1991.
- [4] A Surface Integral Equation Method for the Finite Element Solution of Waveguide Discontinuity Problems - O.M.Ramahi & R.Mittra - IEEE Trans on Microwave Theory and Techniques - Vol.MTT-39, No.3, p.604-p.608, March 1991.

- [5] Using the Least-Squares Boundary Residual Method to Model the Symmetrical Five-port Waveguide Junction - A.L.Cullen & S.P.Yeo - Proc of the IEE. Vol.134, No.2, p.116-p.124, April 1987.
- [6] A Moment Solution for Waveguide Junction Problems - H.Auda & R.F.Harrington - IEEE Trans on Microwave Theory and Techniques - Vol.MTT-31, No.7, p.515-p.519, March 1983.
- [7] A Moment Method Analysis for Coplanar Waveguide Discontinuity Inductances - C-W.Chiu & R-B.Wu - IEEE Trans on Microwave Theory and Techniques - Vol.MTT-41, No.9, p.1511-p.1514, September 1993.
- [8] Solution of Waveguide Discontinuities by Modal Analysis - A.Wexler - IEEE Trans on Microwave Theory and Techniques - Vol.MTT-15, No.9, p.508-p.517, September 1967.
- [9] Numerical Solution of Waveguide Discontinuity Problems - P.J.B.Clarricoats & K.R.Slinn - Proc of the IEE. Vol.114, No.7, p.878-p.886, July 1967.
- [10] Computer Field-Matching Solution of Waveguide Transverse Discontinuities Problems - P.H.Masterman & P.J.B.Clarricoats - Proc of the IEE, Vol.118, No.1, p.51-p.63, January 1971.
- [11] A Numerical method for the Solution of the Junction of Cylindrical Waveguides - H.Oraizi & J.Perini - IEEE Trans on Microwave Theory and Techniques - Vol.MTT-21, No.10, p.640-p.642, October 1973.
- [12] The circular Waveguide Step-discontinuity Mode Transducer - W.J.English - IEEE Trans on Microwave Theory and Techniques - Vol.MTT-21, No.10, p.633-p.636, October 1973.
- [13] Fields and Waves in Communications Electronics – S.Ramo, J.R.Whinnery & T.Van Duzer– Wiley, New York, 1994, ch.8, p.428.
- [14] Theory of Guided Electromagnetic Waves – R.A.Waldron – Van Nostrand Reinhold Co, London, 1970.
- [15] Applied Bessel Functions – F.E.Relton - Blackie & son, London,1946.
- [16] Comparative Study of Mode-Matching Formulations for Microstrip Discontinuity Problems – T.S.Chu, T.Itoh & Y-C.Shih - IEEE Trans on Microwave Theory and Techniques, Vol.MTT-33, No.10, p.1018 - p.1023, October 1985.
- [17] Antenna Theory, Part 2 – R.E.Collin & F.J.Zucker – McGraw-Hill Book Company, New York, 1969.
- [18] Theory of dielectric Optical Guides – D.Marcuse, Academic Press, New York, 1974.

- [19] The Numerical Solution of Waveguide Discontinuity Problems – P.H.Masterman – Ph.D. thesis, Leeds University, 1969.
- [20] Propagation Characteristics of Cylindrical Frequency Selective Guides – G.I.Loukos – Ph.D. Thesis, Loughborough University, 1997.
- [22] Theory of Guided Electromagnetic Waves - R.Waldron - Butler & Tanner, London, 1970.
- [23] Applied Bessel Functions - F.E. Relton - Blackie & son, London, 1946.
- [24] Guided Complex Waves Part 1. Fields at an interface & Part 2. Relation to radiation patterns – T.Tamir & A.A.Oliner – proc I.E.E., vol 110, No2, February 1963, p310 & p325.
- [25] On Leaky Mode Approximations for Modal Expansion in Multilayer open Waveguides – S-L.Lee, Y.Chung, L.A.Coldren & N.Dagli – IEEE J. Quantum Electronics, Vol 31, No 10, October 1995.
- [26] Leaky Modes on a Dielectric Waveguide: Orthogonality and Excitation – R.Sammut & A.W.Snyder – J.Applied Optics, Vol 15, No 4, April 1976, p1040.
- [27] Propagation Characteristics of Cylindrical Frequency Selective Guides – G.I.Loukos, Ph.D. thesis Loughborough University 1997.

## 5. Transition Analysis by Finite Element Method

With the transition analysis failing to produce results of any accuracy, see Chapter 4, an alternative method of modeling the FSG to solid waveguide transition was required. Mode matching was chosen primarily as it was the only method which could give the amplitudes of the modes in each guide structure. None of the other methods could provide this and in this respect there was little to choose between many of the other numerical routines. Another concern, at the time that the decision was taken to use mode matching, was that of computer memory requirements. Many of the methods needed far more computer memory than mode matching, although advances in computer hardware were starting to reduce these concerns. By the time that an alternative method was required the availability of computer memory was sufficiently high to enable most numerical methods to simulate very complex structures. The computer that the junctions eventually simulated on, was a Hewlet Packard J5000 workstation with four gigabytes of RAM. This represented at least a ten fold increase in the amount of computer memory available over the lifetime of the project.

The opportunity to use a computer with a large amount of RAM was given to the author by BAE SYSTEMS, Cowes, Isle of Wight. It was the use of this machine that drove the choice of the Finite Element method as the numerical method to simulate the FSG to solid waveguide junction. This was because BAE SYSTEMS have a commercial finite element program installed on this machine. The finite element simulator was Ansoft's High Frequency Structure Simulator (HFSS) v6/v7. The combination of a fast machine with a large amount of memory and an established simulation tool whose accuracy was well known, was a powerful package. The availability and easy of use of this combination, along with the fact that there was only short time remaining to carry out the simulated investigation into the FSG junctions, meant that the J5000 and HFSS were the obvious combination to carry out the work.

## 5.1 Fundamentals of Finite Element method

The Finite Element method is a numerical technique that can be used iteratively to solve an electromagnetic boundary problem. As described in the literature review of chapter 4, it works by splitting a structure into a large mesh of points and approximating the fields at the mesh nodes that obey the boundary conditions of the structure. By an iterative successive approximation technique the field approximations can be refined, until a reasonably accurate set of field values is obtained.

The HFSS implementation of this technique is described in the HFSS help manual [1]. In summary, any three dimensional structure can be entered as the model to be simulated by using the integral drawing package. This drawing is then made into the model required model by defining the materials and the boundaries from which it is made. Once the model is submitted for simulation HFSS must create an initial mesh of points. Unlike many other packages HFSS can calculate the initial mesh itself with no user input required, although it is possible to do this meshing manually if required. The mesh that is built is made up of many tetrahedrons, all adjacent points in the mesh are joined by triangles, and this is the most efficient mesh for solving the field values. Very long and thin tetrahedra give poor field accuracy and to avoid producing these HFSS uses the Delaunay Tessellation procedure. This maximises the sum of the minimum angles in the tetrahedra to virtually eliminate long thin ones. It also automatically adds extra tetrahedra around the boundaries of different objects in the model and ensures that the distance between the vertices of the tetrahedra is less than a tenth of a wavelength.

The field is calculated at the tetrahedron vertices and the mid points of each edge giving 10 calculation points. The field is approximated with a second order quadratic polynomial:-

$$A_z(x, y) = a_0 + a_1x + a_2y + a_3x^2 + a_4y^2 + a_5xy$$

Equation 5-1

At each of these points the approximation is refined with a variational method. However, instead of using Poisson's equation, Equation 5-2, for this, it is replaced by the energy function Equation 5-3, which is minimised to give a better value of  $A_z$ .

$$\nabla^2 \mathbf{A} = -\mu \mathbf{J}$$

Equation 5-2

$$F(\mathbf{A}) = \frac{1}{2} \int_v \left( \frac{\nabla \mathbf{A} \cdot \nabla \mathbf{A}}{\mu} + \mathbf{A} \cdot \mathbf{J} \right) \cdot dv$$

Equation 5-3

Over all the triangles on the faces, a sparse matrix equation can be formed  $[S][A]=[J]$ . This matrix equation is solved by either the sparse gaussian elimination method or the pre-conditioned conjugate gradient method.

The accuracy of the overall solution produced is dependent on the mesh. If the mesh is not fine enough then significant characteristics of the field in a particular part of the model may be missed. Conversely if the mesh is too fine then the simulation will use large amounts of memory and take a long time to execute for little improvement in the accuracy of the result. To overcome the problem of getting the mesh size optimised HFSS will solve the field solution for the initial mesh as described above, but then it will put the solution of  $A_z$  back into Poisson's equation to find error function in each tetrahedron. The mesh is refined, or adapted, using a proprietary refinement algorithm that identifies each tetrahedron that has too large an error function and makes that tetrahedron and those around it smaller. The program can calculate the S parameters for the model, based on the areas defined as the ports of the structure, at each level of mesh adaptation. The S parameters for the current mesh and the previous mesh are then compared and the re-meshing will continue until the S parameters have converged to a user defined level.

The field solving and mesh adaptation can only take place at a single frequency. This is a major draw back of the finite element method. Traditionally, if multiple frequencies were required, the model would have to be solved at each individual frequency unlike the FDTD method, where a pulse response is found and using



Fourier transforms the frequency response of the structure calculated. However Ansoft have developed a couple of frequency sweep options, fast and discrete, to reduce the amount of time needed to calculate a frequency response. They both require the adaptive solution to be found for a single frequency, as a rule of thumb this should be three quarters of the highest frequency in the band. The fast sweep relies on an algorithm to extend the single frequency solution over a range of frequencies, while the discrete sweep uses the single frequency mesh to solve the fields at each specified frequency in the sweep range. Both methods are band limited and the discrete method is more accurate although it has a far longer execution time compared the fast sweep.

Finite elements with their tetrahedra are far better than the FDTD method for modelling curved surfaces. As the FDTD method uses a mesh made of “sugar cubes” any curve can only be approximated by a ‘staircase’ quantisation of the curve. This staircase can have a large affect on the results produced by the FDTD simulation if the quantisation steps are not small enough. However HFSS with its tetrahedra can approximate curved structures far better. A curve in HFSS is split into a number of points and chords are drawn between each point, as can be seen in the figures in Section 5.2. The circles are all polygons with 20 to 24 sides. The FSG elements are each made of 8 segments across the curve. The close approximation of the many curved surfaces of the FSG to solid waveguide model makes the HFSS finite element package a memory efficient way for it to be simulated. The staircase method would have required a finer mesh and more memory.

#### 5.1.1 Presentation of Results Produced by HFSS.

HFSS produces a large amount of information from the converged solution that can be presented in different forms. As stated previously HFSS can calculate the S parameters of the structure if the input or output ports are declared. In the model developed for the solid waveguide to FSG junction the port can only be defined in the solid waveguide. This is because the port must be able to resolve the mode that would exist in the port cross section. The port solving algorithm in HFSS is unable to resolve the hybrid mode that would exist in the FSG and so only one port can be placed in the

single junction case. A model with only a single port can by definition only have one S parameter the  $S_{11}$  value. If a second waveguide is added to the other end of the FSG then a port can be defined at the end of that waveguide as well so that a two port model is created. A two port structure will have not only an  $S_{11}$  value but also  $S_{21}$ ,  $S_{12}$  &  $S_{22}$  values. There is no limit to the number of ports that can be added to a model, but it is dependent on the layout and requirements of the structure being simulated. For each port it is also possible to calculate the characteristic impedance and propagation constant of the mode that the port supports.

In addition to the port data, field data may also be displayed. It is possible to plot E and H field magnitude contours, phase contours or both combined in vector form and Poynting vectors on any cut-plane through the model. The phase of the feed or the position of the cut-plane can be varied to produce a movie like animation that can be replayed at different speeds. This facility is very useful for studying the field distribution and the power flow at various points in the model. The animations allow large amount of data to be presented easily so that propagation details can be easily seen. These can easily be missed on standard static plots. As well as cut-planes, volume plots of the field magnitude can also be made and animated. These have the appearance of a 'snowstorm' type plot. The plotted dots are colour coded with the colour giving the field magnitude. A dot is only printed at a point in space where the field crosses a colour threshold. This plot is very useful as it too can be animated and can be rotated on the screen to given a three dimensional view of the fields from any viewing angle.

If a structure is an open one, a special type of boundary is required to enable the problem to be solved. Obviously the fields extend for a considerable distance from the structure, which would require a large number of tetrahedra in order to simulate unbounded free space. This obviously would not be solvable, so a special absorbing 'radiation' boundary condition is placed around the open structure to be simulated. This radiation boundary has the special property that it will absorb the propagating fields as if they did exist out to infinity. There are two possible implementations of the radiation boundary, the ABC and the Perfectly Matched Layer (PML). The ABC boundary is a surface on the outside of the model that absorbs virtually all power incident upon it from a near normal direction. However it is very poor at absorbing

power from waves incident upon it at any angle away from the normal. In this case a PML must be used. This is a layer of lossy anisotropic dielectric such that it absorbs most field incident upon it from any angle. It is not as efficient an absorber as the ABC boundary near normal incidence, but is better at all other angles of incidence.

If an open structure has a radiation boundary then HFSS is able to take the fields that are incident upon it and extrapolate them to give field patterns outside the confines of the model. Both far field and near field, patterns are possible. These radiation patterns can display field polarisation information in all the principal conventions and the gain and directivity of the radiating structure. It will be possible to compare the predicted S parameters and radiation patterns with those that have been measured to ascertain the validity of this model.

## 5.2 Development of Transition Model

Although the J5000 had plenty of memory it was initially unclear as to how much of the transition structure it would be possible to model in HFSS. With no analytical method capable of estimating the size of the model which could be simulated, trial and improvement was the only way to find out what size of junction could be modelled.

To this end a whole series of models were drawn using the HFSS drawing package to represent the FSG junction; each one with increasing complexity. The increases in the complexity were carefully incremented with steps such that any change in the results could be directly attributed to a particular cause. For most of the simulations the Mylar dielectric layer, that supported the elements of the FSGs that were measured in Chapter3, was omitted. This was done because, although it was recognised that its presence would alter the propagation properties of the FSG by dialectically loading the elements, the very thin layer would require a very large number of tetrahedra to mesh it, increasing the memory requirements of the model. Therefore, to ensure that the largest FSG structures could be simulated in the shortest possible time, the dielectric layer was generally omitted. The dielectric was included for one of the smaller models to see if its affect on the model was the same as that seen in the

measurements. When this was done the number of tetrahedra increased significantly along with the simulation time.

The first model simulated was the least complex, which was the three element whole ring FSG. It consisted of a section of solid metal waveguide feeding the first three rings of elements from a FSG, see Figure 5-1. This consisted of a 10mm long section of solid circular waveguide, 7.65mm in diameter, that intersected a conducting plane which also had a 7.65mm diameter hole cut in it coincidental with the waveguide aperture. The FSG dimensions that were modelled were those of FSG 1 from Chapter 3. The radius of the imaginary cylinder on which the conducting elements were placed was 7.85mm. The square elements had a side length of  $L_{z,\phi}=6.6\text{mm}$ , periodicity  $D_{z,\phi}=8.22\text{mm}$  and loop width  $W=0.95\text{mm}$ . The first ring of elements were placed a distance of half the gap between elements  $L_z - D_z/2=0.81\text{mm}$  from the conducting plane. The FSG consisted of only three rings of elements in the  $z$  direction making the total length of the waveguide and FSG was 33.85mm. The radiation boundary was a cylinder 29.35mm long with a radius of 18mm and was of the ABC type. This type of boundary is very effective at absorbing fields that fall upon it with near normal incident, hence the cylindrical shape of the boundary so that most fields from the FSG are propagating in a near normal direction to the boundary. This meant that the radiation boundary was 10.15mm radially from the FSG elements and 5.5mm from the last ring of elements along the axis. This ran successfully using 25649 tetrahedrons, 0.87Giga Bytes (Gbytes) of RAM and 0.46Gbytes of disc space, converging to  $\Delta S=0.016$  at 14.8 GHz. Where the  $\Delta S$  value is the aggregate change in the scattering matrix for the model from one HFSS adaptive pass to the next, and is the user defined convergence criteria.

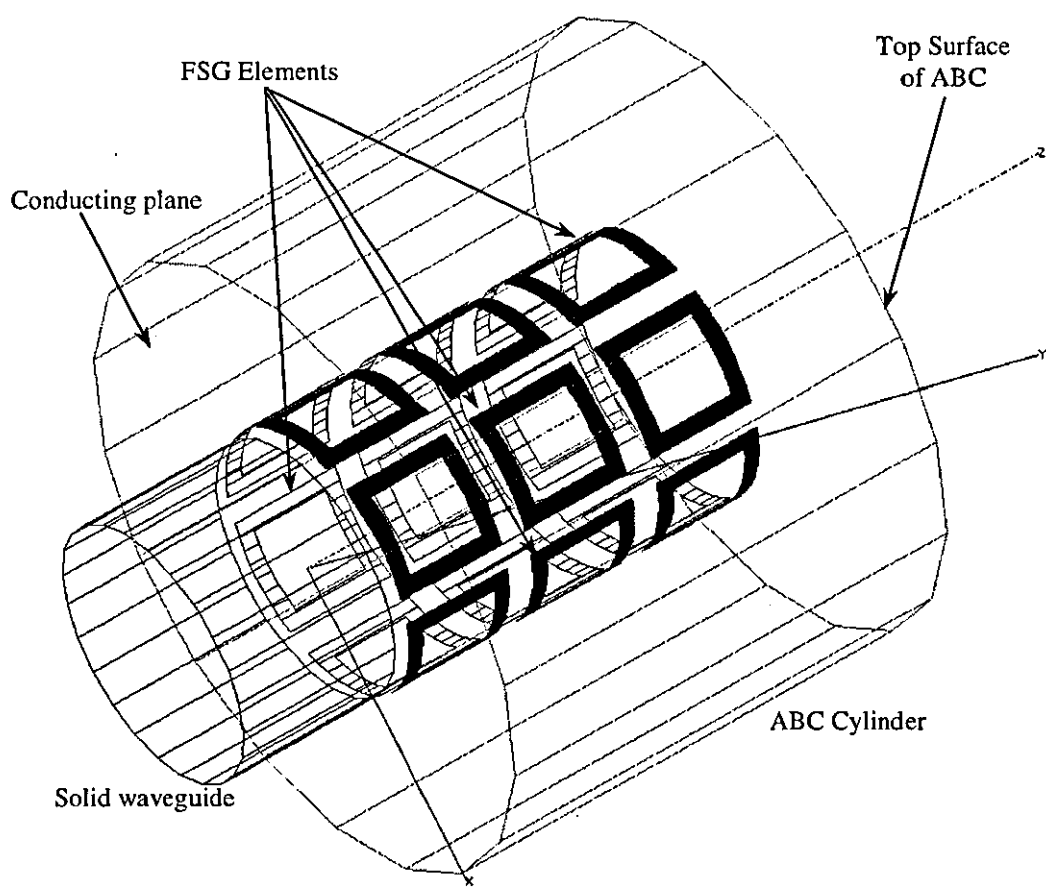


Figure 5-1 The Three Element Whole Ring Model – a junction of a solid waveguide to an FSG.

The size of the model simulated above was then increased to four rings of FSG elements. As this also ran successfully the number of rings was increased further to six, see Figure 5-2. This six element whole ring model was the same as the three element whole ring model except that the total overall waveguide and FSG length was considerably longer at 58.51mm, an increase of 70%. An FSG of six elements in the z direction is approximately three wavelengths long at the resonant frequency. This is a highly desirable number as the theory of planer phased arrays requires the radius of an array of radiating elements to be at least three wavelengths before the coupling affects of the edge elements on the centre element can be considered negligible. So for an FSG longer than three wavelengths in length, the coupling effects of the elements beyond the sixth element from the junction would also be negligible. Thus the simulation of the junction of the six element whole ring FSG to the solid waveguide has, with respect to the aperture, taken into account the majority of the coupling affect that would be present had the FSG been longer.

The orientation of the polarisation vector of the  $TE_{11}$  field in the solid waveguide feed could be altered. It was decided to see if the FSG was sensitive to orientation of the of the polarisation vector in relation to the elements on the FSG surface. Two orientations were chosen; the first with the polarisation vector passing through the centre of an element and the second with the vector passing through the mid point of the gap between two adjacent elements. These two orientations have an angular separation of  $30^\circ$ , exactly half the angular periodicity of the FSG. This is the maximum possible separation for the two polarisations and if the FSG is sensitive to polarisation it should be apparent in these two simulations. The radiation boundary was a cylinder 54.01mm long with a radius of 18mm and was of the ABC type. This meant that the radiation boundary was 10.15mm radially from the FSG elements and 5.5mm from the last ring of elements along the axis. This ran successfully for both polarisation orientations, the polarisation passing through the mid point of the gap between two adjacent elements used 53639 tetrahedrons, 1.4Gbytes of RAM and 1.4Gbytes of disc space, converging to  $\Delta S=0.018$  at 15.35 GHz. For each polarisation, the model was solved over the frequency range 13.9GHz to 16.5GHz. This model was deemed to be the largest that could be simulated with the memory available on the J5000 machine, as an attempt to simulate 7 rings of elements failed with an out of memory error.

Having found that the six element whole ring was the largest model that could be simulated, a way of assessing the transition with the Mylar support sheet in position was required. The addition of the dielectric should make the simulated results more like those of the measured structure. However if the dielectric were added to the six ring model, which was already at its maximum simulation size, it would not be possible to get the simulation to converge before it ran out of memory. The number of rings could have been reduced back to three or four and the dielectric added. However this would remove some the coupling effects from elements further down the FSG and would affect the calculated aperture fields.

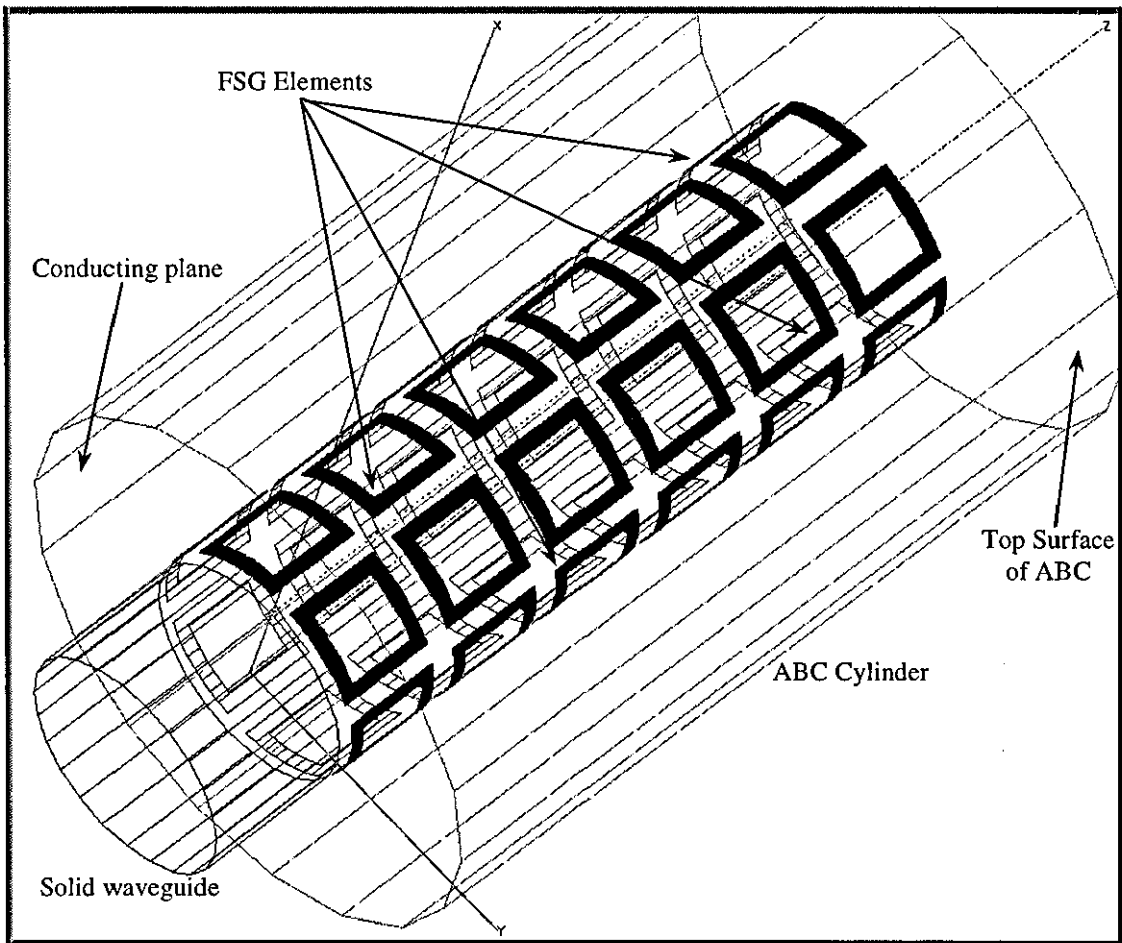


Figure 5-2 The Six Element Whole Ring Model – a junction of a solid waveguide to an FSG.

A solution was found in the form of an artificial boundary that could be placed in the model along a plane of symmetry. HFSS has a set of boundary conditions, which can be placed along a plane of either E or H plane symmetry, resulting in only half the actual model needing to be simulated. Using a symmetry boundary the model remained at six elements along the z axis, but with only half a ring of elements, three instead of six. It will be referred to as the “six element half ring” model. A symmetrical boundary was placed such that it cut through the circumference of the FSG halfway between two elements on both the top and bottom of the guide and contained the z axis. This reduction in the amount of memory required to simulate the junction should allow the dielectric to be added to the model.

Before the dielectric was added the symmetrical six element half ring model was simulated to ensure that there was sufficient agreement between it and the full six ring

model. Both types of symmetry plane were investigated and required a different polarisation of the input field for each one. The H symmetry plane required the polarisation vector of the  $TE_{11}$  field to be in the plane of the symmetry plane and perpendicular to the z axis. The E symmetry plane required the polarisation vector of the  $TE_{11}$  field to be perpendicular to the symmetry plane and perpendicular to the z axis. This also gave two models that mirrored the six element whole ring model with a polarisation vector passing through the centre of an element and gap between adjacent elements. The model was identical to that of the full six element whole ring model, see Figure 5-2, but simply divided into two halves, one of which was then removed to leave half of the model, as can be seen in Figure 5-3. This ran successfully using 39628 tetrahedrons, 0.94Gbytes of RAM and 1.55Gbytes of disc space, converging to  $\Delta S=0.017$  at 14.8GHz. For each polarisation and boundary condition the model was solved over the frequency range of 13.7GHz to 16Ghz.

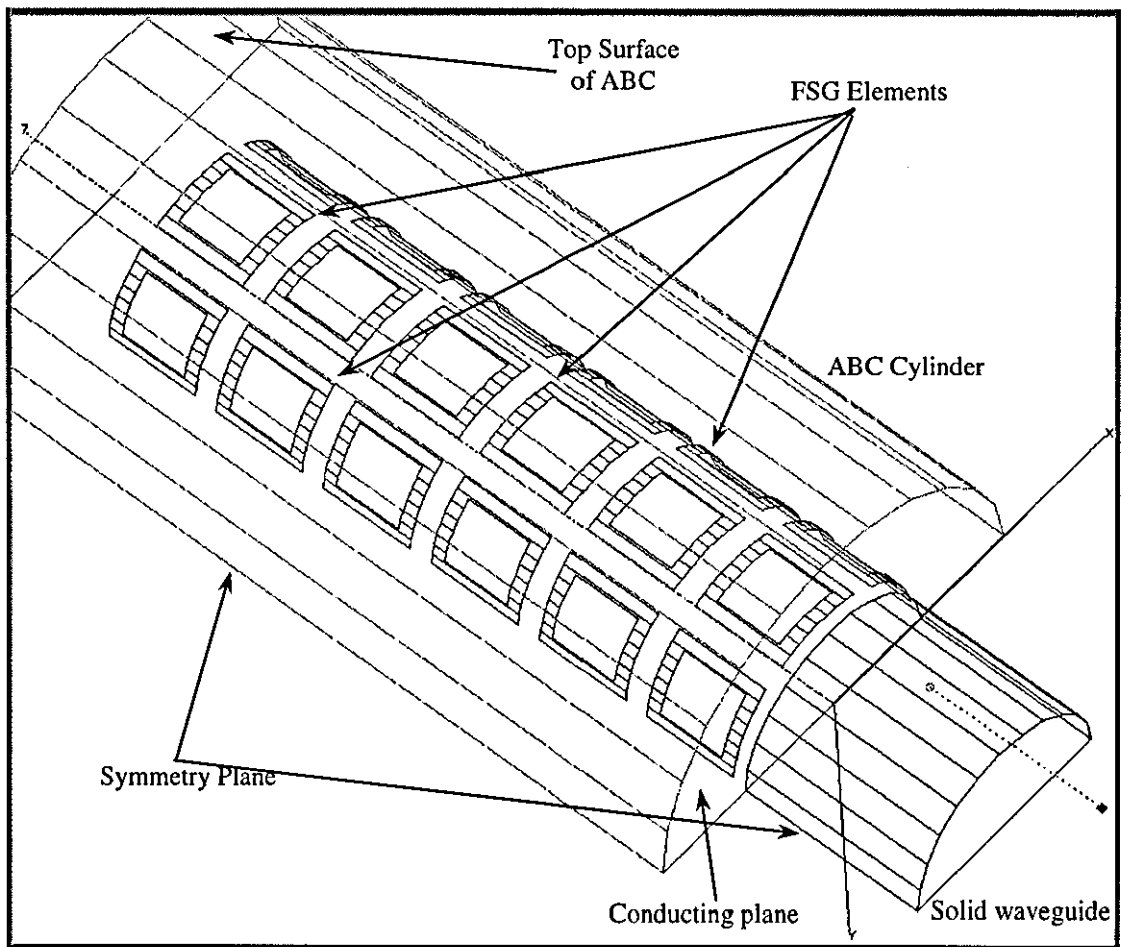


Figure 5-3 The Six Element Half Ring Model – a symmetrical model of junction of a solid waveguide to an FSG.



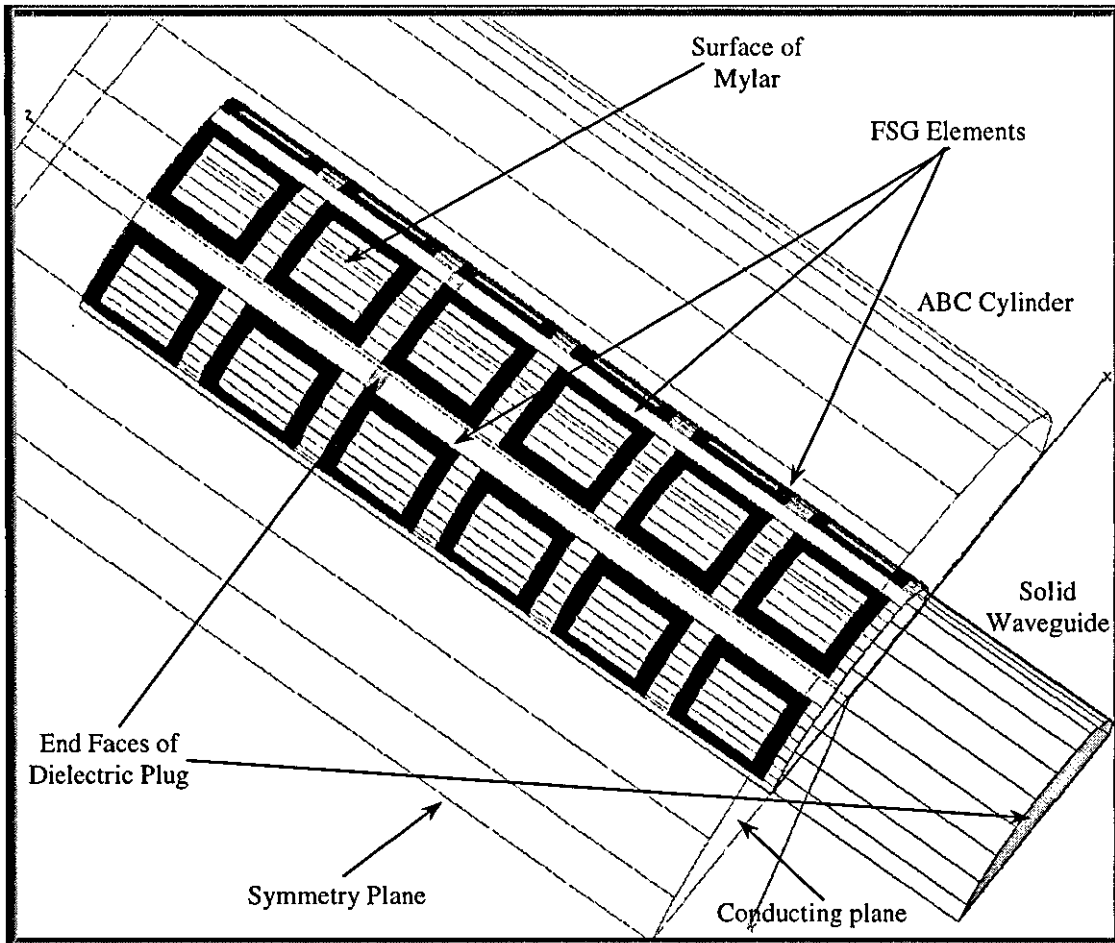


Figure 5-4 The Six Element Half Ring Dielectric Model – a symmetric solid waveguide to FSG junction with Mylar sheet and expanded polystyrene plug.

The mylar dielectric sheet 0.04mm thick was then added to produce the six element half ring dielectric model. The Mylar sheet was positioned so that its outer surface was in contact with all the conducting elements on the FSG surface. At one end the mylar sheet was in contact with the infinite conducting plane and was concentric around the aperture. This was the same positioning of the dielectric as employed in the test setup for the measurements taken in Chapter 3. At the other end the mylar sheet ended flush with the end of the last half ring of elements. To further make the model reflect the Chapter 3 measurement setup, an expanded polystyrene mating plug was added at the junction. As polystyrene has an effective dielectric constant  $\epsilon_r=1.03$  it was expected that this would have little affect on the simulated results. The plug was stepped in the middle having two radii, one 7.65mm completely filling the waveguide and the other 7.77mm in the FSG, completely filling the inner dimension of the Mylar tube. The waveguide section of the plug was 10mm long and the FSG

section of the plug was 32mm ending nearly flush with the end of the 4<sup>th</sup> element along the length of the FSG. The whole structure can be seen in Figure 5-4 & Figure 5-5 at two different orientations, and clearly shows the 0.03mm thick dielectric sheet of mylar and the expanded polystyrene plug.

The six element half ring dielectric model ran successfully using 73580 tetrahedrons, 1.92Gbytes of RAM and 1.85Gbytes of disc space, converging to  $\Delta S=0.041$  at 14.9GHz. The dielectrically loaded FSG model was simulated over the frequency range of 13.7GHz to 16GHz.

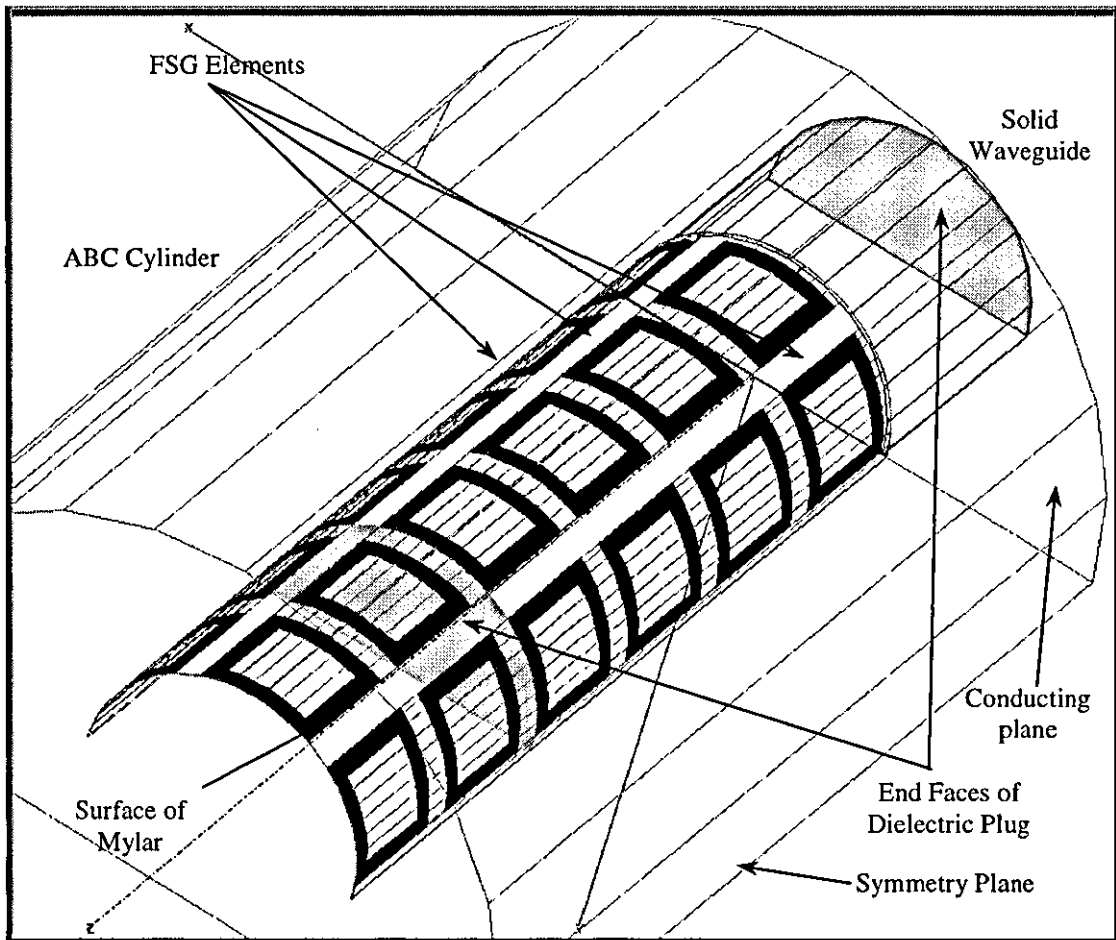


Figure 5-5 The Six Element Half Ring Dielectric Model – a symmetric solid waveguide to FSG junction with Mylar sheet and expanded polystyrene plug.

As with the measurements taken in chapter 3, the effect of just the Mylar sheet without the FSG elements and the expanded polystyrene plug on the waveguide junction was assessed. This was achieved by simply deleting all the FSG square loop

elements from the model in Figure 5-4 and keeping all the remaining dimensions unaltered. The resulting half cylinder dielectric model that was simulated is shown in Figure 5-6. This ran successfully using 29328 tetrahedrons, 0.5Gbytes of RAM and 0.65Gbytes of disc space, converging to  $\Delta S=0.004$  at 14.6GHz. This gave a baseline prediction of the operation of the waveguide junction without the FSG elements, which graphically illustrates their effect on the junction propagation characteristics. The band of frequencies over which this model was swept was limited to 14.3GHz to 15.3GHz because it was simulated to confirm that the dielectric had no effect itself on the  $S_{11}$  results.

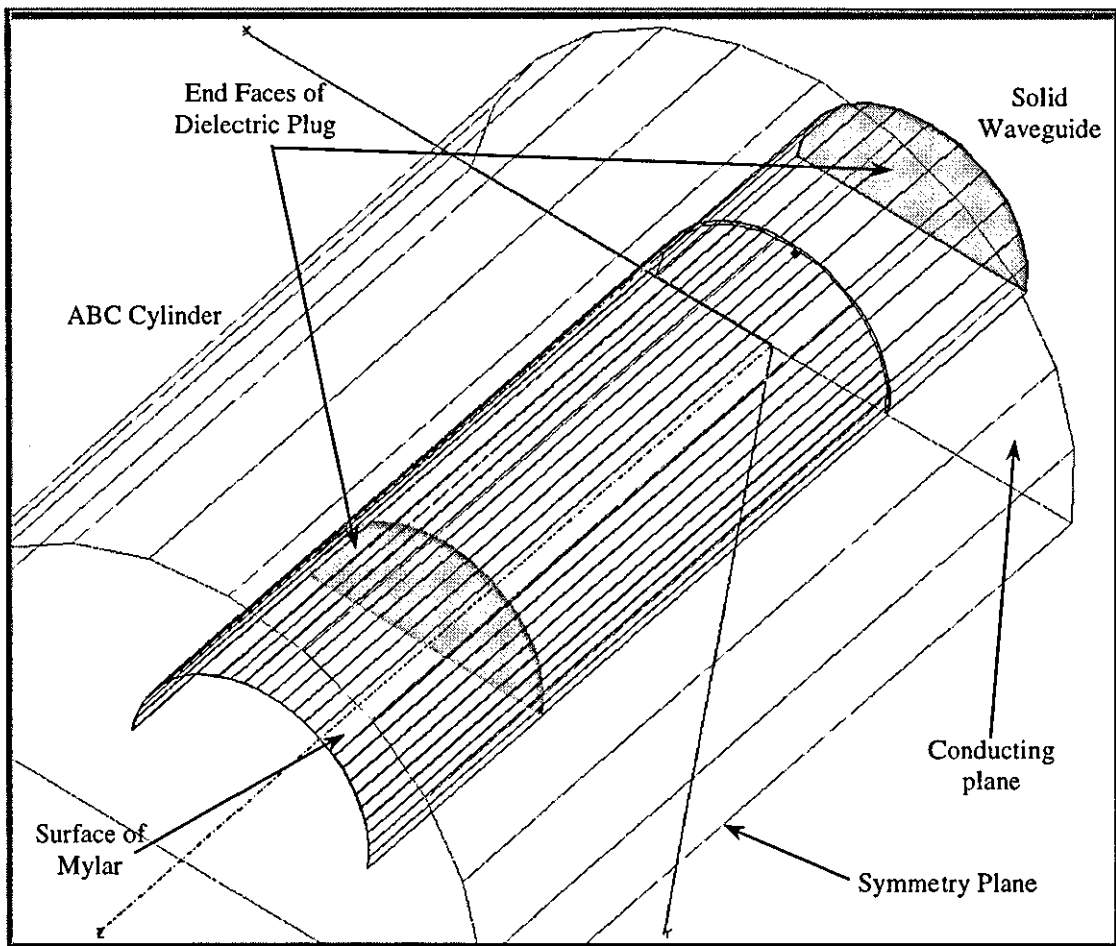
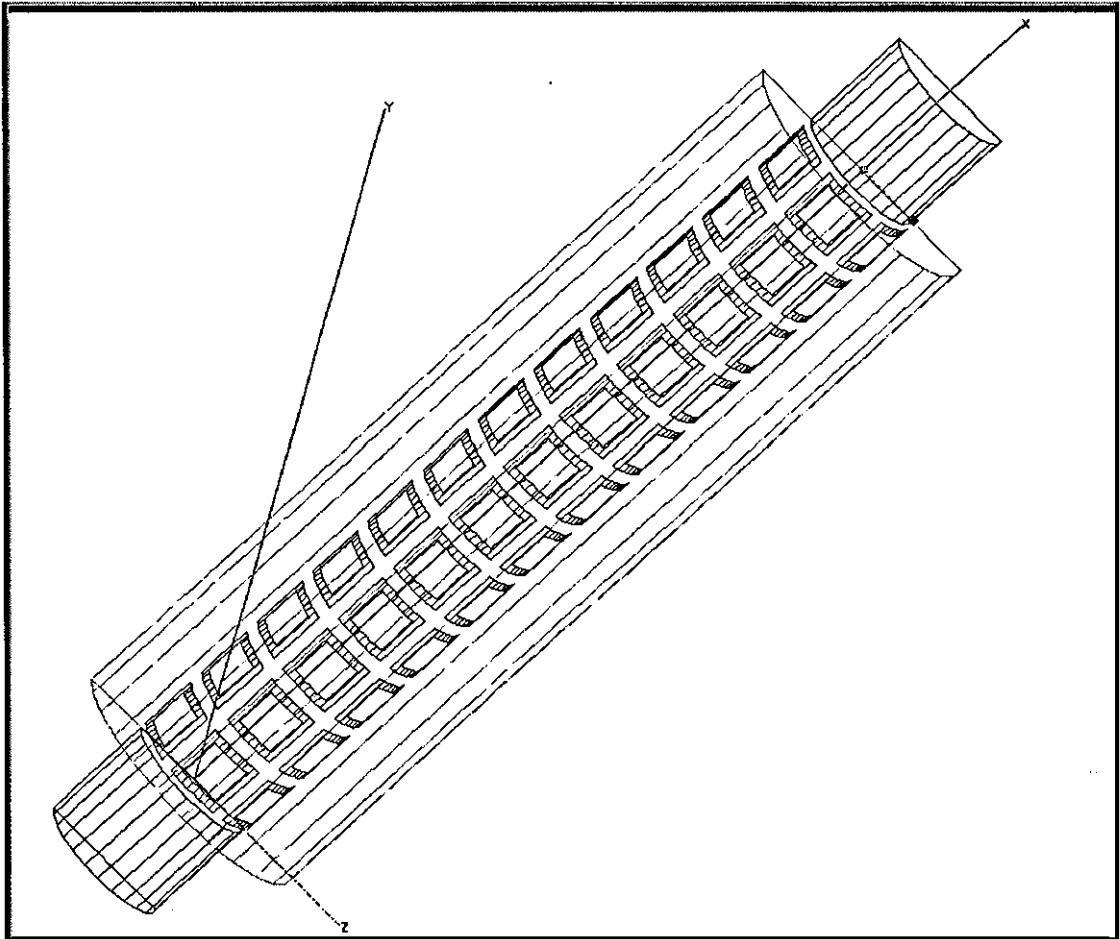


Figure 5-6 The Half Cylinder Dielectric Model – a junction between a solid circular waveguide and a tube of Mylar sheet.

The FSG measurements of Chapter 3 were all taken with the length of FSG under test suspended between two solid waveguides. As discussed in Chapter 3 the measured structure was a cascade of a solid waveguide to FSG junction, followed by a length of lossy structure with another FSG to solid waveguide junction at the end. It would be

desirable if the HFSS model could be made to mirror the measurement setup of Chapter 3 more closely. In the single feed waveguide structures described above, the structure under test consisted of a solid waveguide to FSG junction and a very short length of FSG followed by a transition into free space. The differences from the measured FSGs were the very short length of FSG and the free space transition. The use of the symmetry boundary to reduce the model size, so that the dielectric could be added, could also be used to make the FSG model longer. The longer the FSG was, with a second solid circular waveguide at the far end, the more like the measured FSG's the HFSS model would look.



**Figure 5-7 The Twelve Element Half Ring Model – an FSG twelve elements long with a junction to solid circular waveguide at each end.**

In fact the six element half ring model was used as a starting point to redraw the HFSS model so that it would have a solid waveguide at each end of the FSG. The existing model was copied and mirrored in the plane  $z=59.32$  (assuming that  $z=0$  is the plane of the input port of the first solid waveguide. This produced a FSG with 12

elements 98.64mm long with 10mm of solid circular waveguide at each end, the “twelve element half ring” model. Both the junctions between the solid waveguides and the FSG were through apertures in conducting planes at  $z=10$  and  $z=108.64$ mm with the port of the second solid waveguide in the plane  $z=118.64$ mm. The structure of the FSG with twelve half rings of elements in the axial direction and solid waveguides at each end can be seen in **Figure 5-7**. This ran successfully using 57562 tetrahedrons, 1.45Gbytes of RAM and 1.98Gbytes of disc space, converging to  $\Delta S=0.0046$  at 14.8GHz. The frequency sweep of this simulation was carried out over the largest frequency range of all the models, from 13.3GHz to 17.3GHz. It was not possible to extend this range either up or down in frequency, as outside this range the simulation would not converge sufficiently before the computer platform exceeded its memory limit.

To ascertain the longest possible FSG that could be modelled in HFSS on the J5000 with the feeds at each end, the number of elements in the axial direction was increased. It was found that the maximum number of elements that could be placed in half rings along the axial direction, before an out of memory termination of the simulation occurred, was sixteen. The dimensions of the model were as for the model in **Figure 5-7**, but with sixteen elements the length of the FSG was now 131.52mm. This ran successfully using 94271 tetrahedrons, 2Gbytes of RAM and 2Gbytes of disc space, converging to  $\Delta S=0.012$  at 15.4GHz. The maximum range of simulated frequencies for this model, with good convergence, was 13.9GHz to 16.9GHz.

### 5.3 Results of HFSS Simulation of an FSG Six Whole Rings in Length with a Single Feed Port.

To validate the results of the simulations produced by HFSS, physical measurements of the simulated structure were required. The measurements taken in section 3 were for FSG’s that were very much longer than could be simulated and had a solid waveguide feed at each end of the FSG. It was decided to measure a short length of FSG consisting of six rings of elements long and with only a single C140 solid waveguide feed, as modelled by HFSS. The omission of the second solid waveguide meant that all the energy not reflected back down the feed waveguide would radiate

into free space, either in the form of a leaky mode from the waveguide walls or else from the aperture at the end of the FSG in 'endfire' mode. The transition into free space, as with the measurements with a second solid waveguide, will affect the measured values of  $S_{11}$ . It is inevitable that some energy will reflect from the free space transition and propagate back through the feed junction. Again the  $S_{11}$  measured and simulated is not that of the junction alone, but that of the entire system.

The short stub of FSG was attached to the end of the solid waveguide with a small plug made from expanded polystyrene. The plug was about 60mm in length, with half of it in the FSG and the other half in the solid waveguide. The diameter of the plug was stepped at the mid point, so that it completely filled the solid waveguide and the FSG. A length of WG18 rectangular waveguide fed the solid circular waveguide, via a rectangular to circular waveguide transition. The rectangular waveguide was in turn fed from the HP8410B vector network analyser by a length of coax cable and a standard probe feed. The equipment setup used to take the measurements is shown in Figure 5-8. The feed network to the end of the circular waveguide was calibrated out of the measurements using a standard technique with a set of short, open and matched terminations. The FSG was then added to the end of the feed network and the  $S_{11}$  measurement was taken over the frequency range 13GHz to 17GHz, the results are shown in Figure 5-9.

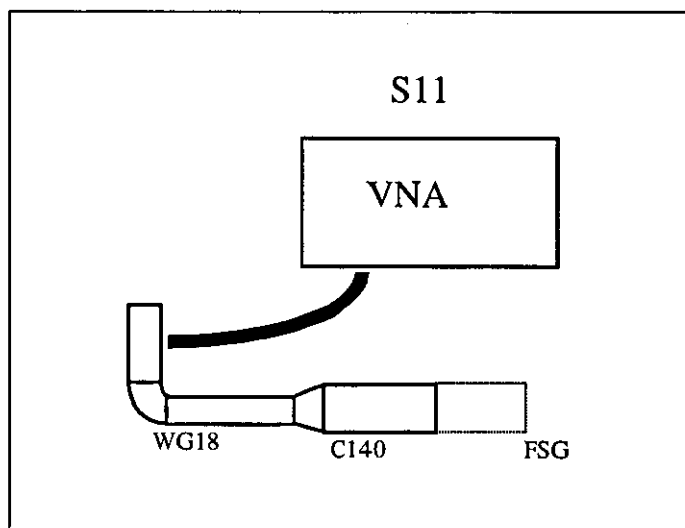


Figure 5-8 Equipment set-up to measure the  $S_{11}$  of a short length of FSG radiating into free space.

5.3.1  $S_{11}$  Results for the Six Element Whole Ring FSG Model – Measured and Simulated.

The results of the models with one solid waveguide feed can now be compared with a set of measured values for a structure comparable to that which was simulated. They are plotted together in Figure 5-9.

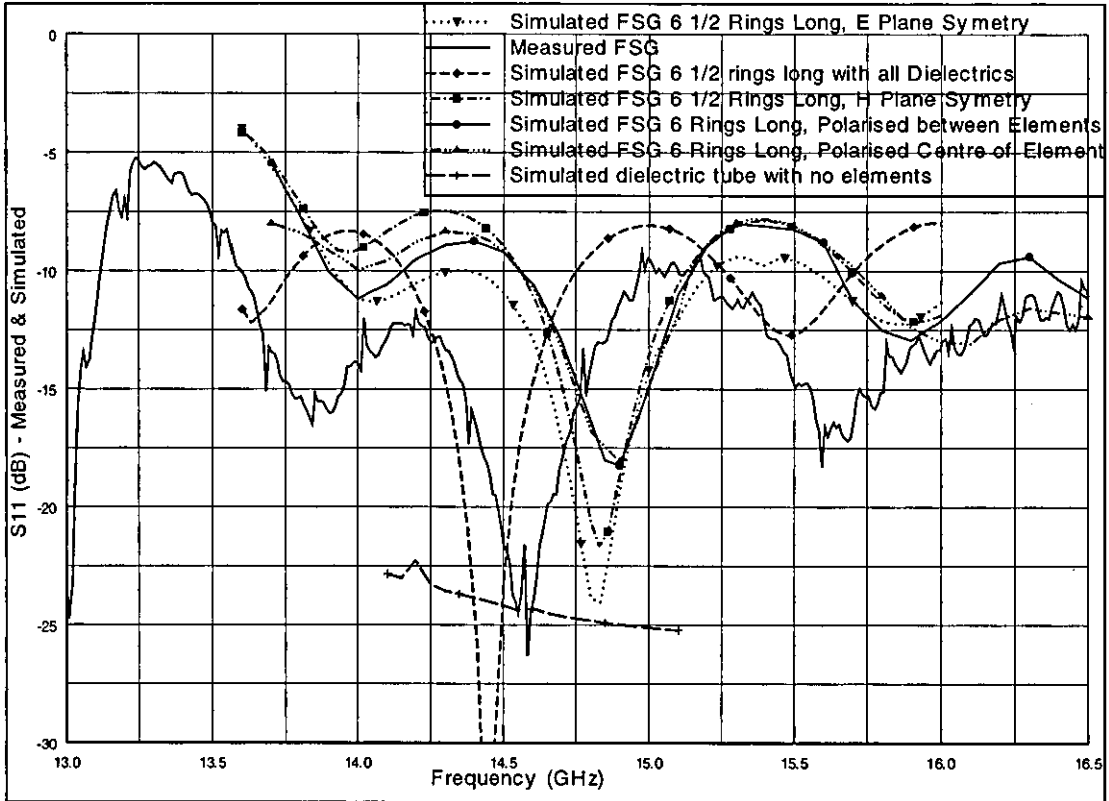


Figure 5-9 Comparison plot of measured & simulated  $|S_{11}|$  of an FSG, 6 elements long.

The comparative difference between the two plots of the six element whole ring FSG simulation with the polarisation vector either at the centre of an element or between two adjacent elements is very small. There is only a significant difference between them above 15.6GHz and below 14.5GHz. The plots are a composite of two sets of frequency swept data from HFSS. As mentioned in section 5.1, HFSS can only produce the very accurate adaptive solution at a single frequency. Using an algorithm the adaptive solution can be swept over a range to approximate the  $S_{11}$  for a band of frequencies. The error in the approximation increases with the distance from the

adaptive frequency. The adaptive frequencies for the six element whole ring plots, for both cases, were 14.7GHz and 15.35GHz. This would explain the high degree of agreement between the two polarisations between 14.5GHz and 15.6GHz and why beyond this band the difference between them slowly increases. This implies that the orientation of the polarisation vector of the field in the input waveguide is not significant to the operation of the FSG.

There is a noticeable difference between the plots of the six element half ring FSG model with different symmetry boundaries, although theory says that there should be no difference between the different symmetry boundaries and the whole ring model. The range over which the agreement between the E plane symmetry and the H plane symmetry is closest is only from 14.85GHz to 15GHz. If the tolerance on agreement is extended to be within 2dB of each other then the range is 14.6GHz to 15.3GHz. The adaptive frequency of these simulations was 14.8GHz. The result of the six element whole ring model that shows that the polarisation vector orientation has no affect means that the polarisation different can also be eliminated as a possible cause for the difference between the two six element half ring models. This implies that any significant difference between the implementations is probably due to the numerical inaccuracies in the way HFSS processes the fields in the gap between the closest elements of the FSG and these two different boundary conditions. Of the two six element half ring models the performance of the model that uses the H symmetry boundary is the closest match to the results for the six element full ring models. All further models that used symmetry boundaries were developed using H plane symmetry boundaries, although it must be noted that there is some discrepancy between the results.

The comparison of the measured  $S_{11}$  for the short length of FSG six elements long to the simulated  $S_{11}$  for the four models with no dielectric show plots of similar shape, but with a variation in the  $S_{11}$  magnitude. There is also evident a noticeable shift in frequency, the plots of the models with no dielectric being shifted up in frequency by about 250 to 300 MHz, depending on the model examined. The measurement work undertaken in chapter 3 suggests that the thickness of the dielectric has a loading effect on the dielectric. The thicker the dielectric the larger the loading effect and the lower the resonant frequency. The addition of the Mylar sheet and the polystyrene



plug to the six element half ring H symmetry plane model gave rise to a 400MHz downward shift in the frequency response. This categorically proves that the dielectric does have a significant loading affect on the frequency of operation of the FSG.

Some of the difference in the levels of the magnitude of the  $S_{11}$  seen in the measured results and those from the simulation can be attributed to the fact that the simulation uses perfect conductors and loss-less dielectrics. The real FSG obviously has losses in the material from which it is constructed. As previously mentioned in chapter 3 it is impossible to ensure that the FSG that is measured is perfectly cylindrical and free from kinks in the surface of the Mylar and copper elements. This can account for other differences in the  $S_{11}$  magnitudes and also why the modelled FSG with the dielectric has a resonance shifted down in frequency by 100MHz compared with the measured  $S_{11}$  response. Another contributor to this 100MHz shift must also be due to the fact that the model with the dielectric has a symmetry boundary. The difference between the whole element and half element models suggests that the effect of the symmetry boundary could account for up to half of the observed 100MHz shift.

The final line on the graph was that of the simulated  $S_{11}$  for the solid waveguide junction with the mylar dielectric tube, without any conducting elements of the surface and the polystyrene plug. This simulation was carried out over a restricted frequency range to ensure that the dielectric tube was not acting as a guiding structure in its own right and that the results were similar to those given in chapter 3 when a similar structure was measured. The fact that the obtained results are very low at less than  $-20\text{dB}$  and a straight line, not following the trends of the simulations with elements, show that the dielectric on its own is not responsible for S parameter responses that were observed. The simulated  $S_{11}$  response for the mylar tube was of the same order of magnitude as that of the measurement from chapter 3 and had the same trend with  $|S_{11}|$  slowly decreasing with increasing frequency.

### 5.3.2 HFSS Field Plots of the Six Element Whole Ring FSG Model at 14.7GHz.

The field plots from the HFSS package reveal a large amount of information about the way in which the fields propagate in the FSG and the transition from the solid

waveguide. From Figure 5-9 it can be seen that in the six element whole ring model there is a minimum in the  $S_{11}$  response at 14.7GHz, where it is well matched to the feed. It was decided to initially model the fields at this frequency as there would be little reflected energy observed travelling back down the structure, which may confuse the field plots somewhat. Field plots were then taken at other frequencies moving both up and down the spectrum, in particular looking at 15.35GHz the resonant frequency predicted by the Loukos program [2]. In every field plot in this section the input  $TE_{11}$  field of the feeding solid waveguide is linearly polarised along the y axis such that E field vector with the largest magnitude passes through the mid point of the gap between two adjacent elements on the surface of the FSG. The model is orientated such that the z axis lies along the axis of the FSG and solid circular feed waveguide and consequently any cross section plane lies parallel to the x and y axis. The junction discontinuity between the FSG and the solid waveguide lies entirely in the xy plane where  $z=0$ .

The first field plot,  $|E|$  shown in Figure 5-10, is on a cut plane through the model along the z and y axis, the plane where  $x=0$ . The field points with the highest magnitude are shown in red and the weakest field strength in blue. The solid waveguide feed is shown on the left-hand side of the plot where no colour has been filled external to the waveguide walls. The FSG elements are just visible in yellow, with three being shown across the diameter of its cross section. The remainder of the cross section outside the FSG is free space out to the radiation boundary. The junction is clearly seen as the point where there is a discontinuity in the boundary dimensions; the step in the plotted colour map.

The plot shows a small amount of field on the outside of the FSG elements with the majority of the field contained within the radius of the FSG. The almost rectangular shape of the area of high electric field strength is exactly as would be seen within a conventional solid waveguide p430 of [3]. The lines of dark blue colour between these high field areas are the field nulls for the mode within the FSG; the distance between the field nulls being the half FSG guide wavelength. This is one magnitude plot, where the input phase was zero degrees, from an animation where the input phase was varied from  $0^\circ$  to  $180^\circ$ , that showed the field propagating from  $-z$  to  $+z$

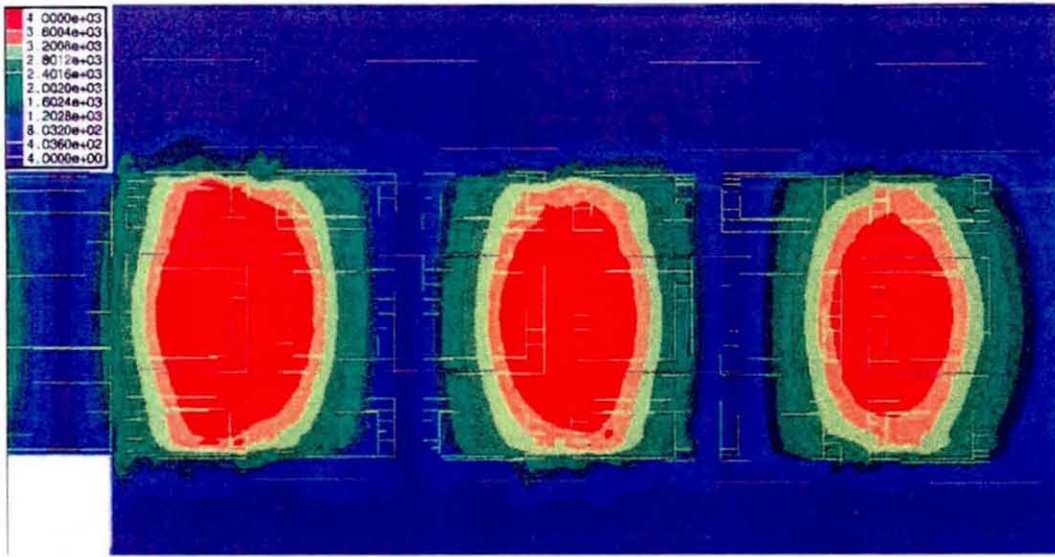


Figure 5-10  $|E|$  for yz cut-plane through axis ( $x=0$ ) at 14.7GHz and I/P phase= $0^\circ$

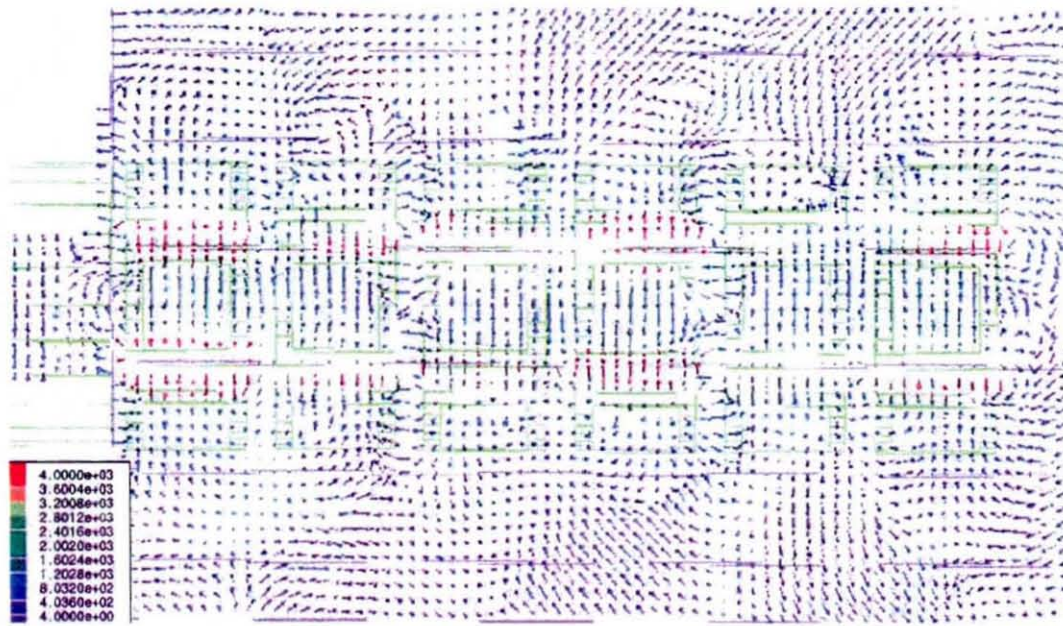


Figure 5-11 E Vector for yz cut-plane at  $x=6.8$  at 14.7GHz and I/P phase= $0^\circ$

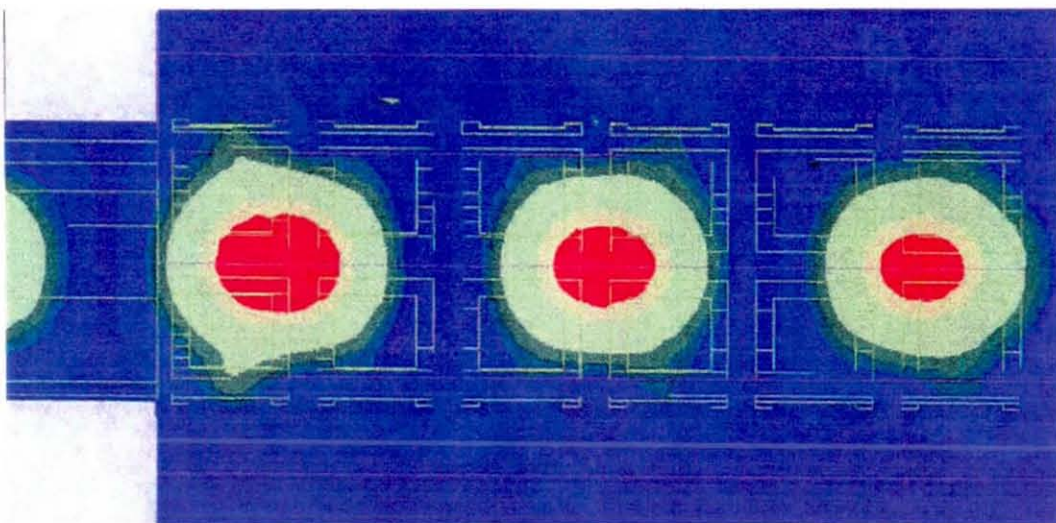


Figure 5-12  $|E|$  for xz cut-plane through axis ( $y=0$ ) at 14.7GHz and I/P phase= $0^\circ$

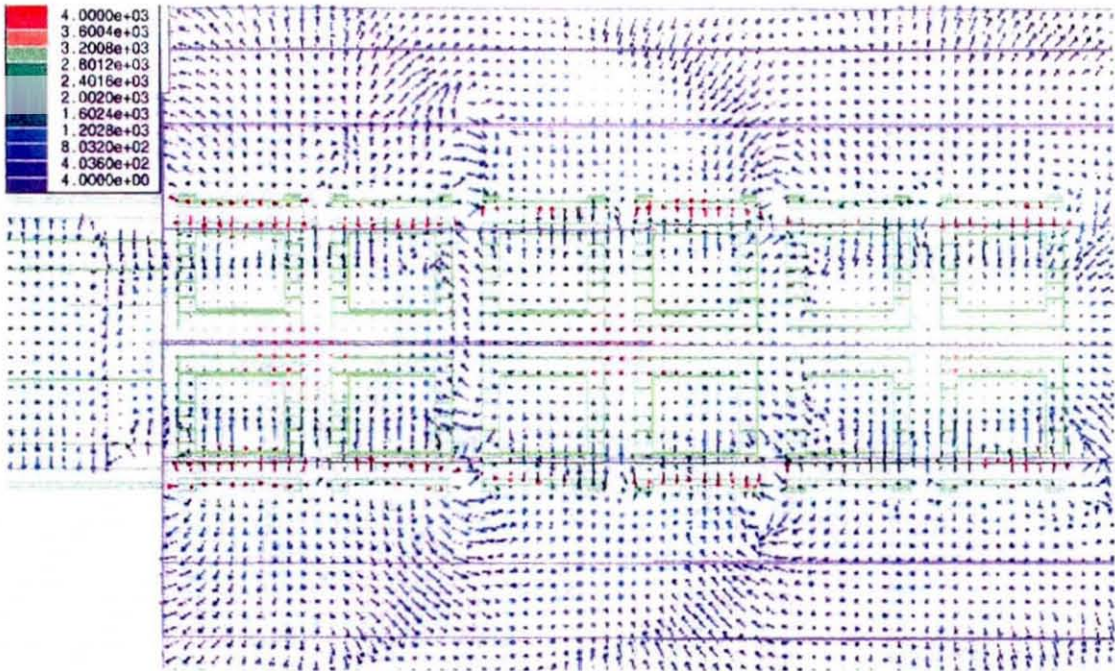


Figure 5-13 E Vectors in xz cut-plane at  $y=3.9$  at 14.7GHz and I/P phase= $0^\circ$

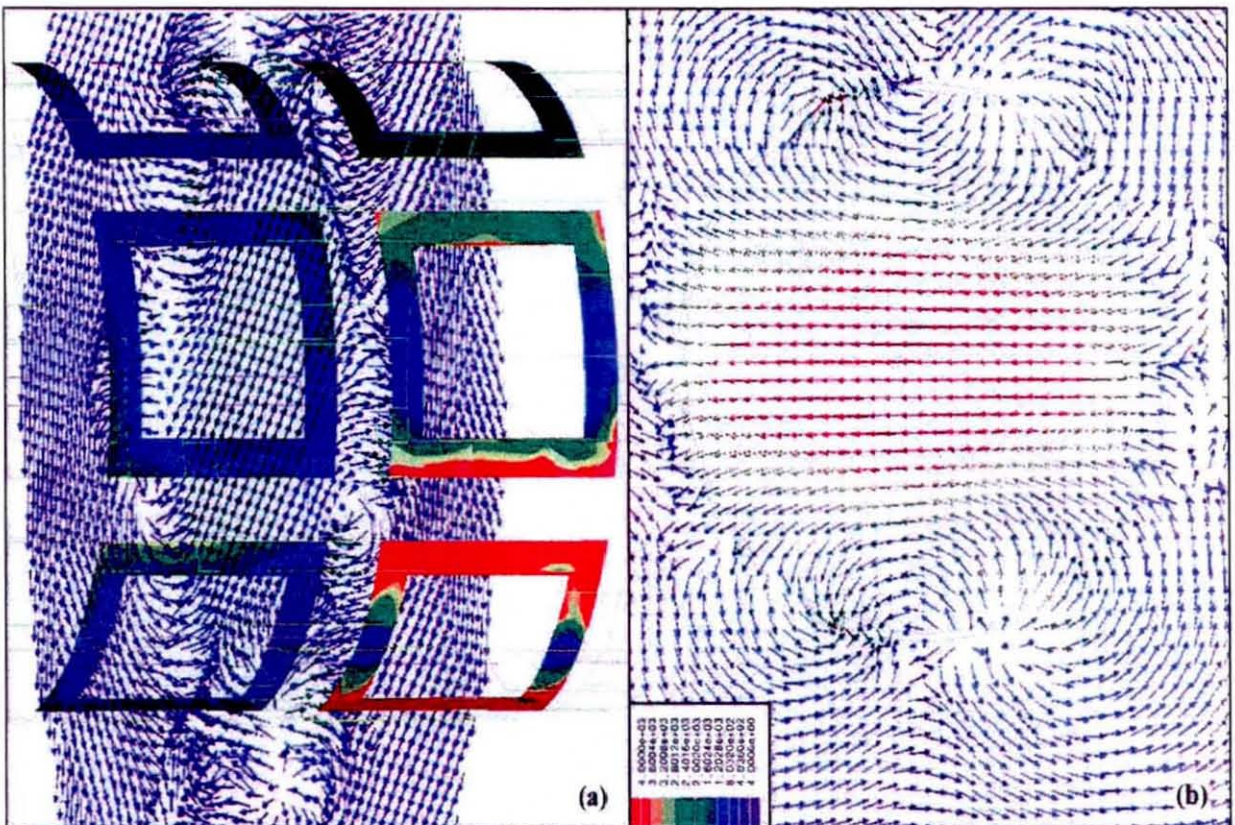
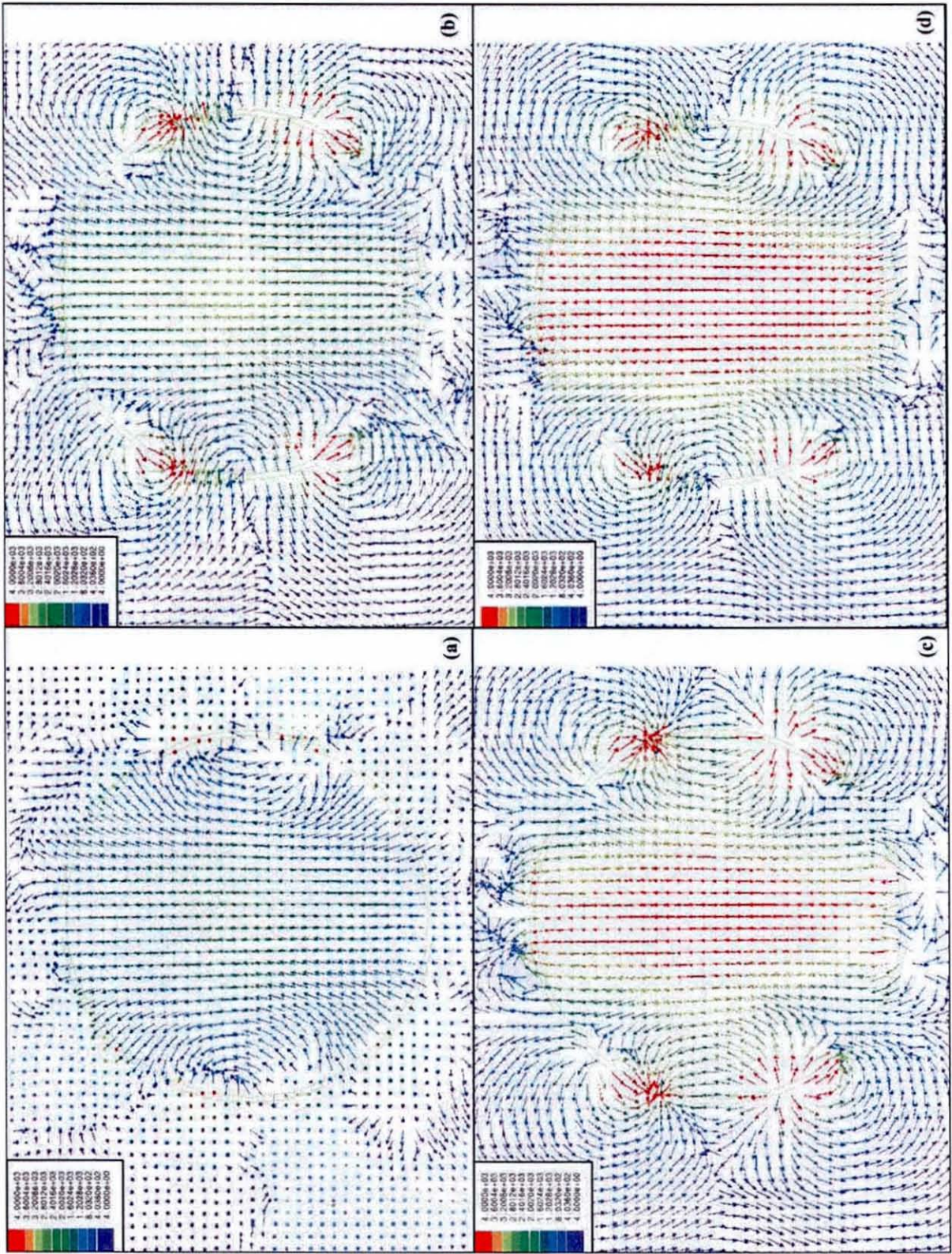


Figure 5-14 Current and E vector information for the 6 whole ring FSG model at 14.7GHz & I/P phase= $0^\circ$ :-

- (a) Current on the surface of 3 of the elements in the first 2 rings, the vector E field shown is in an xy cut-plane 8.2mm from the aperture.
- (b) The vector E field in an xy cut-plane 8.2mm from the aperture.



**Figure 5-15 Four E vector cut-planes for the 6 whole ring FSG model at 14.7GHz & I/P phase=0°:-**

- (a) The vector E field shown is in the xy aperture plane.
- (b) The vector E field in an xy cut-plane 1.2mm from the aperture.
- (c) The vector E field in an xy cut-plane 4.1mm from the aperture.
- (d) The vector E field in an xy cut-plane 7mm from the aperture.

along the inside of the solid waveguide and the FSG. As the fields move to the right the field strength in the FSG diminishes and the areas of high field strength move from the highly rectangular shape seen in the solid waveguide to a very much more elliptical shape.

Up to and at the junction the fields are perfectly contained in the aperture in the conducting discontinuity plane and instantly spread out along the surface of the plane once out of the aperture. The intensity of the spreading field increases with some small distance down the FSG. However, this spreading ceases and is reversed at the point where the first element of the FSG starts. After this point along the length of the FSG the E fields do not appear to extend radially from the FSG with any great magnitude or for any considerable distance. At the end of the FSG, where the elements stop, considerable spread outwards of the E fields can be seen. This is exactly the pattern that would be expected from an open end of a solid waveguide radiating into free space. If it was possible to have placed the radiation boundary further away from the end of the FSG it is expected that radiated fields would clearly be observed propagating spherically outward from the end of the FSG.

Figure 5-10 alone shows very clear evidence that the FSG contains the fields and guides them along the inside of the FSG although it is obviously a lossy structure. Further field plots are included to build of this basic position and give more detail of the propagation method and the operation of the junction. Figure 5-11 shows the cut-plane parallel to that of Figure 5-10 but positioned at  $x=6.8\text{mm}$ . This cut plane passes through the gaps, between adjacent elements, both above and below the element that is uppermost when viewed in the  $yz$  plane. The type of plot has also changed to a vector plot, where the colour of the vector represents the field magnitude and the arrow gives the vector direction in three dimensions. Although the cut-plane gives the vectors on a two dimensional plane only, the field direction is not restricted to being in that plane. Therefore any vector that appears to be shortened has some component in the  $x$  direction and any vector that appears as a point or dot is entirely in the  $x$  direction.

The vectors in the solid waveguide generally have their largest component along the  $y$  axis which is consistent with the expected fields of a  $TE_{11}$  mode p430 in [3]. Inside

the FSG the majority of the vectors are also aligned along the x axis, which suggests that a mode similar to the  $TE_{11}$  mode is propagating in the FSG. This matches the theory put forward in Loukos [2] is that the fundamental hybrid mode in the FSG is indeed composed mainly of a  $TE_{11}$  component. An aspect of the HFSS plotting of vector fields is evident from Figure 5-11, when a vector has a very small magnitude the vector direction becomes difficult to plot. This manifests itself at the null points of the modal field. The vectors cease to line up and start to rotate through  $180^\circ$  in preparation for next half wavelength where the field vectors lie in the opposite direction. The areas within the FSG in Figure 5-11 where the vectors appear to lie parallel to the z axis match exactly the null points in the field magnitude in Figure 5-10. These areas are where the vector orientations “flip” and are very good for visualising the position and shape of wave fronts in the HFSS plots. This can be seen very well outside the FSG where these regions of vector orientation flip extend outwards and then curve, increasing back towards the junction.

This is the shape that would be expected if a wave front were radiating away from the wall of the FSG. As Figure 5-10 suggests that the FSG is lossy, due to the decrease in field strength along its length and the theory suggests that the propagation should be in the form of a leaky mode when radiation from the surface would be expected. The reason that this radiating E field is not seen in Figure 5-10 is that the radiation is weak and the field magnitude is small, and is below the value at which the next colour contour is plotted. A good match between the position of the areas of highest field intensity is seen between Figure 5-10 and Figure 5-11 although the highest vector field strengths (shown in red) appear to be between adjacent longitudinal arms of the first, second, fourth and sixth rings of elements. More will be explained about the significance of this later in this section, but for now it must be noted that the field maximums lie between the elements and not at the centre of the FSG.

The cut plane for the magnitude plot shown in Figure 5-12 has been rotated through  $90^\circ$  about the z axis from its position in Figure 5-10 so that it lies in the xz plane where  $y=0$ . The field in the feed waveguide is identical to that in Figure 5-10 and is as expected for a slice through the centre of a  $TE_{11}$  mode, see p430 in [3]. The contours

of constant magnitude being fairly circular in shape with a circular area of maximum field halfway between two null points, the second null point is not shown on Figure 5-12. In the FSG the field shape generally retains the same shape as that of the field in the solid waveguide. However, there are points where the field varies from the circular shape, where the field bulges out through the centre of an element. The amount that the field bulges out through the element centre seems to be linked to the proximity and size of a field maximum to the element centre. This is the most obvious sign so far that the containment induced by the FSG elements is far from perfect. Also visible is the same trend, as in Figure 5-10, that the field strength decreases as the field propagates down the FSG.

At the junction the field confinement at the discontinuity is far better and although some field exists outside the FSG radius along the conducting plane, the magnitude is not as high and it does not extend as far as observed for the yz plane. However the fields that appear to propagate away from the side of the FSG do show up in light blue as the fields that propagate in this cut are of a higher strength than before. When the animation was run for changing phase the light blue field strengths exterior to the FSG propagated away from the FSG surface at some angle from its normal as would have been expected for a leaky mode. Spherical type radiation is again observed from the end of the FSG.

Figure 5-13 is again an offset cut-plane, but this time parallel to the xz axis at  $y=3.9\text{mm}$ , showing the three dimensional vectors of the E field sample on that two dimensional plane. The cut-plane was positioned so that it passed through the centre of the gaps between two sets of adjacent elements. The gaps in this instance were the first ones reached on either side of the FSG when the cut-plane was move from  $y=0$  along the positive y axis. The majority of the vectors are end on to the plot as would be expected for a  $\text{TE}_{11}$  solid waveguide mode that was viewed looking down in the direction of the polarisation vector. The mode in the FSG again conforms to the hypotheses in [2] that the hybrid field of the fundamental mode in the FSG would consist mainly of TE type modes, with most of the vectors pointing in or out of the plane of the cut.



The high field magnitudes, vectors coloured red, can again be seen in identical positions as the field maxima seen in Figure 5-12. The vectors that show the highest field strength are again between the longitudinal arms of the elements on either side of the gap through which the cut-plane passes. This is to be expected as both vector cut-planes pass through the same gap. The flipping of the vectors along lines of low field strength at nulls is also more clearly visible in Figure 5-13 than it is in Figure 5-11. The wave front that is shown in Figure 5-13 outside the FSG surface is clearly shown as curved surfaces which move away from the surface at some angle as the animation in phase is run. Note also that these wave front nulls also lie halfway between the adjacent areas of higher field intensity that were seen to propagate away from the external surface of the FSG in Figure 5-12.

The two plots in Figure 5-14 (a) and (b) show the cross sectional vector E field in the gap between the first and second ring of elements, 8.2mm from the waveguide junction and the current that exists on the surface of the elements in these first two rings. Figure 5-14 (b) is viewed from the normal to the xy cut-plane along the z axis and so the FSG elements are not visible as they are being viewed edge on and have been modelled as infinitely thin conducting two dimensional sheets. Figure 5-14 (a) is viewed at an angle to the cut-plane and so that the elements and the cut-plane are visible simultaneously. The field on the cut plane is the same vector E field, but the elements have the magnitude of the current shown as a colour coded contour map on their surface. The colours of the vectors and current magnitudes on the elements may appear different but this is due to an in built HFSS shading tool that cannot be turned off. It makes the two dimensional object appear three dimensional by changing the colour, however this makes it difficult to compare the relative field or current strengths. It is however still the best way for HFSS to display this information.

The vector plot in Figure 5-14 (b) looks almost totally  $TE_{11}$  inside the radius of the FSG elements. It has the characteristic maximum field magnitude in the centre of the FSG with vectors all lining up in a straight line across the centre of the FSG and curving more until they become semi-circular at the edges of the circle, see p430 in [3]. However, as there is no confining conductor on the FSG surface, the fields continue onward out into free space. The fields that pass out of the top of the FSG, where the polarisation vector crosses the FSG circumference, bend back around

towards the FSG surface at  $90^\circ$  to the polarisation vector. Around the circumference of the FSG surface there are many points where the field vectors have either some small or large z component. This can be seen in (a) where the E fields are coupling from the edges of the first ring of elements to the adjacent edges of the second ring of elements.

Also on each side of the circumference, just below the line at  $90^\circ$  to the polarisation vector, is a point from which field vectors appear to emanate and just above the line is a point to which field vectors appear to converge. If these points are traced to the current plot in (a) it corresponds to points in the gap just above the two longitudinal arms with red current magnitude of the lower left hand element. This element and the one on the exact opposite side of the FSG have the highest current magnitudes and from the animation resonates like a loop antenna. The centre of the top and bottom circumferential arms always having null points and the longitudinal arms having currents alternating from a maximum along its length to zero and then back to maximum. This is why the E field vectors appear to flow from one longitudinal arm of this element to the other. One longitudinal arm has the current moving in the positive z direction and the other must have the current flowing in the negative z direction in order to obey Kirchofs current Law. By Maxwell's equations the E fields must therefor appear to flow from one arm to the other.

The element shown in the centre of the right hand ring in (a) has a very different current distribution from that of the bottom element. The current in the two longitudinal arms is unbalanced, with the arm nearest to the bottom element having a much high magnitude. However the higher current is not uniform across the width of this longitudinal arm. The high current magnitude appears only down the bottom edge of the arm and it is thought that this is most likely to be an impressed current from the neighbouring element. The top element shown on the right hand ring is a mirror image of the centre element because the field polarisation vector passes through the centre of the gap between them.

The current on the second ring of elements has not yet become very intense as the field maximum has not yet reached the proximity of the second ring and it is the

proximity of the field magnitude which gives rise to the very high currents seen on the element surfaces. Although a similar type of distribution of current to that on the first ring is evident on the surface of this ring it has a much reduced magnitude.

Figure 5-15 shows four cross sectional E vector field plots, (a), (b), (c) & (d), that show how the E field changes from the aperture to the field observed at  $z=8.2\text{mm}$ , which was shown in Figure 5-14. Particular points are chosen along this 8.2mm length to illustrate all the possible field characteristics in the vicinity of the first ring of elements. (a) is a cross section through the aperture plane at  $z=0$ . The expected  $TE_{11}$  E vector field is evident, but is not the only mode present in the aperture. Around the aperture edge, especially in the vicinity beneath the two elements with very high currents seen in Figure 5-14 (a), there are some vectors with components in the z axis direction. A true  $TE_{11}$  field would have no such component it is, by definition, a mode with only transverse E fields. The presence of the FSG has altered the fields around the edge of the aperture so that the field is matched into the FSG, however, despite the presence of these higher order waveguide modes the aperture field appears to be overwhelming composed of a  $TE_{11}$  mode. The fields outside the aperture on the conducting plane are not wholly axial as the boundary condition for a perfect conductor dictates. The plot shows a small transverse component to the field, but this is very small and due to numerical inaccuracies.

The next cut-plane (b) is placed such that  $z=1.2\text{mm}$  from the aperture. This cut plane passes through each element in the first ring, close to the centreline of the bottom circumferential arms. In this cut plane there are six strips of metal which almost form a complete circle around the FSG, the gaps between the elements accounting for less than 20% of the circumference. The two elements at the left and right hand side of the FSG in the plot have fields internally that emanate away from half of it below the centreline of the FSG and rejoin the same element above the centreline. The semi-circular curve that these fields follow from the lower half to the upper half is similar to that which is seen in a standard  $TE_{11}$  field, but more exaggerated with the fields seeming to curve further into the centre. The cause of this is the currents in the vertical arms, which cause the very high fields previously seen in the gaps between the adjacent elements. The vectors of these high magnitude fields lie in the direction opposite to that which would normally be seen in a  $TE_{11}$  mode. These are the fields in

red in (b) and can clearly be seen to go from the elements at the top and bottom of the cross section as viewed to the elements at the left and right of the FSG. This causes the extra curvature in the fields at the left and right of the internal cross section. These then are the basic features of the FSG fields that have been observed. The centre strip contains fields that are generally similar to a  $TE_{11}$  mode, but the fields to the left and right of this strip have fields that are obviously far more complex.

(c) is a cross section at  $z=4.1$  mm through the centre of the element. The very high fields emanating from and to the currents in the longitudinal arms of the left and right elements are even more evident in this plot. In this case there is no metal connecting them together as in (b) and so the field is not so curved as before in this area and it can take a direct path from one arm to another. The apparent leakage of the field through the centre of the elements seen in Figure 5-12 is directly attributable to the fact that the field taking a direct path from one arm to another is a reasonably high strength field. The coupling of E fields from these arms to the impressed currents in the upper and lower elements is also very strong. This field pattern different from that in (b), but still has predominantly  $TE_{11}$  fields in the centre strip and more complex fields to the left and right. Note also that the field magnitude in the centre of the FSG has increased. This is not a consequence of the cut-plane being in the centre of the element, but the fact that the input phase of zero degrees puts the first field maximum at  $z\approx 8$  mm as seen in Figure 5-12.

Finally plot (d) is the cross section through the centreline of the circumferential conductor of the elements of the first ring at  $z=7$  mm. As could be expected the field here is similar to that seen in (b), except that the vector magnitudes are higher as the cut-plane is closer to the field maximum value. This can easily be explained because the cross section of the structure seen here is identical to that seen in the cross section of the lower arm.

### 5.3.3 HFSS Field Plots of the Six Element Whole Ring FSG Model Over an Extended Frequency Range.

Having investigated the fields of the FSG and junction at 14.7GHz where the match was very good the frequency was changed and to frequencies where the match was not as good to observe the change in the fields. The first frequency chosen was 13.7GHz as this was at the lower end of the band of simulated frequencies and the match was not very good, at  $S_{11}=-8\text{dB}$ . In this section the polarisation vector of the feed  $\text{TE}_{11}$  mode is identical to that used for the 14.7GHz simulation, i.e. along the y axis.

Figure 5-16 shows four plots showing the vector E fields in the cross sectional cut-planes of  $z=0\text{mm}$  (b), 1.2mm (c), 4.1mm (d) and 8.2mm (a) along with the currents on three of the elements on one side of the FSG on the bottom 2 rings of elements (a). The current distributions on the surface of the elements are similar to that seen at 14.7GHz. The highest magnitude is seen on the element that is on the lower right hand side, which is in an identical position in relation to the polarised field as the lower left hand element in Figure 5-14 (a). At 13.7GHz the element still has large current flowing the longitudinal arms and a null in the middle of its circumferential arms. The centre element in Figure 5-16(a) has a much larger field flowing in the longitudinal arm adjacent to the right hand element and the field flowing elsewhere on its surface are also larger than seen before. The currents on the second ring of elements are similar, but lower in magnitude than at 14.7GHz. The effect of this can be seen in the cut-plane at  $z=8.2\text{mm}$  because the coupling field between the elements is very large.

This increased E field coupling between the elements is seen in both (c) and (d). The vector plots in both cases being dominated by the inter-element coupling between the elements on both the right and left hand sides of the plots. Some semblance of the  $\text{TE}_{11}$  type vector field can be seen in (a) and (c) although it is very weak in strength. The field plot in (d) coincides with a null in the  $\text{TE}_{11}$  incident field and so the vector field is dominated completely by the field coupling between elements. A visual inspection of this plot reveals how hard it would be to extract the modal amplitudes of

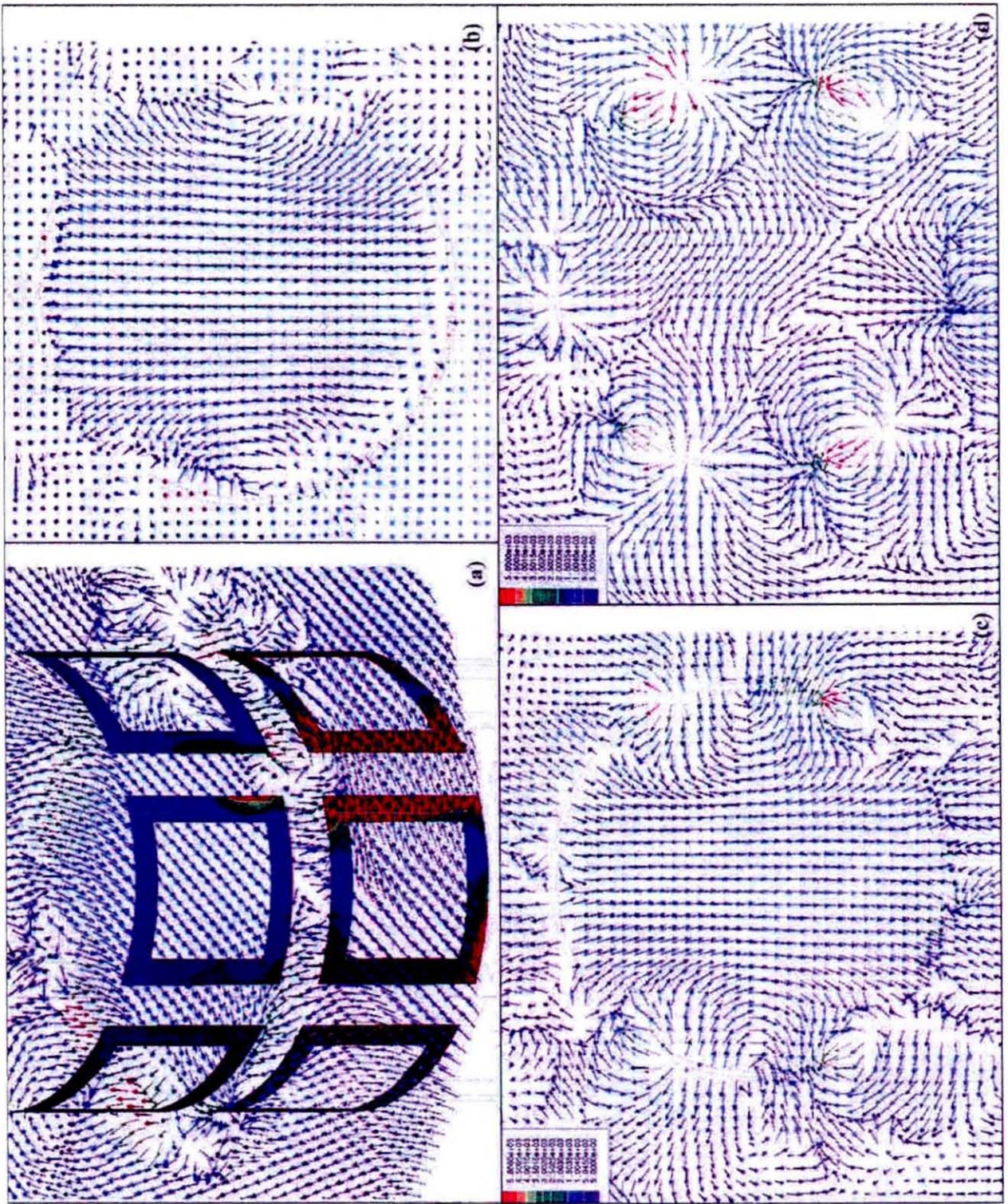


Figure 5-16 Current and E vector information for the 6 whole ring FSG model at 13.7GHz & I/P phase=0°:-

- (a) Current on the surface of 3 of the elements in the first 2 rings, the vector E field shown is in the xy cut-plane 8.2mm from the aperture
- (b) The vector E field shown is in the xy aperture plane
- (c) The vector E field in an xy cut-plane 1.2mm from the aperture
- (d) The vector E field in an xy cut-plane 4.1mm from the aperture



Figure 5-17 |E| volume plot viewed from y axis at 13.7GHz I/P phase=0°

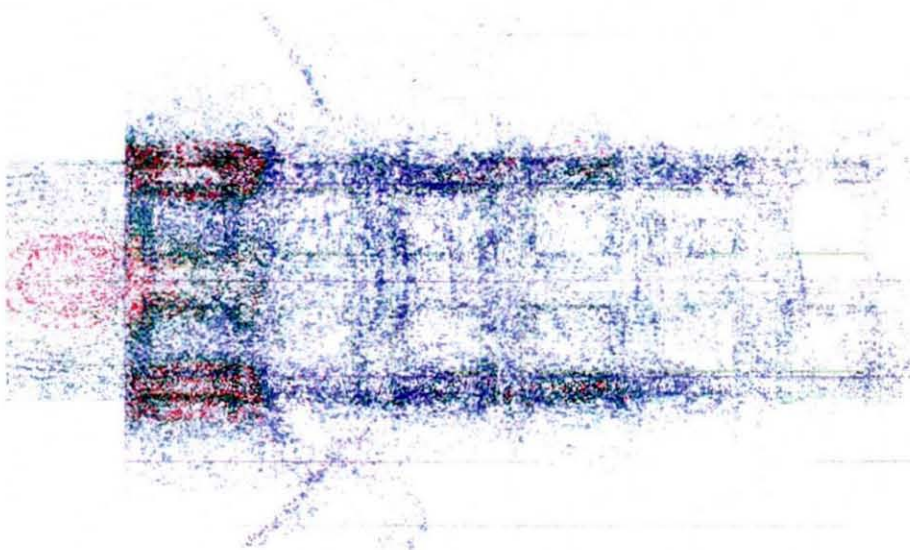


Figure 5-18 |E| volume plot viewed from y axis at 13.7GHz I/P phase=60°

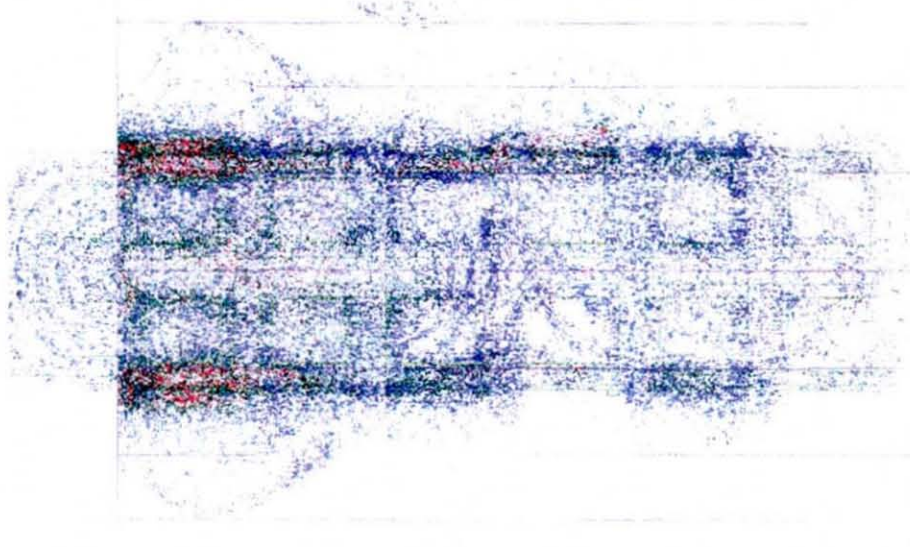


Figure 5-19 |E| volume plot viewed from y axis at 13.7GHz I/P phase=120°

the possible component modes of this field. The aperture field in (b) shows the  $TE_{11}$  of the input field from the solid waveguide clearly, however, unlike the 14.7GHz aperture field, the 13.7GHz field shows considerable distortion from the expected  $TE_{11}$  vector plot. There is heavy distortion on both sides with many longitudinal vectors showing coupling to the lower element ring. This increased distortion of the aperture field would be sufficient to cause the very poor matching seen in the  $S_{11}$  value at this frequency.

To show the movement of the fields along the FSG it was decided not to plot multiple cut-planes, but to use the final type of HFSS field plotting output the magnitude of the E field volume plot. The volume plot in Figure 5-17 shows the six element whole ring model viewed from the y axis looking down on the element surface. The colour coded 'snow storm' of points that correspond to the magnitude of the E field has been superimposed on this drawing as if the fields were being viewed from the same place. The phase in this plot is set to  $0^\circ$ . To show how badly the fields propagate along the FSG, Figure 5-18 shows the same model except with the phase of the input changed to  $60^\circ$  and Figure 5-19 has the input phase changed again to  $120^\circ$ . These three figures clearly show the field propagating in the solid waveguide, with the area of maximum field density, of the  $TE_{11}$  mode, moving from left to right as the input phase increases. Although difficult to tell from the printed plot the animation of this clearly showed the expected increase in guide wavelength because the frequency of operation was lower. In all three plots the only significant very intense inter-element coupling fields are around the first ring of elements. The link observed in the previous section that high inter-element coupling occurs near the field maxima has disappeared. In fact very little field can be seen to propagate inside FSG. Large fields are seen propagating away from the surface at some acute angle, although these are not plotted very well on the graphs.

This all seems to suggest that the FSG has become leaky and does not propagate a well confined field. The very high coupling around the first ring of elements seems to act as a choke to the incident fields in the solid waveguide.



The frequency was increased to 15.35GHz, the theoretical resonant frequency of this FSG, and the volume magnitude of E fields at input phase of  $0^\circ$ ,  $60^\circ$ ,  $120^\circ$  were plotted in Figure 5-20 to Figure 5-22. These plots clearly show that the field is well confined. There is no appreciable field propagating away from the surface of the FSG, although there is a large field attached to the outside of the edge elements as noted in Figure 5-12. This external field is associated with the areas of very high inter-element coupling and decays away very rapidly in radial direction. The large inter-element coupling fields again seem to be associated with the positions of the field maxima inside the FSG. These field maxima propagate seamlessly from the solid waveguide into and down the FSG. The coupling moves down the FSG and does not sit only on the first ring of elements.

A pulsing effect is seen in the field maxima as they propagate down the structure, the maxima in Figure 5-22 are much larger than those in Figure 5-20 or Figure 5-21. This is always a sign that a standing wave is present in the structure. The point at which the pulsing ends in a propagating field's path is the point at which the standing wave is being generated from. In this case the pulsing continues down the entire length of the solid waveguide and the FSG. This means that the cause of the poor  $S_{11}$  measurement at this frequency is not the junction between the solid waveguide and the FSG, but the mismatch between the FSG and free space. This is good proof that at this frequency the FSG is acting more like a transmission line and less like an antenna structure. The good match seen in the 14.7GHz simulation is due to the fact that the FSG is still reasonably well matched to the solid waveguide at this frequency and the FSG is well matched to free space. The FSG at this frequency is operating as an effecting transition between the waveguide and free space.

The wavelength of the fields in the structure are shorter than seen in any of the previous simulations, as would be expected at a higher frequency. However, that fact that the wavelength in the FSG is about the same as that in the solid waveguide is another mark of how good the match between the FSG and the solid waveguide is at this frequency.

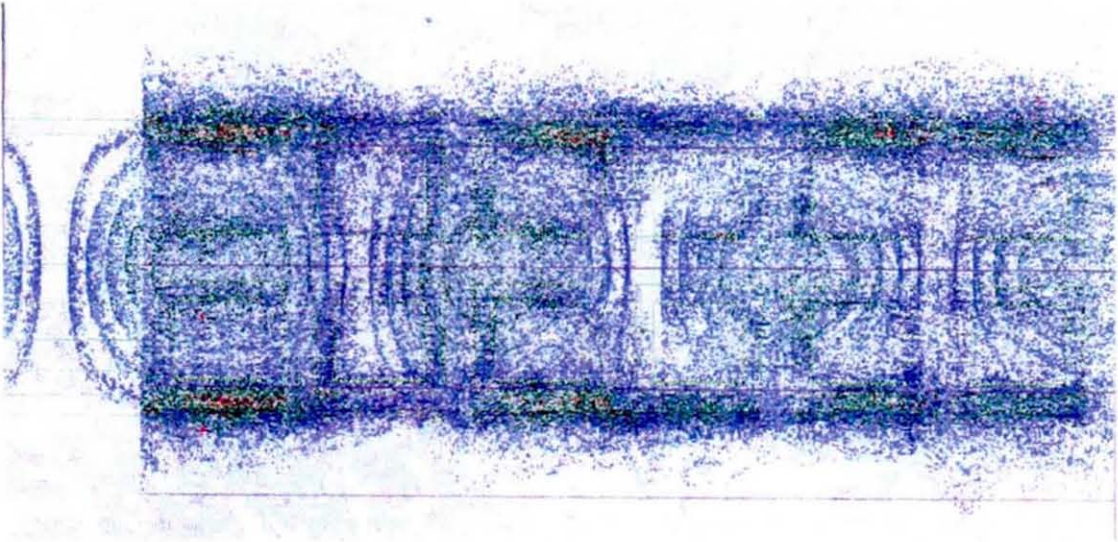


Figure 5-20 |E| volume plot viewed from y axis at 15.35GHz I/P phase=0°

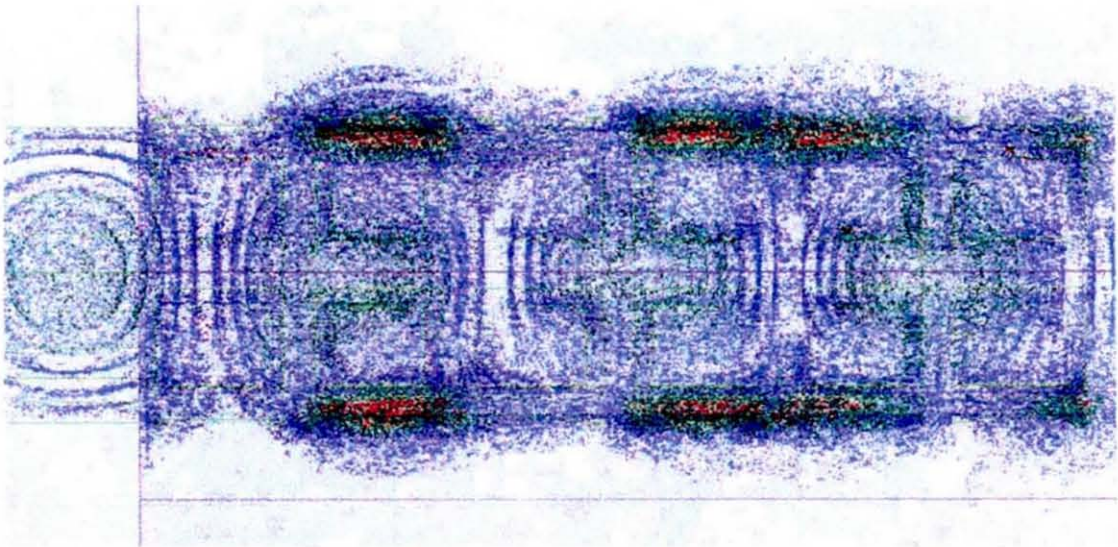


Figure 5-21 |E| volume plot viewed from y axis at 15.35GHz I/P phase=60°

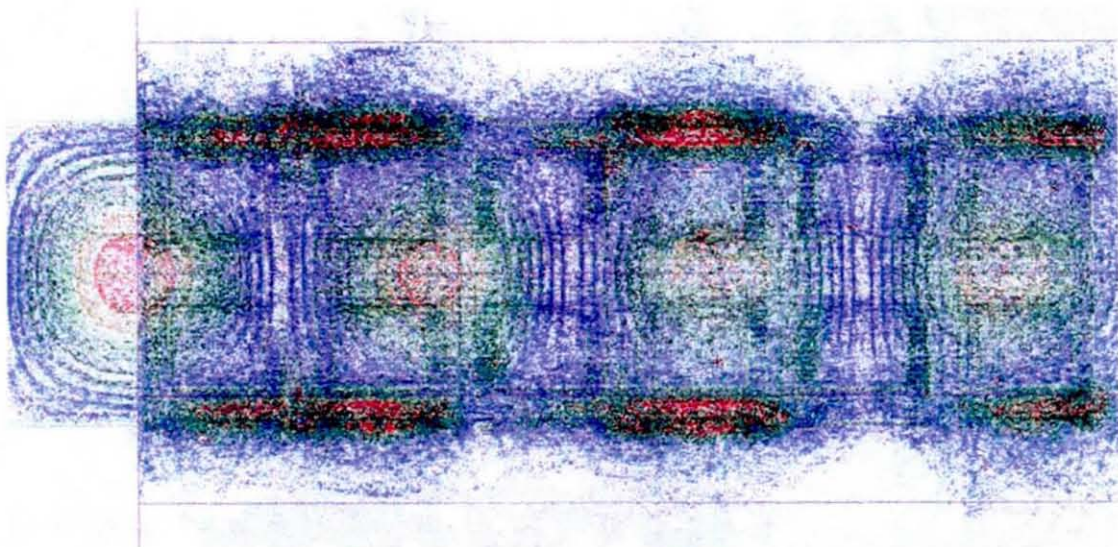


Figure 5-22 |E| volume plot viewed from y axis at 15.35GHz I/P phase=120°

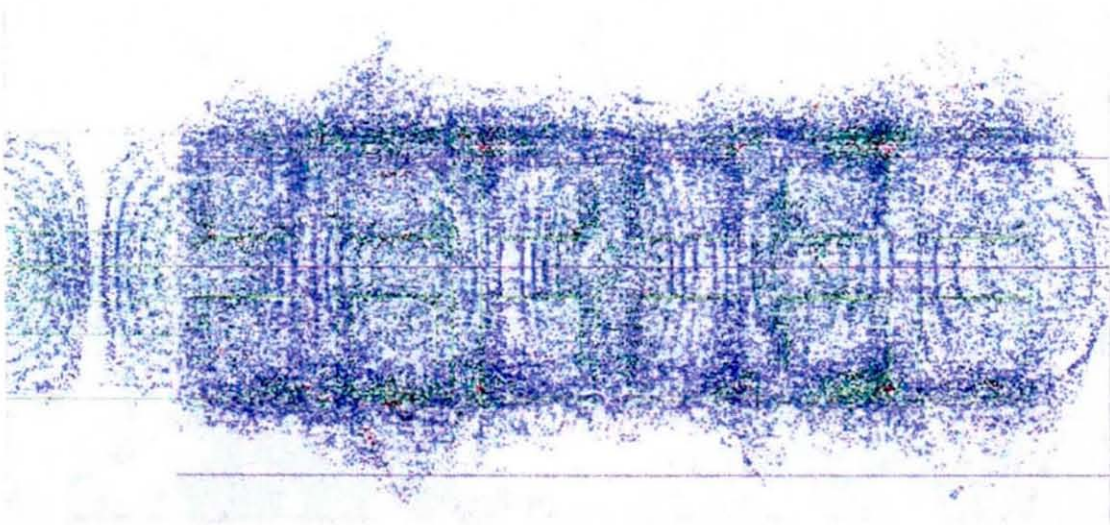


Figure 5-23 |E| volume plot viewed from y axis at 16.6GHz I/P phase= $0^\circ$

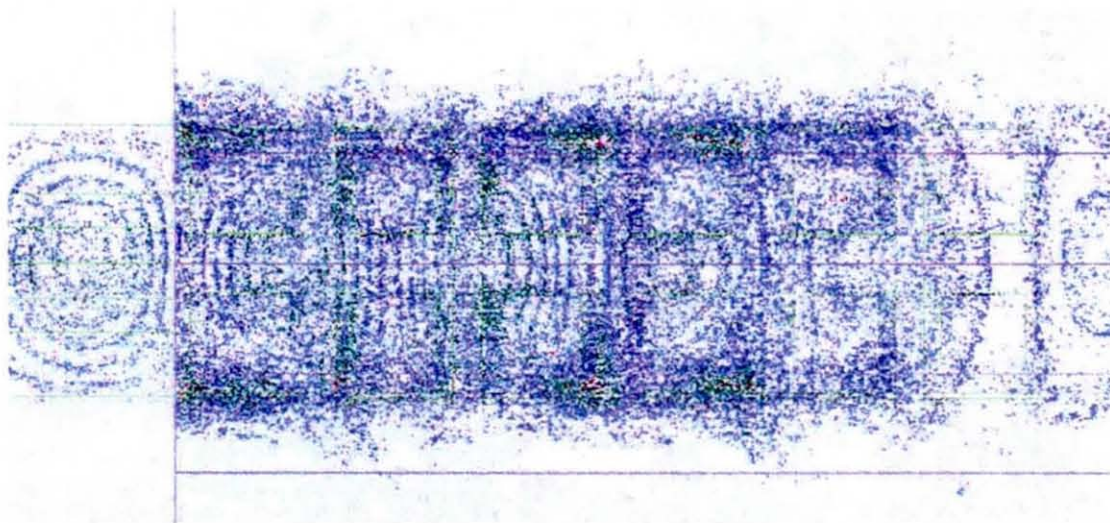


Figure 5-24 |E| volume plot viewed from y axis at 16.6GHz I/P phase= $60^\circ$

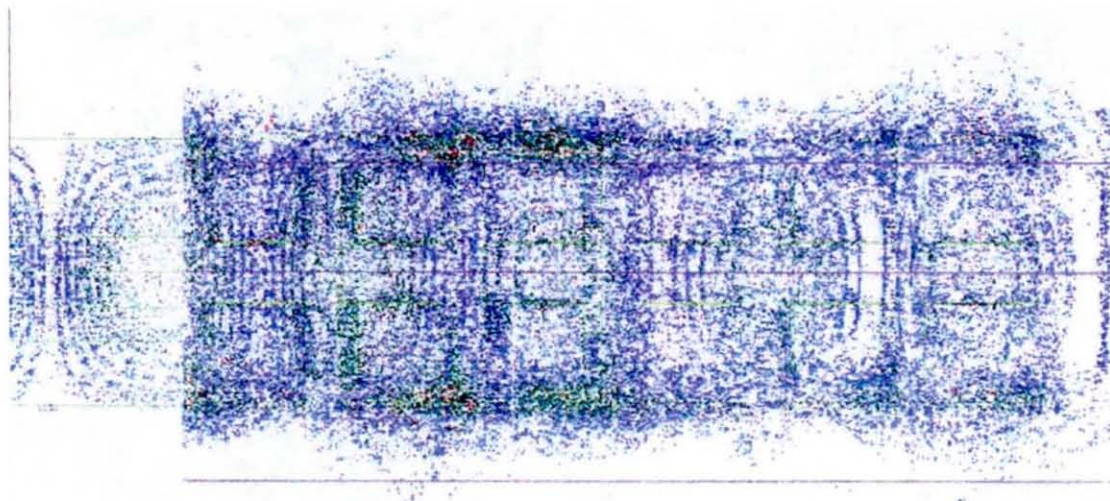
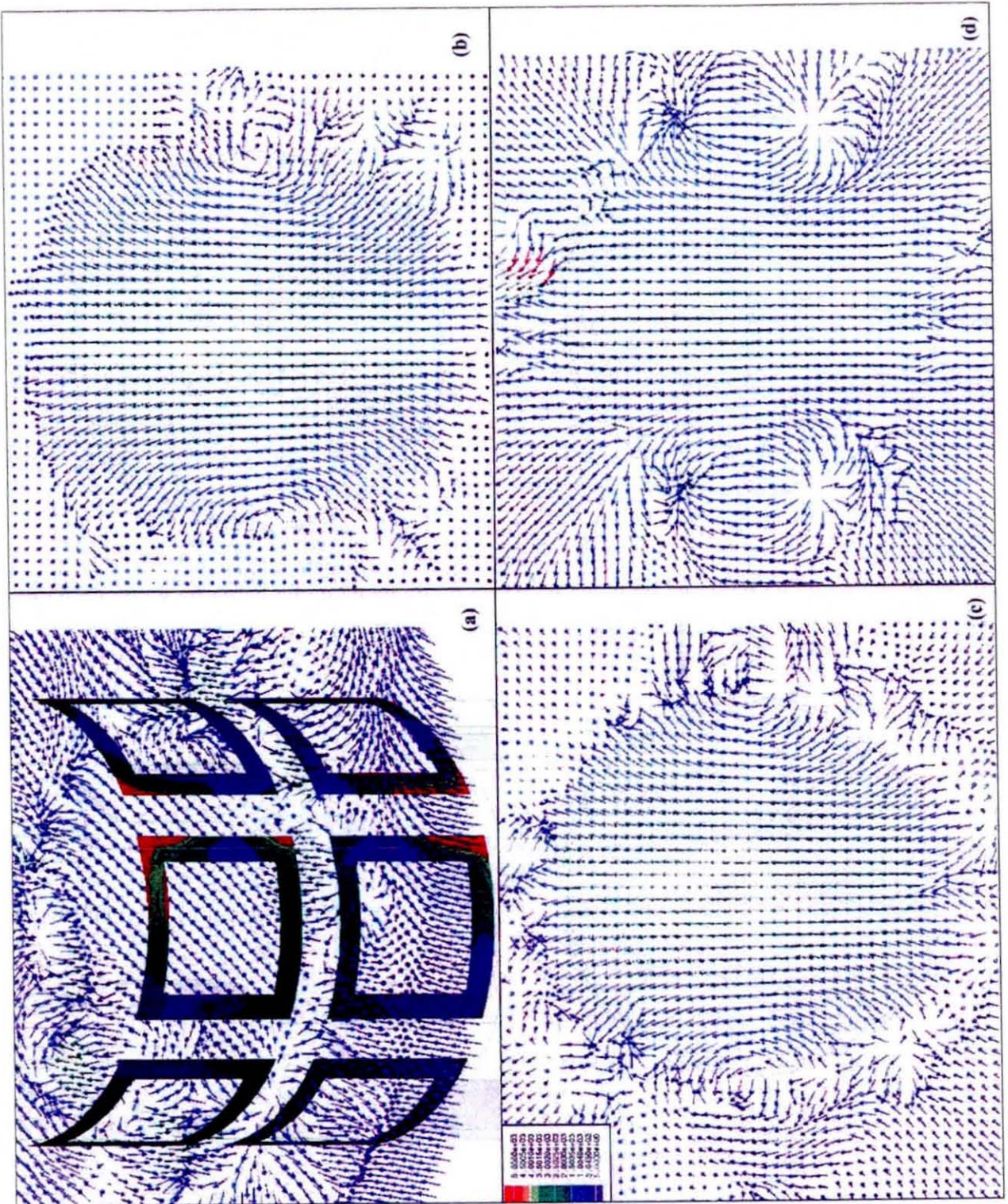


Figure 5-25 |E| volume plot viewed from y axis at 16.6GHz I/P phase= $120^\circ$



**Figure 5-26 Current and E vector information for the 6 whole ring FSG model at 16.6GHz & I/P phase=0°:-**

- (a) Current on the surface of 3 of the elements in the first 2 rings, the vector E field shown is in the xy cut-plane 8.2mm from the aperture
- (b) The vector E field shown is in the xy aperture plane
- (c) The vector E field in an xy cut-plane 1.2mm from the aperture
- (d) The vector E field in an xy cut-plane 4.1mm from the aperture

The frequency was increased again to 16.6GHz, the very top end of the simulated band and where the  $S_{11}$  match of the system was a just reasonable  $-12\text{dB}$ . The volume plots showing the magnitude of the E field were re-plotted for this higher frequency in Figure 5-23 to Figure 5-25. The fields propagate down the structure in the expected manner except that the wavelength in the FSG is now shorter than that in the solid waveguide. The fields appear to be reasonably well contained in the FSG, but closer inspection did reveal a small, but not insignificant field propagating away from the surface of the elements. The field also propagates away from the end of the FSG into free space very well. This combined with an FSG to solid waveguide junction match that does not scatter too much energy is the reason for the  $-12\text{dB}$  match for the model input.

The localised very high inter-element coupling seems to have disappeared and has been replaced by inter-element coupling of moderate field strength along virtually the whole length of the FSG. This still seems to be linked to the positions of the maxima, but the reduced wavelength means that these are now only approximately  $1\frac{1}{4}$  periodic cells apart and hence why a large length of the FSG seems to be excited most of the time.

For the top of the band the plots showing the cross sectional vector E fields and the current on the surface of the elements were again plotted. This is shown in Figure 5-26 and as before the four cut-planes chosen were placed at  $z=0\text{mm}$  (b),  $1.2\text{mm}$  (c),  $4.1\text{mm}$  (d) and  $8.2\text{mm}$  (a). Again the current magnitudes plotted were on six elements of the FSG over the bottom 2 rings of elements (a). The increase in frequency produces different current distributions on the surface of the elements from that seen at  $14.7\text{GHz}$  or  $13.7\text{GHz}$ . The currents of largest magnitude were still present on the elements, or section of elements, away from the point where the polarisation vector crossed the gap between elements. The highest current values were congregated in the corners of the elements and extended down both arms for a short distance. The null points between these current maximums can now exist at the mid point of either the longitudinal or the circumferential arms. Although they do not seem to occur on connected arms at the same time. The currents on the elements are clearly resonating in some higher order state other than that observed previously.

The reduction in the inter-element coupling can be seen in all the cross section vector plots. In (a) the z orientated vector magnitude between the first and second rings is much reduced. In the aperture (b) the similar axial vector magnitudes is again very much reduced. In (c) and (d) the very high intensity vector fields that went from one longitudinal arm to another on the left and right sides are very much reduced in magnitude and are only really noticeable in (d). In all the vector plots the field looks very much more like the standard  $TE_{11}$  field distribution. However the lack of inter-element coupling appears to allow the fields to spread out beyond the radius of the FSG elements. Even in the aperture the field has spread out beyond the confines of the solid waveguide radius. This can be seen to continue down the guide and is very evident in (d) even though this is the plot with the highest inter-element coupling. Although still present the inter-element coupling appears to be of insufficient magnitude to confine the field to the vicinity of the FSG.

#### 5.4 Results for the Twelve Element Half Ring FSG Model with Two Feed Solid Waveguide Ports

The results of the twelve element half ring FSG model were very similar to those obtained for the fourteen and sixteen element models. There were some differences, which will be included in the appropriate area, but essentially the majority of results given in this section are for the twelve element model. These form the representative set of results for the half ring models with a solid waveguide at each end of the FSG.

##### 5.4.1 $S_{11}$ Results for the Half Ring FSG Model – Measured and Simulated.

The  $S_{11}$  results were taken from the feed port of the solid waveguide, which was exciting the FSG. The  $S_{22}$  results were taken from the feed port of the other solid waveguide at the other end of the FSG and were identical to the  $S_{11}$  results. The  $S_{21}$  and  $S_{12}$  scattering parameters were also identical to each other; the system must be fully reciprocal, as would be expected.

The  $S_{11}$  results from the measured FSG1 data from chapter 3 and the twelve, fourteen and sixteen element half ring FSG models is presented in Figure 5-27. The mode in the solid circular feed waveguide (both simulated and measured) is that of the fundamental  $TE_{11}$  mode and so the S parameters, in Figure 5-27 and Figure 5-28 are those for this mode only.

The three simulated  $S_{11}$  plots are very similar, each having the shape of a minimum curve or a “valley”, but with a large amount of ripple in the curve around the minima which are centred roughly on 15.5GHz. In the regions of the curve where no ripple is present the agreement between the curves is very good. The ripple in each plot is a series of peaks and troughs in the plot and they all have roughly similar magnitude, but occur at slightly different frequencies. This is exactly the response that would be expected if a small standing wave were present in the FSG. As the length of the FSG increase the difference in frequency between adjacent peaks or troughs decreases.

Although there is poor agreement between the measured  $S_{11}$  plot and any of the predicted plots, there is very good agreement between the general shape of the  $S_{11}$  plots. The measured plot also follows the general trend of a minimum curve and has a large amount of ripple around the minimum centred roughly on 15GHz. It also has a decreasing amount of ripple in it up to 13.2GHz. Only the twelve element model was simulated at frequencies below 13.5GHz and there is a suggestion that there may be a ripple at the lower end of the band for this model. The  $S_{11}$  of the 12 element model has a sudden dip in its value at 13.5GHz. It was not possible to see if this dip developed into a standing wave ripple as the model would not converge sufficiently for any frequency below 13.3GHz before the simulation died due to a lack of memory resource.

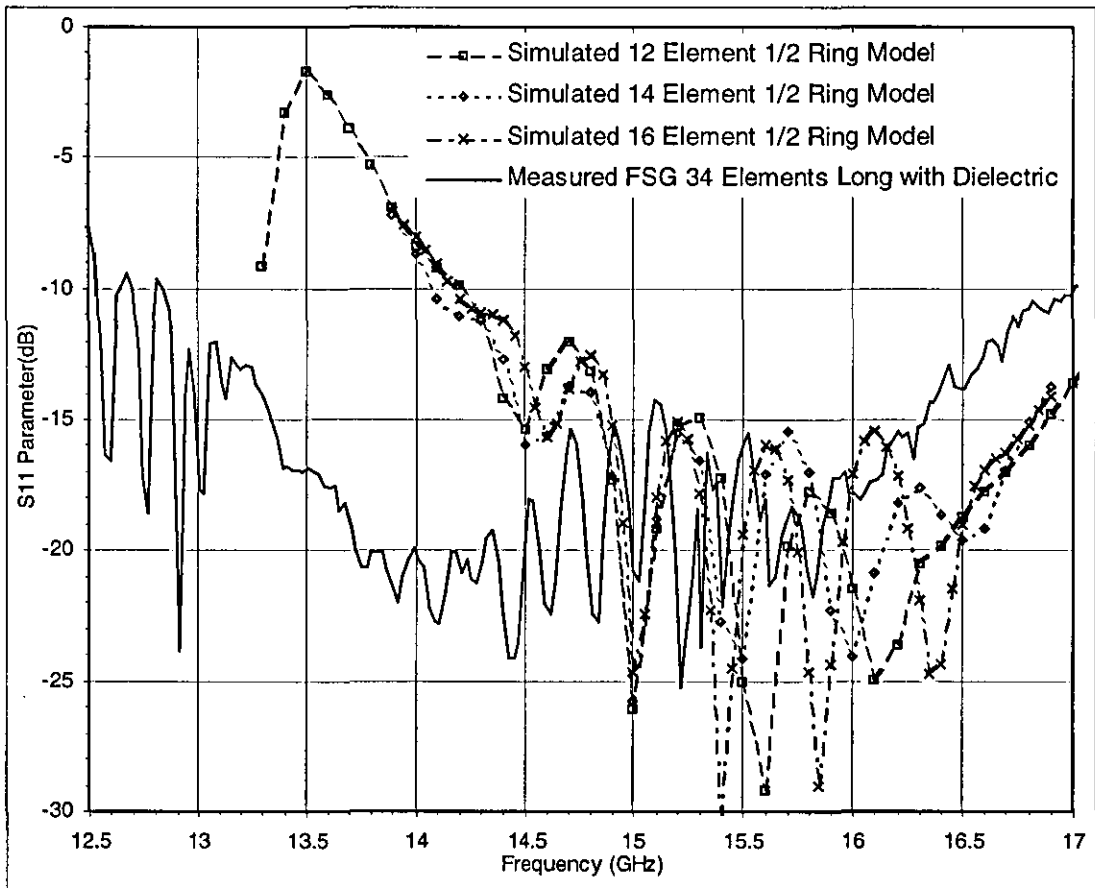


Figure 5-27  $|S_{11}|$  Comparison between a measured FSG, 34 elements long, and the simulated half ring models, 12,14,16 elements long

The agreement between the simulated and the measured results would be improved if the predicted plot were shifted down in frequency by about 0.5GHz. The fact that the Mylar sheet and polystyrene plug included in the structure of the measured FSG is known, from chapter 3, to cause a dielectric loading effect could account for this shift in frequency. The  $S_{11}$  values at frequencies above the ripple in the minimum region would then be very similar. There would still be some difference in the magnitude at frequencies below the ripple, but the difference would be significantly reduced. The reduced  $S_{11}$  magnitudes in the measured results can be explained because the dielectric, ohmic and radiative losses in the structure attenuate all the measured values. The perfect conductors in the simulated models will ensure that the reflected and transmitted power will be the maximum possible value. More energy is also lost from the measured FSG in the form of radiation due to its greater length over which more radiation can take place.



#### 5.4.2 $S_{21}$ Results for the Half Ring FSG Model – Measured and Simulated.

The  $S_{21}$  values plotted in Figure 5-28 are for the same twelve, fourteen and sixteen element half ring FSG models and are compared with the measured values of a real FSG taken from chapter 3. As with the  $S_{11}$  measurements of Figure 5-27, Figure 5-28 shows excellent agreement between the plots of  $S_{21}$  taken for the three different simulations. The plots follow the shape of a maximum curve or “hill”, with the highest value of  $S_{21}$  equal to  $-0.8\text{dB}$  at  $15.5\text{GHz}$ .

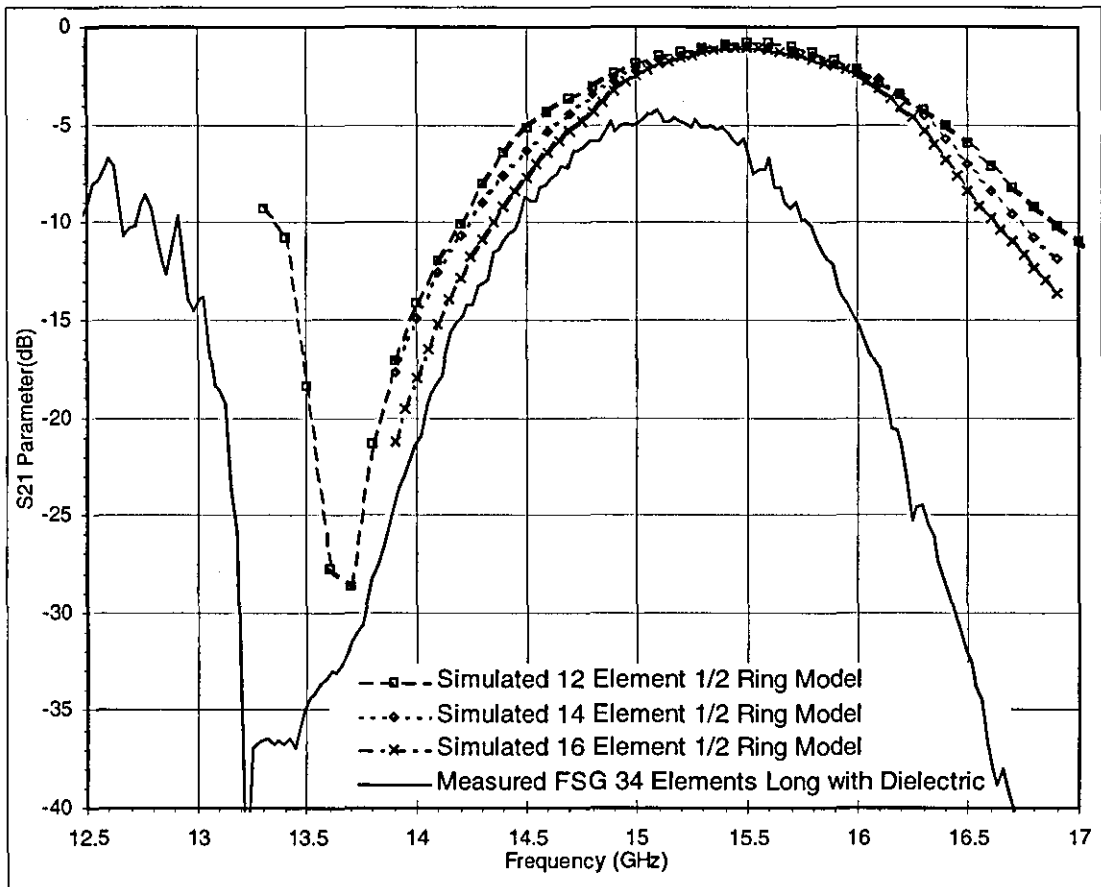


**Figure 5-28 |  $S_{21}$  | Comparison between a measured FSG, 34 elements long, and the simulated half ring models, 12,14,16 elements long**

The only difference between the three simulations is that the bandwidth of the curve is reduced as the length increases. This simulated result, showing that the length of the FSG affects the bandwidth of the  $S_{21}$  response curve, is excellent confirmation of the existence of this effect, which was also observed in the measured results of chapter 3.

The comparison of the simulation with the measured  $S_{21}$  is very good in that the curves have very similar shapes. The maximum value of the measured  $S_{21}$  is  $-4.5\text{dB}$  at  $15.1\text{GHz}$ , which if the affect of the dielectric loading and losses, dielectric, ohmic and radiative are taken into account, could be said to be of an expected level in relation to the simulated values. The maximum portion of the measured curve is also narrower than the simulated curves, which is also to be expected due to the significantly longer length of the measured FSG reducing the bandwidth of the  $S_{21}$  response.

The rapid increase in the  $S_{21}$  value of the measured FSG below  $13.2\text{GHz}$  is seen in the simulated twelve element model at  $13.7\text{GHz}$ , again note the shift in frequency of about  $400\text{MHz}$ . The magnitude of this region of rapidly increasing values is still higher than the measured  $S_{21}$  even when the shift in frequency is taken into account. However, convergence simulation problems prevented further investigation below  $13.3\text{GHz}$  to see if a similar ripple in  $S_{21}$  occurred.

The scattering parameters of the measured FSG and simulated models match very well, given that the memory limitations meant that simulations could only be done for short models with no dielectrics or ohmic losses. They consistently show responses that have virtually identical shape to that of the measured response and that the effect of the differences between the simulated and real FSG is to increase the bandwidth due to shorter lengths, increase the magnitudes due to reduced losses and to add a frequency shift of roughly  $400\text{MHz}$  to  $500\text{MHz}$  due to the lack of dielectric loading. Significantly, the response of the six element whole ring model was also shifted up in frequency from that of the measured values by about  $500\text{MHz}$ .

However HFSS has the ability to excite any mode in the solid waveguide feed. So in addition to the fundamental  $\text{TE}_{11}$  mode in the twelve element half ring FSG model the next higher order mode  $\text{TM}_{01}$  was also excited. The higher order mode was only excited in the twelve element waveguide because its shorter length and reduced memory requirements meant that it could be simulated to a higher frequency than either the fourteen or sixteen element lengths. As a general rule with numerical models, as the frequency increases the number of points required in the mesh increases. The higher order mode was only added to the simulation for frequencies

above 15GHz because the  $TM_{01}$  mode will only propagate in the solid circular feed waveguides above 15.3GHz. Below this frequency it will always be evanescent and so could not propagate down the short length of waveguide to the measuring port.

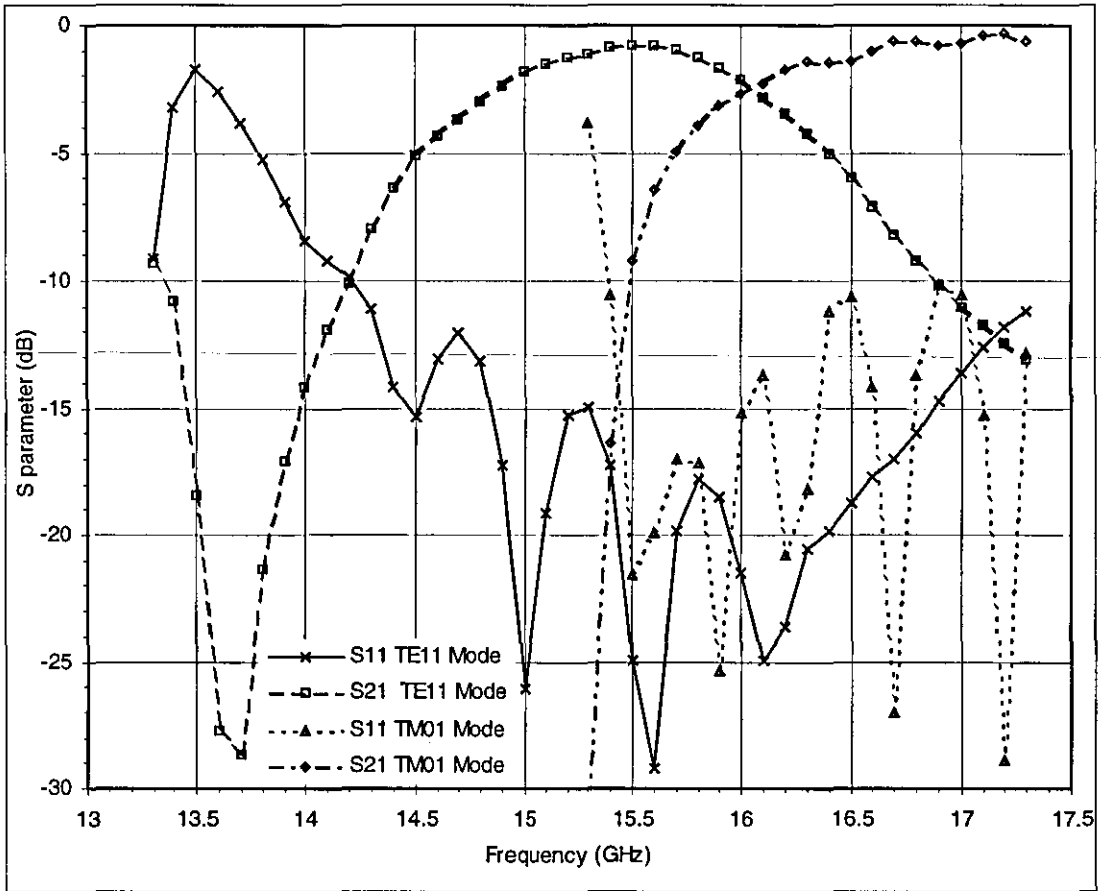


Figure 5-29 Comparison of  $|S_{11}|$  and  $|S_{21}|$  values for the  $TE_{11}$  and  $TM_{01}$  modes of the simulated 12 element half ring model.

The results of this investigation into the higher order mode are shown in Figure 5-29. No measured results are available to confirm the behaviour of the simulated higher order mode as the transitions required to set-up a  $TM_{01}$  mode were not available. However as the simulation has been successful in its prediction of the behaviour of the model with a  $TE_{11}$  mode in the feed waveguide there is no reason to believe that the simulation will not be correct for the  $TM_{01}$  mode feed. The cut-off frequency of the solid waveguide higher order mode is clearly visible at the point where the  $TM_{01}$  mode suddenly begins to propagate after 15.3GHz,  $S_{11}$  rapidly drops and the value of  $S_{21}$  undergoes an equally rapid increase. From 15.5GHz to 17.3GHz, the largest frequency that could be simulated, the plot of  $|S_{11}|$  has a great number of ripples that

increase in magnitude. This suggests a standing wave propagating in the FSG again between the two FSG to solid waveguide junctions.

Unlike the fundamental mode, the  $TM_{01}$  mode also has a small ripple in its  $S_{21}$  response. This ripple starts when the response reaches  $-2\text{dB}$  at  $16.3\text{GHz}$  and has the same periodic wavelength as that of the mode's  $S_{11}$  ripple. After the initial rapid increase in  $|S_{21}|$  at the cut-off frequency, the rate of increase slows, but continues to the end of the simulated region at  $17.3\text{GHz}$ . The average value of  $|S_{21}|$  at  $17.3\text{GHz}$ , excluding the effect of the ripple, is  $-0.5\text{dB}$ . This value is higher than that for the fundamental mode and suggests that there must be better confinement of the  $TM_{01}$  mode along the FSG to give a higher transmission of power to the receiving solid waveguide on the far end of the FSG.

#### 5.4.3 HFSS Field Plots of the Simulated 12 Element Half Ring FSG Model.

As with the fields of the six element whole ring model of sections 5.3.2 & 5.3.3, the fields for the twelve element half ring model were plotted at several different frequencies. The first frequency chosen to examine the field plots at was the resonant frequency, identified in section 5.4.2 as  $15.5\text{GHz}$ . At this frequency the confinement of the fields within the FSG should be clear and well defined. The method by which the fields propagate in the FSG can then be determined at this resonant frequency.

The next frequency that was investigated was  $13.8\text{GHz}$  which was very close to the frequency ( $13.7\text{GHz}$ ) where minimum transmission of power in to the second solid waveguide occurs, i.e. where  $|S_{21}|$  for the structure is a minimum. Investigation at this frequency will reveal the reason for this reduction in  $S_{21}$  and the increase in  $S_{11}$  at this frequency. The next significant frequency of investigation is that of the lowest frequency in the simulated range,  $13.3\text{GHz}$ , where the value of the  $S_{21}$  rises considerably from the minimum value seen at  $13.7\text{GHz}$ . The  $|S_{11}|$  also falls so the power contained in the fields is again propagating through the structure. The measurements in chapter 3 suggested that this region below the minimum  $|S_{21}|$  value may be a surface wave mode, the field plots will reveal if this is the case. It would be

desirable to have investigated the possibility of the existence of this mode at a lower frequency, but as previously mentioned this was not possible due to problems getting the model to converge at frequencies below 13.3GHz. Finally a frequency at the other end of the simulated spectrum, 17GHz is investigated. Here of course, as shown in Figure 5-29, there are sets of field plots to be made, one for each of the possible input modes in the solid circular waveguide.

Figure 5-30 shows the longitudinal E field magnitude plots for the twelve element half ring FSG at 15.5GHz. A mixture of volume plots (a) & (b), with the E field magnitude shown by the colour snowstorm and a cut-plane plot (c), with the E field magnitude shown by coloured contours, give a good description of the fields propagating down the inside of the FSG structure. The volume plots are viewed in the yz plane and the cut-plane is through the z axis along the xz plane. The phase of the input mode is also altered to improve the information available even further. It is set to 0° for the first volume plot (a) and for the cut-plane (c), but changed to 60° for the second volume plot (b). This allows some information on the propagation process to be extracted. When viewed in HFSS many more input phases can be defined and the plots stitched together to form an animated movie.

As with the six element whole ring model at 15.35GHz, Figure 5-20, most of the field in Figure 5-30 is contained within the FSG or along the surface elements. Some fields of low magnitude can be seen to propagate away from the surface at some angle as a leaky mode field would. The reduction in field magnitude as the field propagates further down the FSG can be seen in (c) with the initial red colour at the centre of the mode at the top of the plot reducing to orange by the time it has reached the other end of the FSG. This is a radiated energy loss, which is still present at resonance, but significantly reduced. The wavelength of the mode in the FSG is about equal to the wavelength in the equivalent solid waveguide at this frequency, which is to be expected as chapter 2 shows that the values of  $\beta$  of these two modes are identical at resonance. The fields in the FSG keep their resemblance to the  $TE_{11}$  along the entire length of the FSG and are very similar to those seen for the six element whole ring FSG model.

The cross sections through and close to the feed junction between the solid waveguide and the FSG for the vector E fields are shown in Figure 5-31. The aperture field (a) shows a large amount of  $TE_{11}$  mode field with a small amount of field coupling out of the plane in the z direction to the edge of the first element situated at  $90^\circ$  to the polarisation vector. Moving 0.4mm down the FSG, in the gap between the first element and the aperture, (b) still shows the large amount of  $TE_{11}$  type mode present in the gap. There is also a significant increase in the magnitude of the  $E_z$  fields coupling the edge of the first element at  $90^\circ$  to the polarisation vector. (c) is the cut-plane through the centre of the lower circumferential arms of the first ring of elements, 1.2mm into the FSG. The fields are still  $TE_{11}$  like, but more curved than might be expected if in a solid waveguide. The circumferential arm of the element  $90^\circ$  from the polarisation vector is acting very much like a dipole causing much stronger fields to curve from one end to the other inside the FSG. The E fields in the z direction have now virtually disappeared and the field is mainly transverse.

The cut-plane through the centre of the element 4.2mm into the FSG still show the very  $TE_{11}$  like mode near the centreline of the polarisation vector, but near to the gaps between adjacent elements the E field vectors are in the opposite direction to that of the main polarisation vector. Here the E field is coupling from the z directed arms of the element perpendicular to the polarisation, to the z directed arms of the adjacent elements. There is also a large field between the two arms of this element. (e) has the cut-plane through the circumferential arm of the first ring of elements furthest away from the aperture. The field pattern is very similar to that of (c), except that the field magnitudes are much less. Figure 5-30 shows the reason for this reduction in the field strength, a null is present in the region around the gap between the first and second rings of elements when the input phase is  $0^\circ$ . The plot does show a large amount of coupling in the z direction between the first and second elements, implying that these coupling fields are partially independent of the field magnitude inside the FSG at that point. The cut-plane (f) through the middle of the gap between the first and second rings of elements, shows a similar picture to (e). The shape of the  $TE_{11}$  mode is present, but the field magnitude is even lower due to this being closer to the null in the z direction for input phase equal to  $0^\circ$ . The high coupling fields between the rings of elements are clearly visible. In fact analysis of the animation for the structure shows

that the high coupling fields are linked to the size of the current flowing in the z directed arms of the element. Once an area of high field strength from the internal field has set up the element currents, the coupling fields will emanate from all the edges of the element to adjacent metal structures. So coupling can be present between elements even when a null is closer to that portion of the element than the field maximum.

The current flowing on the arms of the elements can be seen in Figure 5-32 for the first two rings of the twelve element model for an input phase of  $0^\circ$  at 15.5GHz. The elements seen at the centre of the picture are those which are perpendicular to the polarisation vector and have the most current flow in the z directed arms. The current flow across both the circumferential arms have minimum values in the centre of their lengths, the whole element then looks like a one wavelength loop resonator. The currents in the other loop elements of a ring have much lower current levels with large induced currents flowing in the edges, caused by the coupling fields from the perpendicular element.

The field plots for 13.8GHz are covered in two plots, the longitudinal plots in Figure 5-33 and the cross-sectional plots in Figure 5-34. Several longitudinal volume plots are given so that the propagation of the fields down the structure can be seen from several angles. The first three plots (a), (b) and (c) are viewed in the xz plane with the input phase varied from  $0^\circ$ ,  $60^\circ$  and  $120^\circ$ . The final two plots (d) and (e) are viewed in the yz plane and only cover the  $0^\circ$  and  $60^\circ$  input phases. In all plots the progression of the area of maximum field density in the solid guide can be clearly seen as the circular red areas on the left hand side of the plot. The other solid waveguide of the right hand side of the plot only has a very small amount of field shown inside it. Low intensity fields can be seen on the FSG surface between the elements with some very low levels of field contained within it. This is why the  $|S_{21}|$  value is so low; virtually no field propagates down the FSG and into the second solid waveguide.

There is also evidence of radiation, especially in plot (d), with field streaming away from the surface of the FSG. In the animations it is possible to see wave fronts of

these fields propagating away from the surface of the FSG. This accounts for some of the power not reaching the second solid waveguide.

The  $|S_{11}|$  plots show that at 13.8GHz most of the energy is reflected back down the feed waveguide. This is clearly seen in the animations with a pulsing of the field magnitude colours. If a perfect standing wave existed in the structure no motion of the field would be seen, as the field strength increased from zero the colour of the fields would change up the magnitude scale to red. This would produce a pulsing colour field. With a significant amount of reflection the pulsing colour changes are superimposed on the slow moving field distribution as the phase changes. The pulsing of the field colours can be seen here in the change in colour, from yellow to red, of the field maximum between (a) and (b) and also in (d) to (e). The fact that in (b), (c) and (d) some of the field at the centre of the maximum has been coloured black is a sign that the field strength is so strong it has gone past the threshold at which HFSS applies for the red colour. So it can not apply a colour to that area, but is surrounded by red indicating that it is in a maximum area of field strength and not a minimum.

The extent of this pulsating marks the extent of the standing wave and so clearly the point where the pulsating ends is the cause of the reflections in the structure. The pulsating of the field colour extends very clearly to the first ring of elements of the FSG with a small amount at the second ring of elements. This is also the only part of the FSG that has any significantly high field strength. There is a small increase in the field strength in the region of the third ring of elements, but within the remainder of the structure it is very low. This suggests that the combination of the solid waveguide to FSG junction and the first few elements of the FSG are responsible for the large reflection of power seen at this frequency. The fact that the FSG itself is partially responsible and not just the junction suggests that the FSG cannot support a significant propagating mode at this frequency.

The cross sectional xy plane plots for this frequency are given in Figure 5-34 (b) through the aperture; (c) through the centre of the circumferential arm closest to the aperture of the first ring of elements; (d) through the middle of the first ring of elements and (e) through the middle of the gap between the first and second rings of



elements. These vector field plots are very similar to those seen in Figure 5-31, where the fields propagated down the FSG with minimum loss and reflection. The only difference found in the plots of Figure 5-34 has been the very high field magnitudes seen in the region of the elements where the polarisation vector, that passes through the centre of the FSG, crosses the FSG boundary at radius  $r_0$ . These very high magnitude vectors are longitudinal in the aperture and between the first and second rings of elements, They are transverse in the region of the first ring of elements. The surface current plot in (a) gives some clue as it appears that all the elements in the first ring of elements are resonating strongly. Note the large amount of red in the current density plot. It appears to be the strong resonance of all the elements in the first ring that that is causing the high field magnitudes around all the longitudinal arms of the elements and reflecting the majority of incident power back down the feed waveguide.

When the frequency is lowered to 13.3GHz the longitudinal field plots are given in Figure 5-35 and the cross sectional vector plots are presented in Figure 5-36. It was suspected that at this low frequency the propagation in the FSG was by means of a surface wave mode, from chapter 3. To aid the confirmation of this the longitudinal field plots were taken with many input phase values, so that the steps between the positions of the propagating fields would be small from plot to plot. This allows details about the mode of propagation to be picked out easily. The cut-plane of Figure 5-35 contains the y and z axes and the plots in (b) to (f) have the input phase changing in  $30^\circ$  steps from  $0^\circ$  to  $120^\circ$ . On the right hand side of the plots the feed solid waveguide can be clearly seen with red circle depicting the maximum values of the  $TE_{11}$  mode E-field distribution. On the left hand side of the plots the second waveguide clearly has the same circular field distribution of the  $TE_{11}$  mode, but with a reduced intensity. This shows that some, but not all, of the power from the feed waveguide propagates to the second waveguide. In both these waveguides the field distributions propagate from right to left with increasing values of input phase.

There is no circular field distribution inside the FSG, except near to the solid waveguides, as was seen inside the FSG at 15.5GHz, see Figure 5-30. If there is no power transfer along the FSG by means of the hybrid mode that looks similar to the

TE<sub>11</sub> mode, then another propagation mechanism must be at work in the FSG at this frequency to transfer power to the second waveguide. Along the length of the FSG reasonably high field concentrations can be seen at the surface of the FSG in the vicinity of the elements. These field concentrations also move along the surface of the FSG as the phase changes. However they move from left to right with increasing phase. It would be expected for a mode to move from right to left away from the source not towards it.

There is a class of modes described by [5] as backward propagating modes. These modes have phase propagation in the  $-z$  direction, but a group velocity and hence power transfer in the  $+z$  direction. Indeed the Floquet mode theory used by [2] to form the propagating hybrid Bloch modes of the FSG means that it is certain that some of the Floquet modes will be backward propagating. If the Floquet mode with dominant amplitude in the Bloch wave were to be backward then the entire mode would appear to be a backward mode. The fact that the fields hug the periodic surface elements and appear to propagate in the  $-z$  direction, with power transferred to the second waveguide in the  $+z$  direction make this mode a backward surface mode. Plot (a) shows the volume plot of the E fields hugging the elements of the FSG at 0° phase.

The surface current distributions in Figure 5-36 (a) appear to be very similar to those seen in all the previous current plots. They are however more symmetrical on each element and each ring of elements has very similar distributions. Whereas the other plots showed current differences from one ring of elements to the next. The vector field cross sections in (b) to (e) are taken at the same cut planes as previously at 60° phase. They clearly show the transition from the TE<sub>11</sub> mode to the surface wave mode. Initially, in (b), the plot looks very similar to that seen at 13.8GHz. The TE<sub>11</sub> field distribution in the aperture with the high longitudinal field vectors around all the elements. As the cuts progress down the FSG the TE<sub>11</sub> mode dies away along with the high intensity coupling fields that were seen at 13.8GHz at the point where the polarisation vector crossed the FSG. The coupling fields between the element perpendicular to the polarisation vector and the element edges on either side in  $\phi$  are still present, but have become completely transverse, even in the gap between the first

and second rings of elements. The fields appear to be tied to the elements on the surface of the FSG, adding the final proof that is indeed a surface wave mode that propagates in the FSG at this frequency.

At 17GHz the field plots are given in two sections, one set of plots for the  $TE_{11}$  input mode and the other for the  $TM_{01}$  input mode. A selection of the plots for the  $TE_{11}$  input mode are given in Figure 5-37 covering the surface currents (a), E field vector cross section plots (b) & (c) and a longitudinal E field magnitude volume plot (d). The surface currents on the elements of the first and second rings (a) are of a similar distribution, but 2/3 of the magnitude, of those seen at 15.5GHz, Figure 5-32. As are the E field vector plots in the aperture cut-plane (b) and through the centre of the first element ring (c) similar to those seen in Figure 5-31. There is however, some difference in the coupling fields between the adjacent elements. As these field vectors follow much smaller looped loci from one longitudinal arm to the next. There is also very little field coupling between the two longitudinal arms of the element positioned perpendicular to the polarisation vector. The volume plot of the E field magnitude in (d) shows a large amount of field external to the FSG. There is clearly a great deal of radiation from the FSG at this frequency. The wavelength of the field is shorter than that of the field in the solid waveguide. This is to be expected as the predicted propagation constant of the FSG, see chapter 2, was much larger than that of the solid waveguide at frequencies above the resonance point. Although weak some field does reach the far end of the FSG and enters the second solid waveguide. This weak field is contained within the FSG along the entire length and is not a different mode, like the surface mode at 13.3GHz produced by the  $TM_{01}$  input mode as will be seen next.

The behaviour of the fields in the FSG at 17GHz with the  $TM_{01}$  mode in the feed waveguide is very different from that seen to date with the  $TE_{11}$  mode feed. The longitudinal plots in Figure 5-38 show the E field magnitude in volume plot format and are viewed in the yz and xz orientations for two different input phases. The change in the input phase clearly shows that the field distributions propagate down the FSG in the +z direction and that there is very little field radiated from the FSG surface. Although it is clear that some E field exists outside the radius of the elements this field seems to be reasonably well bound to the surface of the structure. The E field distributions in the solid waveguides and inside the FSG are those expected for a

$TM_{01}$  mode. The view of the internal E field distribution in the FSG is obscured by surface E fields that extend in bands circumferentially around the FSG in the gaps between elements. These areas of surface coupling between elements are linked to the proximity of an internal E field maximum, in a similar manner to that seen for the  $TE_{11}$  mode feed at 15.5GHz.

The conformation that the mode is  $TM_{01}$  in origin is seen in Figure 5-39 (b). This cross-sectional H field vector plot is taken through the feed port of the solid waveguide and clearly shows vector distribution of the magnetic fields of a  $TM_{01}$  mode. The remaining cross sectional plots (c) to (e) combine the vector E and H field plots, each one having a different colour scale as seen on the diagrams. As the cut-plane is moved from the aperture down the FSG the field patterns do not change significantly. The circular H field distribution remains evident in each plot and appears to change little between each plot. The E field distribution is a little complex, having longitudinal field components, but it is not significantly different from that which would be expected for the E fields of any  $TM_{01}$  mode in a solid waveguide. The E fields between the rings of elements are longitudinal, and have very high values coupling from one element to another.

The current plots of Figure 5-39 (a) are completely different from those observed for the  $TE_{11}$  mode feed. Instead of the longitudinal arms of the elements carrying the currents with the highest magnitudes, they have the null points situated half way down their lengths. The circumferential arms now have the currents with the largest magnitudes on them. Also all the elements around the circumference have similar current distributions and magnitudes on their surfaces unlike the  $TE_{11}$  mode feed at 15.5GHz, where only the element perpendicular to the polarisation vector had high current magnitudes present.

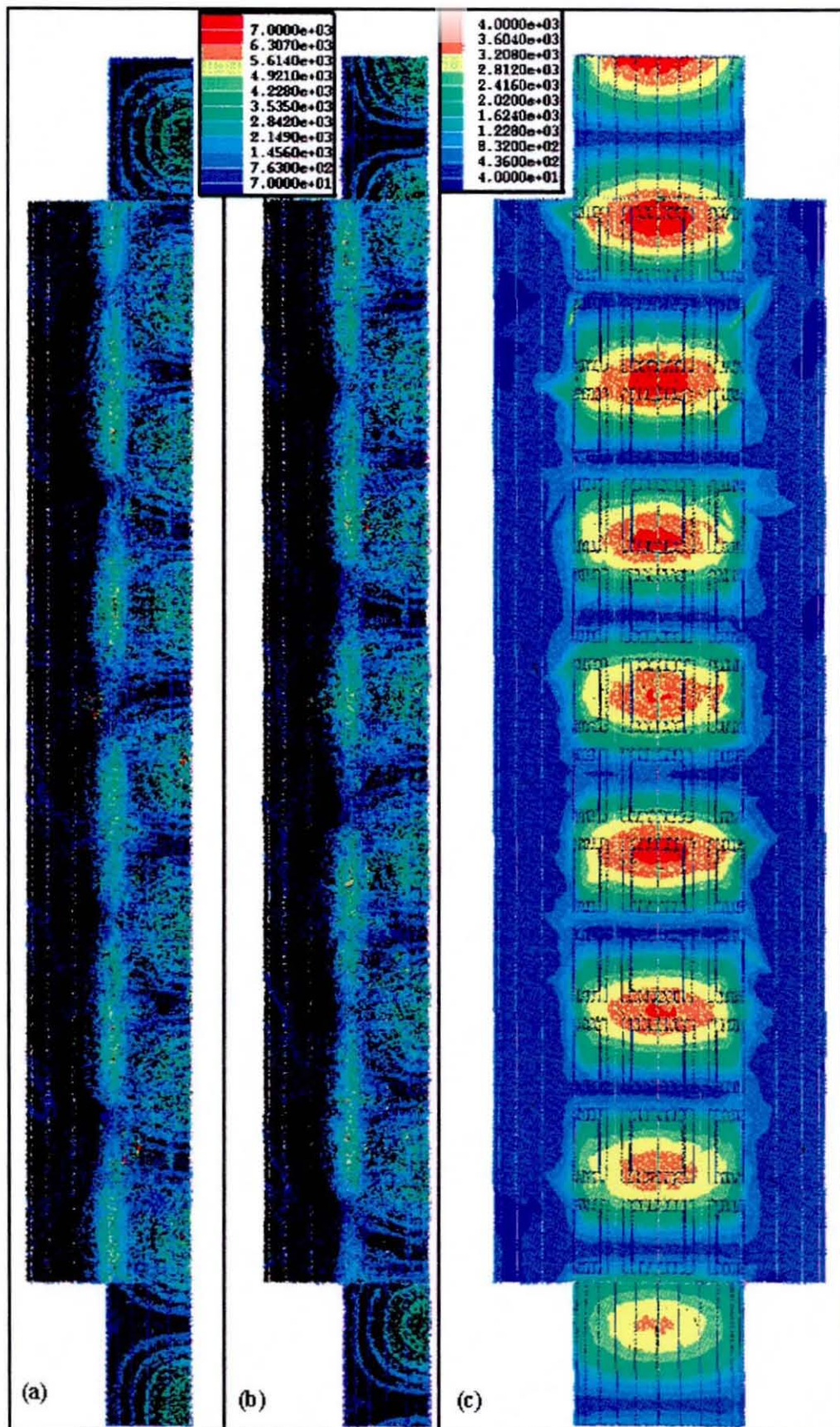


Figure 5-30  $|E|$  along the length of the 12 element half ring FSG model at 15.5GHz:-  
 (a) for volume plot yz view at I/P phase= $0^\circ$ .  
 (b) for volume plot yz view at I/P phase= $60^\circ$ .  
 (c) for xz cut-plane through axis ( $y=0$ ) at I/P phase= $0^\circ$ .

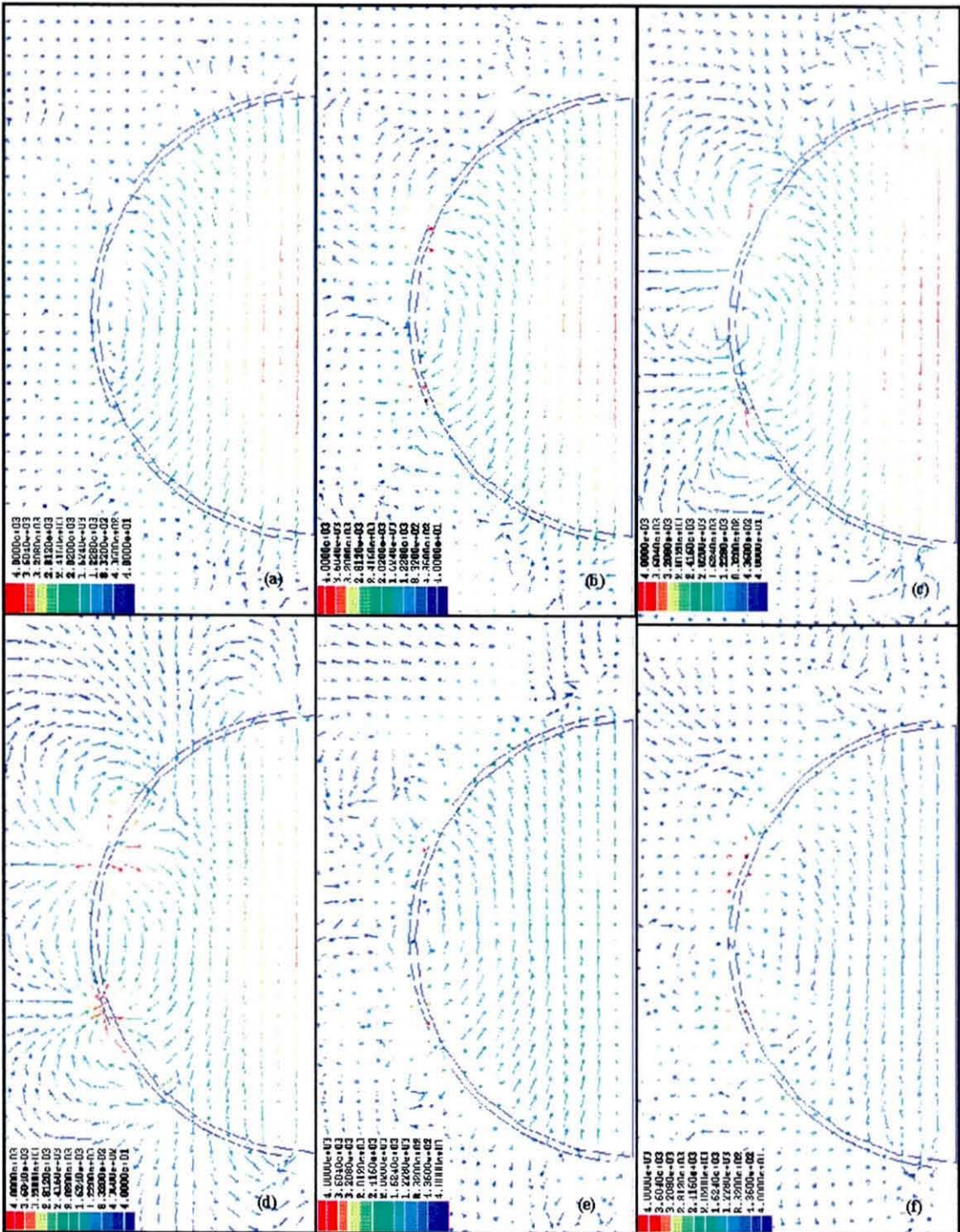
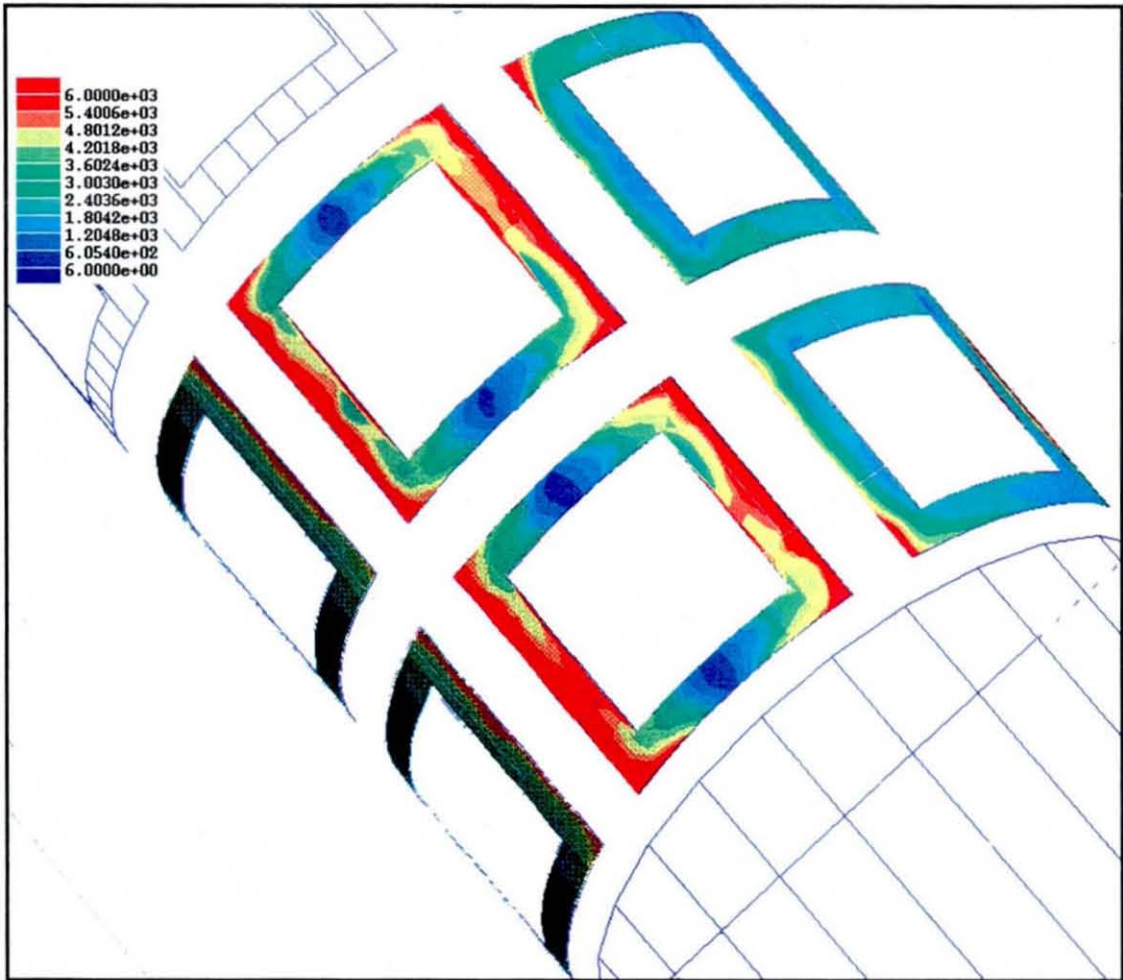


Figure 5-31 E Vector cross-section plots for the 12 element half ring FSG model at 15.5GHz & I/P phase=0°:-

- (c) The vector E field in an xy cut-plane through the aperture.
- (d) The vector E field in an xy cut-plane 0.4mm from the aperture.
- (e) The vector E field in an xy cut-plane 1.2mm from the aperture.
- (f) The vector E field in an xy cut-plane 4.1mm from the aperture.
- (g) The vector E field in an xy cut-plane 7mm from the aperture.
- (h) The vector E field in an xy cut-plane 8.2mm from the aperture.



**Figure 5-32** Current plot on the surface of the elements of the first 2 rings of the 12 element half ring FSG model at 15.5GHz & I/P phase=0°.

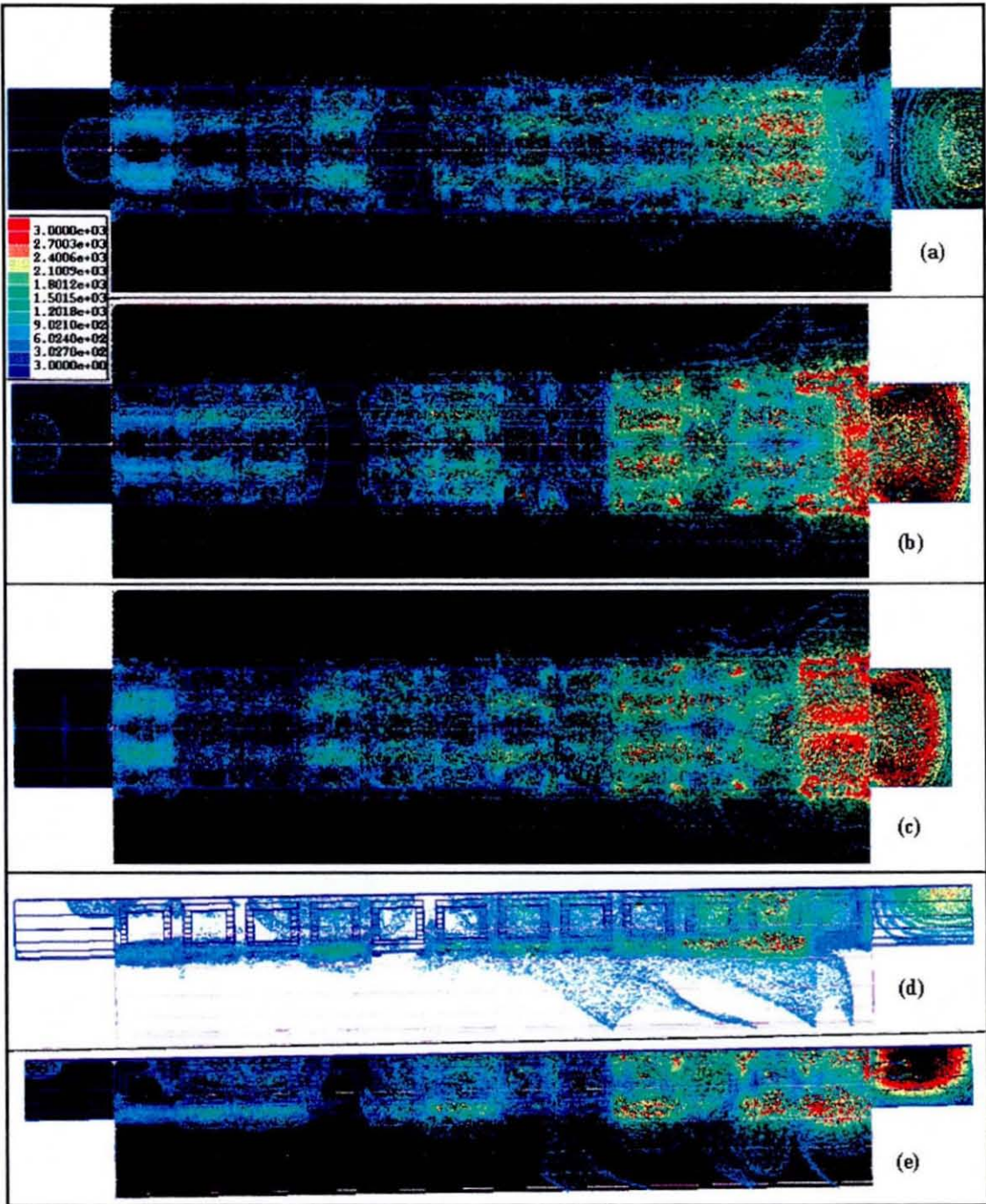
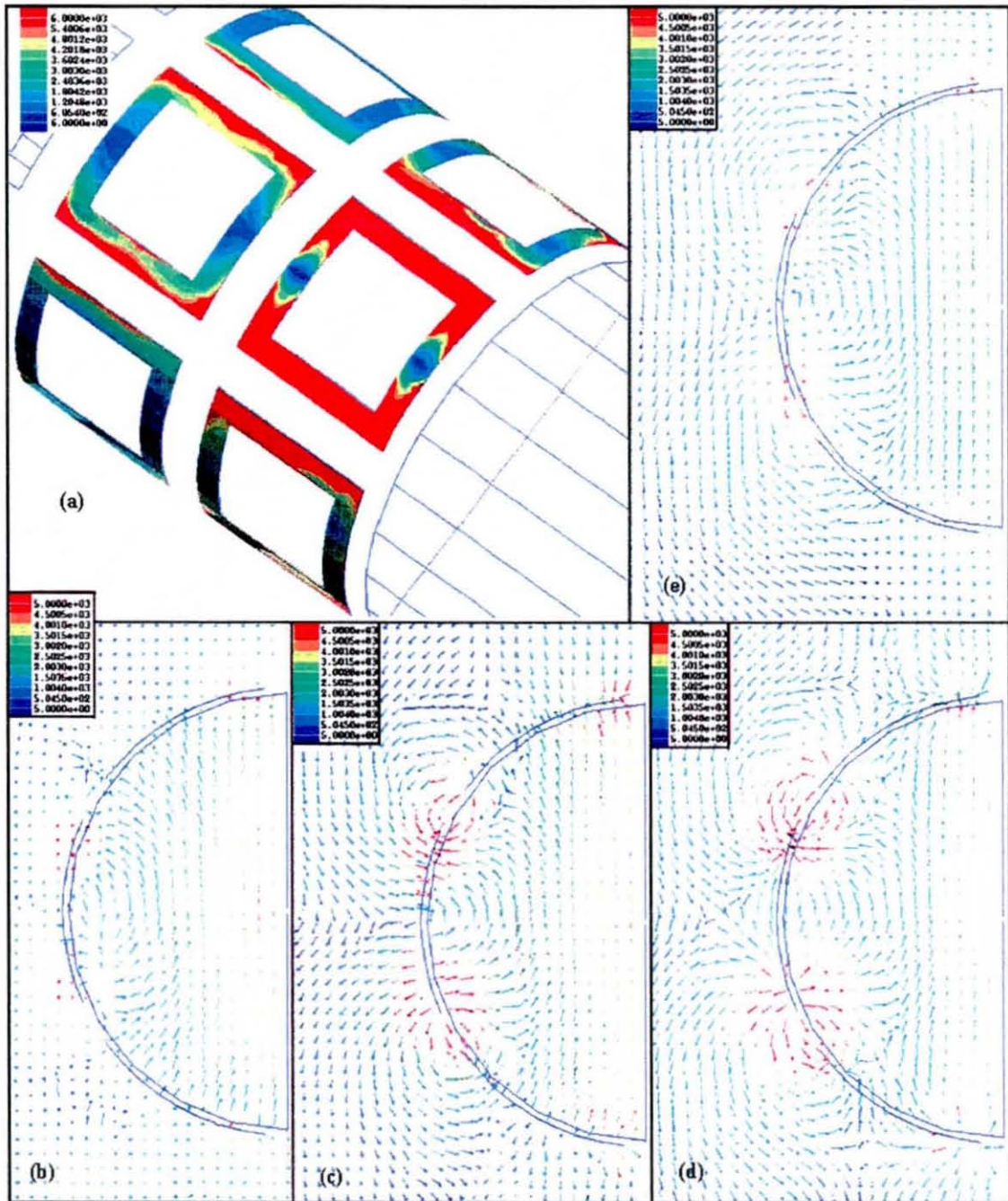


Figure 5-33  $|E|$  along the length of the 12 element half ring FSG model at 13.8GHz:-

- (a) for volume plot xz view at I/P phase= $0^\circ$ .
- (b) for volume plot xz view at I/P phase= $60^\circ$ .
- (c) for volume plot xz view at I/P phase= $120^\circ$ .
- (d) for yz cut-plane through axis ( $y=0$ ) at I/P phase= $0^\circ$ .
- (e) for yz cut-plane through axis ( $y=0$ ) at I/P phase= $60^\circ$ .





**Figure 5-34 Current & E vector cross-section plots for the 12 element half ring FSG model at 13.8GHz & I/P phase=120°:-**

- (a) The current plot on the surface of the elements of the first 2 rings.
- (b) The vector E field in an xy cut-plane through the aperture.
- (c) The vector E field in an xy cut-plane 1.2mm from the aperture.
- (d) The vector E field in an xy cut-plane 4.1mm from the aperture.
- (e) The vector E field in an xy cut-plane 8.2mm from the aperture.

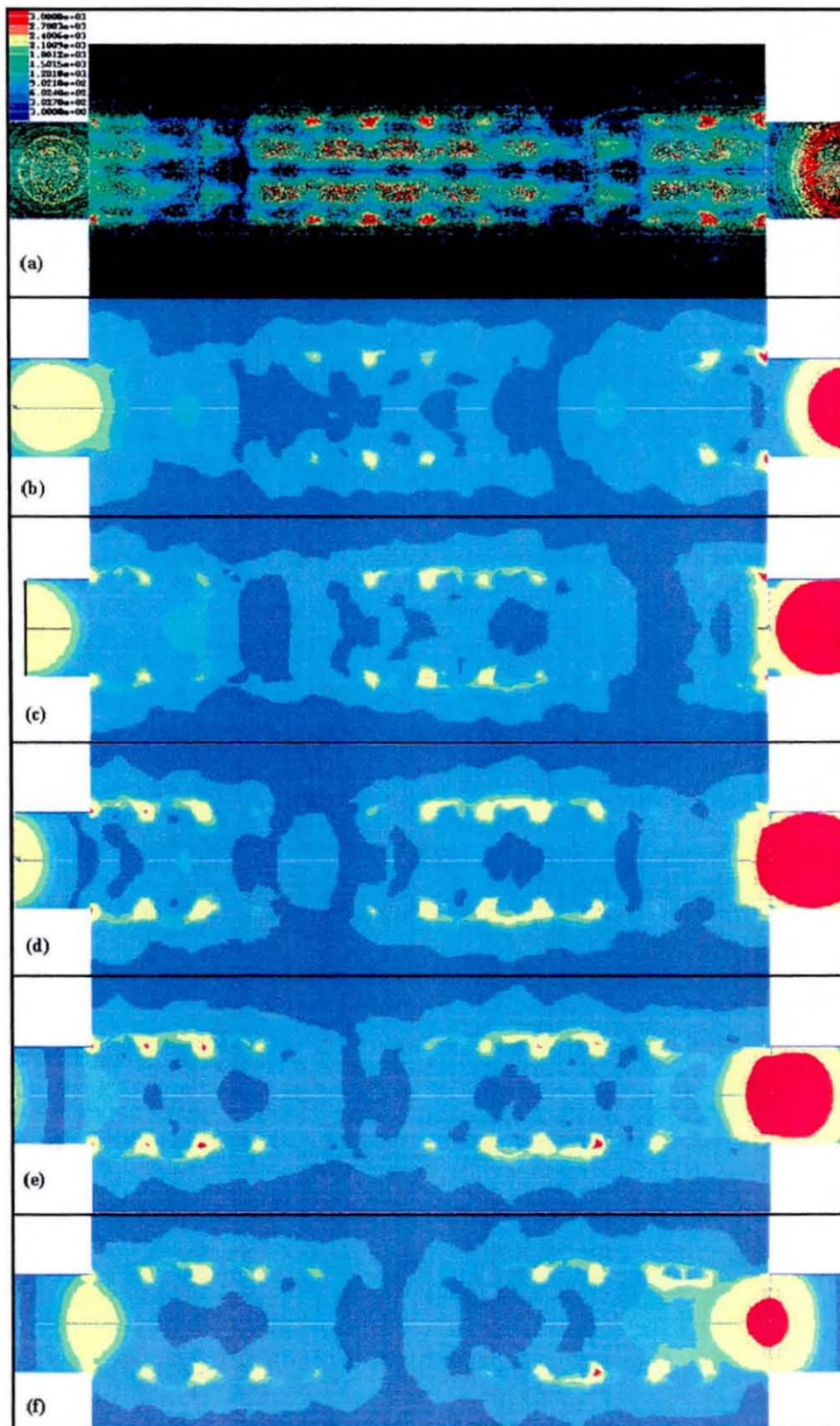
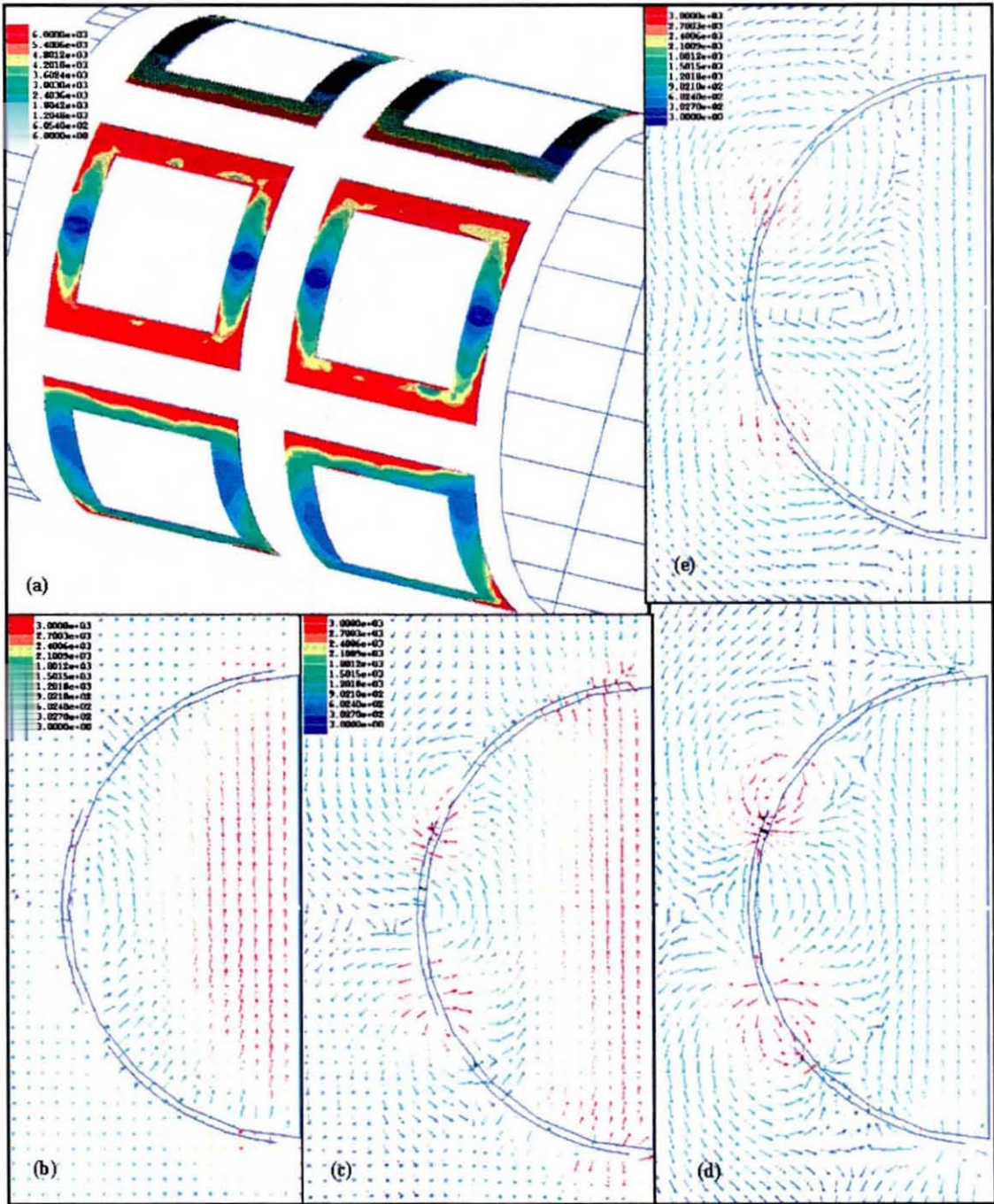


Figure 5-35  $|E|$  along the length of the 12 element half ring FSG model at 13.3GHz:-  
 (a) for volume plot xz view at I/P phase= $0^\circ$ .  
 (b) for yz cut-plane through axis ( $y=0$ ) at I/P phase= $0^\circ$ .  
 (c) for yz cut-plane through axis ( $y=0$ ) at I/P phase= $30^\circ$ .  
 (d) for yz cut-plane through axis ( $y=0$ ) at I/P phase= $60^\circ$ .  
 (e) for yz cut-plane through axis ( $y=0$ ) at I/P phase= $90^\circ$ .  
 (f) for yz cut-plane through axis ( $y=0$ ) at I/P phase= $120^\circ$ .



**Figure 5-36 Current & E vector cross-section plots for the 12 element half ring FSG model at 13.3GHz & I/P phase=60°:-**

- (a) The current plot on the surface of the elements of the first 2 rings.
- (b) The vector E field in an xy cut-plane through the aperture.
- (c) The vector E field in an xy cut-plane 1.2mm from the aperture.
- (d) The vector E field in an xy cut-plane 4.1mm from the aperture.
- (e) The vector E field in an xy cut-plane 8.2mm from the aperture.

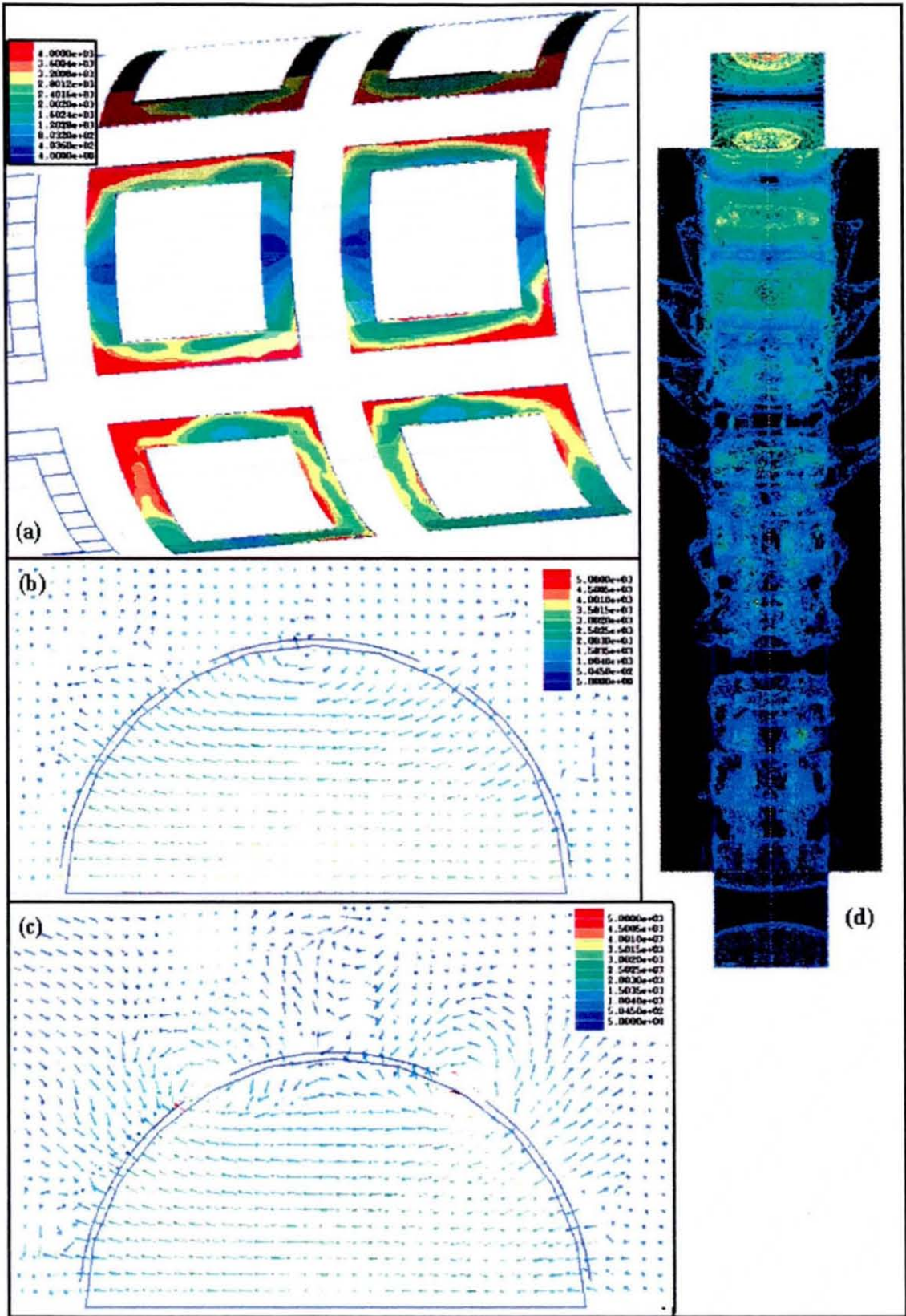


Figure 5-37 [E], current & E vector cross-section plots for the 12 element half ring FSG model at 17GHz for the fundamental  $(TE_{11})$  I/P mode & I/P phase= $0^\circ$ :-  
 (a) The current plot on the surface of the elements of the first 2 rings.  
 (b) The vector E field in an xy cut-plane through the aperture.  
 (c) The vector E field in an xy cut-plane 4.1mm from the aperture.  
 (d) The  $|E|$  volume plot xz view.

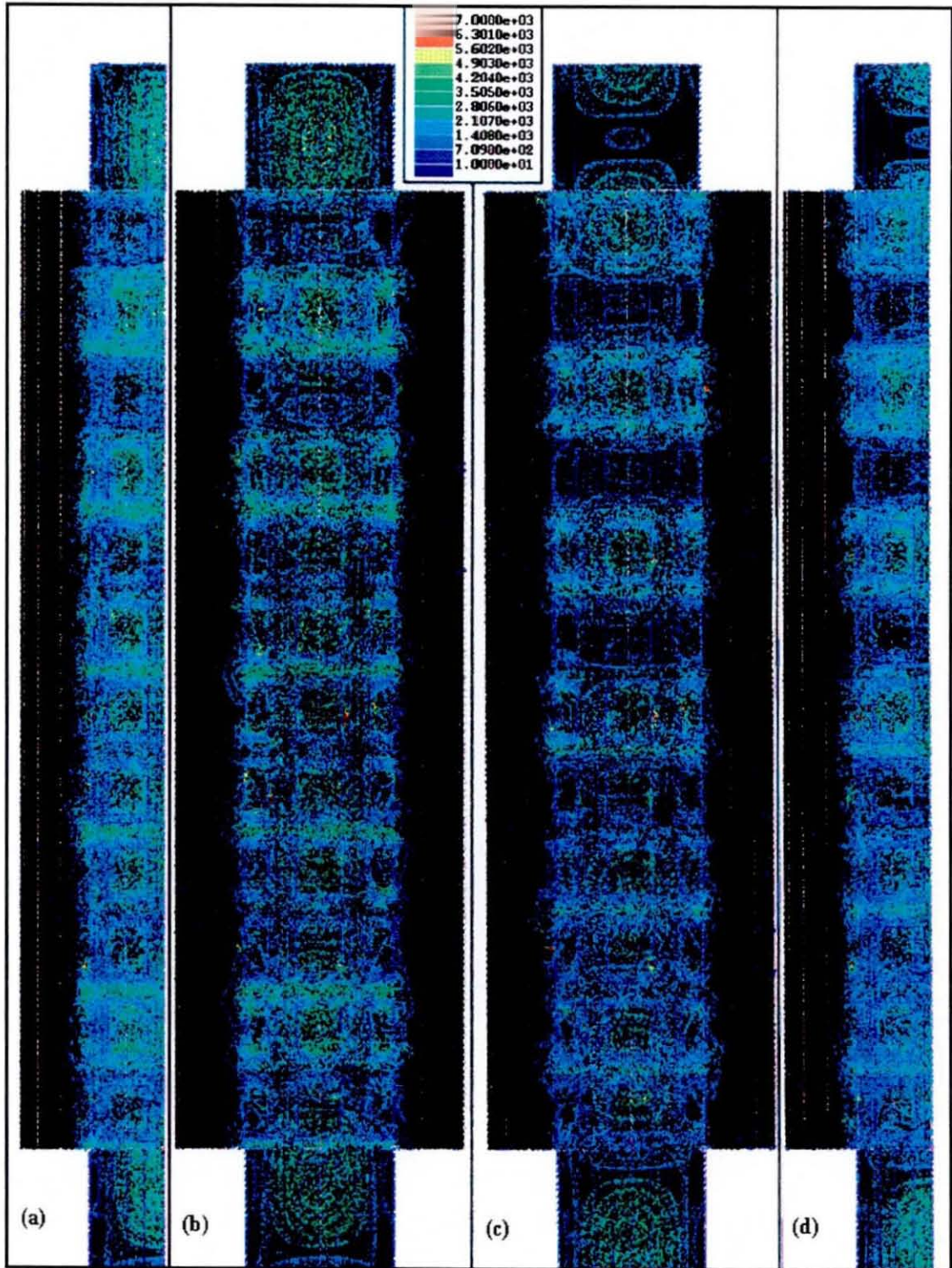


Figure 5-38  $|E|$  along the length of the 12 element half ring FSG model at 17GHz for the second higher order ( $TM_{01}$ ) I/P mode:-

- (a) for volume plot zy view at I/P phase= $0^\circ$ .
- (b) for volume plot zx view at I/P phase= $0^\circ$ .
- (c) for volume plot zx view at I/P phase= $60^\circ$ .
- (d) for volume plot zy view at I/P phase= $60^\circ$ .

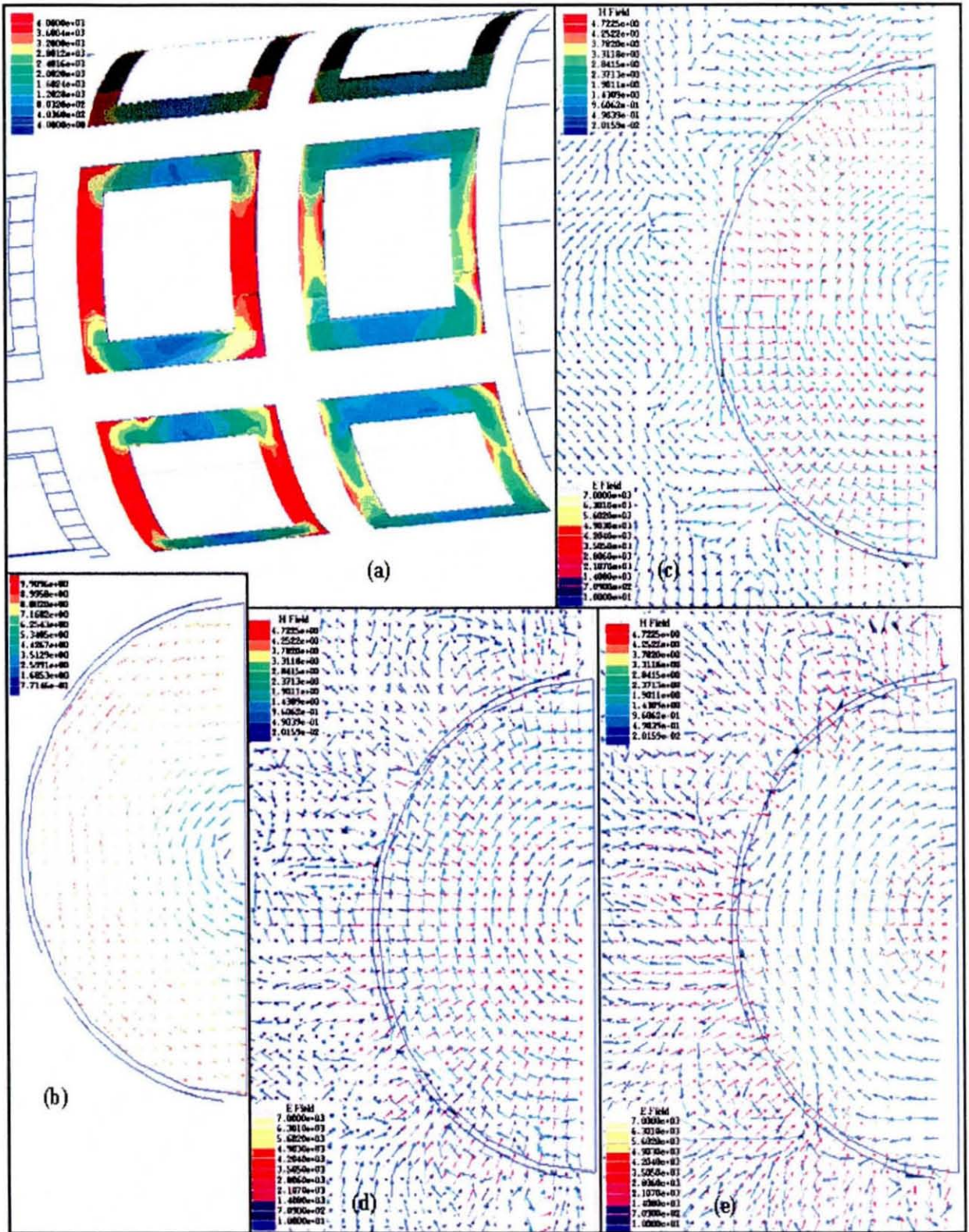


Figure 5-39 Current & E & H vector cross-section plots for the 12 element half ring FSG model at 17GHz for the second higher order ( $TM_{01}$ ) I/P mode & I/P phase= $0^\circ$ :-

- (a) The current plot on the surface of the elements of the first 2 rings.
- (b) The vector H field in an xy cut-plane through the solid waveguide feed.
- (c) The vector E & H field in an xy cut-plane through the aperture.
- (d) The vector E & H field in an xy cut-plane 1.2mm from the aperture.
- (e) The vector E & H field in an xy cut-plane 4.1mm from the aperture.

#### 5.4.4 Radiation patterns for the Half Ring FSG Model – Measured and Simulated.

The radiation patterns produced by HFSS for the 12 element half ring model were compared with the measured radiation patterns from chapter 3. Although similar in set-up, each one having a solid waveguide at each end of the FSG, the length of the two FSGs was different, twelve rings long for the simulation compared to thirty four rings long for the measured. The measured also had the dielectric loading affects of the Mylar sheet. The radiation patterns for each, taken in 0.5GHz steps from 13.5 GHz to 16.5GHz, are shown in Figure 5-40. The measured patterns are shown with solid lines and the simulated patterns are shown with dashed lines. Plots of similar colour denote measured and simulated patterns at the same frequency.

It should be noted that no comparison can be made between the E field magnitudes of the simulated and measured plots, because the measured plots were never normalised, see chapter 3. The scale of the y axis of the graph is included to allow comparisons between plots of different frequencies from the same source, measured or simulated. It is evident from Figure 5-40 that there is very good agreement between the simulated and measured data in the region of the main beam. At all frequencies, except 16GHz, the angle of the simulated main beam is within  $1.5^\circ$  of the measured angle of the main beam. The simulated value at 16GHz does not in fact follow the same trend as all the other simulated main beams. It is thought that there may be a problem with this simulated result and further investigation around this frequency would be recommended. However, this aside the remaining frequencies point to excellent agreement in the angle of the main beam between the simulated and measured results.

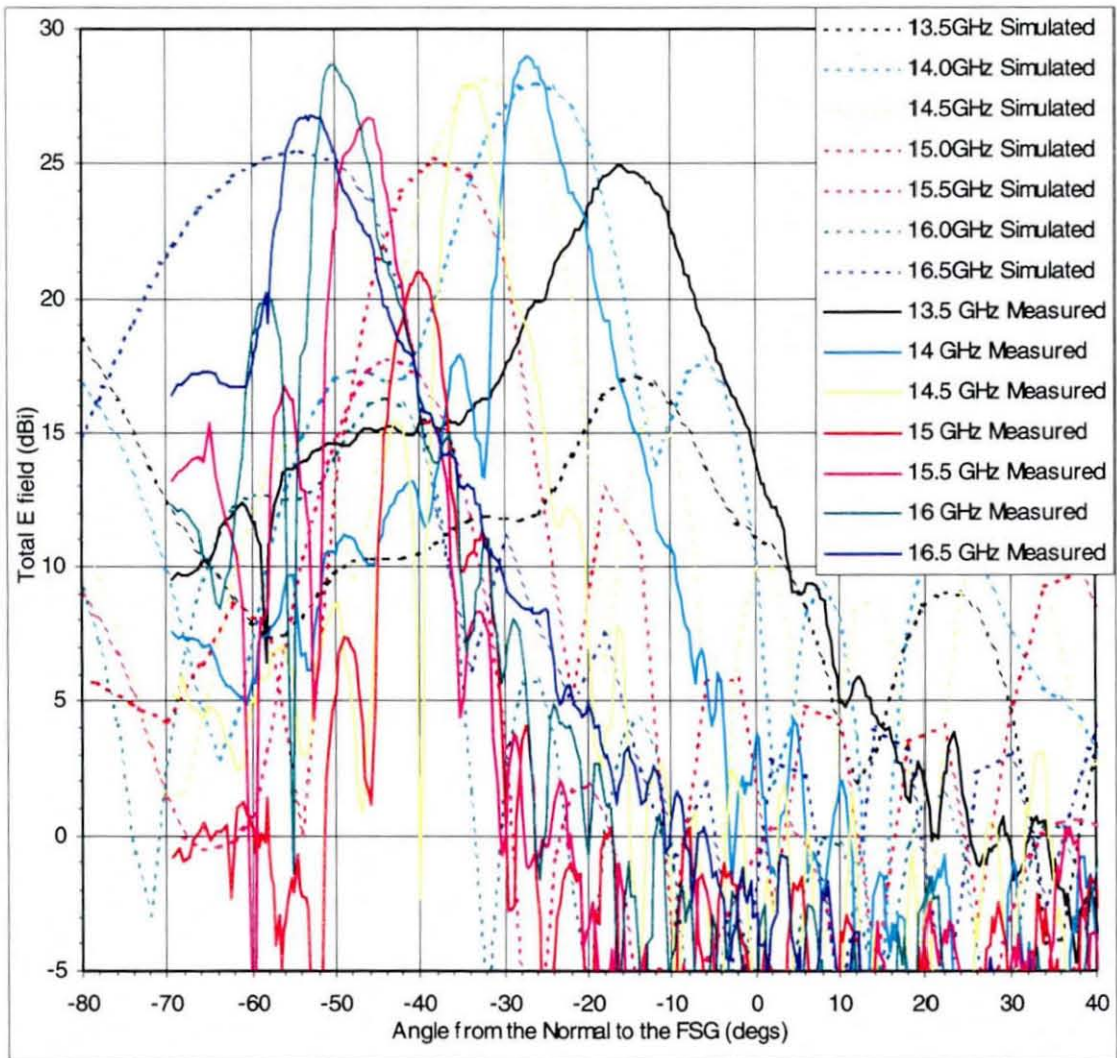


**Figure 5-40 Comparison of radiation patterns from simulated 12 element half ring model and measured FSG 34 elements long.**



There is a large difference in the width of the main beams between the simulated and measured patterns. The beam widths of the measured patterns are considerably narrower for all frequencies except at 13.5GHz. This is to be expected again due to the difference in length of FSG that was simulated compared to that which was measured. The standard antenna theory of an aperture antenna provides the rationale for this difference [4]. The beam width of any antenna in a particular direction is inversely proportional to its width in the same direction. The larger the antenna the narrower the main beam will be. The measured FSG is longer than the simulated FSG so the main beam of the measured FSG should be narrower than that of the simulated one.

One other thing to note from the radiation pattern graph is that the minimum value of the main beam for the measured FSG is at 15GHz. The minimum value of the main beam for the simulated FSG is at 15.5GHz. This is consistent with the theory put forward in chapter 3, that when the FSG is resonating, leakage from the FSG will be at a minimum. This is the point where the attenuation of the leaky mode is at a minimum and the maximum amount of power is transmitted down the inside of the FSG structure. The fact that the maximum value of the  $S_{21}$  plot coincides with the minimum value of the main beam in the radiation plots, for both the simulated data and the measured data, proves the hypotheses about the operation of the fundamental hybrid FSG mode at resonance.

## 5.5 References

- [1] HFSS version 6 Help Manual – Ansoft Corporation
- [2] Propagation Characteristics of Cylindrical Frequency Selective Guides – G.I.Loukos, Ph.D. thesis Loughborough University 1997.
- [3] Fields and Waves in Communications Electronics – S.Ramo, J.R.Whinnery & T.Van Duzer– Wiley, New York, 1994.
- [4] Antenna Theory Analysis and Design – C.A.Balanis – Wiley, New York, 1997.
- [5] Guided Complex Waves Part 1. Fields at an interface & Part 2. Relation to radiation patterns – T.Tamir & A.A.Oliner – proc I.E.E., vol 110, No2, February 1963, p310 & p325.

## 6. Conclusions and Recommendations for Future Work

In order to undertake the transition modelling a detailed understanding of the FSG was required. The determination of a large proportion of the mode spectrum was carried out using the previously developed modelling program for FSGs of infinite length. The eigenvalues of the spectrum were found using a graphical technique over a large frequency range. The modes found in the FSG consisted of either surface wave modes or leaky modes. The surface wave modes found consisted of the fundamental surface mode and many higher order complex surface modes that were lossy, which in many cases were backward propagating Floquet modes. The leaky modes were found to exhibit behaviour similar to a mode in a solid waveguide, appearing to have a cut-off frequency above which they propagated very freely in the structure and below which they remained highly evanescent.

It was observed that there was an increase in the number of modes that suddenly appeared in the mode spectrum when propagation constants had large imaginary values and the normalised free space wave number was also large. The appearance of these modes in the solution space should be investigated further to ascertain if they are physical modes. This would require a change in the way that the modelling program chooses the radial propagation constant. The value of the imaginary part of the propagation constant of a mode should be taken into account when the choice of radial propagation constant is made.

The measurement study evaluated three ways of extracting the propagation constant information of an FSG from a series of measurements. The real and imaginary propagation constants, found by using the short circuited leaky wave antenna method, were in good agreement with the values found by the modelling program. The accuracy of this method is good, although it does require an anechoic chamber for accurate measurement of radiation patterns and can only measure the propagation constant over the frequency range where the structure supports a leaky mode.

The radiation pattern measurements and the scattering parameters were examined without reference to the information obtained from the modelling program and confirmed the presence of surface and leaky modes. The data revealed the presence of a resonant frequency where the radiation of the leaky mode is reduced to a minimum value and the power transmitted through the FSG is at a maximum. At frequencies away from this resonant frequency the FSG becomes increasingly leaky. Below the band of frequencies where the leaky mode exists the surface wave is evident. Above this leaky mode band the end of the feed waveguide radiates into free space as if the FSG were not present. The interpretation of these measured values agrees very well with the operation that would be expected from the predicted modes found from the simulation program.

A parametric study of the FSG was carried out experimentally with different sizes of element, periodicity, radius and dielectric thickness. The changes to the dielectric thickness revealed a larger than initially expected dielectric loading effect. However, if the field strengths were high between the elements on the surface, the loading effect would be large. The presence of high strength coupling fields was shown to be correct when the structure was modelled using the finite element method. Increasing the radius of the FSG and keeping the element periodicity constant gave a reduction in the value of the resonant frequency and a reduced amount of radiation loss through the FSG walls. This FSG has more elements around its circumference, but a significantly oversized radius compared to that of a solid waveguide feed. Adding more elements to the circumference of the FSG, with a possible reduction in size achieved by loading the structure with dielectric, may reveal an FSG with very low levels of loss. The main effect of changing the size and periodicity of the elements was to alter the frequency of resonance. Making the element size and periodicity larger would, as expected, reduce the frequency at which the structure resonates. If these structures are to be used widely then it would be advantageous to have design curves available that give rough information on the value of the resonant frequency and the strength of the resonance, in terms of how little loss there is in the structure.

The junction modelling was attempted using mode matching. This initially seemed like a very good method, allowing the amplitudes of the modes excited by the junctions to be ascertained. However the improper nature of the leaky modes meant

that many approximations were required, which affected the accuracy of any results produced. These approximations also meant that the solid waveguide to FSG junction could not be modelled. The approximations required by the presence of leaky modes broke down at this junction as it was essentially a source and leaky modes are not an accurate representation of the radiation field at this point. The implementation of the mode matching method gives results that are inherently approximations of the actual solutions. This is because of the truncation of the infinite set of solid modes and Bloch modes used to model the aperture field in each structure. These approximations are amplified by the FSG, as the Bloch waves are constructed from a doubly infinite set of Floquet modes. The number of these modes must also be truncated to allow the numerical solution to be found. Had results been produced, careful consideration of the validity of the results would have been required to assess the minimum number of modes required. The method was ultimately abandoned due to the difficulty in normalising the portion of the leaky mode inside the FSG. It is still unclear where the cause of this problem lies, but given the limitations of this method in terms of large approximations and its lack of transportability to other problems it was considered not worth pursuing further, especially when the success of the junction simulation by the finite element method is considered.

The finite element package, HFSS, produced a huge amount of data on the scattering parameters, radiation patterns and the field distributions. The scattering parameters and radiation patterns matched those of the measured FSGs given the practical constraints imposed. The scattering parameters prove that the dielectric load effect was high even though only a thin sheet of dielectric was present. Large coupling fields between elements were shown to exist which accounted for the high dielectric loading effects that were seen. The reasonably close match between simulated and measured radiation pattern data means that the propagation constant of the HFSS model must be very close to that of the measured FSG. As the measured propagation constant was also close to that predicted by the infinite length FSG model the two simulation methods reinforce each other.

The field plots of the HFSS models give insight into the methods of propagation in the FSG structure at various frequencies. At resonance it was shown that the field magnitudes are highly confined within the FSG radius and propagated with a

wavelength similar to that seen in the solid waveguide. The high coupling fields between the elements excited by the large currents on the longitudinal arms of each element appear to be the mechanism by which the field is contained. Further work would be advantageous in understanding the mode of propagation completely. The predicted presence of the surface mode was shown to be correct at the lower end of the simulated frequency band. Surprisingly, this mode was a backward propagating mode. This was unexpected, but not inconceivable, as the Bloch mode is constructed of many forward and backward propagating Floquet modes.

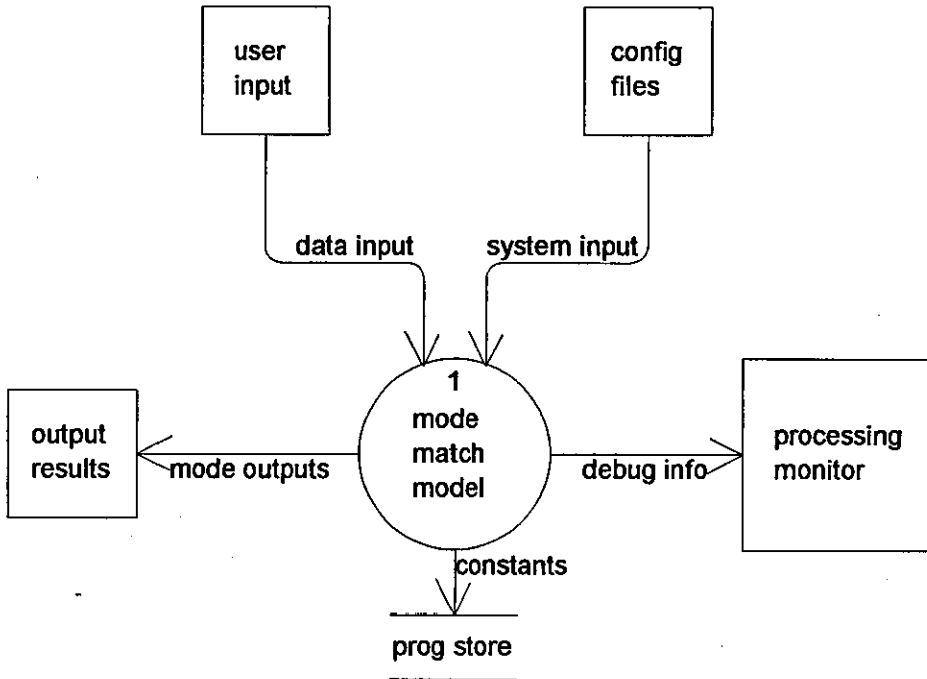
The elements of the FSG were also shown to support a well defined leaky mode only over a band of frequencies centred around the resonant frequency. At the edges of this band the field does not propagate in the FSG and the power is either reflected back down the feed guide or else radiated into free space. This confirmed the results found by the measurement of leaky modes on a real FSG.

Finally, the discovery of the mode that propagates from a  $TM_{01}$  feed mode in the solid circular waveguide is very exciting. It does not appear to match any mode found by the infinite length modelling program and has not been measured due to a lack of equipment. The mode has a predicted transmission loss through the FSG of roughly half of that seen at resonant frequency of the  $EH_{11}$  mode. The mode of propagation is also interesting as the  $TM_{01}$  mode field appears to continue down the length of the FSG without any visible change in the field distributions, as were seen in the  $EH_{11}$  mode. More work into the nature of this mode should be carried out, as it may be a low loss transmission mode and could have many applications.

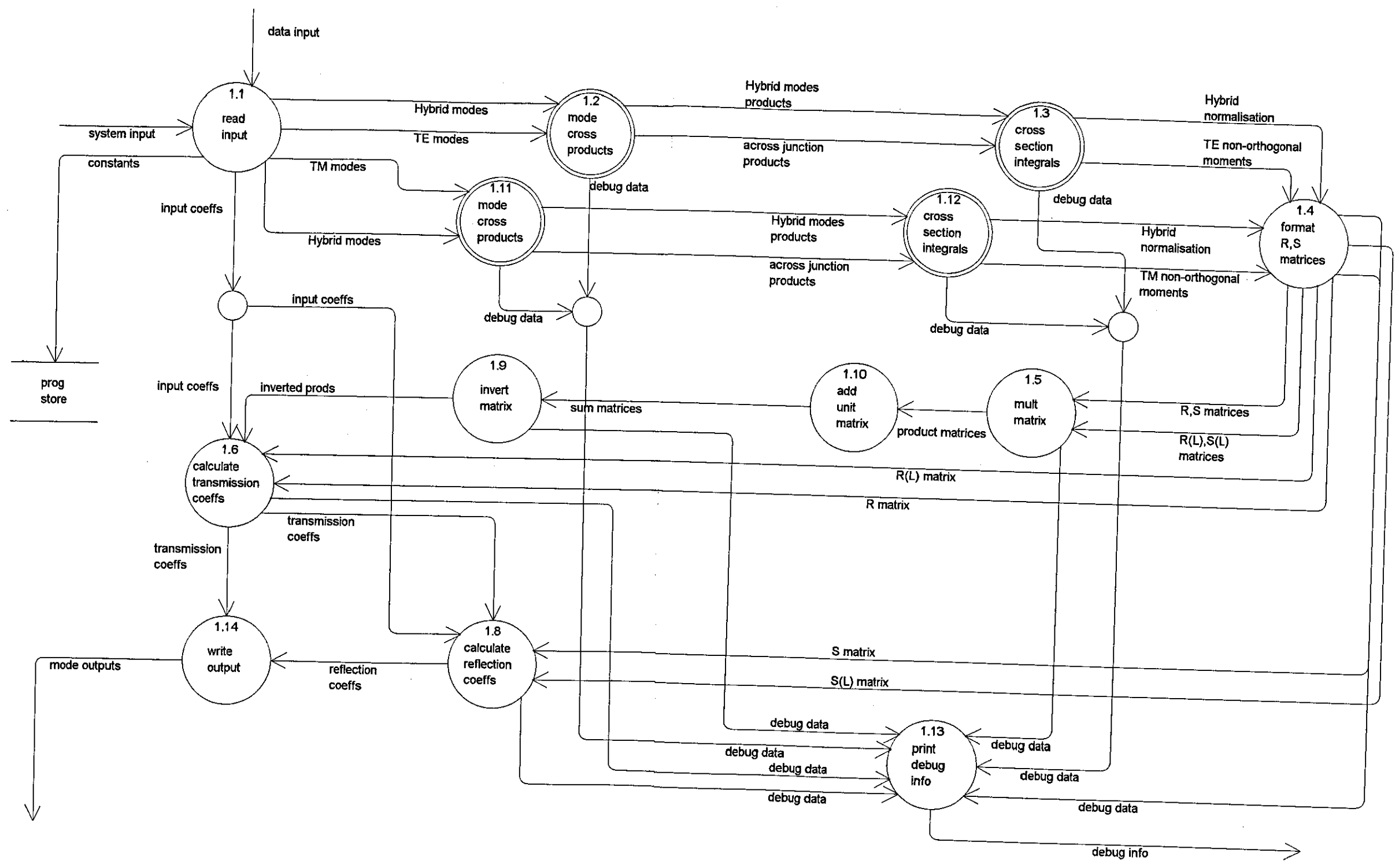
This thesis has expanded the number of modes known to exist in the FSG and identified previously unknown characteristics of these modes. The validity of the infinite length mode was demonstrated by measurements made on manufactured FSGs. These measurements have confirmed many of the characteristics that the FSG modes were thought to have from the analysis of the propagation constants. The junctions and short lengths of FSG were modelled successfully using a finite element approach. The results of these simulations matched those of the measured data very well and identified the mechanisms of propagation of the FSG modes.

**APPENDIX A.**

Project Name: FSG\_Solid\_trans  
Project Path: d:\codede~1\fsg\_sol2\  
Chart File: dfd00003.dfd  
Chart Name: mode match contex diagram  
Created On: Jun-12-1996  
Created By: james eade  
Modified On: Nov-08-2000  
Modified By: james eade

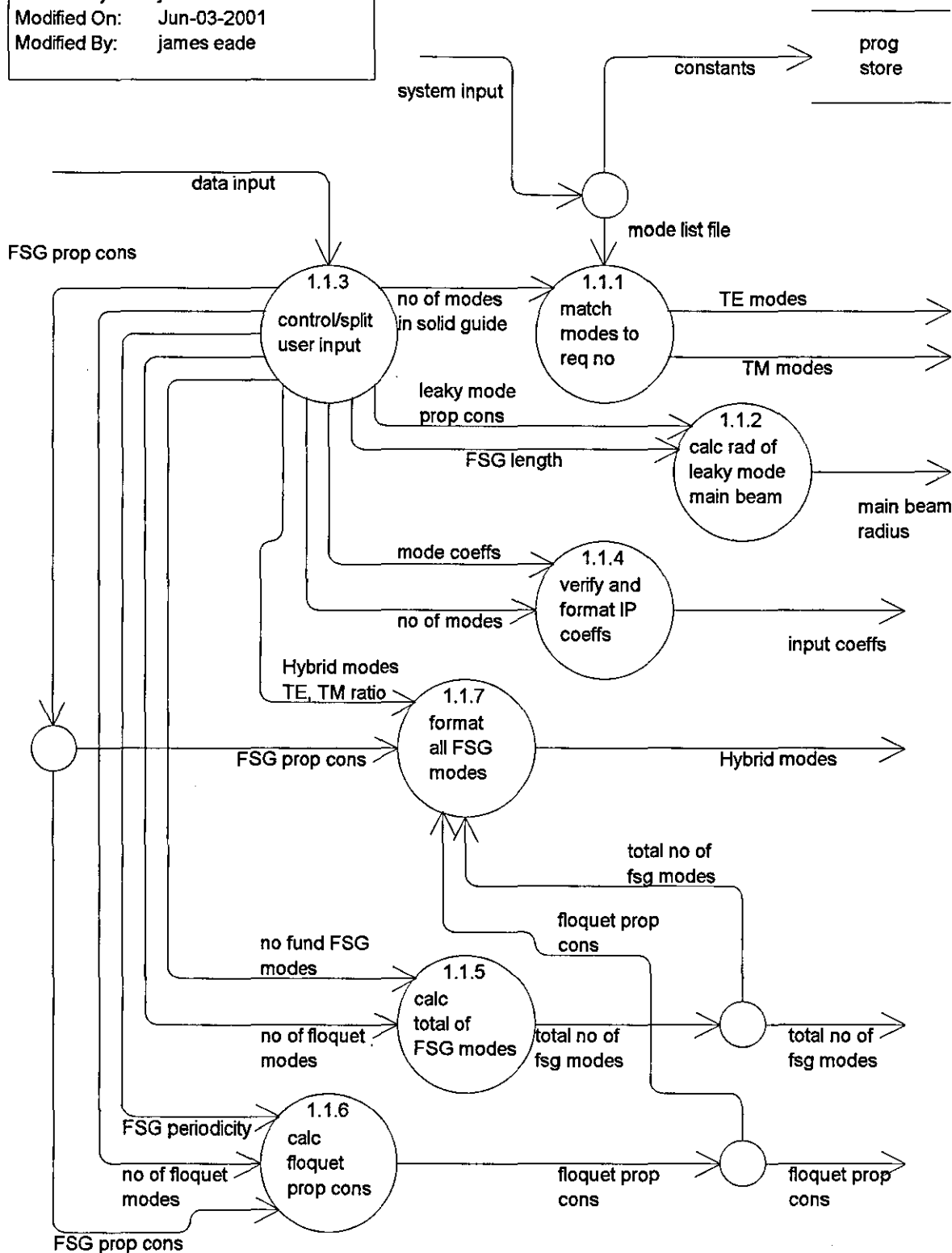


Project Name: FSG\_Solid\_trans  
 Project Path: d:\codede-1\fsg\_sol2\  
 Chart File: dfd00002.dfd  
 Chart Name: mode match model  
 Created On: May-24-1996  
 Created By: james eade  
 Modified On: Jun-03-2001  
 Modified By: james eade

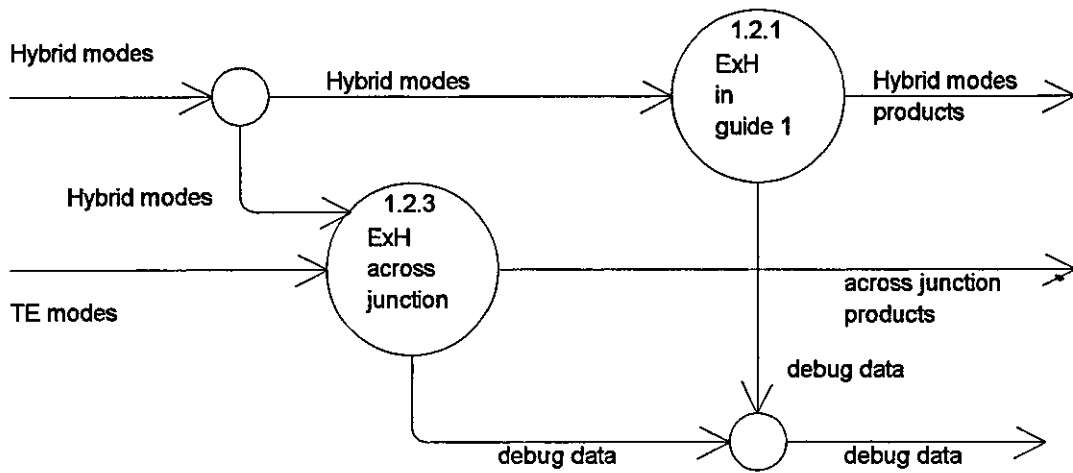




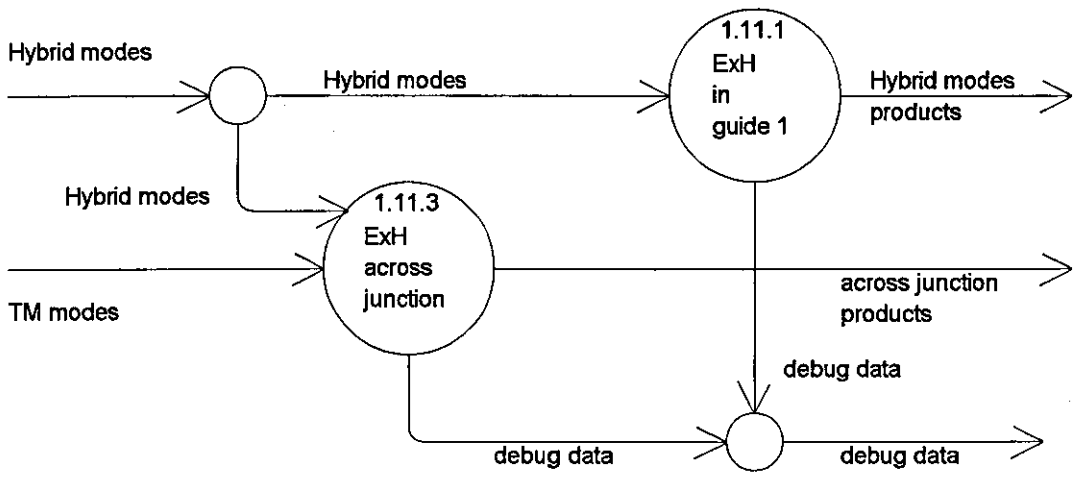
Project Name: FSG\_Solid\_trans  
 Project Path: d:\codede~1\fsg\_sol2\  
 Chart File: dfd00004.dfd  
 Chart Name: read input  
 Created On: Jun-12-1996  
 Created By: james eade  
 Modified On: Jun-03-2001  
 Modified By: james eade



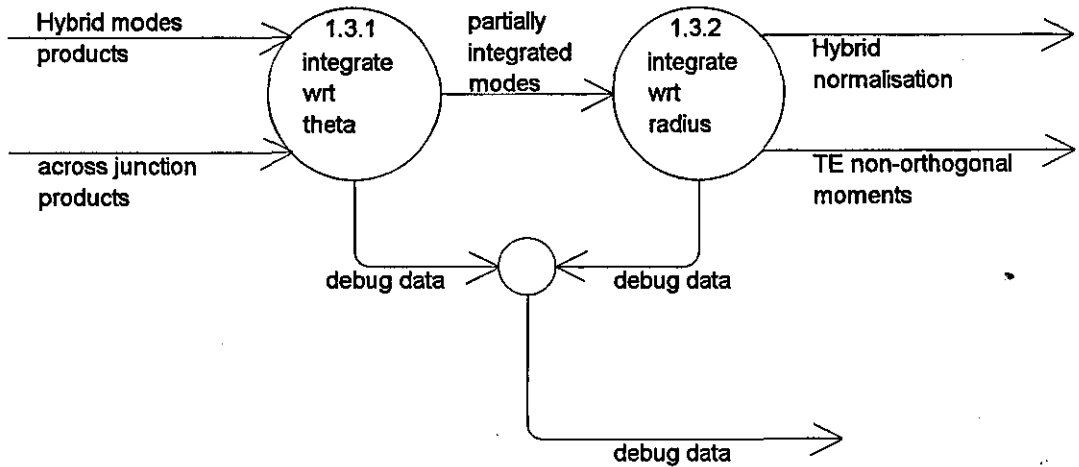
Project Name: FSG\_Solid\_trans  
 Project Path: d:\codede~1\fsg\_sol2\  
 Chart File: dfd00005.dfd  
 Chart Name: mode cross products  
 Created On: Jun-13-1996  
 Created By: james eade  
 Modified On: Nov-08-2000  
 Modified By: james eade



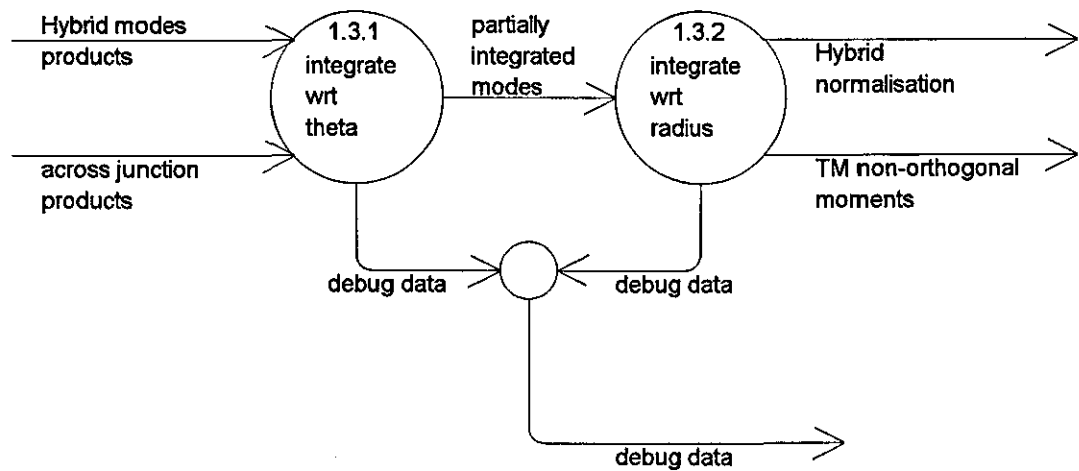
Project Name: FSG\_Solid\_trans  
 Project Path: d:\codede~1\fsg\_sol2\  
 Chart File: dfd00005.dfd  
 Chart Name: mode cross products  
 Created On: Jun-13-1996  
 Created By: james eade  
 Modified On: Jun-03-2001  
 Modified By: james eade



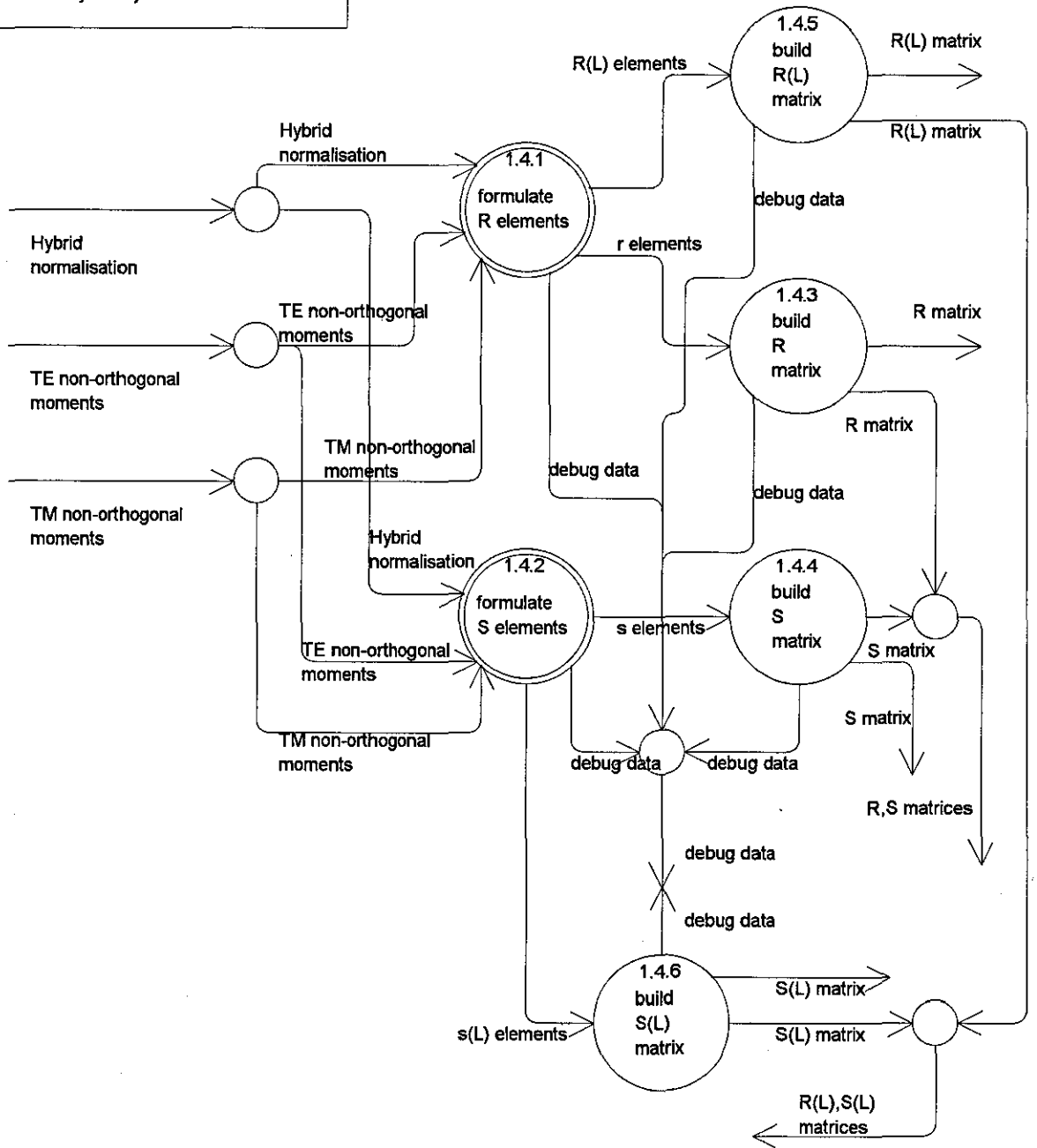
Project Name: FSG\_Solid\_trans  
Project Path: d:\codede~1\fsg\_sol2\  
Chart File: dfd00006.dfd  
Chart Name: cross section integrals  
Created On: Jun-13-1996  
Created By: james eade  
Modified On: Nov-08-2000  
Modified By: james eade



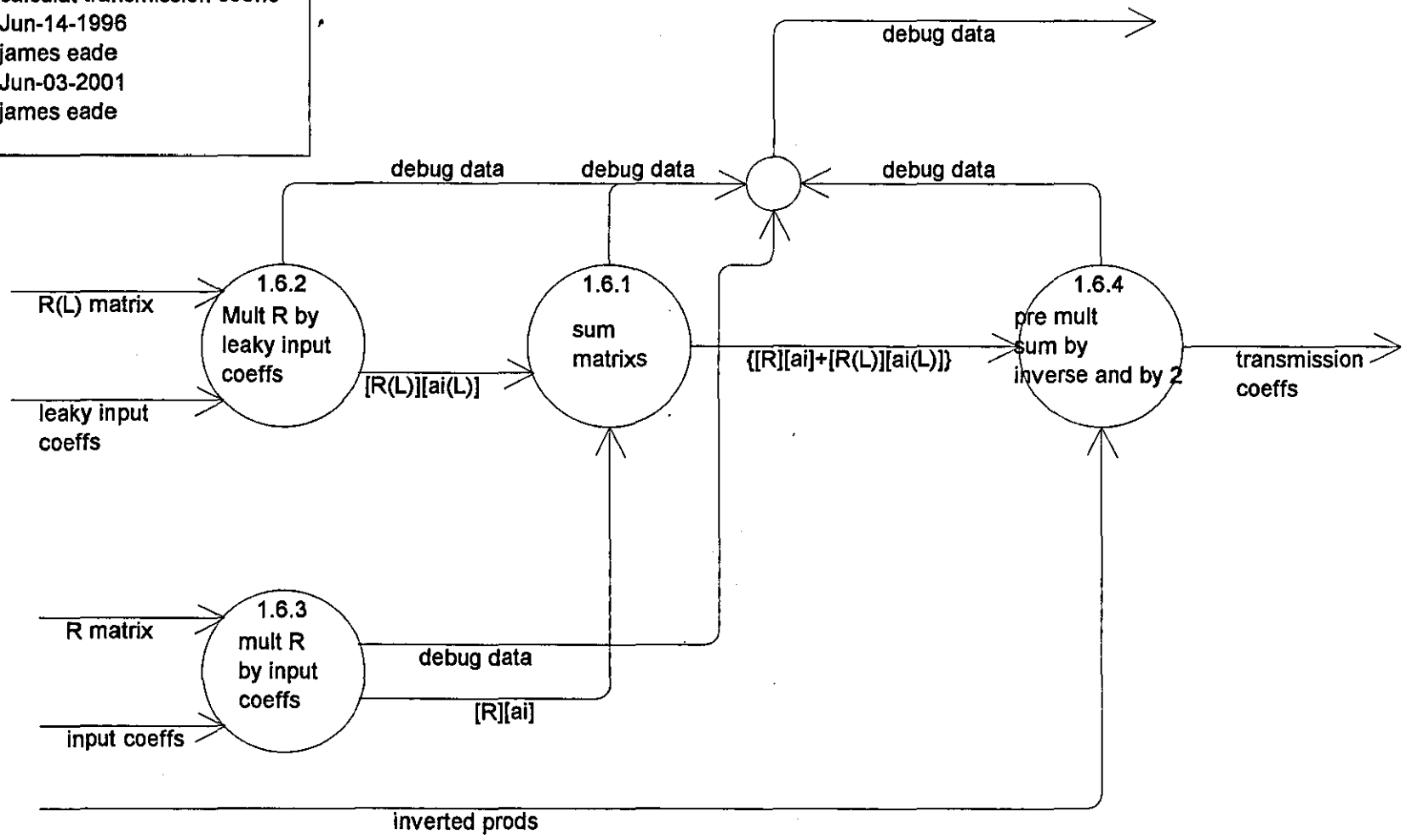
Project Name: FSG\_Solid\_trans  
Project Path: d:\codede~1\fsg\_sol2\  
Chart File: dfd00006.dfd  
Chart Name: cross section integrals  
Created On: Jun-13-1996  
Created By: james eade  
Modified On: Nov-08-2000  
Modified By: james eade



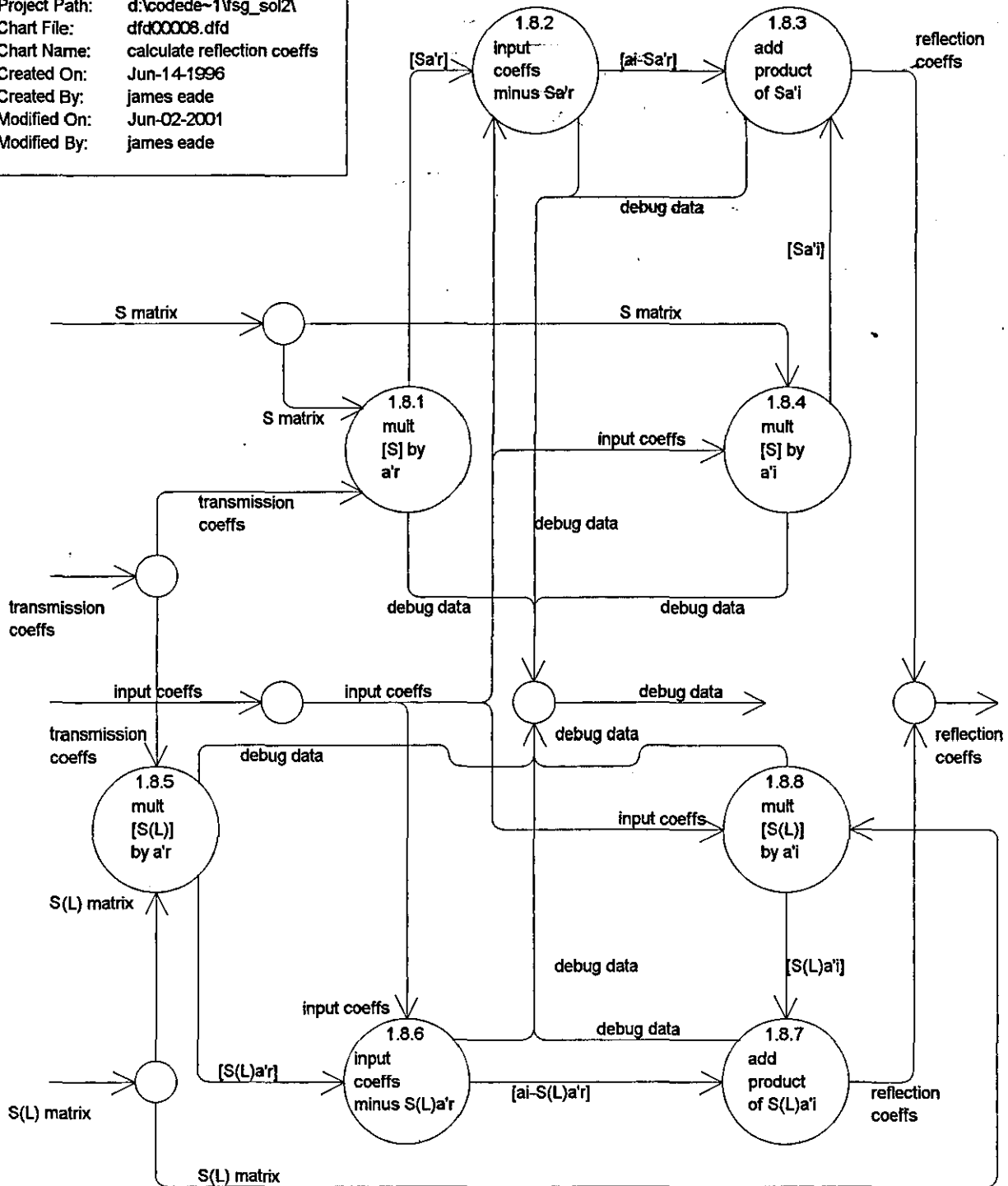
Project Name: FSG\_Solid\_trans  
 Project Path: d:\codede-1\fsq\_sol2\  
 Chart File: dfd00007.dfd  
 Chart Name: format R,S matrixs  
 Created On: Jun-13-1996  
 Created By: james eade  
 Modified On: Jun-03-2001  
 Modified By: james eade



Project Name: FSG\_Solid\_trans  
 Project Path: d:\code\de~1\fsg\_sol2\  
 Chart File: dfd00009.dfd  
 Chart Name: calculat transmission coeffs  
 Created On: Jun-14-1996  
 Created By: james eade  
 Modified On: Jun-03-2001  
 Modified By: james eade



Project Name: FSG\_Solid\_trans  
 Project Path: d:\code\de~1\fsg\_sol2\1  
 Chart File: dfd00008.dfd  
 Chart Name: calculate reflection coeffs  
 Created On: Jun-14-1996  
 Created By: james eade  
 Modified On: Jun-02-2001  
 Modified By: james eade



### **1.2.3 & 1.11.3 E x H Across Junction**

The transverse E and H modes are vector cross multiplied across the junction. The E field is taken from the 1st guide and the H field is taken from the 2nd guide. The result is the (product of 2 bessels + the product of a bessel and a differential of a bessel) multiplied by a  $\sin(n \theta)\sin(m \theta)$  term. Plus the product of the differentials of the 2 bessels + the product of a bessel and a differential of a bessel) multiplied by a  $\cos(n \theta)\cos(m \theta)$  term.

### **1.3.1 & 1.12.1 Integrate wrt Theta**

When the mode cross product is integrated wrt theta the  $\sin\sin$  terms and the  $\cos\cos$  terms are the ones that are integrated. Now these will be subject to orthogonality principle. If the order  $n$  &  $m$  is different (i.e  $n \neq m$ ) then the result of the integration is zero and the modes are said to be orthogonal. If the order is the same ( $n = m$ ) then when  $n=0$  the  $\sin$  squared term integrates to give zero and the  $\cos$  squared term integrates to give  $2\pi$ ; when  $n \neq 0$  then the  $\sin$  squared and  $\cos$  squared terms integrate to give  $\pi$ .

This result simplifies the integration of the bessel functions as now we are only concerned with the integration of a bessel product where they are of the same order, but the arguments can still differ. We have definite formulas for the integration of the bessel products.

N.B. If a  $\sin(x)*\cos(x)$  or  $\cos(x)*\sin(x)$  product is produced then this can be turned into a  $\sin(x)*\sin(x)$  or a  $\cos(x)*\cos(x)$  term by twisting the output fields through  $\pi/2$ . this means that a TE, TM interaction can take place.

### **1.3.2 & 1.12.2 Integrate wrt Radius**

Use definite integral formula. The one which is used depends on the order and whether a TE or TM mode is considered.

If the integral is of the cross junction vector product it is taken over the radius of the solid guide - as E tangential is zero of the surface of the rest of the flange surface.

If the integral is of the modes in the solid guide then it is taken over the radius of the solid guide and similarly if the modes are those in the fsg the radius used for surface wave is 0 to infinity and 0 to main beam radius for leaky modes in the integration.

### **1.4.1 Formulate R Elements**

The value of the R elements is the cross section integral of the vector product taken across the guide junction divided by the normalisation of the fields in the FSG. Normal R elements use the hybrid surface wave fields. R(L) elements uses the hybrid leaky fields only.

N.B. the fields in the solid guide have already been normalised.

### **1.4.2 Formulate S Elements**

The S element is the cross section integral of the vector product taken across the guide junction divided by normalisation of the FSG modes. Normal S elements use the hybrid surface wave fields. S(L) elements uses the hybrid leaky fields only. N.B. the solid guide modes have already been normalised.

### **1.5 multiply matrix**

Post multiply the R matrix by the S matrix to give a p' by p' matrix, where p is the number of test modes in the output guide. Post multiply the R(L) matrix by the S(L) matrix to give a p' by p' matrix, where p is the number of test modes in the output guide.

### **1.8.4 Mult [S] by a<sub>i</sub>'**

This process will normally be zero as a<sub>i</sub>' is usually zero and the second guide is considered infinite or matched.

### **1.8.8 Mult [S(L)] by a<sub>i</sub>'**

This process is usually zero as a<sub>i</sub>' is normally zero as the second guide is considered to be infinite or matched.

### **1.9 invert Matrix**

Invert the sum of  $[R(L)S(L)]+[RS]+[I]$  to give the inverse matrix.

### **1.10 Add Unit Matrix**

Add a p by p unit matrix to RS product matrix and add in R(L)S(L) product matrix.

### **User Data Input**

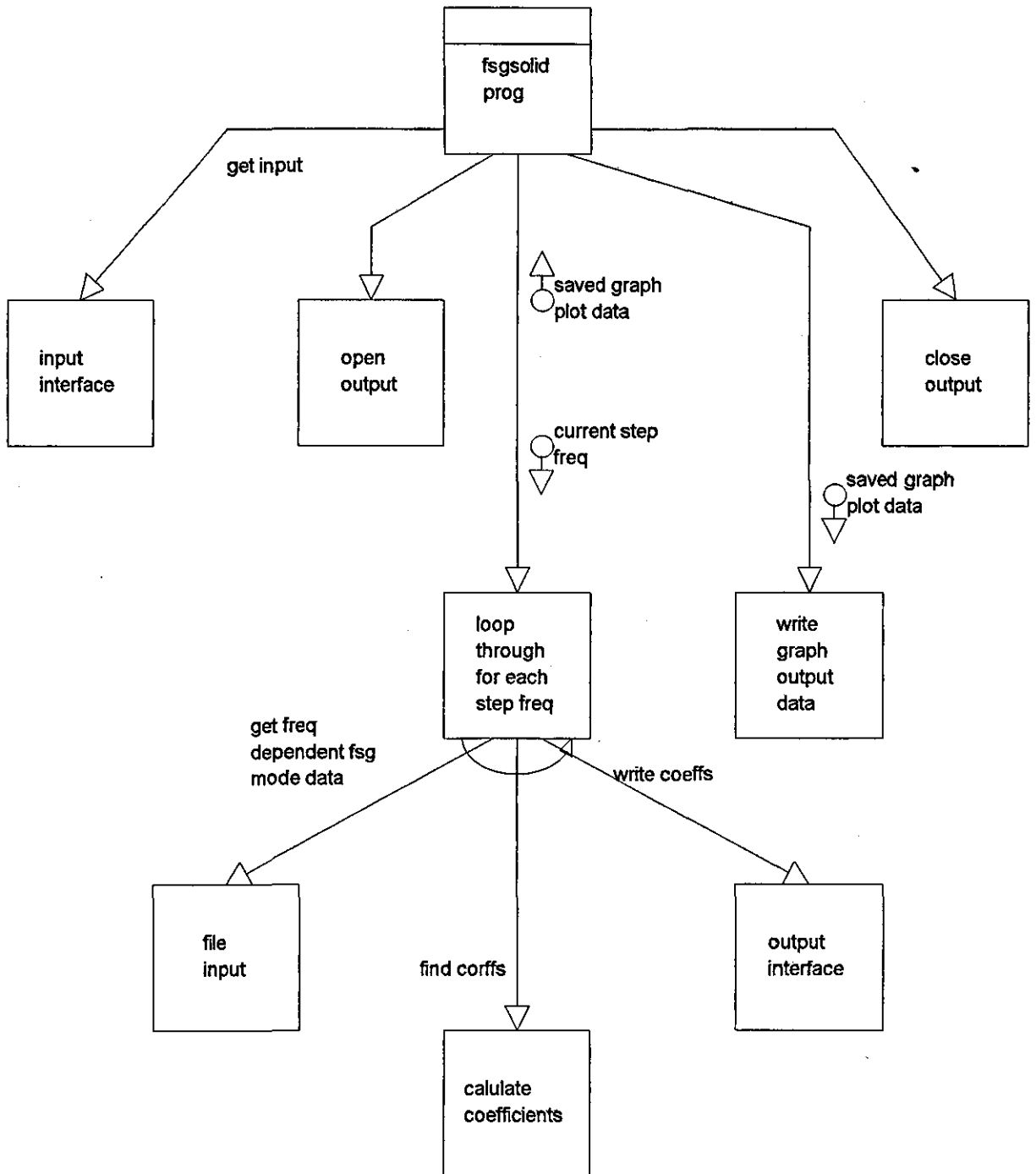
The structure radius'; Number of modes in the solid waveguide; i/p mode coefficients; FSG propagation constants; Number of Floquet modes; relative levels of the TE to TM in the hybrid mode; number of Bloch modes in the FSG; the FSG length from the source.

### **System Input**

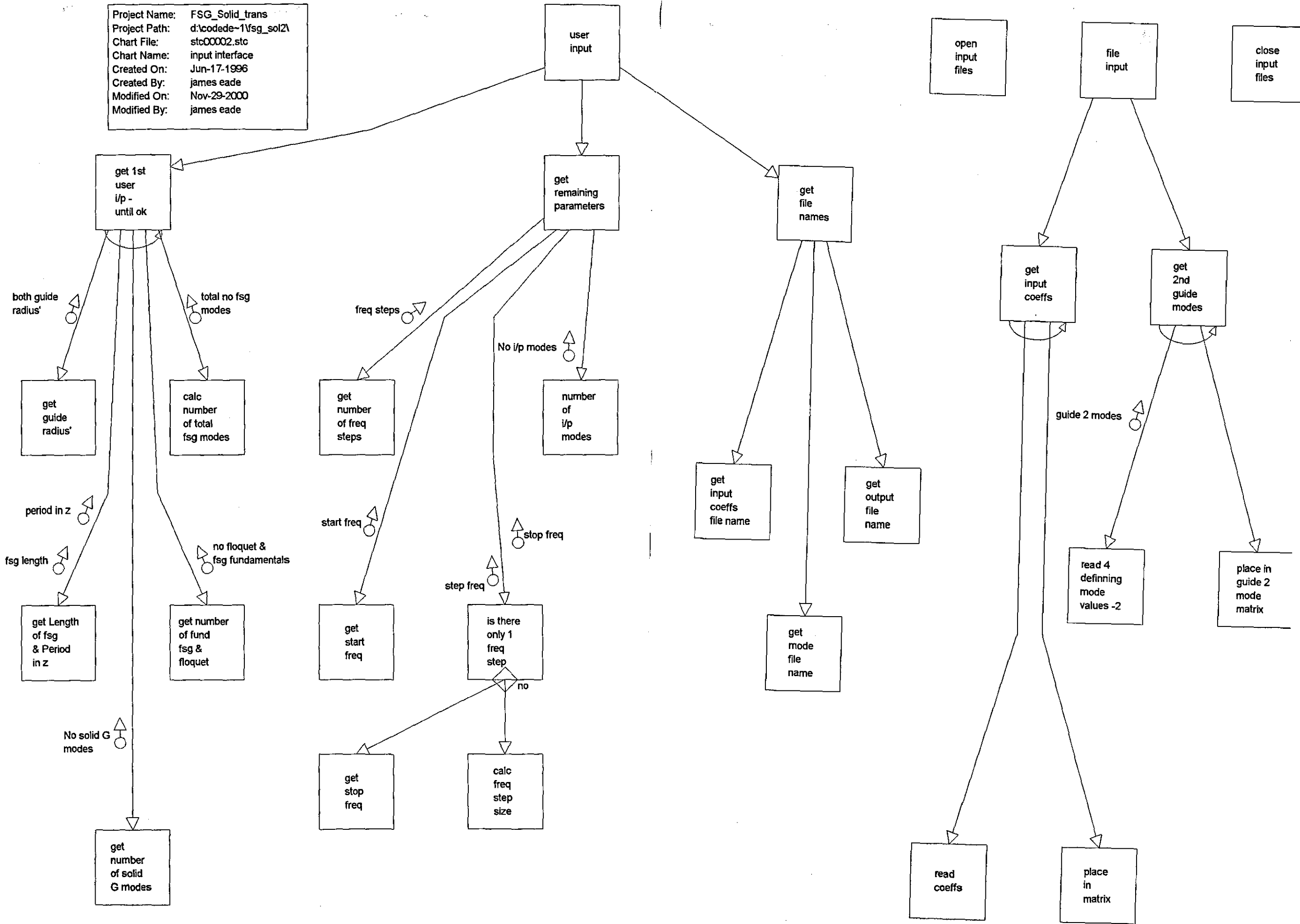
All physical constants and the propagation constants of the solid waveguide.



Project Name: FSG\_Solid\_trans  
 Project Path: d:\cocode~1\fsg\_sol2\  
 Chart File: stc00001.stc  
 Chart Name: StepTrans prog  
 Created On: Jun-17-1996  
 Created By: james eade  
 Modified On: Nov-29-2000  
 Modified By: james eade



Project Name: FSG\_Solid\_trans  
 Project Path: d:\code\code-1\fsq\_sol2\1  
 Chart File: stc00002.stc  
 Chart Name: input interface  
 Created On: Jun-17-1996  
 Created By: james eade  
 Modified On: Nov-29-2000  
 Modified By: james eade

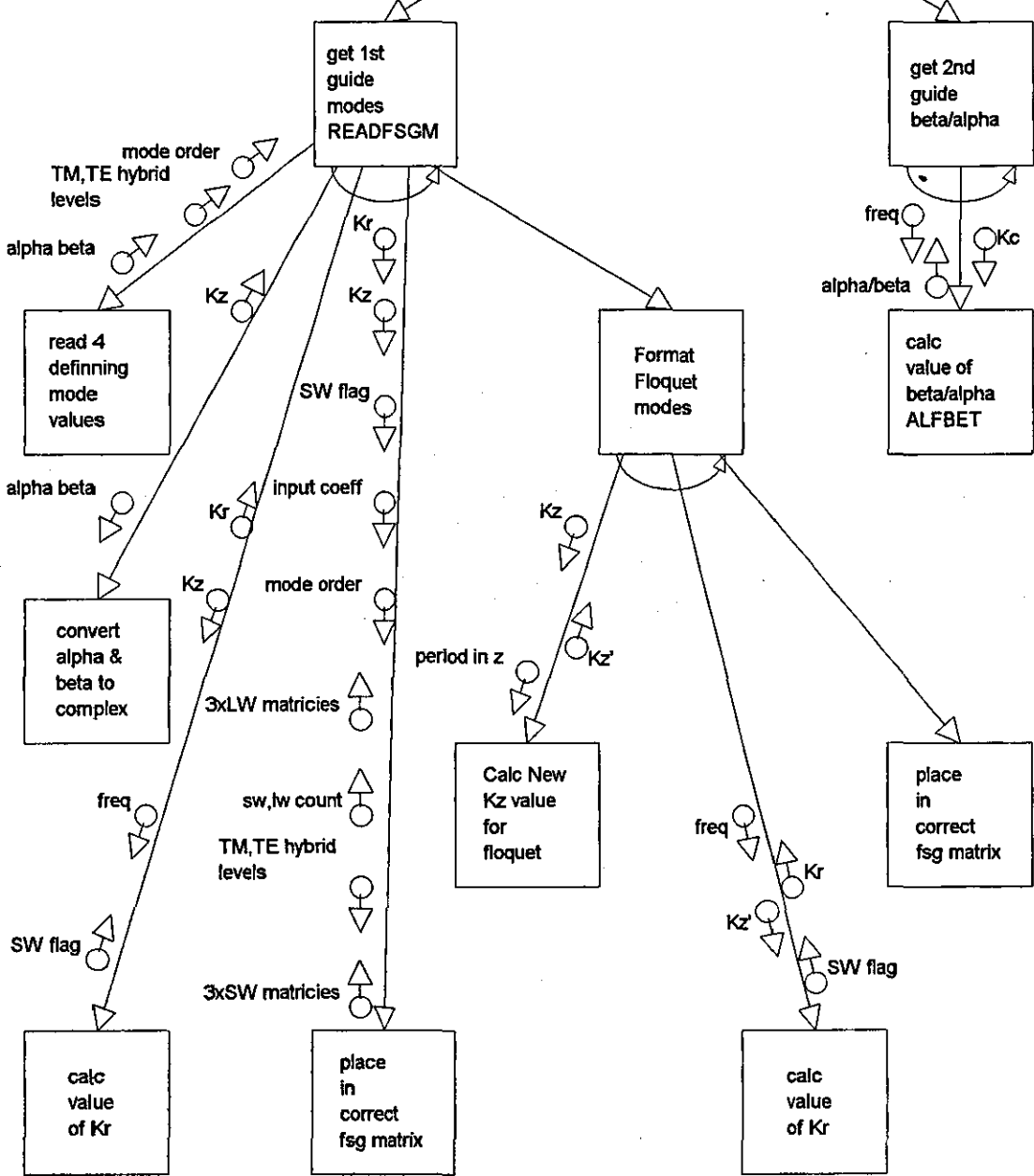


Project Name: FSG\_Solid\_trans  
 Project Path: d:\codede-1\fsg\_sol2\1  
 Chart File: stc00031.stc  
 Chart Name: file input  
 Created On: Jul-10-1998  
 Created By: james  
 Modified On: Nov-29-2000  
 Modified By: james eade

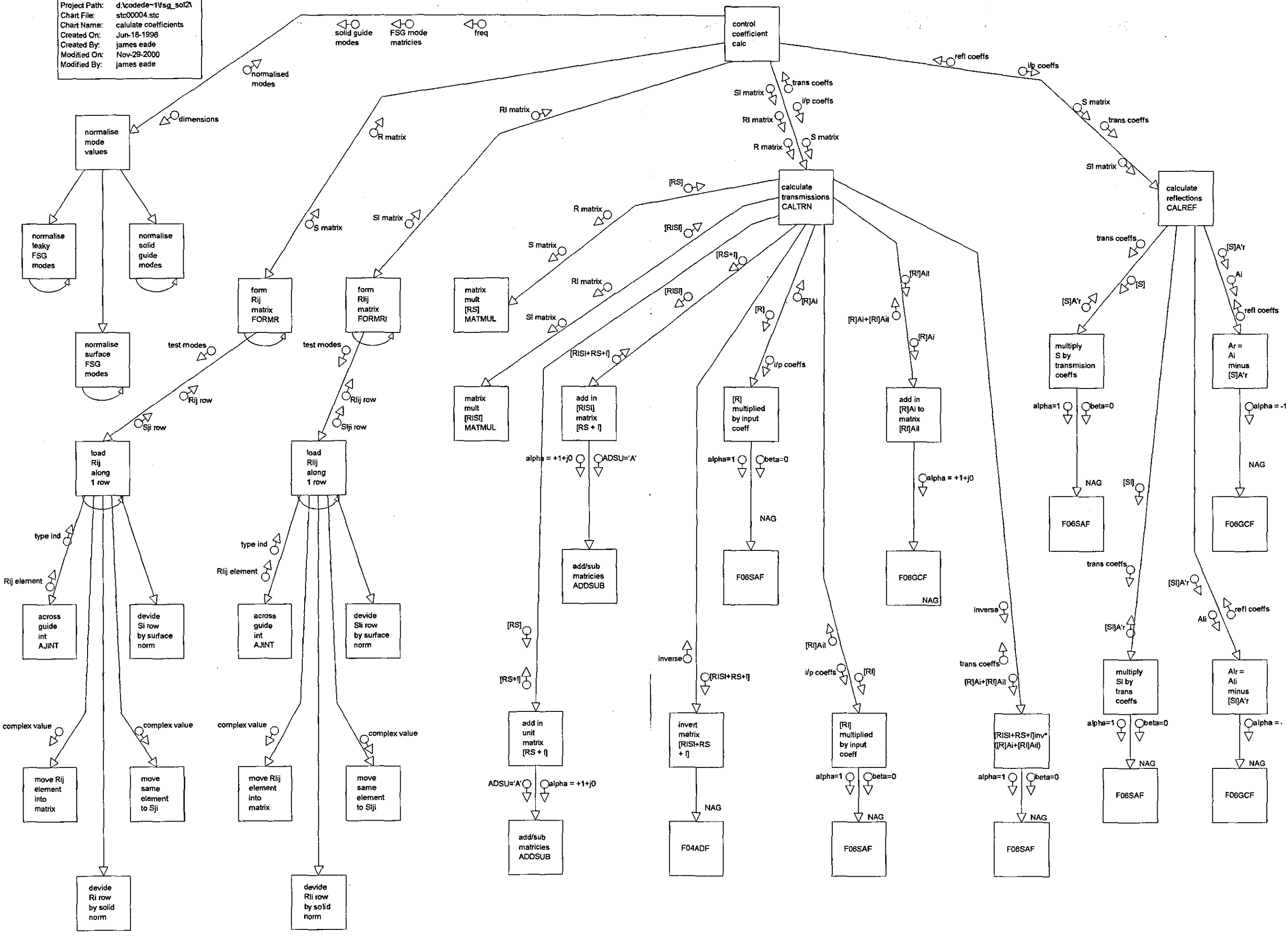
open fsg mode data files

obtain freq depend mode data

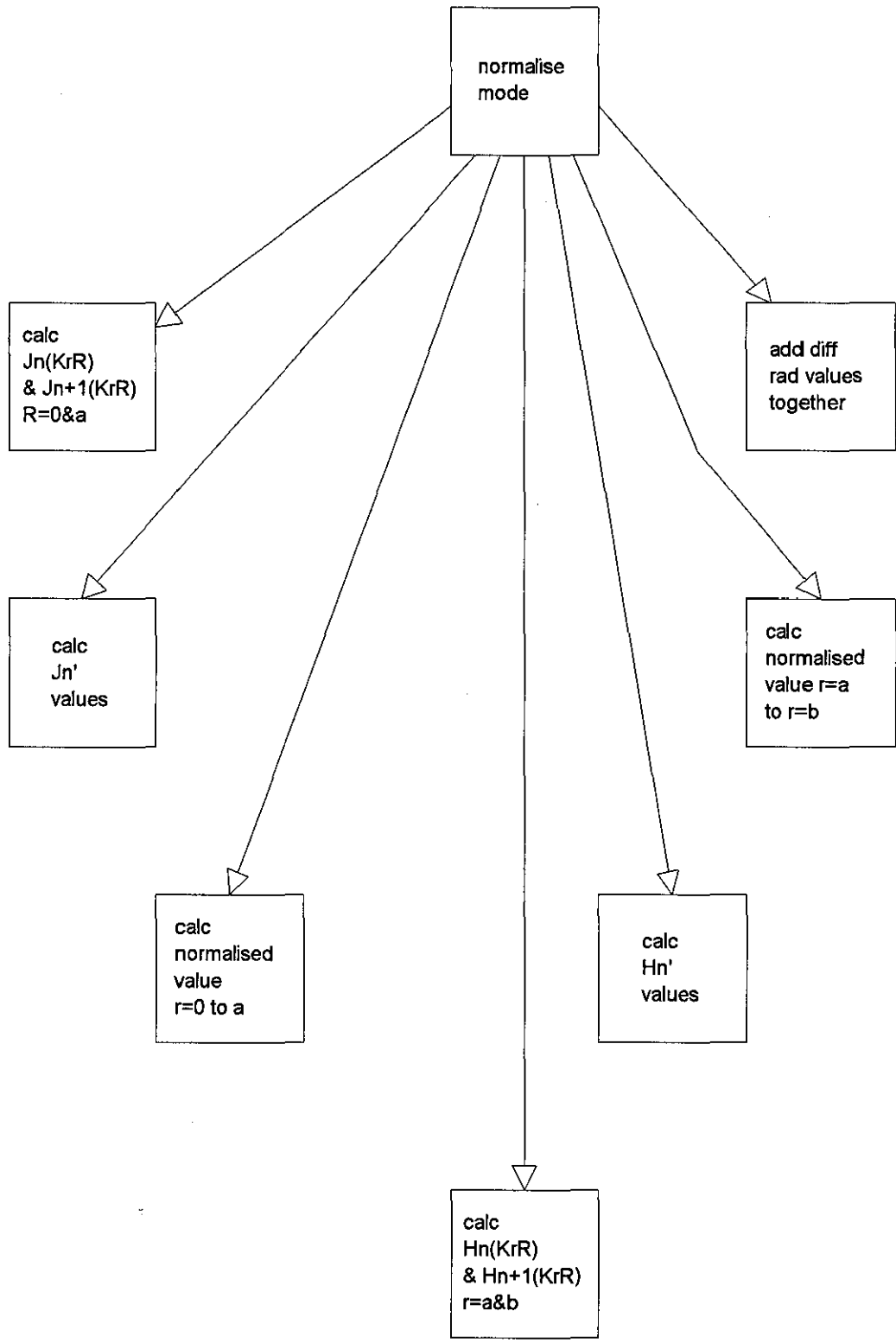
close fsg mode data files



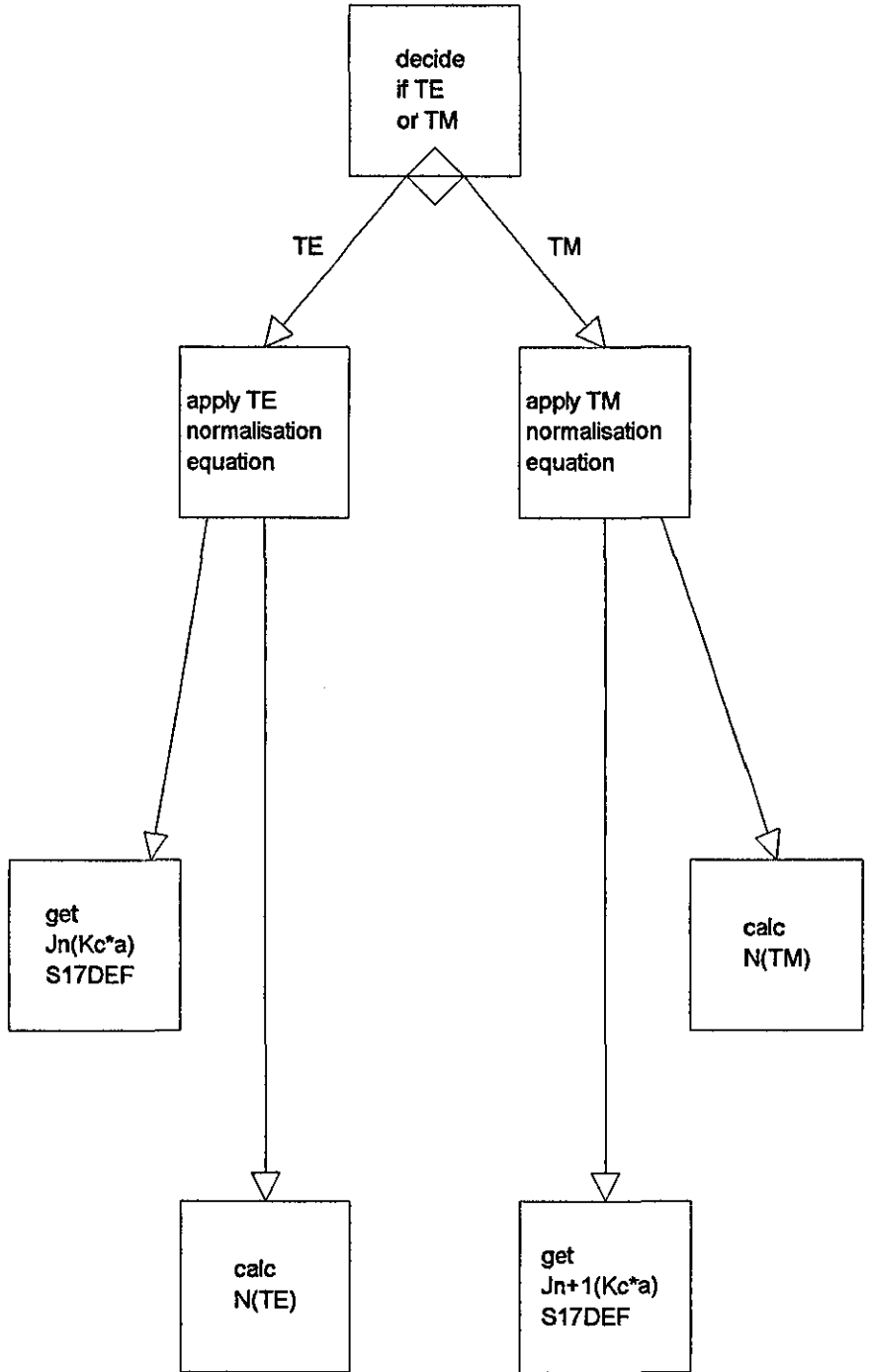
Project Name: FSG\_Solid\_trans  
 Project Path: d:\code\1\vsg\_sol2\1  
 Chart File: stc00004.stc  
 Chart Name: calculate coefficients  
 Created On: Jun-18-1996  
 Created By: james eade  
 Modified On: Nov-29-2000  
 Modified By: james eade



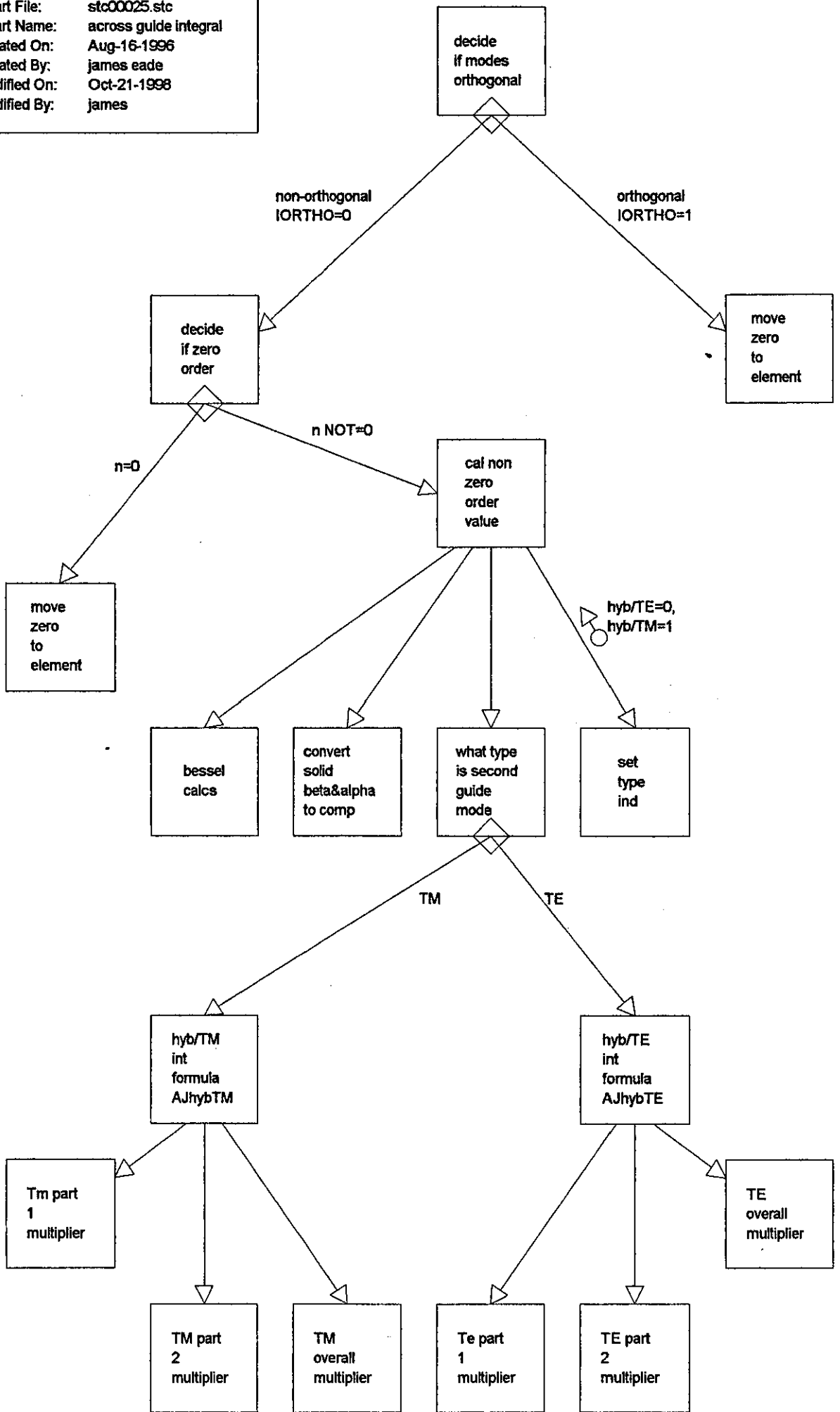
Project Name: FSG\_Solid\_trans  
Project Path: d:\codede~1\fsg\_sol2\  
Chart File: stc00041.stc  
Chart Name: normalise leaky FSG modes  
Created On: Jul-22-1998  
Created By: james  
Modified On: Jun-03-2001  
Modified By: james eade



Project Name: FSG\_Solid\_trans  
Project Path: d:\code\de-1\fsg\_sol2\  
Chart File: stc00040.stc  
Chart Name: normalise solid guide modes  
Created On: Jul-15-1998  
Created By: james  
Modified On: Jul-22-1998  
Modified By: james



Project Name: FSG\_Solid\_trans  
 Project Path: d:\codede-1\fsg\_sol2\stc00025.stc  
 Chart File: stc00025.stc  
 Chart Name: across guide integral  
 Created On: Aug-16-1996  
 Created By: james eade  
 Modified On: Oct-21-1998  
 Modified By: james



Project Name: FSG\_Solid\_trans  
Project Path: d:\code\de~1\fsg\_sol2\  
Chart File: stc00011.stc  
Chart Name: output interface  
Created On: Jun-18-1996  
Created By: james eade  
Modified On: Jun-03-2001  
Modified By: james eade

